

**EFFECT OF GRAPHITIZATION ON THE STATIC MECHANICAL
PROPERTIES OF SERVICE EXPOSED ASTM A516 Gr. 65
STEAM PIPE METAL**

By

CHRISTIAAN DU PREEZ

Submitted in fulfilment of the requirements for the degree

Magister Scientiae

in the Faculty of Science at the

Nelson Mandela Metropolitan University

April 2017

Supervisor: Dr. J.E. Westraadt

Co-supervisors: Prof. D.G. Hattingh and Prof. J.H. Neethling

Declaration

I, **Christiaan du Preez, S211275557**, hereby declare that the dissertation for the degree Magister Scientiae is my own work and that it has not previously been submitted for assessment or completion of any postgraduate qualification to another university or for another qualification.

Signature: _____

Date: _____

Summary

The focus of this research project is to establish what effect graphitization has on the static mechanical properties of service exposed ASTM A516 Grade 65 steam pipe material, which operated for prolonged periods above 425 °C.

The research study was conducted on three graphitized service exposed steam pipe weldment samples and on a newly welded and post weld heat treated sample with graphitized service exposed steam pipe material. Macro samples were removed from each of the samples at two positions and these were evaluated with regard to graphite nodule size, nearest neighbour spacing and % planar graphitization in the parent pipe and HAZ regions on either side of the welds. It was found on all of the service exposed samples that the graphite nodules of the HAZ regions have a smaller median nodule size, smaller median nearest neighbour spacing and increased % planar graphitization in comparison to the parent pipe material.

The service expose parent pipe material on either side of the weldments of the respective samples was chemically analyzed. This was done with the focus being on the deoxidizing element content (Si and Al) of the respective parent pipe regions and to what extent these elements influenced the development of planar graphitization in these regions. No correlation could be identified between the level of deoxidizing elements and the levels of % planar graphitization in the parent pipe material.

Tensile and Charpy impact samples were removed from the respective service exposed samples parent material on either side of the weld and from the HAZ regions on the side with the highest levels of planar graphitization. These samples were tested and the yield and ultimate tensile strength and Charpy impact toughness of the respective samples were then evaluated to establish how these static mechanical properties were influenced by the % planar graphitization.

The yield and ultimate tensile strength of the service exposed material did not show a statistically significant correlation with the % planar graphitization. The Charpy impact toughness results did however show a statistically significant negative correlation towards the % planar graphitization. This was clearly evident from the results of the HAZ regions of the service exposed weldments (Samples A-C) which had the highest levels of % planar graphitization and the lowest impact toughness, while the newly welded and post weld heat treated Sample D had no planar graphitization outside the HAZ and the highest impact toughness.

This research project not only investigated how planar graphitization affects the static mechanical properties of service exposed pipe material, it also investigated on a microstructural basis, how planar graphitization nucleates and grows.

The microstructural investigation showed that the free carbon required for the development of planar graphitization originated from the regions outside the HAZ, which were formed when the pearlite bands were dissolved during the welding of the steam pipe. The heat input from the welding sensitized this region for the development of planar graphitization, probably due to the formation of a “carbon-rich” matrix due to the partial dissolution of the cementite precipitates. All the carbide precipitates in this region consisted of M_3C . aluminium-rich precipitates were found inside newly nucleated graphite nodules, indicating its role as a possible heterogeneous nucleation site. Growth of newly formed graphite nodules showed a preference towards high-angle grain boundaries and regions with dislocations for the initial growth stages of the graphite nodules.

The microstructure of the region outside the HAZ of the newly introduced seam weld on the service exposed steam pipe material (with graphitization), was also investigated using advanced electron microscopy methods and it yielded no evidence of the development of planar graphitization.

Acknowledgements

I would like thank God my creator and savior for His grace and strength which carried me through my studies. I would also like to thank my wife and two boys for their patience, support and encouragement throughout my studies, especially during the difficult times.

I would also like to thank my promotor Dr. Johan Westraadt and my two co-promoters Prof. Danie Hattingh and Prof. Jan Neethling for giving me the opportunity to work on this research project. Thanks for all your support, assistance and encouragement through my research and for believing in me. I really do appreciate it a great deal.

I would also like to thank Sasol and eNtsa for the financial support and assistance throughout the research project, enabling me to further my studies. I really do appreciate it from the bottom of my heart.

I would also like to thank Mr. Charl Orsmond for his support and metallurgical advice, I really do appreciate it a great deal.

I would also like to thank all of the personnel at eNtsa and the Mechanical engineering workshop and the Centre for HRTEM your support and assistance throughout my research. I could not have done it without you.

Contents

Summary	i
List of Tables.....	xix
Glossary of terms and explanation.....	xx
Chapter 1 : Introduction	1
1.1. Introduction:.....	1
1.2. General Objectives:	1
1.3. Problem Statement:	2
1.3.1. Sub problem one:	2
1.3.2. Sub problem two:.....	2
1.3.3. Sub problem three:.....	2
1.3.4. Sub problem four:.....	2
1.4. Hypothesis:.....	2
1.5. Delimitations:	2
1.6. Assumptions:	3
1.7. The Significance of the Research	3
1.8. Research Methodology.....	3
Chapter 2 : Literature Review	5
2.1. Material Properties and Chemistry.....	5
2.2. Typical Microstructure of Low Carbon Pressure Vessel Steels	6
2.3. The Influence of Welding as a Fabrication Process on the Microstructure of Low-Carbon Pressure Vessel Steel	12

2.3.1. Introduction.....	12
2.3.2. The Fusion Zone Solidification and Microstructure.....	13
2.3.3. The Heat Affected Zone Microstructural Regions.....	14
2.3.4. The Effect of Multipass Weldments on the Microstructure of the Fusion and Heat Affected Zones	16
2.4. The Effect Elevated Temperature Operation has on the Microstructure of Carbon Steel Steam Pipe Material	18
2.4.1. Introduction.....	18
2.4.2. The Graphitization Phenomenon.....	18
2.4.3. The Different Forms of graphitization that Develop During Over-aging	20
2.4.4. Factors Contributing to the Formation of Graphitization in Carbon Steels:	23
2.4.5. The Effect of Graphite on the Hardness, Tensile Strength and Impact Toughness of Service Exposed Steam Pipe Material.....	25
Chapter 3 : Graphitization - Evaluation Techniques and Influence on Static Mechanical Properties	27
3.1. Introduction.....	27
3.2. Chemical Evaluation of Selected Service Expose Steam Pipe Material Samples.....	27
3.2.1. Bulk Chemical Analyzing	28
3.2.2. Carbon and Sulphur Analyzing.....	28
3.2.3. Combined Chemical Evaluation Results.....	29
3.3. Evaluation of the Graphitization in the Service Exposed Pipe Samples .	31
3.3.1. Introduction.....	31

3.3.2. Procedure used to Prepare the Macro Samples.....	31
3.3.3. Initial Findings with regard to HAZ Graphitization of the Service Expose Pipe Samples	34
3.3.4. Graphite Nodule Size Evaluation.....	35
3.3.5. Graphite Nodule Spacing Evaluation.....	37
3.3.6. Percentage Planar Graphitization Evaluation	39
3.4. The effect of Graphite on the Hardness of the Service Expose Steam Pipe Samples	41
3.4.1. Introduction.....	41
3.4.2. Procedures used during the Hardness Evaluation of Pipe Samples	41
3.4.3. Micro Vickers Hardness Profile Evaluation Results.....	42
3.5. The Effect of Graphite on the Yield and Tensile Strength of the Service Exposed Steam Pipe Samples	47
3.5.1. Introduction.....	47
3.5.2. Tensile Sample Orientation and Pipe Regions being Evaluated	47
3.5.3. Room Temperature Tensile Testing	50
3.5.4. Elevated Temperature Tensile Testing.....	51
3.5.5. Yield and Tensile Strength Evaluation Results of Service Exposed Steam Pipe with graphitization	52
3.6. The effect of Graphite on the Charpy Impact Toughness of Service Exposed Steam Pipe Material	65
3.6.1. Introduction.....	65
3.6.2. Charpy Impact Sample Orientation and Pipe Regions being Evaluated	65

3.6.3. Room Temperature Charpy Impact Testing	66
3.6.4. Impact Toughness of Service Exposed Steam Pipe with Graphitization	68
3.6.5. Evaluation of Newly Introduced Connection Seam Weld.....	79
3.7. The effect of chemical composition on the formation of graphite.....	80
3.8. Summary	81
Chapter 4 : Experimental Methods used for Microstructural Characterization ..	83
4.1. Introduction.....	83
4.2. Scanning Electron Microscopy and Associated Techniques.....	84
4.2.1. Electron - specimen interactions	84
4.2.2. Imaging using Secondary and Backscattered Electrons.....	84
4.2.3. Energy Dispersive X-ray Spectrometry.....	88
4.2.4. Electron Backscattered Diffraction.....	90
4.3. Focused Ion Beam SEM.....	92
4.4. Transmission Electron Microscopy and Associated Techniques	94
4.4.1. Scanning Transmission Electron Microscopy	94
Chapter 5 : Microstructural Evaluation of the Welded Steam Pipe Samples.....	97
5.1. Introduction.....	97
5.2. Light Microscopic Evaluation of the Welded Samples	98
5.3. Scanning Electron Microscopy Evaluation of Welded Samples.....	101
5.3.1. Backscattered Electron.....	101
5.3.2. Electron Backscattered Diffraction Analysis	104
5.4. Transmission Electron Microscopy of Selected Areas.....	107

5.4.1. Sample A's Parent Material	107
5.4.2. Sample A's Planar Graphitized Zone.....	108
5.4.3. Evaluation of Sample D's Microstructure Outside the HAZ	114
5.5. Summary of Microstructural Evaluation	116
Chapter 6 : Discussion of Research Results and Conclusions	118
6.1. Introduction.....	118
6.2. Discussion of Chemical Evaluation Results of Graphitized Service Exposed Steam Pipe Material and Findings based on these Results.....	118
6.3. Discussion of the Graphite Nodule Size, Spacing and Percentage Graphitization found to be present in the Evaluated Service Pipe Samples	119
6.4. Discussion of Hardness Evaluation Results of Service Exposed Pipe samples and how the Current Levels of Graphitization Influenced it	119
6.5. Discussion of the Yield and Tensile Strength Evaluation Results of Service Exposed Pipe Samples and how the Current Levels of Graphitization Influenced it	120
6.6. Discussion of the Charpy Impact Strength Evaluation Results of the Service Exposed Pipe Material and how the Current Levels of Graphitization Influenced it	122
6.7. Discussion of the Microstructural Evaluation Results of Samples A and D obtained using Advanced Electron Microscopy	123
6.8. Conclusions Drawn from the Results of the Different Evaluation Processes.....	124
6.9. Future Work and Recommendations	126

List of Figures

Figure 2-1: An image of a Bessemer converter, used for the deoxidization of fully killed steels during the 1950's [2].	6
Figure 2-2: Schematic flow chart of the different manufacturing steps used for the manufacturing of fully killed plate material [2].	7
Figure 2-3: The pancake arrangement of the ferrite and pearlite	7
Figure 2-4: Iron-Iron Carbide phase diagram showing the different microstructural	8
Figure 2-5: An illustration of the mechanism of banding [5].	9
Figure 2-6: Schematic Representation of Transformations of Carbon steel during slow cooling	10
Figure 2-7: The variation of manganese and silicon across representative bands in the specimen shown in Figure 2-3, using EPMA [3].	11
Figure 2-8: Schematical representation of the mechanism of banding in Carbon steels containing substantial levels of manganese Sulphides [5].	12
Figure 2-9: Schematic illustration of the essential constituents of the primary microstructure in the columnar austenite grains of a steel weld deposit [7].	13
Figure 2-10: Showing a scanning electron micrograph of the primary microstructure of a steel weld	14
Figure 2-11: Schematic illustration of the microstructural variation to be expected in the heat affected zone of Carbon steel welds [7].	15
Figure 2-12: Schematical illustration of the primary deposited weld metal (P) and the reaustenitized regions (where temperatures are in the region of A_3 and A_1)	16
Figure 2-13: Schematic showing the different subzones that can form in the coarse grained region of the HAZ of a multipass weld:	17

Figure 2-14: The temperature-time plot of pearlite decomposition by spheroidization and graphitization [15].	19
Figure 2-15: An example of random nodular graphitization in a carbon steel, with the graphite nodules pointed out by the arrows [11].	20
Figure 2-16: A macrograph of welded carbon steel, which were service exposed/over-aged resulting in the formation of the planar or “eyebrow” graphitization pointed out by the arrows [14].	21
Figure 2-17: A reheater tube which failed due to the formation of planar base metal graphitization, which formed specifically at high strained regions [14].	22
Figure 2-18: The variation with time of the volume fraction of graphite formed and the hardness [21].	25
Figure 3-1: The SpectromaxX Spark spectrometer used to determine the bulk chemical composition of the service exposed steam pipe samples.	28
Figure 3-2: The Bruker Caron Sulphur analyzer, used to accurately determine the Carbon and Sulphur content of the service expose steam pipe samples.	29
Figure 3-3: The typical regions from where the macro sample samples were removed from the service pipe samples.	31
Figure 3-4: The ATM Saphir 550 semi-automatic polishing machine used to fine ground and polish the large macro samples and smaller micro samples.	32
Figure 3-5: An example of how the large macro samples were secured to the universal polishing head (L/H side) and the final polished macro samples (R/H side).	32
Figure 3-6: A typical example of one of the polished and etched macro samples.	34
Figure 3-7: The areas evaluated with regard to graphite nodule size and spacing and % planar graphitization.	35
Figure 3-8: Illustration showing the graphite nodule size measuring method.	36

Figure 3-9: Graphical summary of the graphite nodule size evaluation results.	37
Figure 3-10: An example of how the spacing between neighbouring graphite nodules was measured on one of the micrographs taken 100X magnification.	38
Figure 3-11: Graphical summary of the graphite nodule spacing evaluation results	38
Figure 3-12: The planar projection method used to calculate the % planar graphitization of the various pipe regions evaluated	39
Figure 3-13: The application of the planar projection method.	40
Figure 3-14: A graphical summary of the % planar graphitization evaluation results.	40
Figure 3-15: The Future tech FM700 automatic Vickers Micro Hardness tester used for the hardness profile measurements on the service exposed pipe samples.	42
Figure 3-16: The areas where the Vickers micro Hardness profile measurements were done.	42
Figure 3-17: A graphical summary of the Vickers micro hardness profile results of Weld Sample A	43
Figure 3-18: A graphical summary of the Vickers micro hardness profile results of Weld Sample B.	43
Figure 3-19: A graphical summary of the Vickers micro hardness profile results of Weld Sample C.	44
Figure 3-20: A graphical summary of the Vickers micro hardness profile results of Weld Sample D.	44
Figure 3-21: The centre areas where the five Vickers micro Hardness profile measurements were done on either side of Weld Sample A.	45
Figure 3-22: Graphical summary of the Vickers micro hardness data from	46

Figure 3-23: The positions where the parent material bulk tensiles were removed.....	48
Figure 3-24: The position where the tensile samples were taken from just outside the HAZ.	48
Figure 3-25: Tensile samples taken from just outside the HAZ and the adjacent micro slices used to determine the exact positions of the HAZ planar graphitization.....	49
Figure 3-26: A drawing of the dimensions of the tensile samples machined from the respective service exposed steam pipe samples.....	49
Figure 3-27: The Instron 8801 servo-hydraulic test platform used to perform the room temperature tensile testing of the tensile samples removed from the different service exposed steam pipe regions.....	50
Figure 3-28: Close up view of the tensile test set up used to test the room temperature tensile samples.....	51
Figure 3-29: One of the round Tensile samples tested at 420°C.	51
Figure 3-30: A graphical summary of converted room temperature Yield strengths at 420°C in relation to the % Planar Graphitization of the respective pipe regions.	53
Figure 3-31: A graphical summary of converted room temperature UTS at 420°C and.....	54
Figure 3-32: A representative parent steam pipe material tensile sample, which fractured in a ductile manner, evident from the necking and cup and cone features.....	55
Figure 3-33: A typical example of how the majority of the tensile taken from just outside the HAZ fractured in the parent steam pipe material.	55
Figure 3-34: Close up view of one of the HAZ tensile sample's necked fracture surface with a dimpled and fibrous appearance, typical of a ductile overload fracture.....	56

Figure 3-35: Higher magnification close up view of Sample A's up stream side (L/H side) and down stream side (R/H side), with more graphite nodules exposed on the down stream side which has higher graphitization levels.57

Figure 3-36: SEM image showing a typical example of the fractured graphite nodules surrounded by a fine dimpled fracture surface formed as a result of MVC.....58

Figure 3-37: Higher magnification SEM image of one of the graphite nodules and surrounding MVC fracture surface, with the fracture going through and not around the nodule.....58

Figure 3-38: Polished and etched cross sectional view of pipe Sample A's up stream tensile, with less micro voids (indicated by arrows) being formed due to lower levels of graphitization.....59

Figure 3-39: Polished and etched cross sectional view of pipe Sample A's down stream tensile, with more micro voids (indicated by arrows) being formed, due to higher levels of graphitization.....59

Figure 3-40: The side view of the only HAZ Tensile sample that fracture along the HAZ interface, where high levels of planar graphitization were evident.60

Figure 3-41: Close up view of the exposed fracture surfaces of the up stream HAZ tensile Sample of Welded pipe Sample B, which fractured along the HAZ outer interface region.60

Figure 3-42: SEM low magnification image of the fracture surface of the one down stream HAZ tensile tested at 420°C, with similar dark colored intermittent regions.61

Figure 3-43: SEM close up image of one of the dark colored regions showing that it is made up of a cluster of what looks like very fine fractured graphite nodules.62

Figure 3-44: SEM close up image showing that the material surrounding the dark colored cluster regions fractured in a ductile manor evident from the MVC.62

Figure 3-45: Element spectral image analysis results of the fracture surface of Sample B's HAZ tensile sample, with the carbon rich regions blue and the iron rich regions green.	63
Figure 3-46: Polished and etched cross sectional view of the uniquely fractured HAZ tensile from pipe Sample B, showing that the fracture coincides with the intermittent planar graphitization.	64
Figure 3-47: The positions where the Charpy Impact samples were removed from the service exposed steam pipe parent material.....	65
Figure 3-48: Shows where the Charpy Impact samples were taken from just outside the HAZ, with the notch coinciding with the planar graphitization.....	66
Figure 3-49: The dimensions of a Type "A" Charpy impact sample as per ASTM E23.	67
Figure 3-50: The Zwick Impact tester used to test the Charpy impact samples of the respective service expose steam pipe samples.	67
Figure 3-51: A graphical summary of Charpy Impact results at room temperature and the % Planar Graphitization of the respective pipe regions. ..	68
Figure 3-52: Graphical representation of recorded impact Load measurements of instrumented parent steam pipe and HAZ Charpy impact samples.	70
Figure 3-53: A typical example of the mode of fracture of one of the parent pipe material Charpy Impact samples.....	71
Figure 3-54: A typical example of the mode of fracture of one of.....	72
Figure 3-55: The fracture surfaces of Charpy impact samples from sample A's parent pipe up stream (L/H side) and down stream (R/H side), with more exposed graphitization on the down stream side.	73
Figure 3-56: SEM image of a typical ductile shear overload fracture surface region of one of the parent Charpy impact samples.....	74

Figure 3-57: SEM image of the shinier final fracture region of one of the parent material Charpy impact samples, with a typical cleavage fracture appearance indicative of a brittle fracture mode.	75
Figure 3-58: SEM close up image of one of the intermittent dark colored regions, with clusters of what appears to be fine brittle fractured graphite nodules.	76
Figure 3-59: SEM close up image of lighter colored fracture surface regions of Charpy impact samples with larger and smaller dimples as a result of MVC....	76
Figure 3-60: The spectral elemental scan results of a small portion of the dark colored fracture surface region, with the dark cluster showing higher levels of carbon (Blue) and the surrounding regions exhibited higher levels of iron (Green).	77
Figure 3-61: Cross sectional view of Sample A's down stream HAZ Charpy impact sample with clear evidence that the dark colored graphite cluster identified on the fracture surface corresponds to the intermittent planar graphitization outside the HAZ.....	78
Figure 3-62: The relation between Aluminium wt.% of parent pipe material and the development of % Planar Graphitization.....	80
Figure 3-63: The relation between Silicon wt.% of parent pipe material and the development of % Planar Graphitization.....	81
Figure 4-1: Illustration showing the A) possible signals generated from the electron-specimen interactions and B) interaction volume of for each signal in the specimen [22].....	84
Figure 4-2: Schematic illustration of the basic SEM configuration (North Arizona University).	85
Figure 4-3: Everhart-Thornley secondary electron detector with a Faraday cage attracting the secondary electrons [24].	86

Figure 4-4: Backscattered electrons form as the result of multiple elastic interactions of the incoming electrons with the specimen atoms [23].	87
Figure 4-5: Two possibilities showing backscattered electrons emerging from either a) near surface interactions (strong BSE signal) or b) deeper penetration (weak BSE signal) resulting in channeling contrast [25].	88
Figure 4-6: A) Generation of characteristic X-rays by the ejection of an inner shell electron which gets replaced by electrons from a higher energy state resulting in the photon emission. B) Naming convention of the possible electron transitions [26].	88
Figure 4-7: Generation of the signals (forward scattered and diffraction cones) when the electrons interact with the sample at an angle of 70° [28].	90
Figure 4-8: Collection, transformation and indexing of the EBSP using dedicated software [28].	91
Figure 4-9: Comparison of the two diffraction geometries for SEM based diffraction orientation mapping with the corresponding Monte Carlo simulation showing the interaction volume [29].	92
Figure 4-10: Secondary electron images of the various stages in the sample preparation using the FIB-SEM (a-e). Image f shows a bright-field TEM image of the sample.	93
Figure 4-11: Schematic illustration of different detectors that can be attached to a STEM system to collect various signals from beam-specimen interactions [30].	95
Figure 4-12: Low angle ADF image showing a combination of atomic number and diffraction contrast.	96
Figure 5-1: DIC Light microscope images of two welded samples showing an overview of the microstructural features	98
Figure 5-2: Light microscope images of the planar graphitized zone located outside the HAZ of the welded Sample A.	99

Figure 5-3: Light microscope image of the microstructural regions at the fusion line of Welded Sample A.....	100
Figure 5-4: a) BSE SEM image of the ferrite/pearlite bands in the parent material, b) BSE image of the pearlite band showing the lamellar ferrite/cementite structure.	101
Figure 5-5: BSE SEM images of a random graphite nodule in the parent material of Sample A, shown at two different contrast settings. (Acceleration voltage = 15 kV).....	102
Figure 5-6: BSE SEM images of a MnS inclusion in the parent material of Sample A, shown at two different contrast settings.....	103
Figure 5-7: BSE-SEM images of the planar Graphitized zone of Sample A located just outside the HAZ zone.	103
Figure 5-8: EBSD analysis of the parent material zone a-b) IPF showing the misorientations surrounding in the pearlite bands, c-d) grain boundaries (GB) (1-5°: green; 5-15°: black; >15°:red), e) local misorientation profile (3x3 pixels) showing low angle GB and f) Grain orientation spread (0°: blue – 5°: red).	105
Figure 5-9: EBSD analysis of the planar Graphitized zone showing a-b) IPF showing the misorientations surrounding the graphite nodule, c-d) grain boundaries (GB) (1-5°: green; 5-15°:black; >15°:red), e) local misorientation profile (3x3 pixels) showing low angle GB and f) Grain orientaiton spread (0°: blue – 5°: red).	106
Figure 5-10: BSE SEM image of showing the location of the FIB-sample (pearlite/ferrite boundary) taken from the Sample A's parent material.	107
Figure 5-11: ADF-STEM image showing the microstructure of the ferrite and pearlite regions as well as the location of the precipitates.	108
Figure 5-12: BSE SEM image showing the location of the FIB-sample taken across two graphite nodules in the planar graphitized zone outside the HAZ of welded Sample A.	109

Figure 5-13: ADF-STEM images showing the a) location of the graphite nodules, carbide precipitates and dislocations, b) higher magnification image of the graphite nodule showing the grain boundaries and dislocations surrounding the graphite nodule.	109
Figure 5-14: TKD analysis done on the TEM with a) the band contrast showing the location of the precipitates and grain boundaries, b) phase map identifying the carbide precipitates as cementite (yellow colored phase).	110
Figure 5-15: BSE SEM image of the second FIB-sample removed from the planar graphitized zone in order to study the spheroidization of the carbide precipitates.	111
Figure 5-16: ADF-STEM image showing the Carbide precipitates as well as two smaller graphite nodules below the surface of the sample.	111
Figure 5-17: TKD analysis performed on the TEM sample showing a) band contrast and b) phase map identified the carbide precipitates as cementite phases	112
Figure 5-18: a) TEM image of a graphite nodule showing the presence of an Al-containing precipitate (indicated by the arrow) located inside and b) ADF-STEM image of the 2 nd graphite nodule showing preferential growth along a particular direction.	113
Figure 5-19: ADF-STEM image showing the location of cementite precipitates (bright) and the small Al-precipitates (dark).	113
Figure 5-20: BSE SEM image of the FIB-sample taken from the region just outside the HAZ of Sample D.	114
Figure 5-21: ADF-STEM image of Sample D's thin foil sample showing enlarged carbide precipitates located on the grain boundaries.	115
Figure 5-22: Phase map (ferrite: red and (Fe, Mn) ₃ C; yellow) showing that the precipitates are cementite.	115

List of Tables

Table 2-1: Chemical specification requirements for ASTM A515 Grade 55 and ASTM A516 Grade 65 pressure vessel / steam pipe material [1].....	5
Table 2-2: Typical mechanical properties of ASTM A515 Grade 55 and A516 Grade 65 pressure vessel material [1].	6
Table 3-1: The experimental matrix of the research study.	27
Table 3-2: Chemical analysis results of service exposed steam pipe material.	30
Table 3-3: Summary of the metallurgical preparation steps used to prepare the macro samples removed from the respective service exposed pipe samples.	33
Table 4-1: FIB parameters for TEM sample preparation.....	93

Glossary of terms and explanation

austenite	Steel microstructural phase in steel heated above 723°C
Al	Aluminium
BF	Bright Field
BSE	Back Scatter Electrons
C	Carbon
DF	Dark Field
EBSD	Electron Back Scatter Diffraction
EDS	Electron Dispersive Spectroscopy
EPMA	Electron Probe Microanalysis
ferrite	Steel microstructural phase known as α - Iron
Fe	Iron
Fe ₃ C	Cementite
FIB	Focused Ion Beam
FM	Maximum impact Force absorbed
Fa	Force at which point the unstable crack extension is arrested
graphitization	The formation of free Carbon in the form of graphite in Iron or Steel
HV	Hardness Vickers
HAZ	Heat Affected Zone
J	Average Impact Energy
ICGC	Intercritical reheated Grain-Coarsened zone

Mn	Manganese
MnS	Manganese Sulphides
Mo	Molybdenum
MPa	Mega Pascal
MVC	Micro Void Coalescence
N	Nitrogen
O	Oxygen
P	Phosphorus
pearlite	Steel microstructural phase with a lamellar structure of alternating Cementite and α - Iron
planar graphite	Localized nucleation and growth of graphite in chains
PM	Parent Material
PWHT	Post Weld Heat Treatment
S	Sulphur
Si	Silicon
SEM	Scanning Electron microscope
SE	Secondary electrons
SCGC	Subcritical Reheated Grain-Coarsened zone
SCGR	Super critical reheated Grain-refined zone
STEM	Scanning Transmission Electron Microscopy
TEM	Transmission Electron Microscope
UAGC	Unaltered Grain-Coarsened zone
UTS	Upper Tensile strength
YS	Yield Strength

Chapter 1 : Introduction

1.1. Introduction:

Graphitization was a commonly reported phenomenon during the 1950's, specifically in the refinery and power generation industries. In an effort to eliminate graphitization from taking place in the pipe material, higher alloyed steels containing chrome and molybdenum were introduced, which virtually eliminated the problem. Despite this breakthrough, some power generating plants still have units in operation, which were manufactured using plain carbon steam pipe material prone to graphitization. This dissertation will provide information with regard to the effect graphitization has on the static mechanical properties of plain carbon steam pipe material, which was exposed to service temperature above the critical graphitization temperature for an extended period. It will also provide information regarding the effect of a newly introduced multiple run seam weld on service exposed steam pipe material.

1.2. General Objectives:

The study aims to satisfy the following objectives:

- To investigate the effect of graphitization on the static mechanical properties of service exposed steam pipe material with multiple run seam welds and newly welded service exposed pipe material.
- Investigate the different microstructural regions in the service exposed and newly welded pipe materials using electron microscopy to gain an understanding of nucleation and growth of graphite nodules in this material, particularly outside the heat affected zone.

1.3. Problem Statement:

Investigate what effect graphitization has on the static mechanical properties of the service exposed steam pipe material, with the aim of gathering information with regards to the following sub problems.

1.3.1. Sub problem one:

Investigate the effect of graphitization on the overall hardness of service exposed steam pipe material.

1.3.2. Sub problem two:

Investigate how the size and distribution of graphite nodules influence the tensile strength of service exposed steam pipe material.

1.3.3. Sub problem three:

Investigate how the size and distribution of graphite nodules influence the impact toughness of service exposed steam pipe material.

1.3.4. Sub problem four:

Investigate the possibility of identifying the positions where preferential graphitization using advanced electron microscopy methods.

1.4. Hypothesis:

Graphitization will reduce the tensile strength and the toughness of the service exposed steam pipe material specifically in the region just next to the heat affected zone of a multiple run seam weld.

1.5. Delimitations:

- The study was limited to three service exposed steam pipe samples with multiple run seam welds.
- The three steam pipe samples evaluated in the study had been in service for approximately the same period of time, which prevented the gathering of data on graphitization related to different in service exposure periods.

- The size of the service exposed steam pipe samples with multiple run seam welds limited the mechanical testing to transverse direction in relation to the seam welds.

1.6. Assumptions:

The study was based on the main assumption that the graphitization in the steam pipe material just next to the heat affected zone (HAZ) of the multiple run seam weld would have the most adverse effect on the static mechanical properties. It was also assumed that the amount of graphitization found in the pipe material next to the HAZ would be similar for this region all along the entire circumference of the seam weld.

1.7. The Significance of the Research

The research will benefit industry by shedding light on the actual effect of graphitization on the static mechanical properties of service exposed steam pipe material, which operated for prolonged periods above the graphitization start temperature of 425°C.

1.8. Research Methodology

The relevant service exposed steam pipe samples with multiple run seam welds were evaluated to determine the respective levels of graphitization, with regards to size and distribution. This information was used to determine if there is any variation with regards to the severity of the graphitization specifically in the regions adjacent to the HAZ.

Tensile and Charpy impact samples were machined from the Graphitized HAZ regions and similar samples were removed from the surrounding up and down stream Graphitized services expose steam pipe material further away from the seam welds. These samples were then tested and the results of the respective pipe regions and samples were then compared to each other.

The fracture surfaces of the tested samples were then evaluated using scanning electron microscopy. Representative cross sectional samples were removed from the tested tensile and impact samples and these were evaluated using an optical microscope and the scanning electron microscope. This was done to establish if there is a correlation between the fracture path and surrounding microstructure and the recorded tensile and impact properties.

A fourth sample with a newly introduced seam weld on Graphitized service expose steam pipe material, was added to the research to establish whether the formation of planar graphitization could be triggered in the region just outside the HAZ. This necessitated an in depth study of the microstructure just outside the HAZ, using high end electron microscopy, to identify preferential microstructural regions where the graphitization would form, seeing as the size of the initiation sites are in the region of a few microns.

Chapter 2 : Literature Review

In this chapter literature pertaining to the general material properties and chemistry of the pipe material will be reviewed. The manufacturing process and the effect thereof on the material microstructure will be discussed. Welding imposes further microstructural changes and the effect of multi-pass welding on the material will be discussed. Changes in the material during long-term service exposure will be reviewed. Graphitization is considered to be the main contributor towards embrittlement in the material during long term service exposure. The general mechanisms and factors controlling graphite formation in the material will be reviewed, in addition to the effect of graphitization on the mechanical properties.

2.1. Material Properties and Chemistry

A typical carbon steel grade used during the 1950's for the manufacturing of steam pipe sections was ASTM A515 Grade 55 and later on ASTM A516 Grade 65 material was used in its place. These two grades of Carbon steel contain the same levels of Phosphorus, Sulphur and silicon, with the Grade 65 material having 0.01% more Carbon and a wider range of manganese (0.85 – 1.20%) as shown in **Table 2-1**.

The ASTM A516 Grade 65 material has improved mechanical properties in comparison to the Grade 55 material. This is due to its increased alloy content in the form of manganese, giving it a finer grain structure and increasing its strength (See **Table 2-2**).

Table 2-1: Chemical specification requirements for ASTM A515 Grade 55 and ASTM A516 Grade 65 pressure vessel / steam pipe material [1].

Material specification	%C - Carbon	%Mn- manganese	%P – Phosphorus	%S – Sulphur	%Si - silicon
ASTM A515 Grade 55	0.28 (max)	0.90 (max)	0.035 (max)	0.04 (max)	0.15 – 0.40
ASTM A516 Grade 65	0.29 (max)	0.85 – 1.20	0.035 (max)	0.04 (max)	0.15 – 0.40

Table 2-2: Typical mechanical properties of ASTM A515 Grade 55 and A516 Grade 65 pressure vessel material [1].

Material specification	Yield strength (MPa)	Tensile strength (MPa)	% Elongation (50mm Gauge)
ASTM A515 Grade 55	205 (min)	380 – 515	27% (min)
ASTM A516 Grade 65	240 (min)	450 – 585	23% (min)

2.2. Typical Microstructure of Low Carbon Pressure Vessel Steels

Fully killed Low Carbon steels were widely used during the 1950's for the manufacturing of critical petrochemical and power generating plants. These fully killed steels were deoxidized in Bessemer-Hall converters by blowing hot air through the molten steel, while making silicon and aluminium additions. From the converter the molten steel was then transferred to a casting ladle used for filling the ingot molds. These ingots were then reheated and hot rolled into slabs and subsequently into plate material, and used for the construction of pressure vessels and steam pipes (See **Figure 2-1** and **Figure 2-2**) [2].

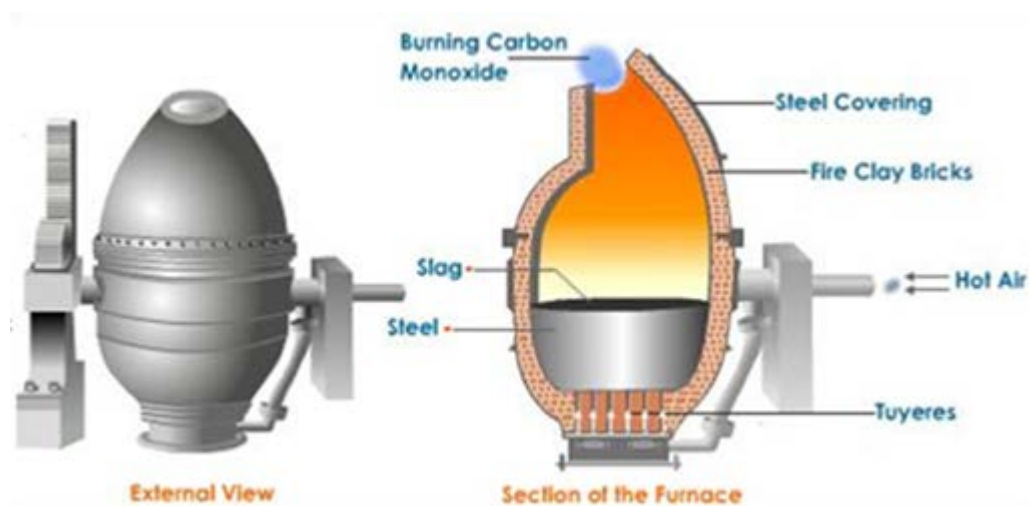


Figure 2-1: An image of a Bessemer converter, used for the deoxidization of fully killed steels during the 1950's [2].

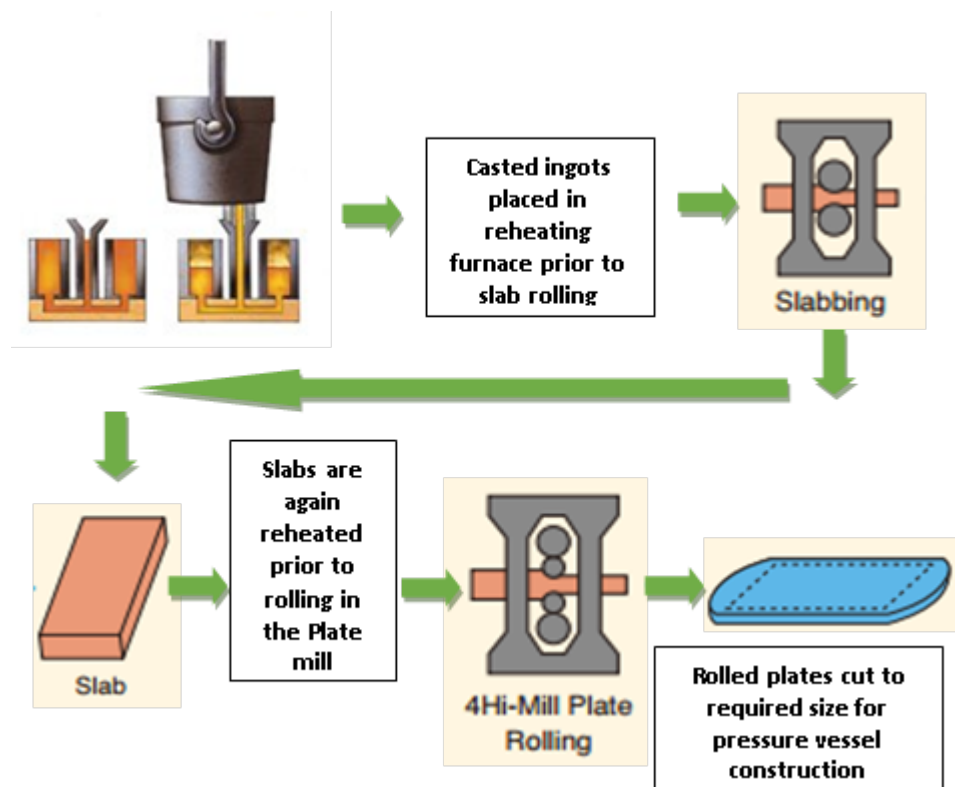


Figure 2-2: Schematic flow chart of the different manufacturing steps used for the manufacturing of fully killed plate material [2].

The steam pipe material manufactured in this way normally showed varying degrees of longitudinal inhomogeneity in the form of preferential grouping of ferrite and pearlite in alternative bands aligned in the rolling direction, as shown in Figure 2-3.

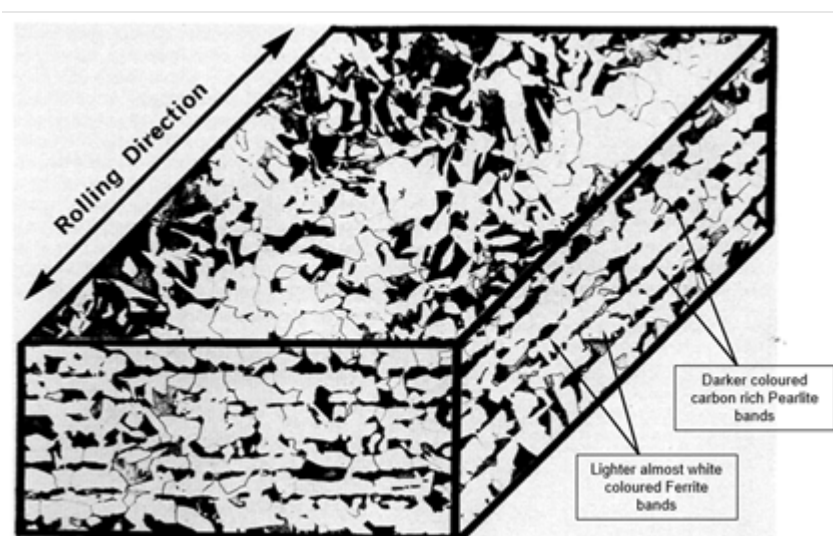


Figure 2-3: The pancake arrangement of the ferrite and pearlite bands in banded plate [3].

This microstructural phenomenon is generally known as banding and the severity depends to a large extent on the composition of the rolled plate. Banding is usually found in steels with carbon contents of 0.1 to 0.5%. Its formation is also promoted by high concentrations of phosphorus, manganese, oxygen, silicon and nitrogen, although none of these elements need to be present for banding to develop.

According to L. Samuels *et al* [3], ferrite-pearlite banding is not only formed as a result of carbon segregation. Segregation of other elements that raise or lower the A_3 temperature shown in **Figure 2-4**, can also contribute to the formation of the banded structure.

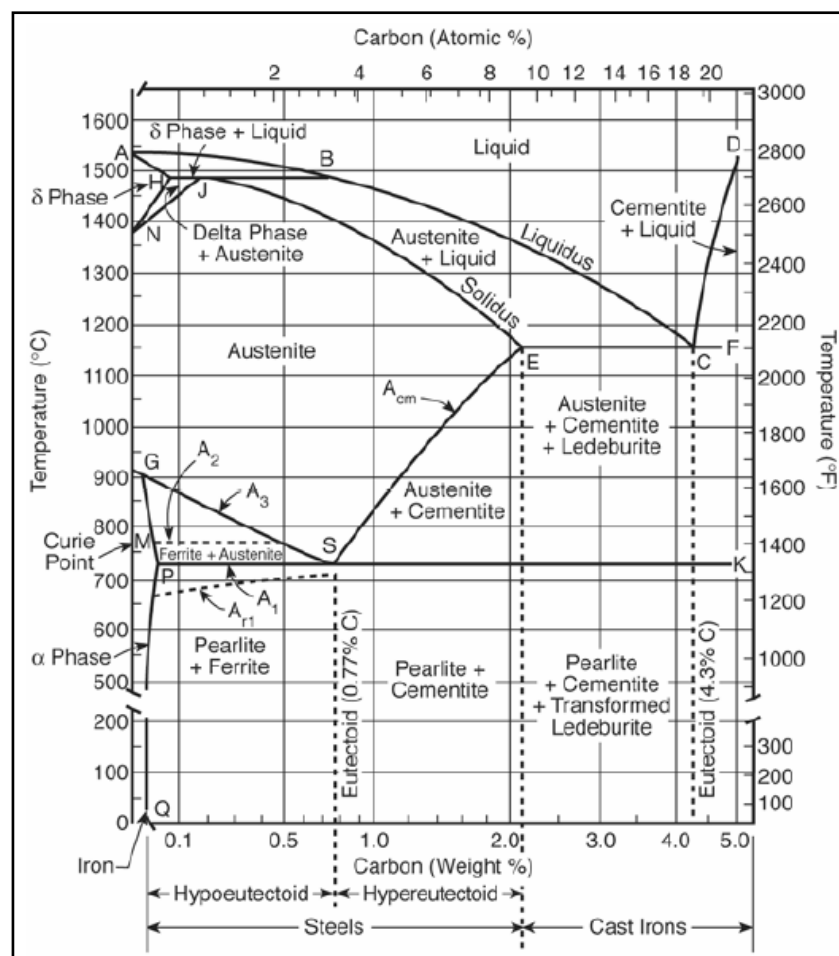


Figure 2-4: Iron-Iron Carbide phase diagram showing the different microstructural phases of low-carbon steels [4].

Alloying elements such as silicon and phosphorus raises the A_3 temperature, which results in the nucleation of pro-eutectoid or α -ferrite during the cooling from the austenitic (γ) condition leading to the formation of ferrite bands in the final microstructure. Regions rich in manganese experience a lowering of the A_3 temperature, leading to the formation of pearlite bands. This corresponds to literature by H.K. Bhadesia *et al.* indicating that regions rich in manganese remain longer in the austenitic (γ) condition, while regions low in manganese form α -ferrite. Carbon then segregates from the low soluble ferrite regions towards the high soluble austenite regions rich in manganese. These Carbon rich austenite regions finally transform into pearlite as shown in **Figure 2-5** [5].

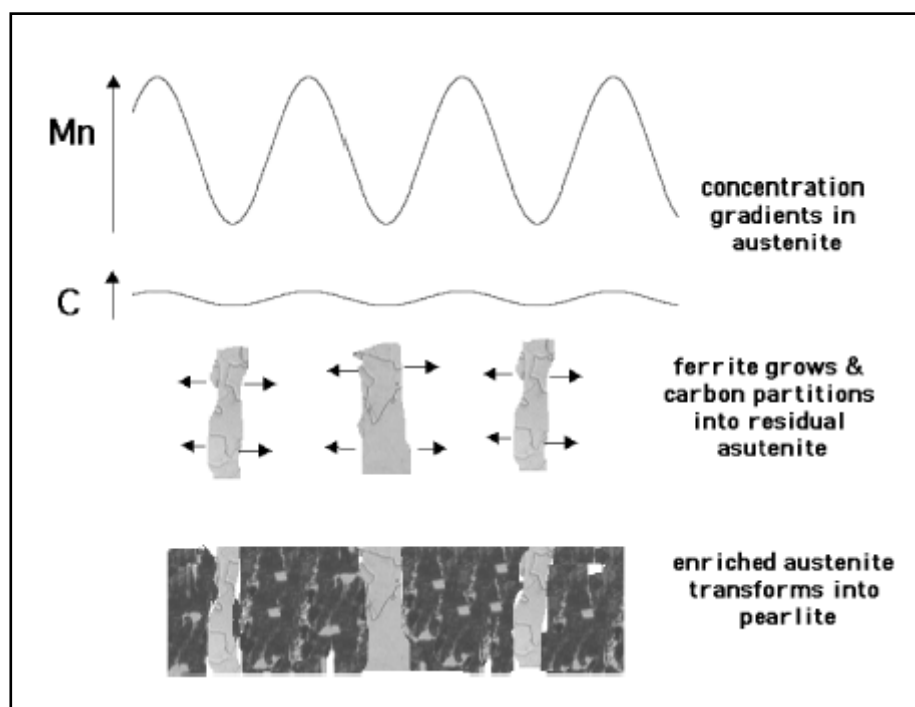


Figure 2-5: An illustration of the mechanism of banding [5].

The main reason for this phenomenon can be attributed to the manganese contributing to the overall Carbon content, which in turn shifts the material towards the Eutectoid position (at 0.8% Carbon content) on the Iron-Iron-Carbide phase diagram, with pearlite being alternating platelets of α -ferrite and Cementite (Fe_3C) as shown in **Figure 2-6**.

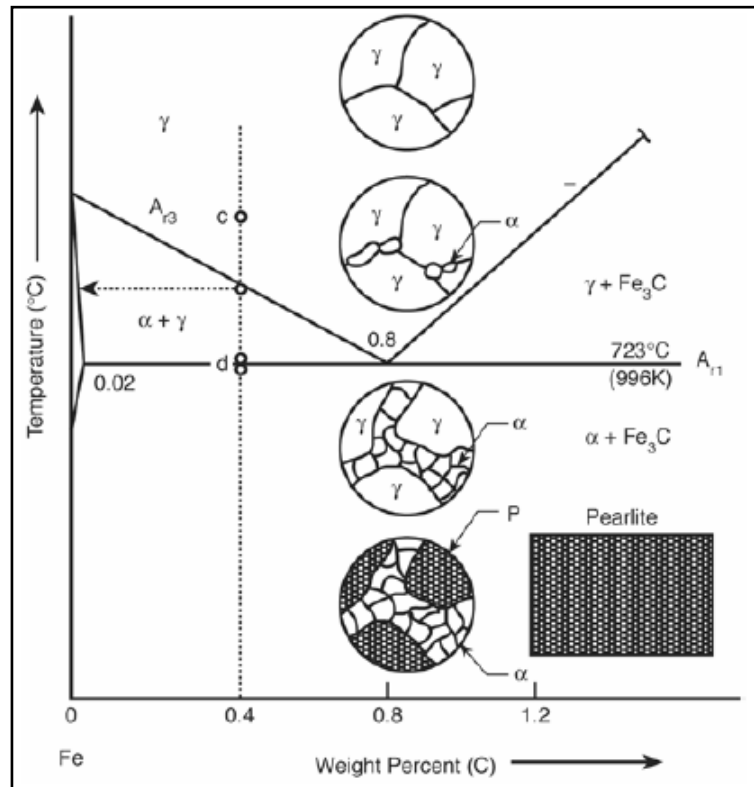


Figure 2-6: Schematic Representation of Transformations of Carbon steel during slow cooling

(α or pro-eutectoid \Rightarrow ferrite, P \Rightarrow pearlite ($\alpha + \text{Fe}_3\text{C}$) and $\gamma \Rightarrow$ austenite) [4].

Electron probe microanalysis (EPMA) of **Figure 2-3** banded ferrite-pearlite structure, showed the absolute variation of silicon to be much less than that of manganese as depicted in **Figure 2-7**. If silicon was the only segregated element, one would expect the silicon-rich bands to correspond to the ferrite-rich bands, however in practice they correspond to pearlite-rich bands because the manganese segregation is more dominant according to L. Samuels *et al.* [3], with similar findings reported on banded Carbon steels by H.K. Bhadesia [5] and G. Krauss [6].

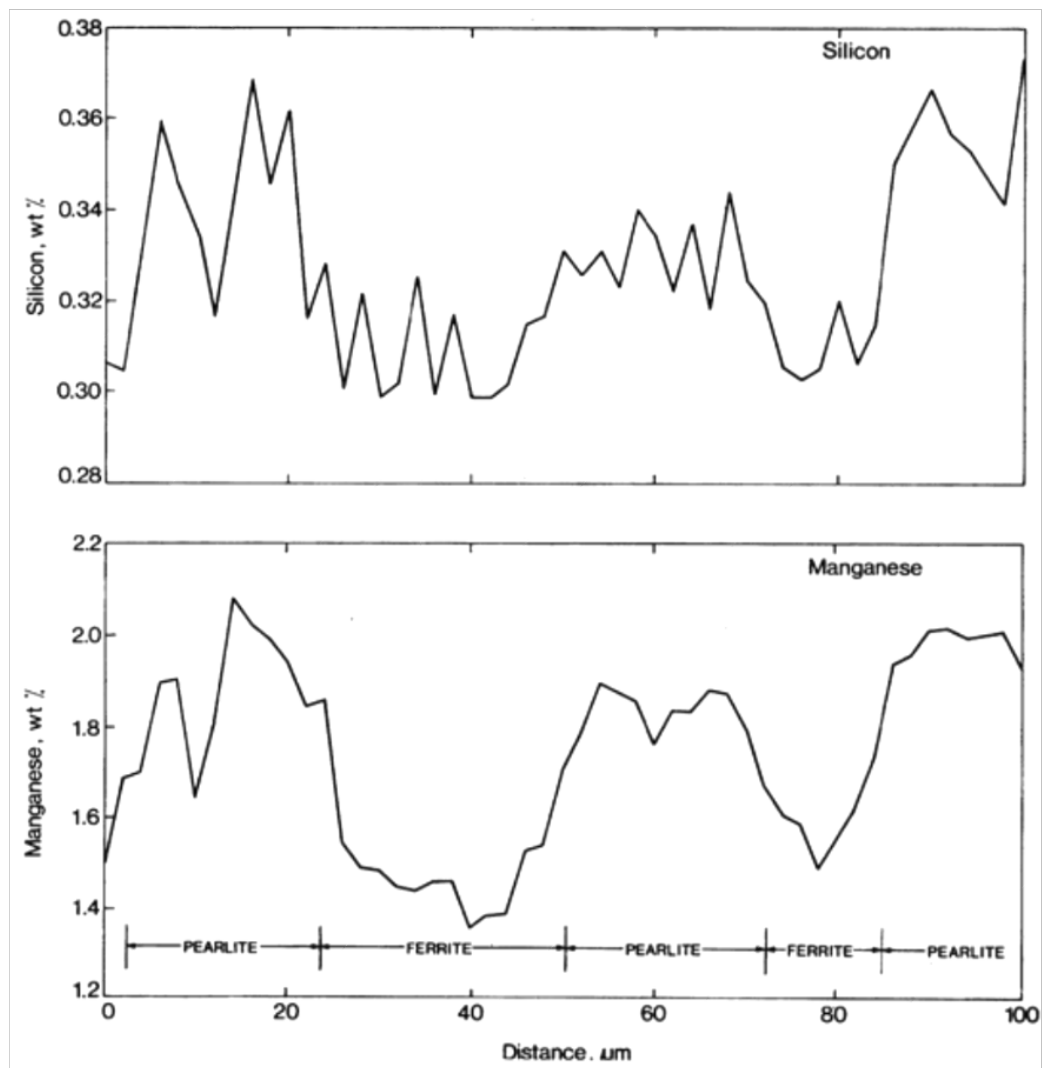


Figure 2-7: The variation of manganese and silicon across representative bands in the specimen shown in Figure 2-3, using EPMA [3].

H.K. Bhadesia [5] and G. Krauss [6] indicated that banding can also form in Carbon steels with higher levels of Sulphur and these steels normally form manganese Sulphides (MnS) within the regions with a higher average concentration of manganese. This then aids the formation of ferrite in the manganese depleted regions and it then surrounds the MnS. As the ferrite forms around the MnS, Carbon is ejected or shifted to the adjacent zones with lower average manganese concentration, and these transform into pearlite. This result in the ferrite bands shifting to positions where the average manganese concentration is higher and they coincide with the MnS inclusions as shown in **Figure 2-8**.

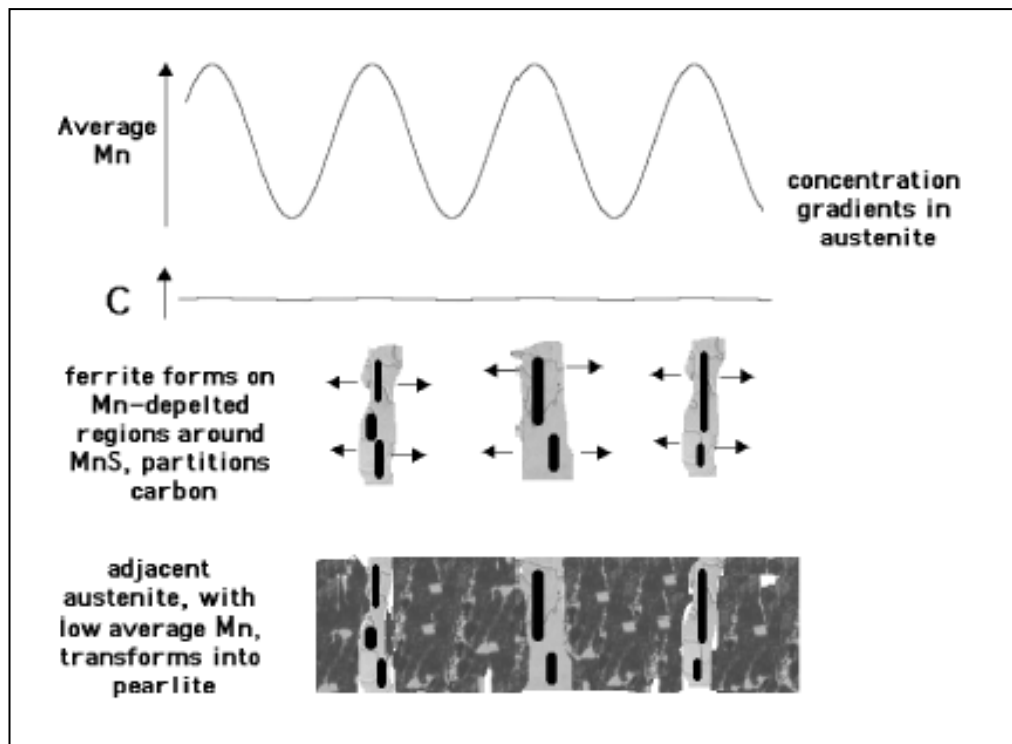


Figure 2-8: Schematical representation of the mechanism of banding in Carbon steels containing substantial levels of manganese Sulphides [5].

2.3. The Influence of Welding as a Fabrication Process on the Microstructure of Low-Carbon Pressure Vessel Steel

2.3.1. Introduction

Welding is one of the key processes used during the fabrication of pressure vessels and steam pipe components. This involves depositing a small amount of molten steel within a gap between the components to be joined, and subsequently welding the components together when the steel solidifies. The metallurgy of the welded joint can be categorized into two major regions; the fusion zone and the heat affected zone (HAZ). The fusion zone comprises of the combination of the deposited metal and the portions of steel components melted during the welding process; while the heat affected zone represents those regions in close proximity to the weld, where the heat input during the welding changes the microstructure without melting the steel.

2.3.2. The Fusion Zone Solidification and Microstructure

The molten component and weld filler metal deposited in the fusion zone starts solidifying from a liquid state at a temperature of 1600°C. As the weld deposit cools down columnar δ - ferrite forms at the hot grain structure of the parent plate at the fusion surface. These columnar grains then grow along the direction of the heat flow and their width increases with distance away from the fusion boundary. Subsequently, the δ - ferrite undergoes a solid-state transformation to austenite (γ) as the temperature decreases. It finally reverts back to α -ferrite as the weld metal continues cooling down to room temperature, during which three distinct forms of α -ferrite are formed.

The three forms of α -ferrite develop as the cooling process progresses, with both Allotriomorphic ferrite (α) and Widmanstätten ferrite (α_w) growing from the austenite (γ) grain boundaries with a columnar structure. Acicular ferrite (α_a) plates on the other hand nucleate at non-metallic particles dispersed throughout the weld, as shown in **Figure 2-9** and **Figure 2-10**. [7]

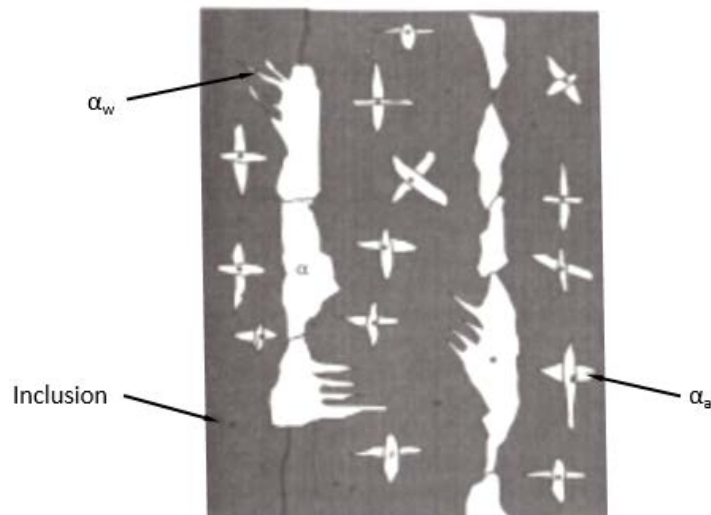


Figure 2-9: Schematic illustration of the essential constituents of the primary microstructure in the columnar austenite grains of a steel weld deposit [7].

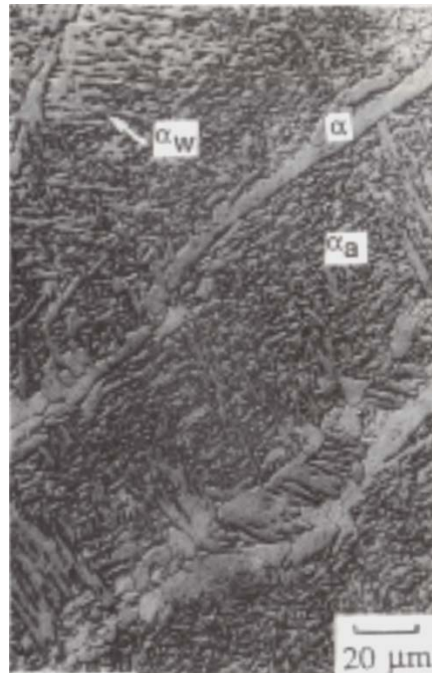


Figure 2-10: Showing a scanning electron micrograph of the primary microstructure of a steel weld

(α = Allotriomorphic ferrite, α_w = Widmanstätten ferrite, α_a = Acicular ferrite) [7].

2.3.3. The Heat Affected Zone Microstructural Regions

The heat affected zone is the portion of the material which has not been melted, but has experienced microstructural changes owing to weld heat input. A significant amount of this heat manages to diffuse from the fusion zone into the adjacent solid regions exposing it to heating and cooling cycles, which vary in severity depending on its distance from the fusion boundary. This causes the formation of different microstructural regions within the HAZ as illustrated in **Figure 2-11**.

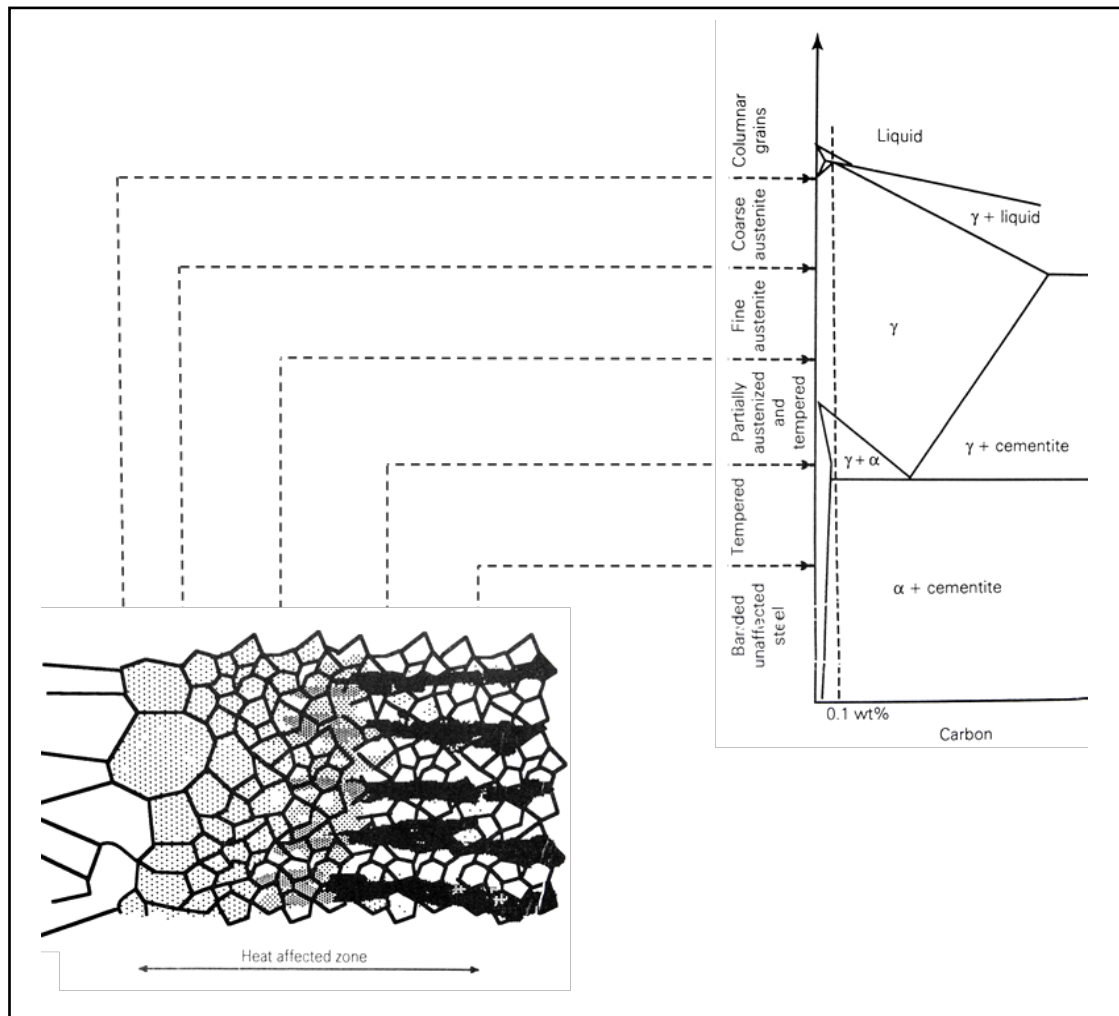


Figure 2-11: Schematic illustration of the microstructural variation to be expected in the heat affected zone of Carbon steel welds [7].

The region immediately adjacent to the fusion boundary is heated for an extended period to temperatures exceeding the A_3 temperature of $\pm 950^\circ\text{C}$, transforming the material in this region into austenite (γ). The austenite in this region remains for quite a while above the A_3 temperature, causing grain growth and coarsening resulting in the formation of the *coarse grained austenite region*. As one moves further away from the fusion boundary less heat gets absorbed and the *fine grained austenite region* is formed.

As the peak temperature in the HAZ decreases further away from the fusion boundary, material only gets partially Austenitized during the heating part of the thermal cycle. The austenite that does form has a rather high Carbon concentration, due to the increased solubility of Carbon in austenite (γ), as the temperature decreases [7] [8], while the part of the material that does not transform to austenite gets tempered, resulting in the formation of the *partially Austenitized and tempered region*. Then there is the HAZ region where the peak temperature of the heat input is less than the A_1 temperature of 723°C , which tempers the material forming the *tempered region* [7].

2.3.4. The Effect of Multipass Weldments on the Microstructure of the Fusion and Heat Affected Zones

A large portion of the welding done on thick walled pressure vessel components require large gaps between components, to be filled by multiple weld runs done sequential to each other. The deposition of each successive layer heat treats the underlying microstructure as depicted in **Figure 2-12**, with the re-austenitized regions being those where the columnar weld microstructure is no longer evident and temperatures experienced range between A_3 and A_1 [9].

Multipass weld runs also have more complex heat affected zone regions (see **Figure 2-13**) in comparison to the HAZ regions of a single weld run shown earlier on in **Figure 2-11** [9].

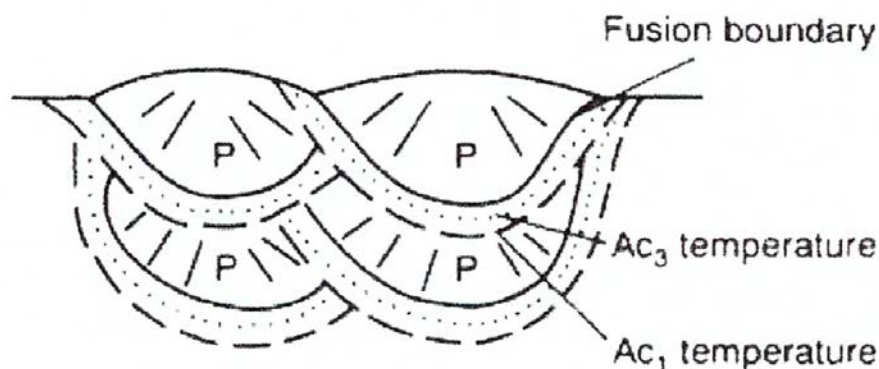


Figure 2-12: Schematic illustration of the primary deposited weld metal (P) and the re-austenitized regions (where temperatures are in the region of A_3 and A_1) adjacent to the weld metal fusion zone of a multipass weld [9].

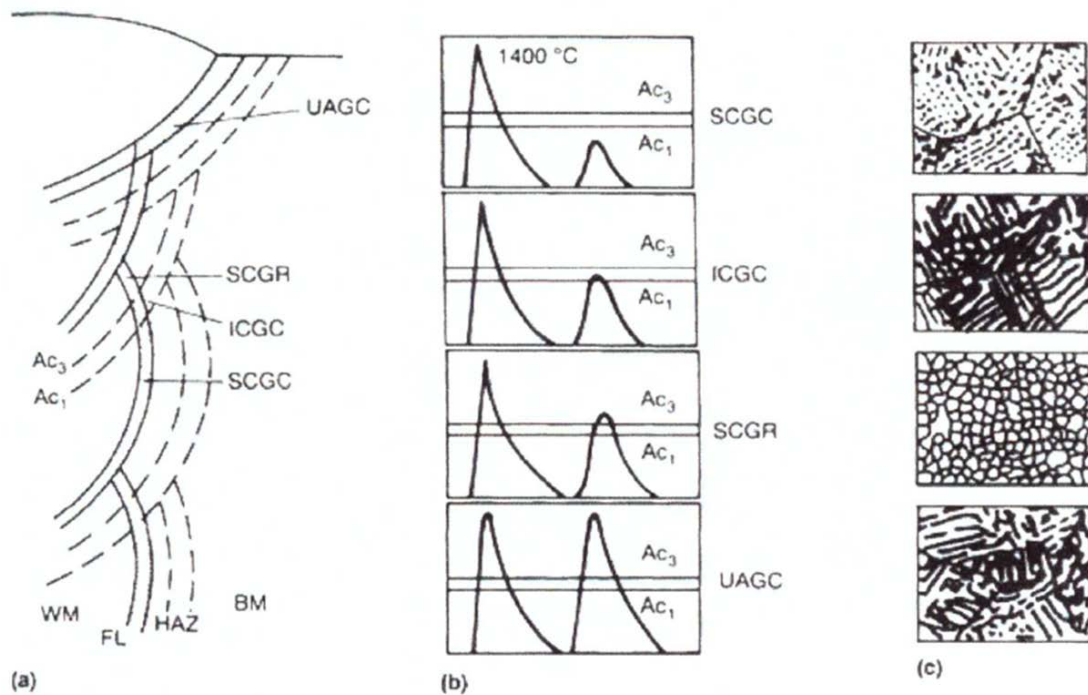


Figure 2-13: Schematic showing the different subzones that can form in the coarse grained region of the HAZ of a multipass weld:

(a) Positions of the subzones relative to the base metal (BM) and weld metal (WM).

(b) Plot of thermal cycles relative to A_3 and A_1 .

(c) Microstructures at the different zones, FL refers to the fusion line [9].

The main reason for the complex heat affected zones formed during multi-pass welds can be attributed to the HAZ's of the different weld runs interacting with each other as shown in **Figure 2-13**. This interaction results in the formation of four distinct HAZ regions, with the first being the Unaltered Grain-Coarsened (UAGC) zone. The UAGC zone forms part of each of the multiple weld runs heat affected zones, resulting in it being exposed to reheating temperatures ranging from 200°C to 1200°C . Subsequently, Supercritical Reheated Grain-Refined (SCGR) zones are formed, as the UAGC zones of the consecutive weld runs gets reheated above the A_3 temperature of $\pm 950^\circ\text{C}$ and below 1200°C . While some of the HAZ regions further away from the UAGC zones only get reheated between the A_1 temperature of 723°C and below the A_3 temperature, resulting in the formation of the Intercritical reheated Grain-Coarsened (ICGC) zone.

As the multi-pass welding process progresses some of the initially formed UAGC zones are reheated to temperatures below the A_1 temperature, resulting in these being transformed to Subcritical Reheated Grain-Coarsened (SCGC) zones [9].

2.4. The Effect Elevated Temperature Operation has on the Microstructure of Carbon Steel Steam Pipe Material

2.4.1. Introduction

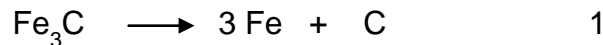
Carbon steels, used at elevated temperatures for pressure vessels and steam pipes, typically have a ferrite and pearlite microstructure. Extended exposure of these carbon steels to temperatures above 420° C causes the pearlite to decompose to form free carbon in a ferrite matrix. As this aging process progresses the steel tends to over-age and this promotes coalescence of the free carbon, which subsequently leads to the formation of graphite nodules, uniformly dispersed inside the ferrite matrix and this reaction is called graphitization [10].

The phenomenon was first observed in 1943 when a carbon- molybdenum (C-Mo) steel steam pipe at the Springdale Power station of the West Penn Power Company ruptured catastrophically at a girth weld [11] [12] [13]. graphitization remains a concern for both the power and petro-refinery industries to the present day, because there are currently aged plants in operation, manufactured with carbon steels affected by this phenomenon due to years of elevated temperature service. The areas of concern / interest for industry are: what affect the graphitization had on the strength of the service exposed steel and how this affected the remaining life of the old plants in operation.

2.4.2. The Graphitization Phenomenon

In general, graphitization may be defined as the formation of free carbon (graphite), C, in iron or steel. graphite formed during the solidification process, called *primary graphitization*, results in the stable Iron-graphite structure as in the case of cast irons such as gray Iron (with flake graphite), ductile iron (with spheroidal graphite), and compacted graphite Iron.

Graphite formation through the transformation of metastable metallic carbides following solidification, is termed *secondary graphitization*, which involves the decomposition of pearlite (iron + iron carbide) by transformation of the iron carbide, Fe_3C (cementite), at an elevated temperature to Iron and graphite:



The age related graphitization of carbon (C) and carbon-molybdenum (C-Mo) steels at elevated temperature service is an example of this *secondary graphitization*. It is generally known that in C and C-Mo steels graphite is the stable form of carbon; carbide spheroidization competes with graphitization in elevated temperature service. Which of the two processes occurs, depends on the steel composition and microstructure, and on the exposure to increasing temperatures favors spheroidization [14].

The Metals Handbook [15] shows, as an example, the temperature regimes within which either carbide spheroidization (above 552°C) or graphitization (below 552°C) can be expected to be the dominant transformation process. In reality, field experience indicated that the graphitization-to-spheroidization transition temperature varies in a manner not predictable, and in a particular instance, may differ significantly from the 552°C value suggested by **Figure 2-14**. Owing to its potentially embrittling effect, graphitization is of far greater concern than spheroidization.

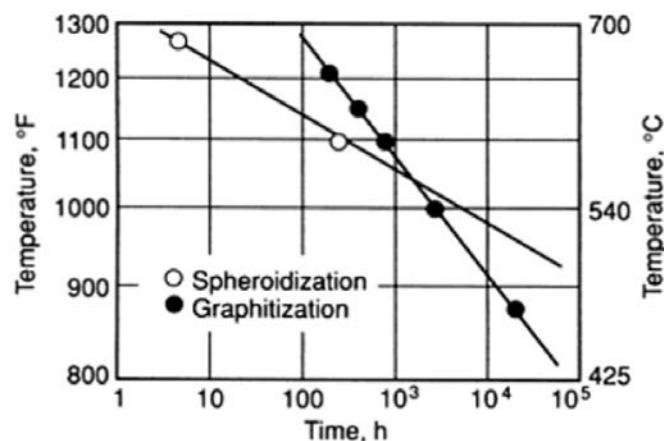


Figure 2-14: The temperature-time plot of pearlite decomposition by spheroidization and graphitization [15].

2.4.3. The Different Forms of graphitization that Develop During Over-aging

One form of graphitization is *randomly dispersed nodules*, which is relatively benign. This form of graphitization has been observed in carbon and low alloy steel weldments and base metal, and is not of major concern since it does not cause serious embrittlement. **Figure 2-15** shows an example of *the random nodular form of graphitization* that has been seen in the base metal of weldments of carbon and carbon- molybdenum steels.

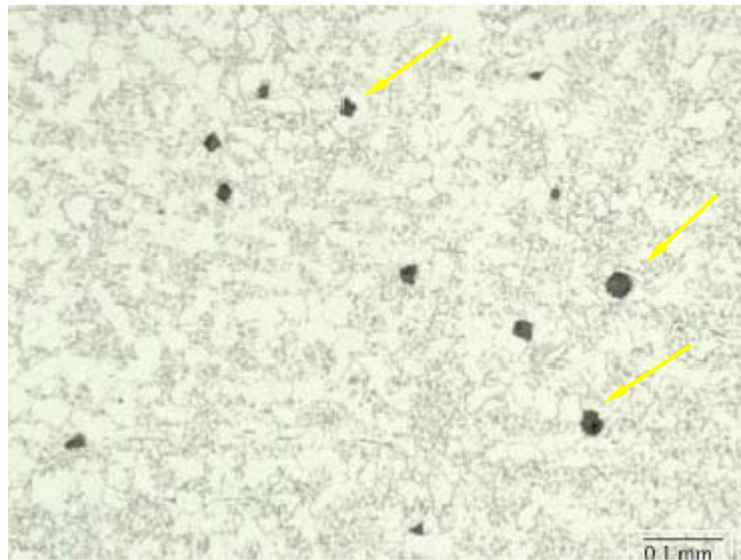


Figure 2-15: An example of random nodular graphitization in a carbon steel, with the graphite nodules pointed out by the arrows [11].

Another form of graphitization is when a *chain or “planar” graphite* is formed by localized nucleation and the growth of such nodules, which result in a significant reduction in the load-bearing capacity of the component affected. This planar or chain graphite increases the potential for catastrophic, brittle fracturing along this plane. There are two types of planar or chain graphitization normally found in service exposed carbon steels; the one type being “weld HAZ graphitization” and the other “base metal graphitization” [11].

2.4.3.1. Weld HAZ graphitization

This form of graphitization has been responsible for several catastrophic failures according to J.R. Foulds *et al.* [14] and others [16]. In this case the graphite forms inside the HAZ of the weld along a plane parallel to and at some distance from the fusion line. The constant distance from the interface where this HAZ graphitization is formed, is largely determined by the peak temperature during the the weld thermal cycle. J.R. Foulds *et al* [14] was of the view that this peak temperature is slightly above the lower critical transformation temperature (A_1), while M. Bharadwaj [16] argues that the peak temperature is slightly below the A_1 temperature. The mechanism by which HAZ graphitization forms is still a subject of debate.

The partial dissolution of pearlite and the formation of super saturated carbon regions, which in turn drives graphite nucleation and growth. Cross sectional samples, taken from service exposed welded regions with this type of HAZ graphitization, show that the graphite is almost parallel to the weld-base metal interface, giving the appearance of “eyebrows”, hence the term “eyebrow graphitization”, see **Figure 2-16**.

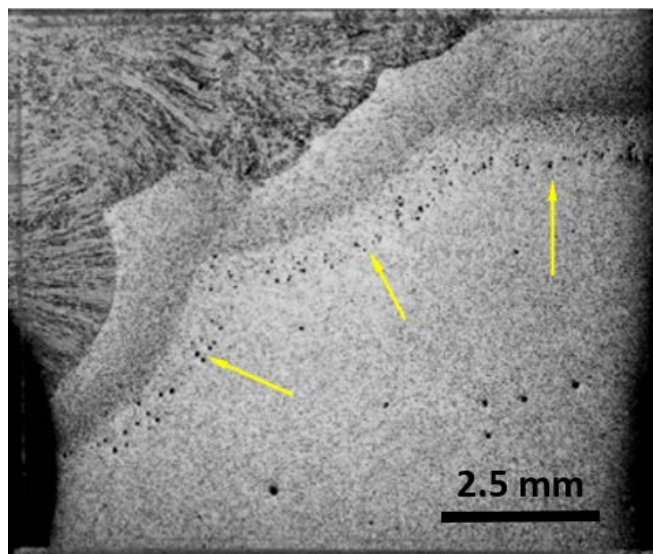


Figure 2-16: A macrograph of welded carbon steel, which were service exposed/over-aged resulting in the formation of the planar or “eyebrow” graphitization pointed out by the arrows [14].

2.4.3.2. Base Metal Graphitization

Evidence of chain or planar graphitization forming in the base metal far away from welded regions was reported to a lesser extent. This form is called “non-weld-related” graphitization and it merits as much concern as the weld HAZ graphitization since it has begun to appear in aging components previously considered at low risk, such as carbon-molybdenum piping operating below 482°C. “Non-weld-related” graphitization is much more difficult to detect, because it can form anywhere throughout the base metal. Evidence of this type of base metal graphitization was found during the evaluation of a power plant reheater tube failure. It is believed that this type of chain base metal graphitization forms in regions, which have experienced significant plastic deformation coinciding with slip bands [17] [18]. **Figure 2-17** shows the failed reheater tube and its corresponding cross section exhibiting this form of base metal graphitization.

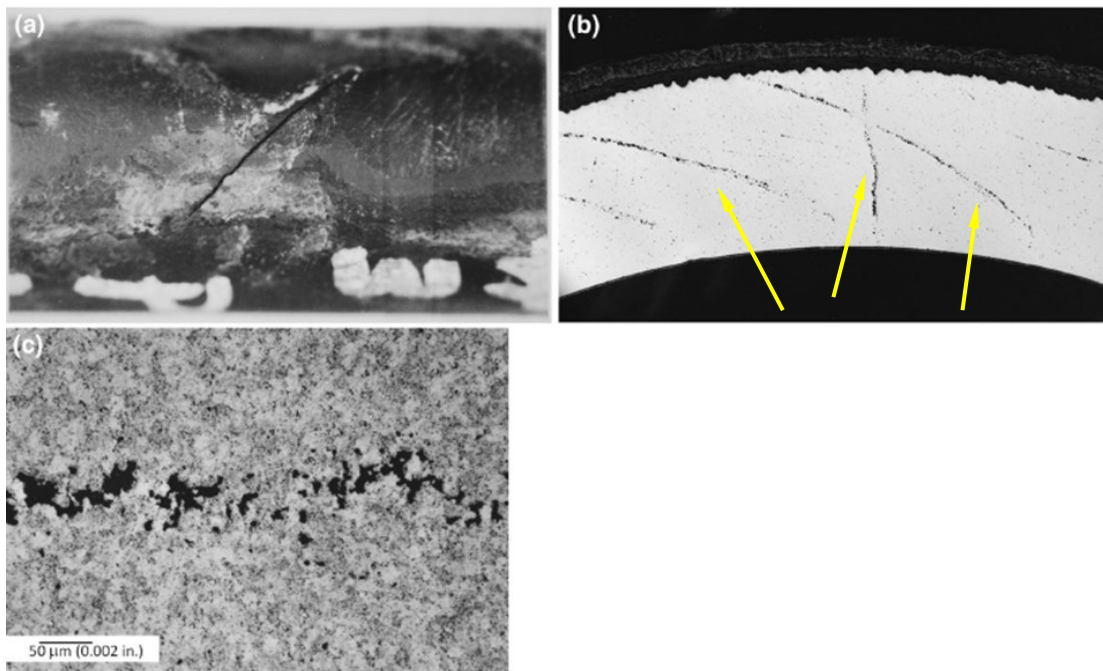


Figure 2-17: A reheat tube which failed due to the formation of planar base metal graphitization, which formed specifically at high strained regions [14].

2.4.4. Factors Contributing to the Formation of Graphitization in Carbon Steels:

According to literature, the four contributing factors to the formation of graphitization in carbon steels are: operating temperature [10],[11], the availability of excess free Carbon for its formation [10],[11],[12],[19], the hardness of the steel [10], [19], which is influenced by plastic strain, and lastly the presence of aluminium alone or in combination with elements like silicon and nitrogen [10],[11], [19],[20].

2.4.4.1. Operating Temperature of Steam Pipe Material

The operation of low alloy carbon steam pipe material above 420°C, causes the pearlite in the material to decompose releasing free carbon. The free carbon coalesces over time as the material over age, leading to the formation of graphitization according to Furtado *et al.* [10]. Foulds *et al.* [11] also indicated that steam pipe material operating conditions above 420°C, increases the diffusion rate of the free carbon, which in turn contributes to graphite nodule growth.

2.4.4.2. Sources of Free Carbon for the Formation of Graphitization

graphitization is normally formed in the base metal as randomly distributed graphite nodules, while planar graphitization forms either just outside the weld HAZ or in the base metal in regions associated with plastic strain as mentioned in section 2.4.3. Both types of graphitization require a source of excess Carbon for their formation.

J. Foulds *et al.* [11] and various other researchers [10],[12],[19] indicated in their papers that the carbon for the formation of the random graphite originates from the decomposition of the pearlite in the base metal, into iron and graphite when the steel operates above 425°C. While the planar graphitization which forms outside the HAZ gets its carbon from the supersaturated region which was exposed to temperatures above the A_1 temperature [14].

2.4.4.3. Hardness of Steam Pipe Material Influences the Development of Graphitization

The hardness of the steam pipe material also contributes to the graphite formation, because the hardness can be linked to the amount of plastic strain the material was subjected to. Plastic strain according to Yang *et al.* [19] causes a change in the internal stored energy of the pipe material. The stored energy exists in the material as point defects, dislocations and stacking faults and these act as heterogeneous nucleation sites for graphitization. This would explain the formation of the planar graphitization bands in the highly strained regions (see **Figure 2-17**) of the base metal where a large amount of micro voids would have formed along the slip planes in these regions. Furtado *et al.* [10] believe that the thermal stresses of the welding process will impose varying degrees of plastic strain or deformation to the surrounding base metal. This deformation would inherently aid in the formation of the planar graphitization just outside the HAZ .

2.4.4.4. The Contribution of Silicon and Aluminium to the Formation of Graphite

Furtado *et al.* [10], Foulds *et al.* [11] and other researchers [20] indicated that steam pipe material containing Si and Al has a greater susceptibility to graphitization. According to Yang *et al.* [19], graphitization forms at sites rich in Al and Si because the carbon gets liberated during the oxidation of these elements and concentrates around these newly formed oxides. This oxide formation mechanism would only explain graphite formation during the primary solidification phase. Yang mentioned that other researchers found secondary graphite nucleation to be near or at the interface of Al and Si inclusion in the matrix.

Yang also indicated that other researchers were of the opinion that Si and Al retard the cementite (Fe_3C) growth resulting in it being finer and less stable thus aiding to the dissolution of cementite to form graphite. L.E. Samuels *et al.* [17], showed similar findings with the Al and Si additions to the carbon steel, influencing the stability of the carbides, by interfering with the diffusion of the carbon in the matrix or by acting as preferential sites for nucleation.

Samuel *et al.*, also indicated that the aluminium and silicon segregate preferentially to the ferrite grain boundaries, with the extent of this segregation being determined by the thermal and physical i.e strain input from the adjacent weld metal next to the HAZ. Any oxygen remaining in the steel would then diffuse rapidly along the grain boundaries, oxidizing the Al and Si. These fine particles might then provide nucleation sites for the formation of graphitization, particularly at grain boundaries.

The latest review by Foulds *et al.* [14] concurred that aluminium and silicon could contribute to the nucleation and near term growth of graphitization in steam pipe material. Foulds could however not link the levels of these elements to the long term development of graphitization.

2.4.5. The Effect of Graphite on the Hardness, Tensile Strength and Impact Toughness of Service Exposed Steam Pipe Material

Graphitization normally has a tendency to grow over time when the Carbon steel operates at temperatures above 425 °C, causing a decrease in the hardness of the aged material over time, as shown in **Figure 2-18**. According Samuels *et al.* [21], graphitization not only reduces the hardness of the aged material, it also influences the ductility and toughness of the affected material.

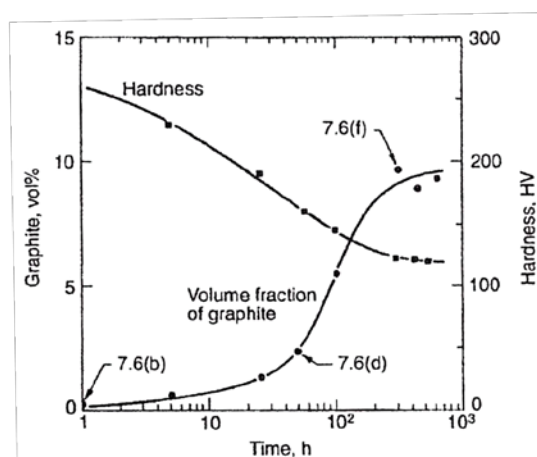


Figure 2-18: The variation with time of the volume fraction of graphite formed and the hardness [21].

Yang *et al.* [19], indicated that steam pipe material affected by graphitization has reduced ductility and toughness, because the graphite nodules contribute to the nucleation of micro voids in or at the interface between the graphite nodules and the matrix. This is mainly due to the difference between the elastic modulus of the graphite and the matrix. The graphite nodules would thus withstand less plastic deformation in comparison to the surrounding matrix material. Samuels *et al.*, also indicated that graphitization produces localized brittle zones, which inherently reduces the load-bearing capacity of the HAZ regions and it also causes a substantial drop in the impact strength [21].

Chapter 3 : Graphitization - Evaluation Techniques and Influence on Static Mechanical Properties

3.1. Introduction

The material evaluated during this research study originated from a steam pipe system, which operated for an extensive period of time above 425 °C, and developed graphitization. Pipe material availability restricted the study to four samples. Each of the samples was evaluated, with regard to their chemical composition, microstructure, overall hardness, tensile and impact strength, to establish how their static mechanical properties were influenced by the graphitization (see **Table 3-1**).

Pipe Sample	Description	Chemical analysis	Microstructure evaluation of Graphite distribution	Micro hardness	Room temperature tensile testing	Tensile testing at 420 ° C	Charpy impact testing
Sample A	Service exposed weldment	X	X	X	X	X	X
Sample B	Service exposed weldment	X	X	X	X	none	X
Sample C	Service exposed weldment	X	X	X	X	none	X
Sample D	Service exposed with new weld + PWHT 600°C for 2 weeks	X	X	X	X	X	X

Table 3-1: The experimental matrix of the research study.

3.2. Chemical Evaluation of Selected Service Expose Steam Pipe Material Samples

The service exposed up and down stream parent pipe material's chemistry was analysed, firstly to establish the composition of the respective pipe sections and to compare this to the chemical specification of ASTM A516 Grade 65 material. Secondly, it was analysed to determine whether there were any noticeable composition differences between the respective pipe sections, which would have contributed to the initiation and growth of graphitization.

3.2.1. Bulk Chemical Analyzing

The respective service exposed steam pipe samples were chemically analysed using a Spectro MaxX Spark Spectrometer as shown in **Figure 3-1**, with the analyses specifically done in the core regions. The calibration of the Spark Spectrometer was verified on a certified chemical standard block, prior to performing the chemical analyses.



Figure 3-1: The SpectromaxX Spark spectrometer used to determine the bulk chemical composition of the service exposed steam pipe samples.

Due to the inherent limitation of the Spark Spectrometer, with regard to analysis of Carbon content, only the bulk or remainder of the chemical analyses were used for each of the samples evaluated.

3.2.2. Carbon and Sulphur Analyzing

From the same service exposed samples, which were chemically analysed using the Spark Spectrometer, small drill shavings were removed from the core regions. These were cleaned and dried and placed in clearly identifiable containers. Certified carbon and sulphur calibration powders were then analysed with the Bruker Carbon Sulphur analyser shown in **Figure 3-2**. The obtained measurements were then used to calibrate the analyser for both low and high measurements.

Each of the service exposed pipe samples saving material were then analysed and the value of each sample was then used as the carbon and sulphur content for the respective pipe sample.

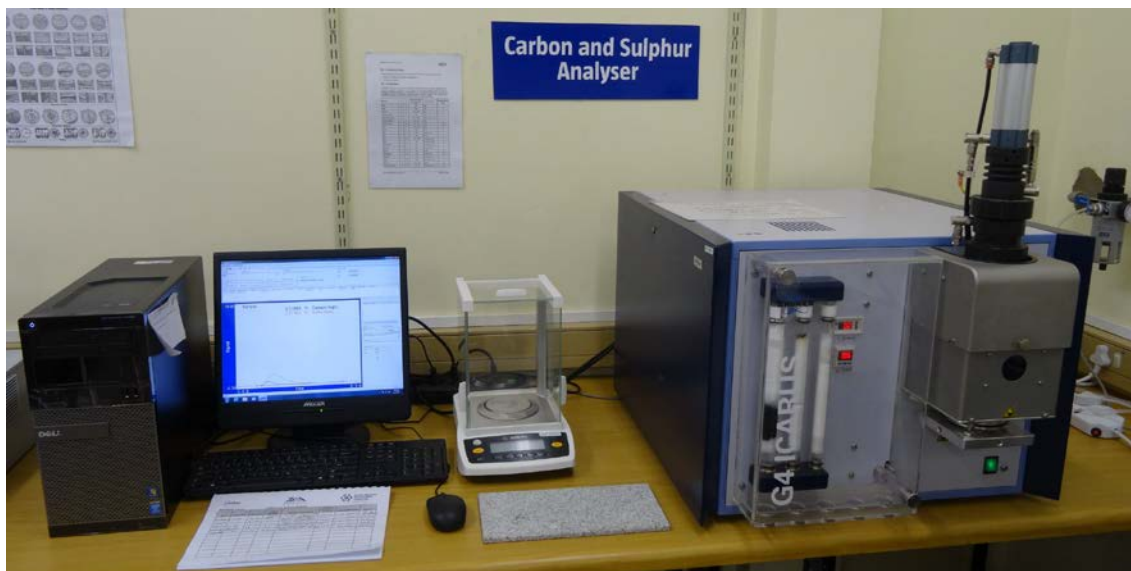


Figure 3-2: The Bruker Carbon Sulphur analyzer, used to accurately determine the Carbon and Sulphur content of the service expose steam pipe samples

3.2.3. Combined Chemical Evaluation Results

The chemical analysis results obtained using the Spark Spectrometer and the Carbon Sulphur analyser were then combined to give a complete chemical composition for each of the respective steam pipe samples (see **Table 3-2**). Evaluation of the chemical results revealed noticeable compositional differences between the up and down stream pipe material of the respective samples, despite the individual elements variance, specifically with regard to the carbon, silicon and aluminium content. It was also evident from the chemical evaluation results that all of the steam pipe sample material used in this research conforms to the chemical specification requirements of ASTM A516 Grade 65.

Table 3-2: Chemical analysis results of service exposed steam pipe material.

Chemical element	Chemical specification of ASTM A516 Grade 65	Sample A				Sample B				Sample C				Sample D			
		Up stream		Down stream		Up stream		Down stream		Up stream		Down stream		LH side		RH side	
		Min	Max	Min	Max	Min	Max	Min	Max	Min	Max	Min	Max	Min	Max	Min	Max
%C - Carbon	0.29 (max)	0,1395	0,1836	0,1069	0,1191	0,1079	0,1216	0,1760	0,1792	0,1703	0,1710	0,1108	0,1145	0,1210	0,1346	0,1288	0,1292
%Mn - Manganese	0.85 - 1.20	0,9	0,91	0,9	0,91	0,9	0,92	0,88	0,89	0,85	0,86	0,89	0,9	0,89	0,92	0,87	0,91
%P - Phosphorus	0.035 (max)	0,017	0,019	0,022	0,023	0,023	0,024	0,016	0,018	0,020	0,022	0,018	0,020	0,020	0,021	0,018	0,020
%S - Sulphur	0.035 (max)	0,0076	0,013	0,016	0,019	0,017	0,020	0,0071	0,0094	0,0066	0,0085	0,024	0,028	0,014	0,020	0,012	0,016
%Si - Silicon	0.15 - 0.40	0,199	0,206	0,258	0,263	0,263	0,265	0,198	0,201	0,221	0,223	0,256	0,266	0,241	0,250	0,244	0,245
%Cr - Chrome	none	0,0069	0,0082	0,03	0,03	0,030	0,031	0,0068	0,0083	0,0084	0,0087	0,040	0,041	0,036	0,037	0,035	0,036
%Ni - Nickel	none	0,020	0,022	0,028	0,029	0,025	0,028	0,020	0,022	0,019	0,023	0,030	0,033	0,025	0,027	0,022	0,026
%Mo - Molybdenum	none	0,0037	0,0042	0,0072	0,0073	0,0072	0,0074	0,0035	0,0044	0,0038	0,0040	0,0085	0,0087	0,011	0,011	0,011	0,011
%Al - Aluminium	none	0,0051	0,0076	0,059	0,061	0,060	0,061	0,013	0,019	0,030	0,031	0,062	0,062	0,063	0,065	0,064	0,07
%Ti - Titanium	none	0,0033	0,0035	0,0026	0,0027	0,0026	0,0028	0,0034	0,0045	0,0027	0,0029	0,0026	0,0028	0,0027	0,0029	0,0026	0,0027
%B - Boron	none	0,0009	0,016	0,0011	0,0011	0,0010	0,0011	0,0013	0,0015	0,0013	0,0014	0,0008	0,0011	0,0009	0,001	0,0009	0,0011
%V - Vanadium	none	0,001	0,001	0,0013	0,0014	0,0011	0,0012	0,0010	0,0014	0,0011	0,0015	0,001	0,001	0,001	0,0012	0,001	0,001
%Cu - Copper	none	0,0054	0,0057	0,039	0,04	0,040	0,041	0,0052	0,0056	0,0076	0,0077	0,068	0,069	0,023	0,023	0,022	0,023
%Fe - Iron	none	98,691	98,600	98,529	98,493	98,522	98,476	98,669	98,636	98,658	98,635	98,488	98,453	98,551	98,486	98,569	98,509

Note: The chemical results of the respective pipe regions are based on six individual Spark Spectrometer analyses done across the pipe material from below the outer surface towards the inner surface and Carbon Sulphur analyses done on shavings collected from the same regions on the respective pipe samples. These analysis results were then combined and the minimum and maximum values of the respective elements were reported in Table 3-2 for the respective pipe samples.

3.3. Evaluation of the Graphitization in the Service Exposed Pipe Samples

3.3.1. Introduction

Initially each of the weld heat affected zones (HAZ) of the service exposed pipe samples were evaluated with regard to the graphitization. This evaluation was done on macro samples, which were removed from either end of the respective samples perpendicular to the connection seam welds, away from the flame cut edges. An example of where the macro samples were removed from the welded service expose steam pipe samples is shown in **Figure 3-3**.

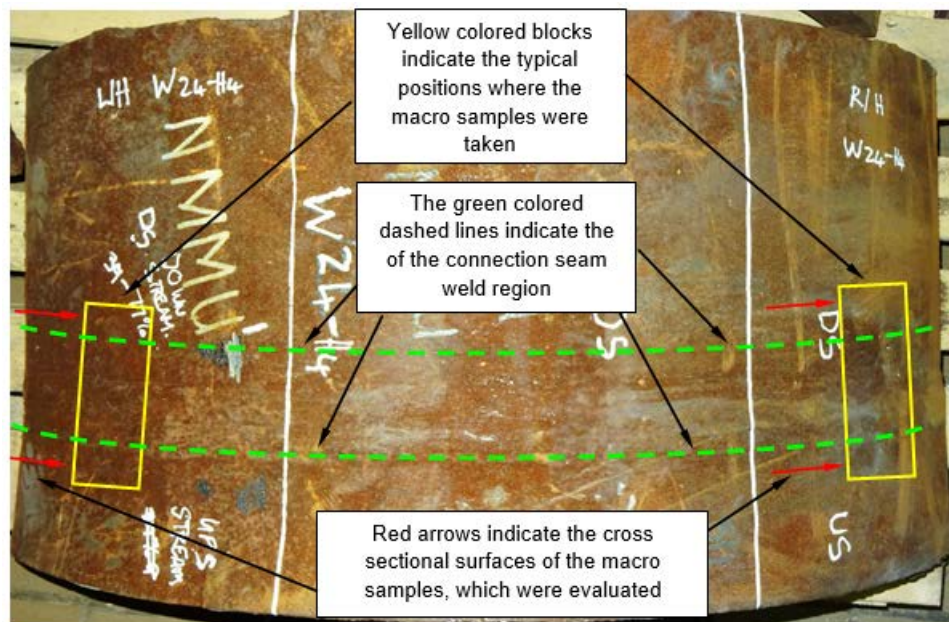


Figure 3-3: The typical regions from where the macro sample samples were removed from the service pipe samples.

3.3.2. Procedure used to Prepare the Macro Samples

The macro samples were then surface ground and subsequently rough ground and polished using the ATM Saphir 550 semi-automatic polishing machine (see **Figure 3-4**). Two macro samples, secured on the universal polishing head, were polished at a time (see **Figure 3-5**) using the metallurgical preparation steps summarized in **Table 3-3**.



Figure 3-4: The ATM Saphir 550 semi-automatic polishing machine used to fine ground and polish the large macro samples and smaller micro samples.



Figure 3-5: An example of how the large macro samples were secured to the universal polishing head (L/H side) and the final polished macro samples (R/H side).

Macro sample preparation steps	Polishing consumable used during the steps	Central Force (N)	Polishing head and wheel (rpm)	Polishing time (min)
80 gritt (rough grinding)	80 gritt diamond resin bonded disc for MD disc use with water	35	150	15
220 gritt (rough grinding)	220 gritt diamond resin bonded disc for MD disc use with water	30	150	10
600 gritt (fine grinding)	600 gritt diamond resin bonded disc for MD disc use with water	30	150	10
1200 gritt (fine grinding)	1200 gritt diamond resin bonded disc for MD disc use with water	30	150	10
9 µm polishing	9 micron diamond suspension used with MD Allegro fine grinding disc	30	150	10
6 µm polishing	6 micron diamond suspension used with MD Mol polishing cloth	25	150	10
3 µm polishing	3 micron diamond suspension used with MD Mol polishing cloth	25	150	7
1 µm polishing	1 micron diamond suspension used with MD NAP polishing cloth	25	150	7

Table 3-3: Summary of the metallurgical preparation steps used to prepare the macro samples removed from the respective service exposed pipe samples.

Figure 3-6 shows an example of one of these macro samples after polishing and etching, with the different sample regions identified.

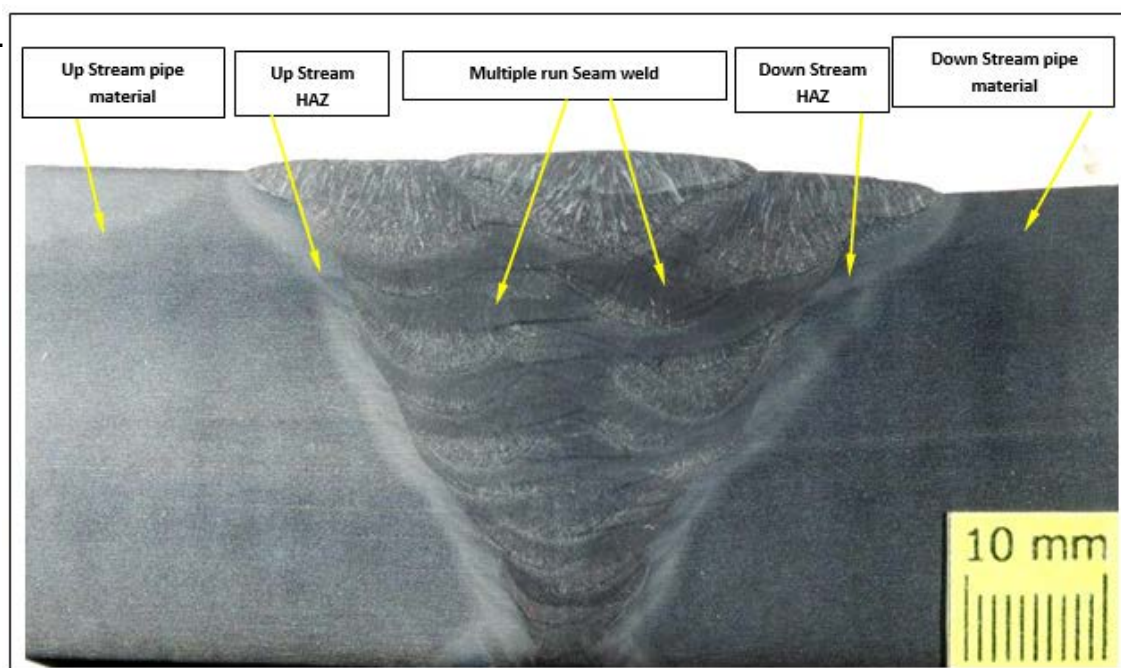


Figure 3-6: A typical example of one of the polished and etched macro samples.

3.3.3. Initial Findings with regard to HAZ Graphitization of the Service Expose Pipe Samples

The respective macro samples taken from the service exposed pipe samples, were compared based on graphite nodule distribution (size, spacing and level of graphitization) specifically in the HAZ regions, to compare either end of the seam welds for Sample A – D. A qualitative review of the graphite nodule distribution results showed only slight variation between the HAZ pipe regions of the respective pipe samples. This led to a decision to broaden the scope of the research by including the parent material on either side of the seam welds, which displayed significantly lower levels of graphitization. A quantitative evaluation of the graphite nodule distribution was performed in the parent pipe and the HAZ regions to evaluate the effect of graphitization on the static mechanical properties and the influence of Al and Si on graphite formation.

3.3.4. Graphite Nodule Size Evaluation

Optical micrographs were taken of the graphitization at 100X magnification; just outside the HAZ and in the parent material, at a set distance below the outer surface, in the centre and at a set distance from the inner pipe surface. This was done on either side of the seam weld as shown in **Figure 3-7**, for the respective macro samples.

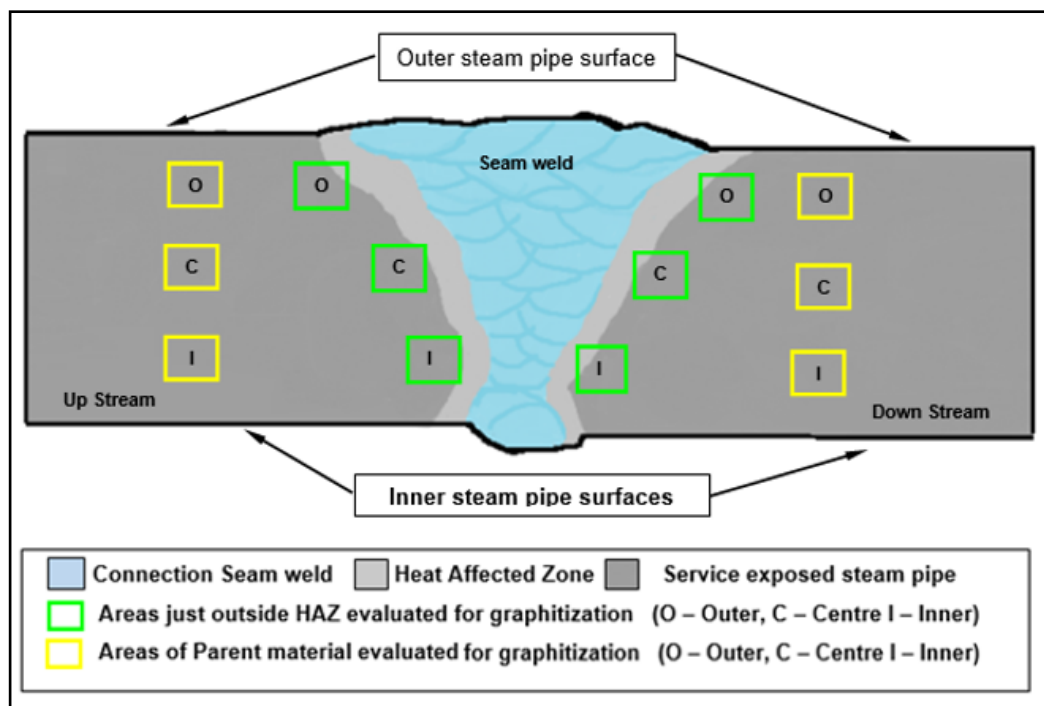


Figure 3-7: The areas evaluated with regard to graphite nodule size and spacing and % planar graphitization.

Calibrated image analysis software was then utilized to manually measure the sizes of the graphite nodules identified on the micrographs of each macro sample. All of the graphite nodule size measurements were done at 100X magnification by the same individual, using the same method. Each nodule size measurement was taken from the outer edge on the one side of the nodule up to the outer edge on the opposite side. This was measured along both the horizontal plane (Measurement A) and the vertical plane (Measurement B) as shown in **Figure 3-8**.

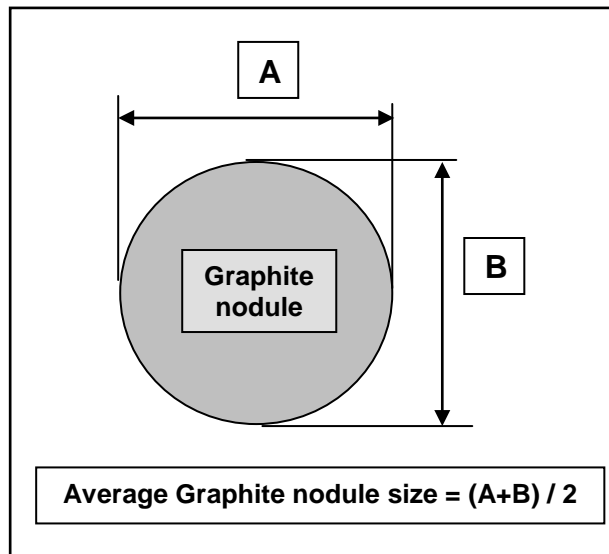


Figure 3-8: Illustration showing the graphite nodule size measuring method

The median, 25% and 75% percentile were then calculated from the graphite nodule size measurements of the outer, centre and inner areas of the respective parent pipe regions and the regions outside the HAZ, on either side of the connection seam weld, for each of the pipe samples. The results were then summarized in a box and whisker plot for comparative data evaluation purposes (see **Figure 3-9**).

The results, of the randomly distributed graphite nodules in the steam pipe parent material, show a larger median size compared to the planar graphitization just outside the HAZ. The detailed Nodule size evaluation results of the respective pipe samples are presented in Appendix A.

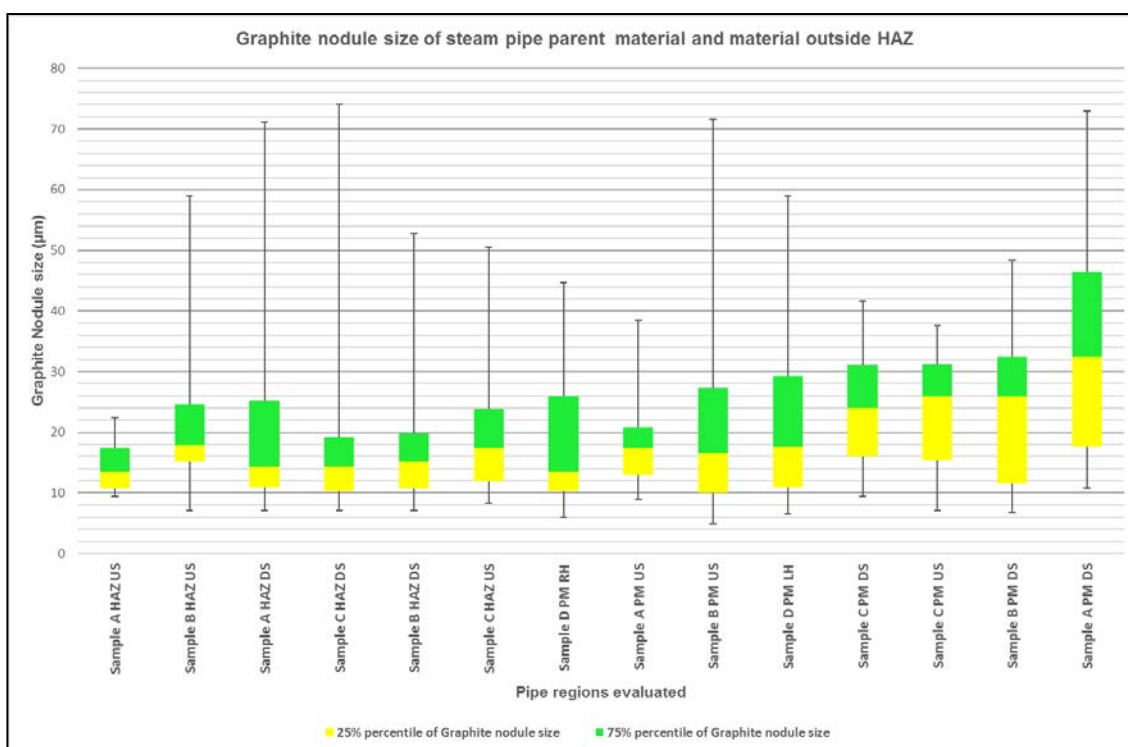


Figure 3-9: Graphical summary of the graphite nodule size evaluation results.

3.3.5. Graphite Nodule Spacing Evaluation

Graphite nodule spacing measurements were taken on the same 100X micrograph images used for the graphite nodule size evaluation. The same calibrated image analysis software was used to manually measure the spacing between the respective nodules and their nearest neighbour, as shown in **Figure 3-10**. All the graphite nodule spacing measurements were done at 100X magnification by the same individual, using the same method. This was done for the respective pipe region's outer, centre and inner areas as indicated in **Figure 3-7**.

The median, 25% and 75% percentile were then calculated from the graphite nodule spacing measurements of the outer, centre and inner areas of the respective parent pipe regions and the region outside the HAZ on either side of the connection seam weld of each of the pipe samples. These results were then summarized in a box and whisker plot for comparative data evaluation purposes (see **Figure 3-11**).

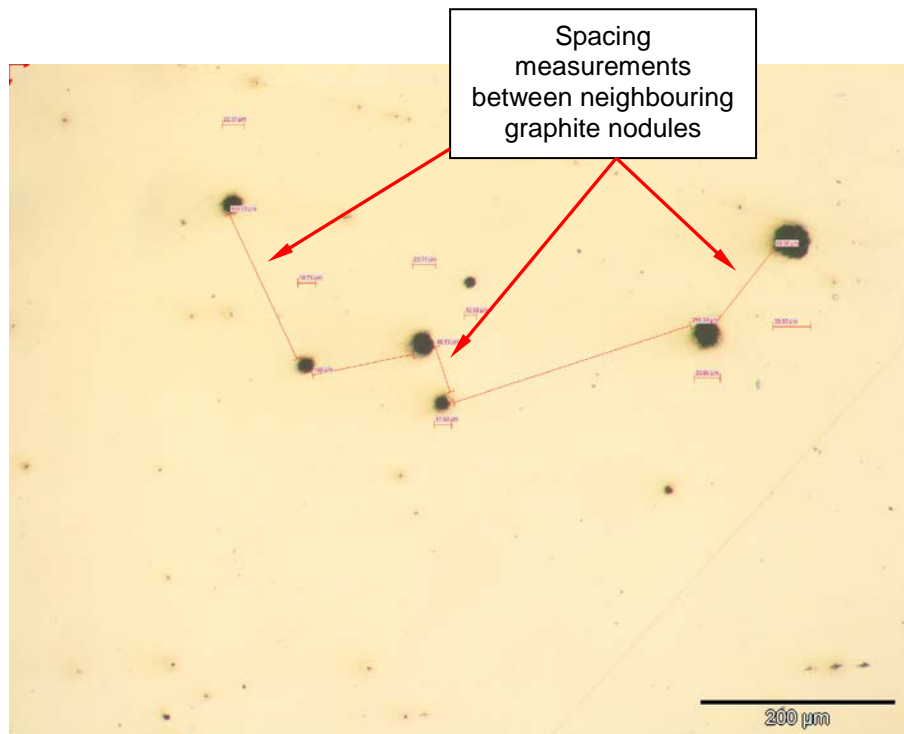


Figure 3-10: An example of how the spacing between neighbouring graphite nodules was measured on one of the micrographs taken 100X magnification.

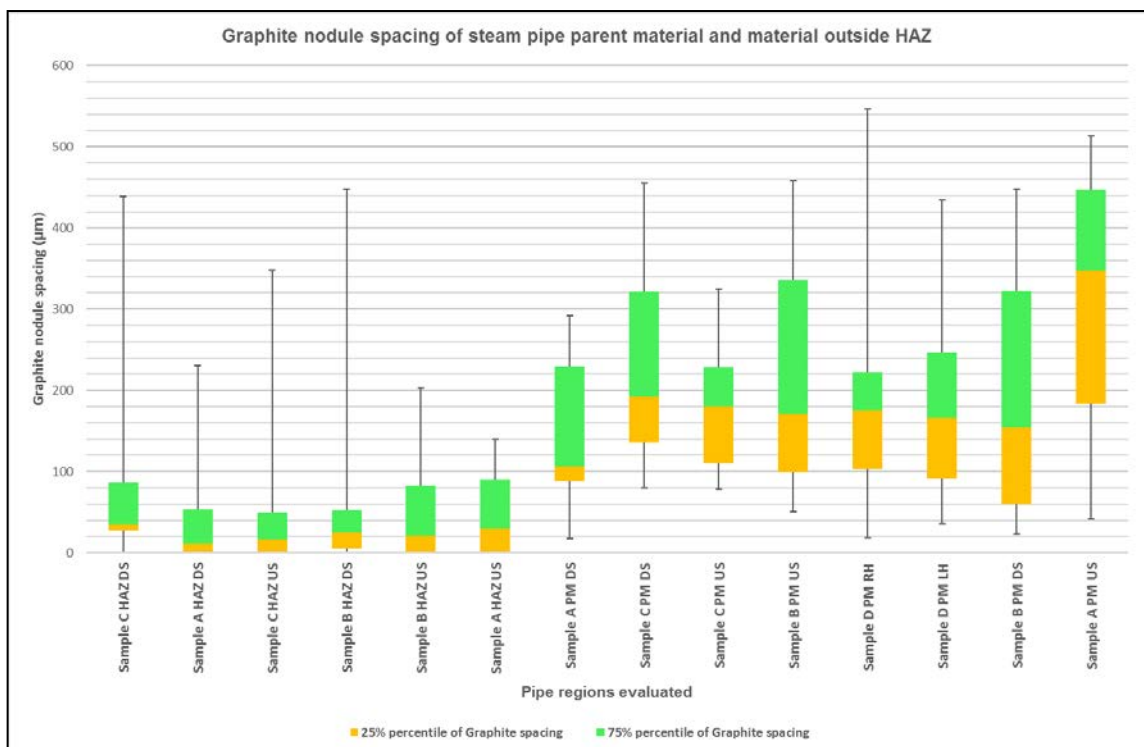


Figure 3-11: Graphical summary of the graphite nodule spacing evaluation results

It is evident from the results that the randomly distributed graphite nodules in the steam pipe parent material, has a larger median spacing (105 - 340 μm) compare to the planar graphitization, just outside the HAZ, which exhibited a median spacing (10 - 40 μm) between the nodules (see **Figure 3-11**). The detailed nodule spacing evaluation results of the respective pipe samples can be viewed in Appendix A.

3.3.6. Percentage Planar Graphitization Evaluation

The percentage planar graphitization for the respective regions was calculated in relation to the outer pipe surface by applying a planar projection method as per **Figure 3-12**. This method involves projecting the individual planar graphitization group lengths down towards the horizontal side of the micrograph. These projected group lengths (refer to the green lines in **Figure 3-13**) were then added, excluding overlaps, and the total projected length was then divided by the overall length of the horizontal side of the micrograph (refer to the blue line on **Figure 3-13**). This figure was then multiplied by 100 to obtain the % planar graphitization for the evaluated area. The actual calculation for the evaluated micrograph is shown in **Figure 3-13**.

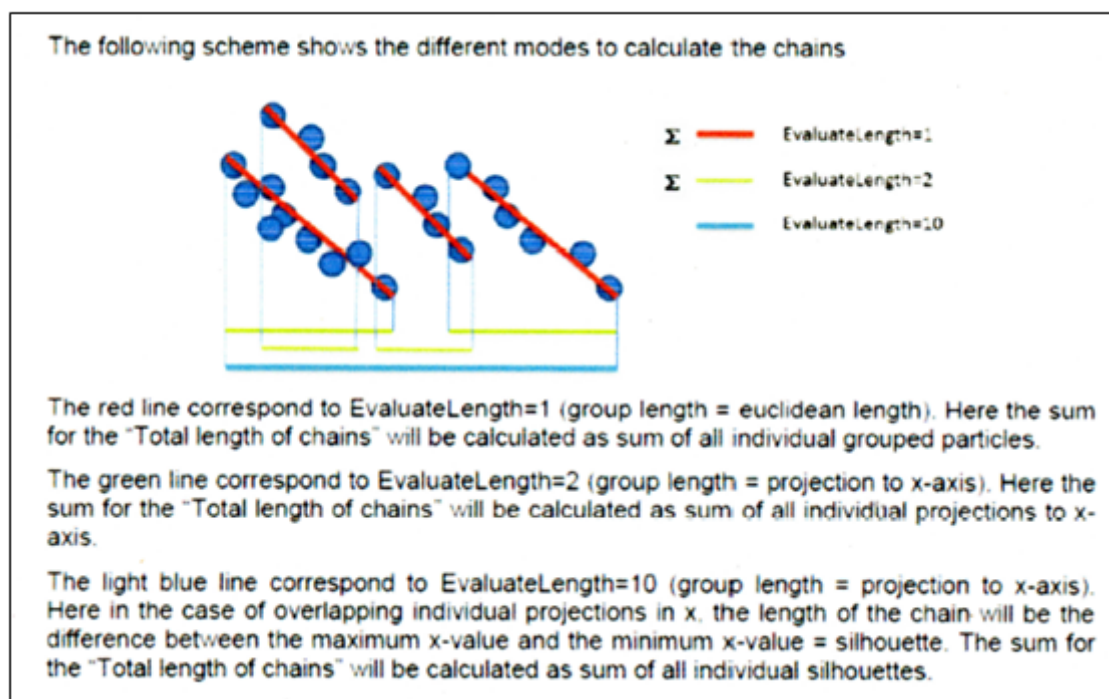
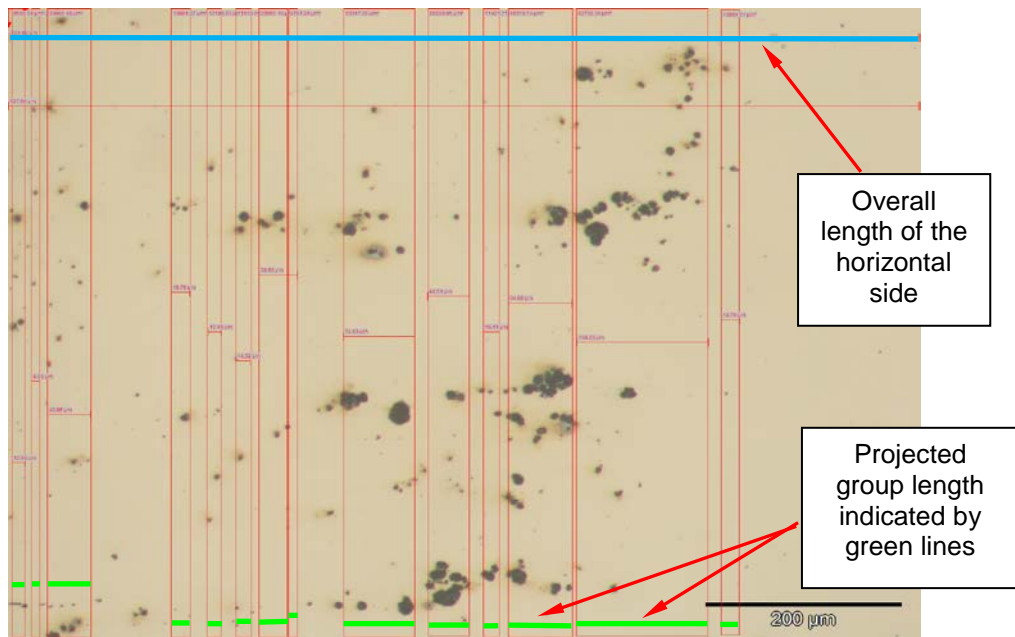


Figure 3-12: The planar projection method used to calculate the % planar graphitization of the various pipe regions evaluated



$$\begin{aligned} \% \text{planar graphitization} &= (\text{Total projected length} / \text{Overall Horizontal length}) \times 100 \\ &= (499.35 \mu\text{m} / 927.96 \mu\text{m}) \times 100 \\ &= 54\% \end{aligned}$$

Figure 3-13: The application of the planar projection method.

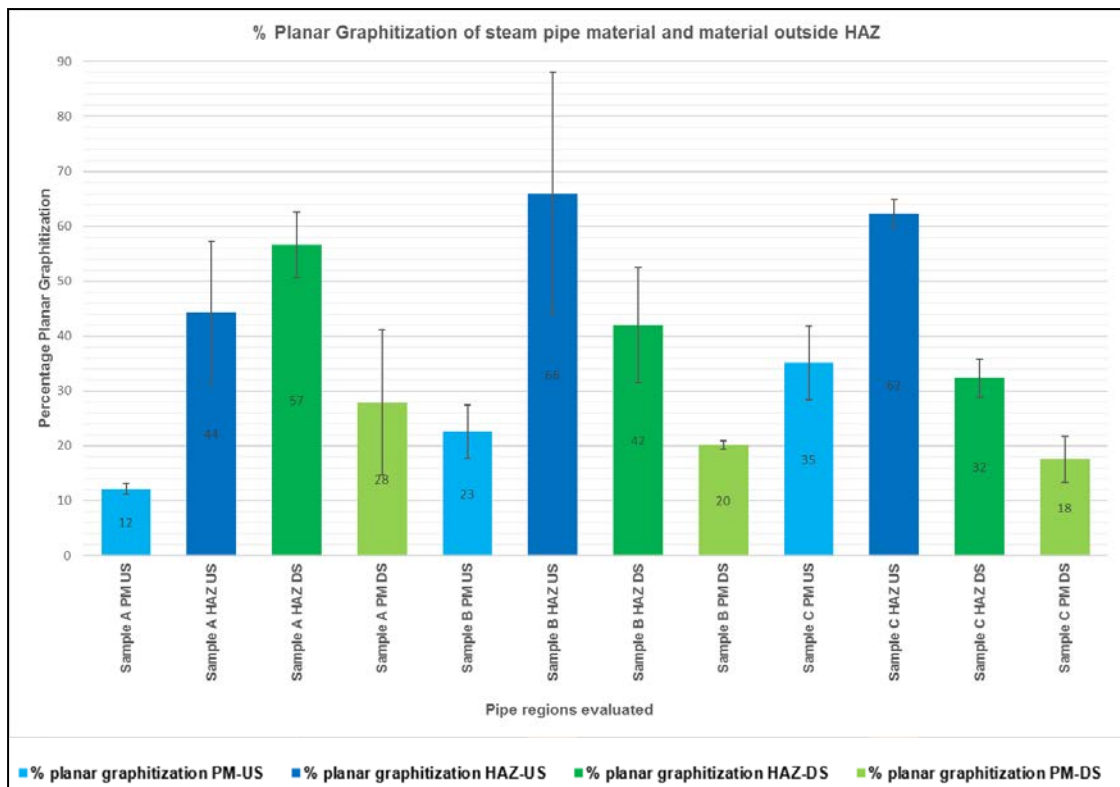


Figure 3-14: A graphical summary of the % planar graphitization evaluation results.

The average percentage planar graphitization of the respective pipe samples and regions evaluated was summarized in a graphical format (see **Figure 3-14**). It is evident from the evaluation results that the HAZ regions of the respective pipe samples have higher levels of planar graphitization in comparison to the parent regions. Variations were noted in the level of planar graphitization on the different sides of the weldment, but these results need to be interpreted with care considering the limitations of the sampling and measurement methods. The detailed percentage graphitization evaluation results of the respective pipe samples can be viewed in Appendix A.

3.4. The effect of Graphite on the Hardness of the Service Expose Steam Pipe Samples

3.4.1. Introduction

Vickers Micro hardness measurements were done, from the parent steam pipe material across the HAZ into the seam weld material, to establish what effect graphitization had on the hardness of the respective service exposed pipe samples.

3.4.2. Procedures used during the Hardness Evaluation of Pipe Samples

A Future Tech FM700 hardness tester shown in **Figure 3-15** was used to perform hardness profile measurements; on either side of the seam weld in the same three areas, just below the outer surface, in the centre and just above the inner pipe surface on the respective macro samples as shown in **Figure 3-16**. These measurements were taken using equal steps of 0.5 mm and a 300 gram load.

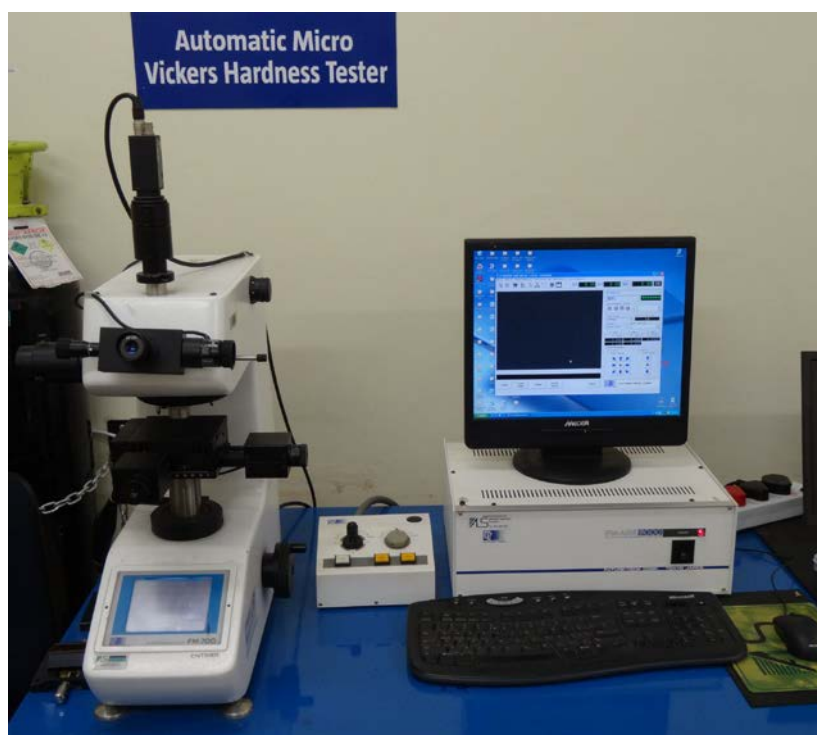


Figure 3-15: The Future tech FM700 automatic Vickers Micro Hardness tester used for the hardness profile measurements on the service exposed pipe samples.

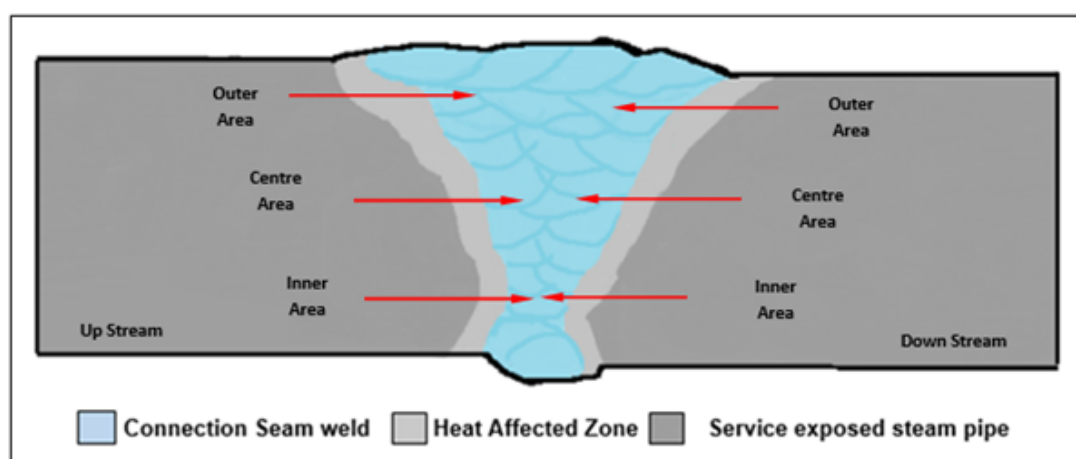


Figure 3-16: The areas where the Vickers micro Hardness profile measurements were done.

3.4.3. Micro Vickers Hardness Profile Evaluation Results

Average hardness profile data were calculated based on the hardness measurements of the three areas i.e. just below the outer surface, in the centre and just below the inner pipe surface. This data was then summarized in graph format for the up and down stream sides of the respective samples for comparative purposes (see **Figure 3-17 to Figure 3-20**). The detailed Vickers micro Hardness profile data can be viewed in Appendix B.

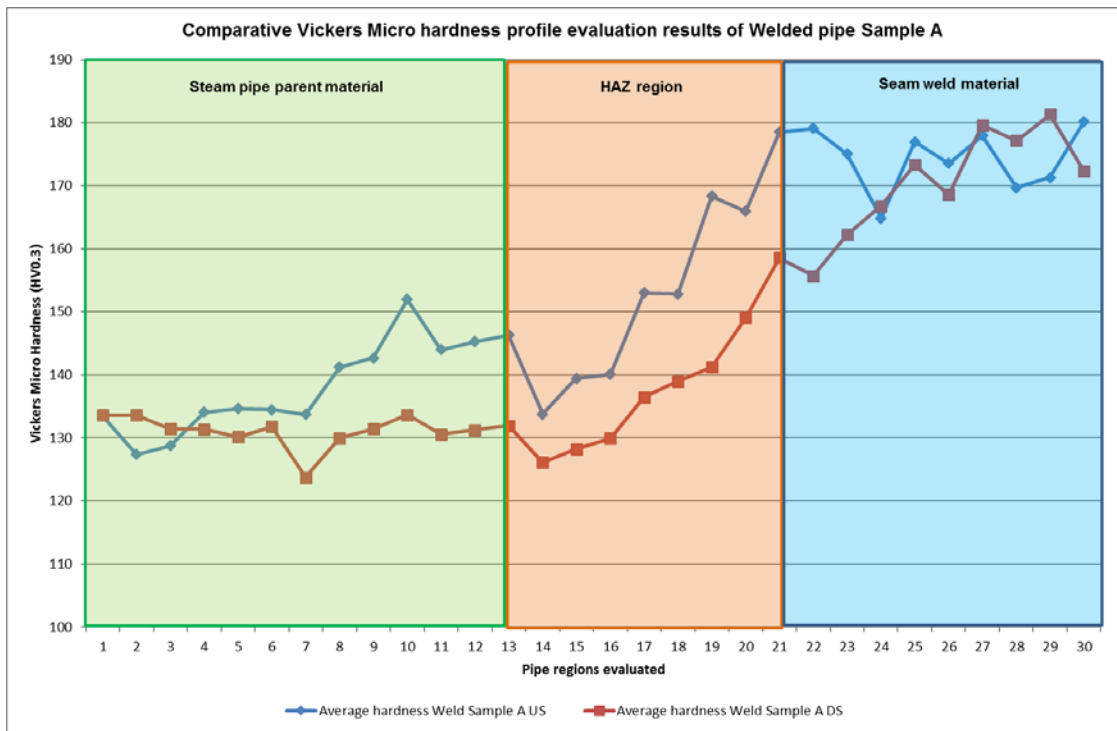


Figure 3-17: A graphical summary of the Vickers micro hardness profile results of Weld Sample A

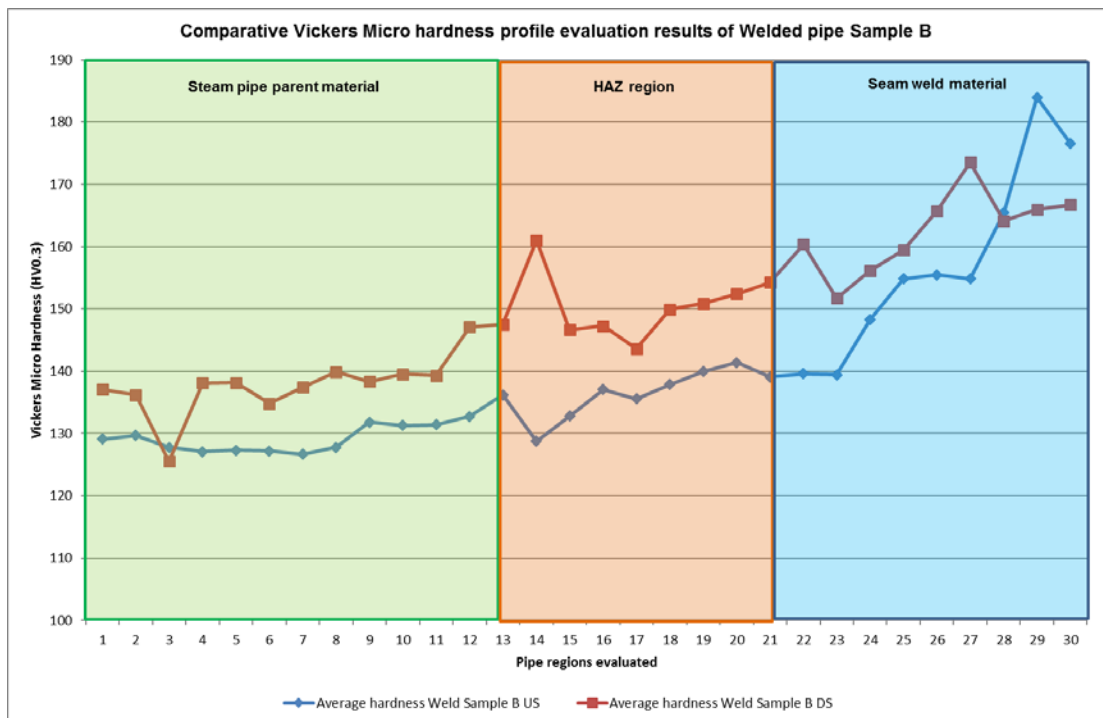


Figure 3-18: A graphical summary of the Vickers micro hardness profile results of Weld Sample B.

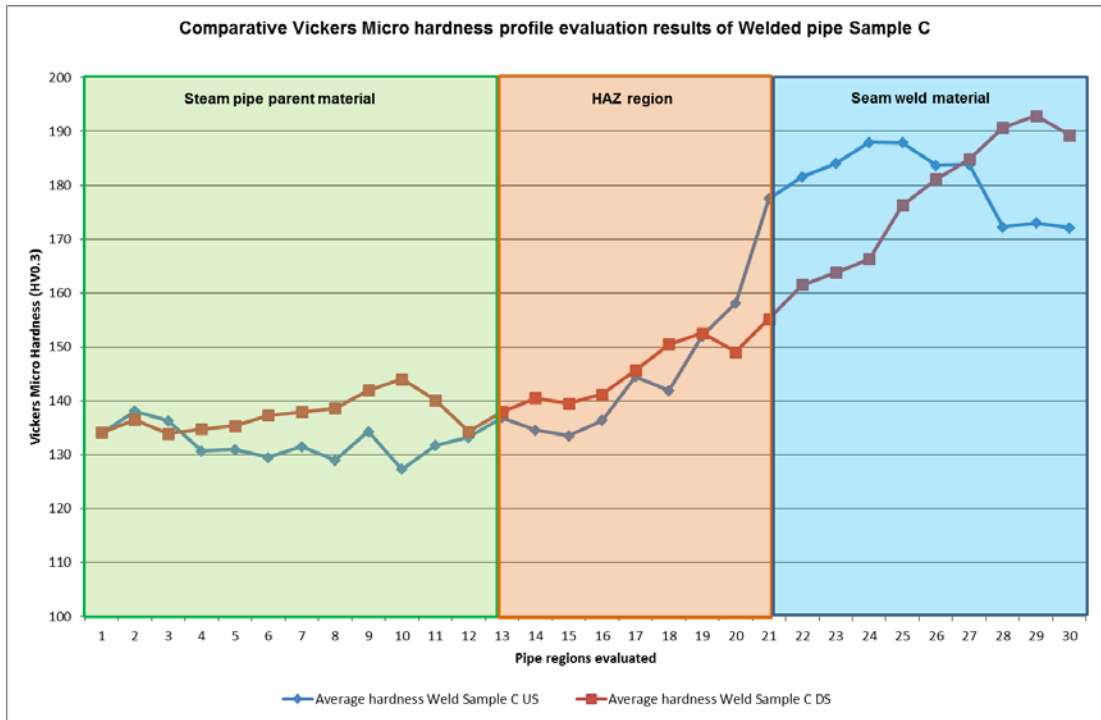


Figure 3-19: A graphical summary of the Vickers micro hardness profile results of Weld Sample C.

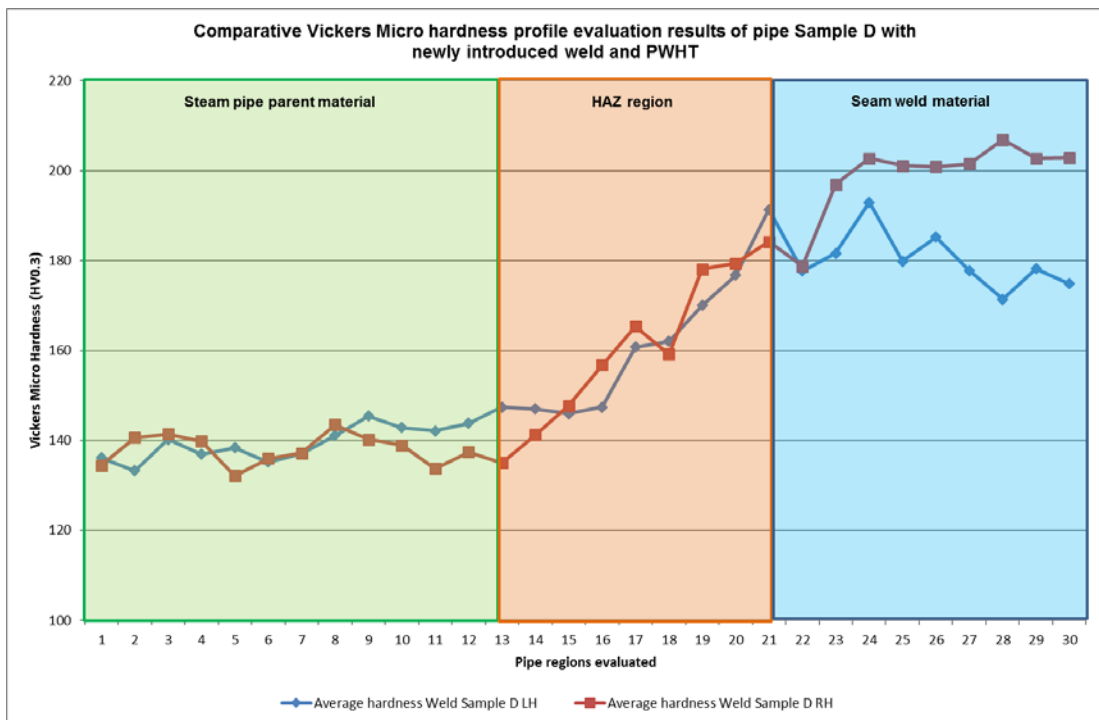


Figure 3-20: A graphical summary of the Vickers micro hardness profile results of Weld Sample D.

Review of the Vickers Micro Hardness evaluation results showed hardness differences between the up and down stream parent material of the respective service exposed pipe samples.

This prompted the need to gather more hardness data to establish whether the difference in hardness is related to:

- a) variation in the measuring platform,
- b) methodology or
- c) due to the hardness variation across the evaluated cross-section.

Subsequently, five additional Vickers micro hardness line profile measurements were performed specifically in the centre regions of the up stream and down stream sides of welded pipe Sample A (see **Figure 3-21**). The hardness profile lines were spaced 1.0 mm apart and the hardness measurements were performed at 0.5 mm intervals. The average hardness was then calculated for the respective positions evaluated from the parent material towards the weld. The data were summarized in graphical format as shown in **Figure 3-22**. The Vickers micro Hardness data of the additional work can be found in Appendix B.

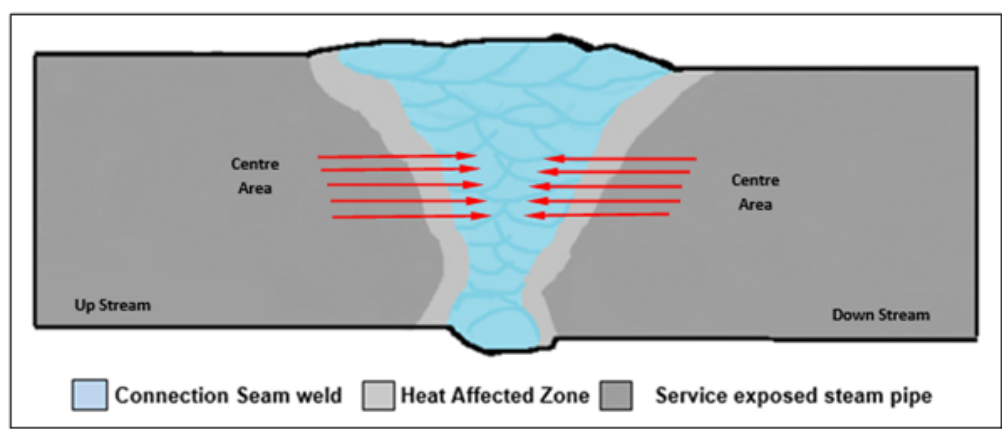


Figure 3-21: The centre areas where the five Vickers micro Hardness profile measurements were done on either side of Weld Sample A.

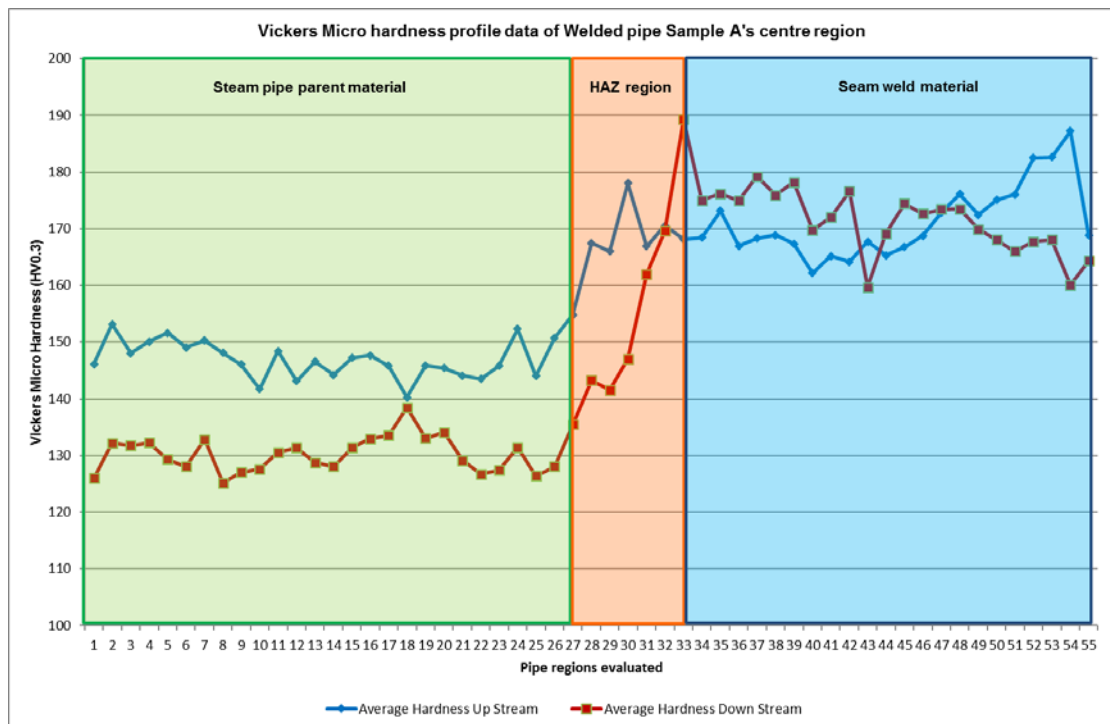


Figure 3-22: Graphical summary of the Vickers micro hardness data from Welded pipe Sample A's up and down stream centre regions.

It is clearly evident from the summarized hardness data in **Figure 3-22** that the down stream parent material has a lower hardness in comparison to the up stream parent material of welded pipe Sample A.

The hardness difference between the up and down stream parent pipe material can most probably be linked to the level of planar graphitization and Carbon content. Higher levels of carbon will result in the formation of more pearlite phase, which is expected to increase the hardness. During graphitization these pearlite regions dissolve leading to an expected decrease in hardness.

Sample A's up stream parent material has 12% planar graphitization and a carbon content of 0.161% giving it an average hardness of 145 HV, while the down stream parent material has 28% planar graphitization and a carbon content of 0.113% giving it an average hardness of 131 HV. The difference in hardness is expected, because higher carbon content and lower % planar graphitization would lead to higher measured hardness.

3.5. The Effect of Graphite on the Yield and Tensile Strength of the Service Exposed Steam Pipe Samples

3.5.1. Introduction

The main aim of this part of the research is to determine what effect graphitization had on the bulk yield and tensile strength of the service exposed pipe samples. Complete evaluation of this phenomenon's effect on the mentioned static mechanical properties was however not possible, due to the limiting size of the service exposed pipe sample material available. This resulted in the tensile samples being orientated perpendicularly to the connection seam welds of the respective pipe samples.

3.5.2. Tensile Sample Orientation and Pipe Regions being Evaluated

Tensile samples were removed from the centre up and down stream pipe regions as indicated in **Figure 3-23**. Further tensile samples were also removed from just outside the HAZ as per **Figure 3-24**, on the side of the seam weld, which had the highest amount of planar graphitization, with the centre of the reduced sections coinciding with the position of the planar graphitization.

The exact centre position of the reduced section of the tensile samples, removed from just outside the HAZ was determined by removing a micro sample sliced adjacent to each tensile sample. The micro sample slices were then polished and etched with 2% Nital to reveal the exact position of the planar graphitization and it was then transferred to the adjacent tensile samples as per **Figure 3-25**.

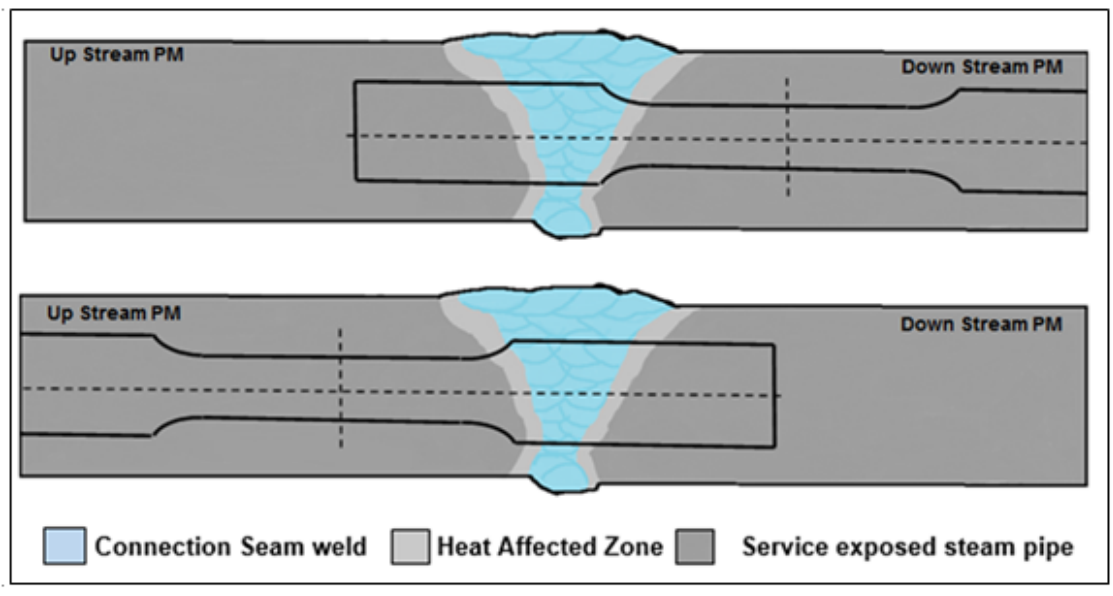


Figure 3-23: The positions where the parent material bulk tensiles were removed.

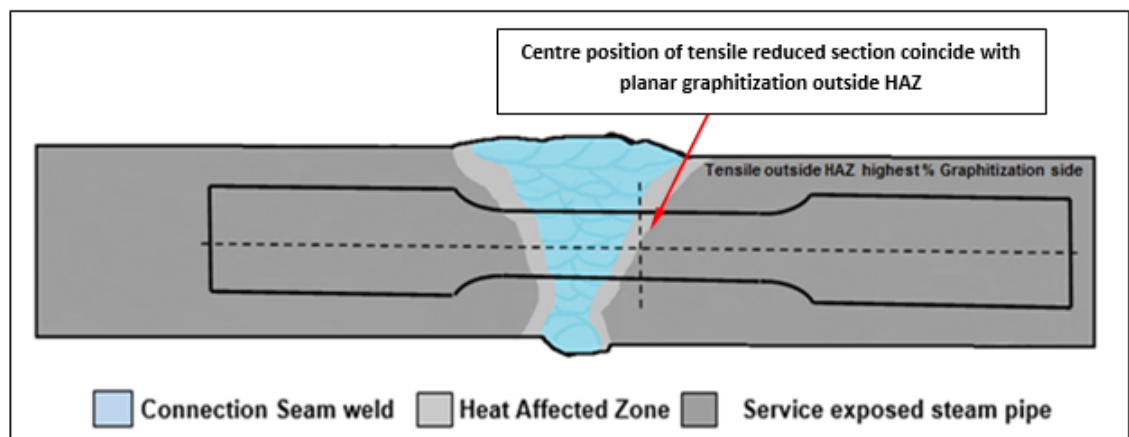


Figure 3-24: The position where the tensile samples were taken from just outside the HAZ.

The tensile samples were machined according to a standard tensile sample size according to **ASTM E8M-01**, as shown in **Figure 3-26**.

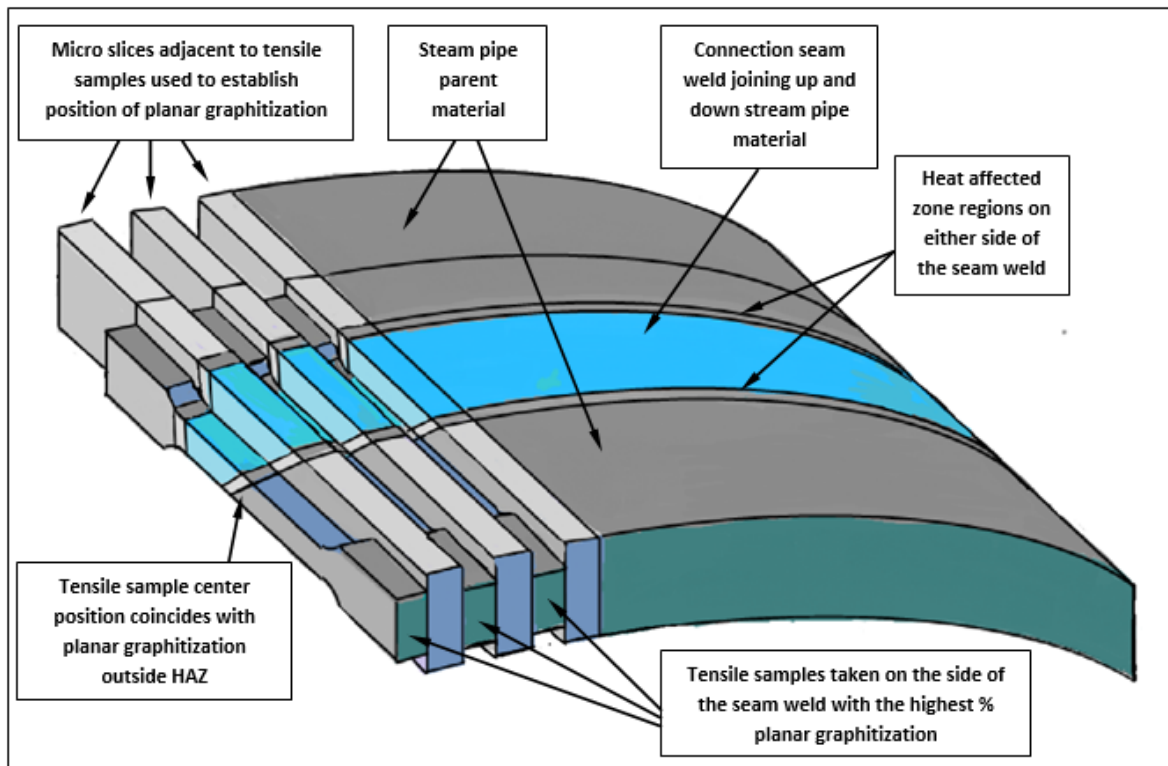


Figure 3-25: Tensile samples taken from just outside the HAZ and the adjacent micro slices used to determine the exact positions of the HAZ planar graphitization.

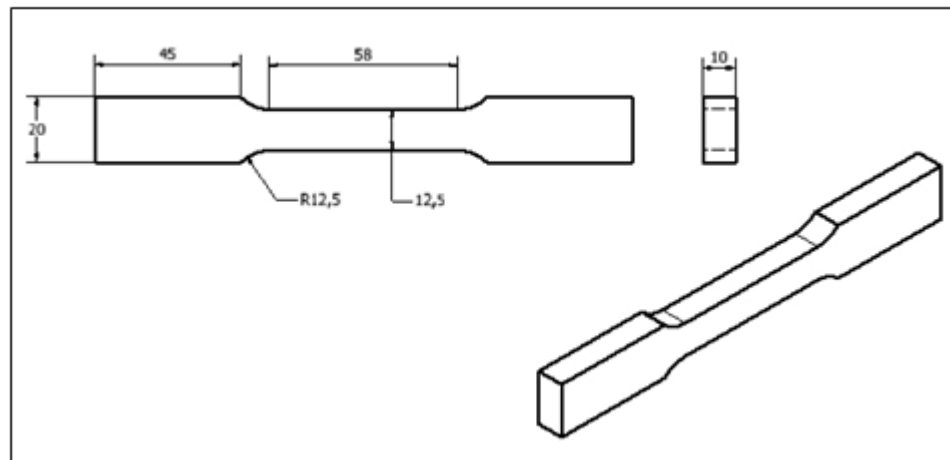


Figure 3-26: A drawing of the dimensions of the tensile samples machined from the respective service exposed steam pipe samples.

3.5.3. Room Temperature Tensile Testing

Tensile samples were tested at room temperature according to the requirements of **ASTM E8M-01**, using an Instron 8801 servo-hydraulic test platform shown in **Figure 3-27**. During the tensile tests, a constant extension rate of 5mm/min was used and no pre-load was applied. A clip on extensometer was used to accurately measure the yield strength (see **Figure 3-28**) and the ultimate tensile strength and % elongation at final fracture were recorded.



Figure 3-27: The Instron 8801 servo-hydraulic test platform used to perform the room temperature tensile testing of the tensile samples removed from the different service exposed steam pipe regions.

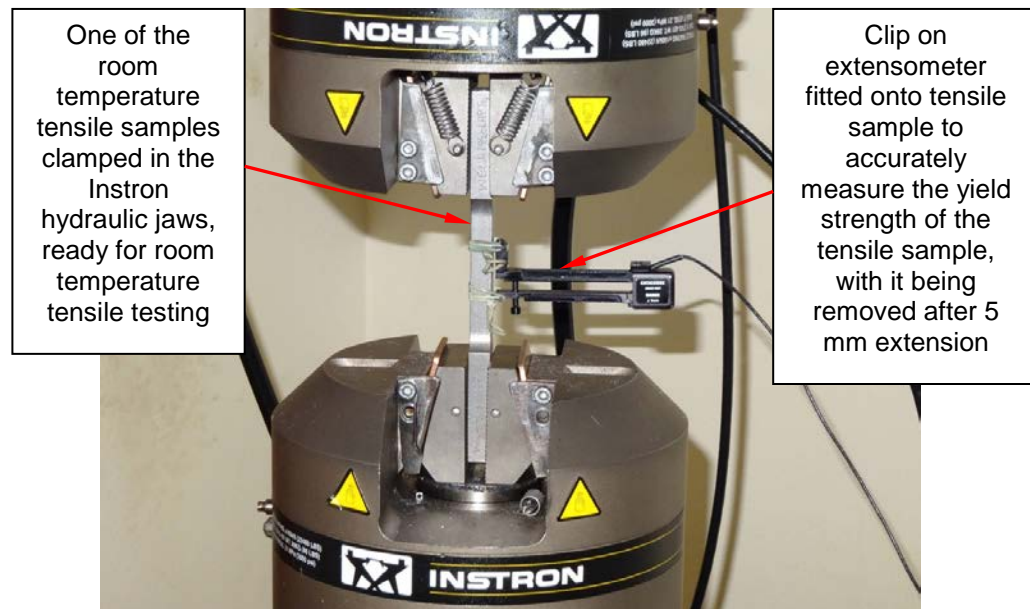


Figure 3-28: Close up view of the tensile test set up used to test the room temperature tensile samples.

3.5.4. Elevated Temperature Tensile Testing

Elevated temperature tensile tests were conducted at 420°C on tensile samples taken from just outside the HAZ on the same sides as the room temperature HAZ samples of weld samples A and D (with new seam weld and PWHT). These elevated temperature tensile tests were done using round tensile samples according to **BS EN 10002-2001; Metallic materials – Tensile testing – Part 5** (Figure 3-29 shows one of the round tensile samples tested at 420°C).

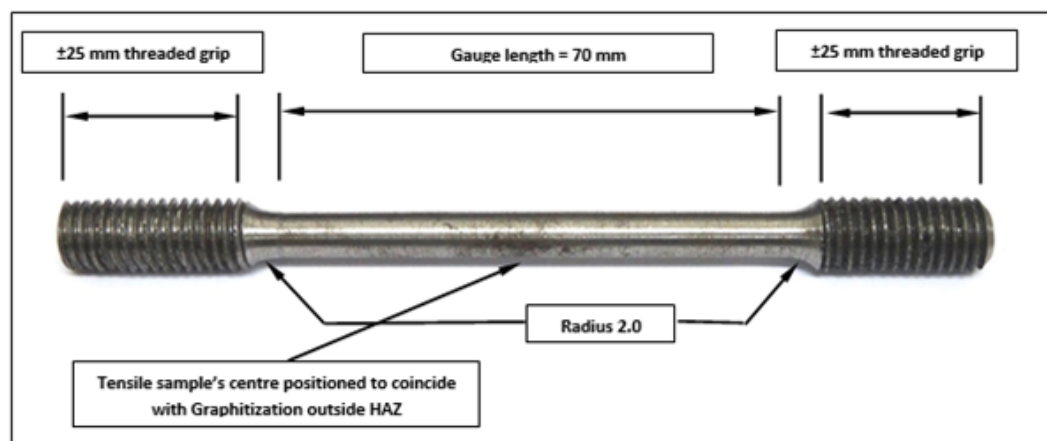


Figure 3-29: One of the round Tensile samples tested at 420°C.

3.5.5. Yield and Tensile Strength Evaluation Results of Service Exposed Steam Pipe with graphitization

The tensile samples removed from the up and down stream pipe parent material and from the region just outside the HAZ, on the side of the weld with the highest % planar graphitization, were tested at room temperature for the respective pipe samples. In conjunction with this, elevated temperature tensile tests were conducted on tensile samples taken from the same service exposed weld pipe samples, specifically from the one with the highest % planar graphitization in the region just outside the HAZ (Pipe Sample A) and also on the right hand side of the newly introduced seam weld done on service exposed pipe material of Sample D. These tests were conducted in an effort to establish a reference with regard to yield and tensile strength at an elevated temperature of 420°C and also to determine how the newly introduced seam weld would affect the elevated temperature mechanical properties.

The room temperature yield and tensile results of the respective service exposed pipe samples now needed to be evaluated against the actual elevated temperature yield and tensile test results. To perform this comparative evaluation, the room temperature yield and tensile strength results were converted to their expected yield and tensile strength values, at an operating temperature of 420°C, using conversion methods as per **API 579-1 Fitness-For-Service** specification. Detailed information concerning these methods is shown in Appendix C.

The results were plotted against the % planar graphitization of the different pipe regions (see **Figure 3-30 (Yield Strength)** and **Figure 3-31 (Ultimate Tensile Strength)**) to investigate the possible relationship. These graphs assisted with the comparative evaluation of the converted room temperature mechanical properties and the actual elevated temperature yield and tensile strength results obtained on the samples tested at 420°C.

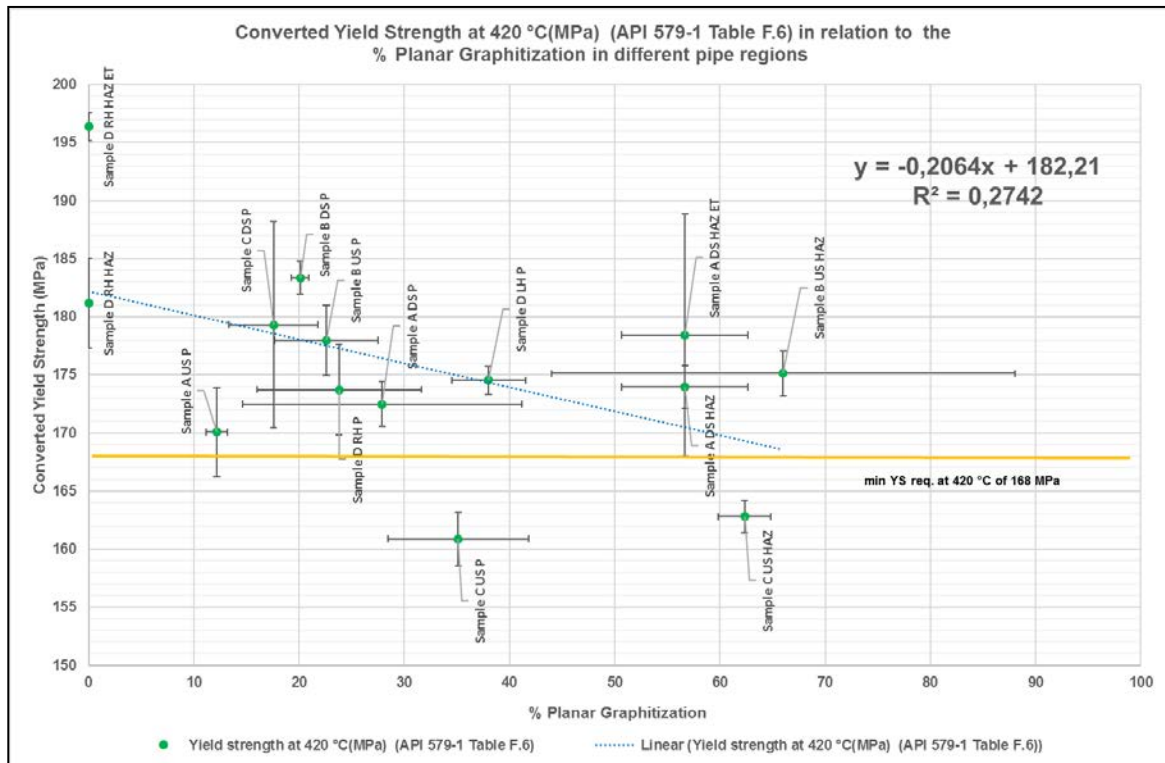


Figure 3-30: A graphical summary of converted room temperature Yield strengths at 420°C in relation to the % Planar Graphitization of the respective pipe regions.

It is evident from **Figure 3-30** that the converted yield strength values calculated are comparable to the actual elevated temperature yield strength measurements obtained from the material outside the HAZ of Welded Pipe Sample A down stream. The majority of the yield strength results were above the minimum requirement of 168 MPa for steam pipe material operating at 420°C as per **API 579-1 Fitness-For-Service** specification. It was only Welded Pipe Sample C's parent material and HAZ tensile samples, that obtained yield strength values below the 168 MPa minimum requirement. **Figure 3-30** also showed that the yield strength of the service exposed pipe material appears to be negatively correlated with the % planar graphitization ($R^2 = 0.27$), but this effect is not statistically significant (Regression analysis: $p > 0.05$).

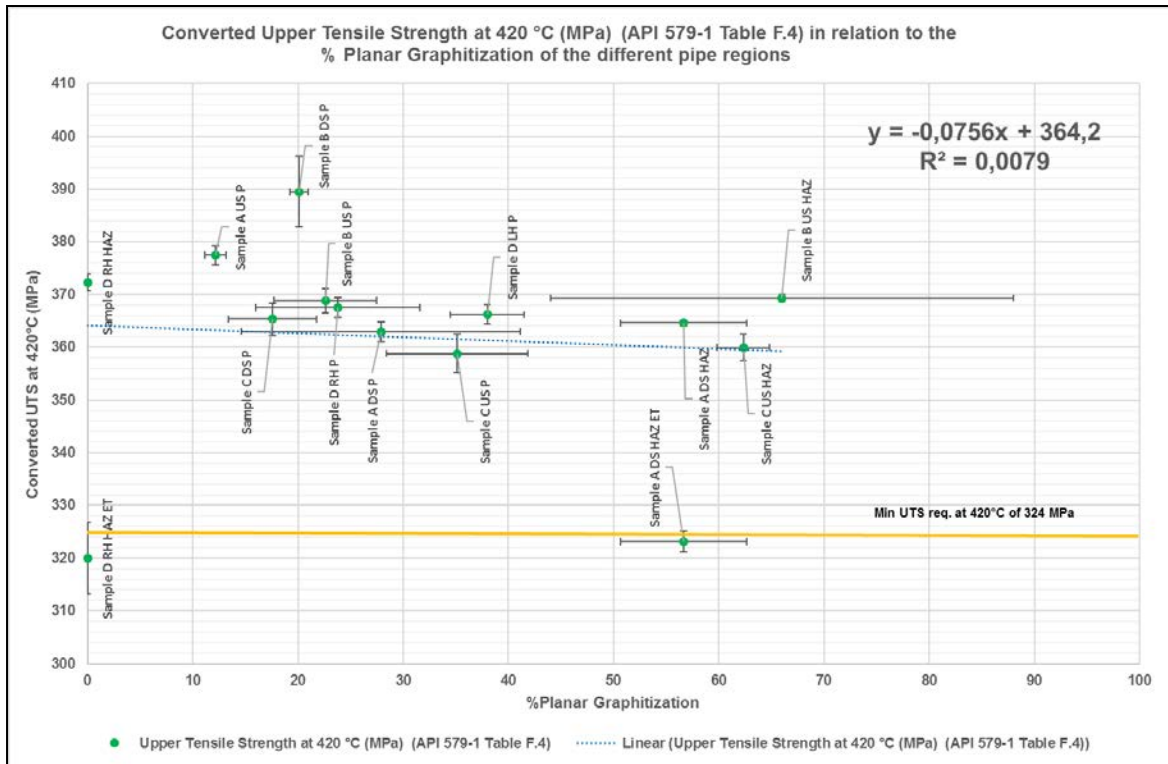


Figure 3-31: A graphical summary of converted room temperature UTS at 420°C and the % Planar Graphitization of the respective pipe regions.

It is evident from **Figure 3-31** that the converted upper tensile strength (UTS) values are higher than the actual elevated temperature upper tensile strength measurements obtained on the material outside the HAZ, down stream on Welded pipe Sample A. **Figure 3-31** indicate that the upper tensile strength of the service exposed pipe material has no correlation to the % planar graphitization ($R^2 = 0.0079$).

3.5.5.1. Evaluation of the Tested Tensile Samples to Determine Graphitization Influence on the Mode of Fracture

The up and down stream pipe parent material tensile samples fractured in a ductile manner with necking (see **Figure 3-32** showing one of the evaluated parent steam pipe tensile samples tested).

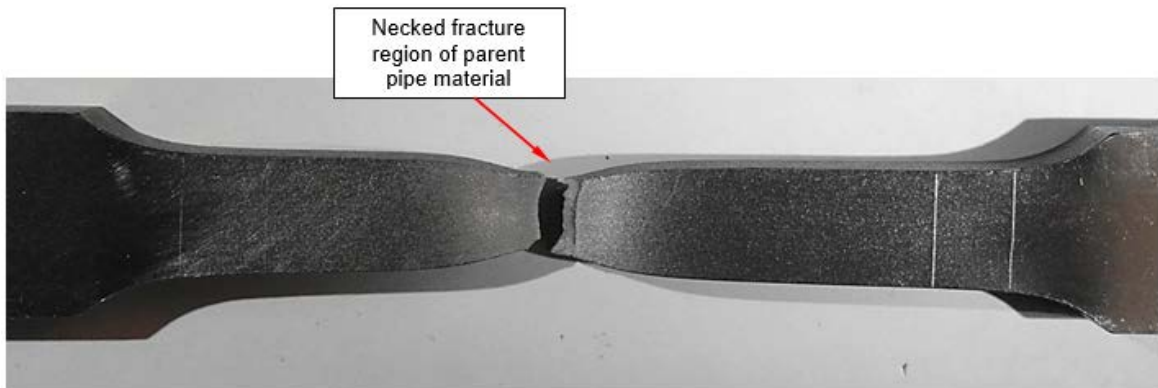


Figure 3-32: A representative parent steam pipe material tensile sample, which fractured in a ductile manner, evident from the necking and cup and cone features.

The majority of the HAZ tensile samples also fractured in a similar manner in the parent material with necking as shown in **Figure 3-33**. Both the parent and HAZ tensile samples showed cup and cone features indicative of ductile overload failures (see **Figure 3-34** showing one of the HAZ tensile sample's fracture surface as an example).



Figure 3-33: A typical example of how the majority of the tensile taken from just outside the HAZ fractured in the parent steam pipe material.



Figure 3-34: Close up view of one of the HAZ tensile sample's necked fracture surface with a dimpled and fibrous appearance, typical of a ductile overload fracture.

Further inspection of the parent material tensile samples' fracture surfaces showed that the up or down stream side with the highest percentage planar graphitization, has a larger number of exposed graphite nodules (see **Figure 3-35** showing Sample A's up and down stream fracture surfaces as a comparative example). Higher magnification inspection of the fracture surfaces using a Scanning Electron Microscope (SEM), confirmed this observation and showed that the graphite nodules were fractured or opened up and that they were surrounded by a dimpled fracture surface, formed as a result of micro void coalescence (MVC), confirming the ductile fracture mode evident on the majority of the tensile samples (see **Figure 3-36** and **Figure 3-37**).

Cross sectional samples removed from these tensile samples indicated that the graphite nodules aided in the formation of elongated micro voids during the tensile testing of the material, more predominately on the side with the highest levels of graphitization as shown in **Figure 3-38** and **Figure 3-39**. This could explain the lower ultimate tensile strength measured on the down stream (UTS = 363 ± 1.8 MPa; % Planar Graphite = 28 ± 13) and up stream (UTS = 377 ± 1.8 MPa; % Planar Graphite = 12 ± 1) (See **Figure 3-30** and **Figure 3-31**).

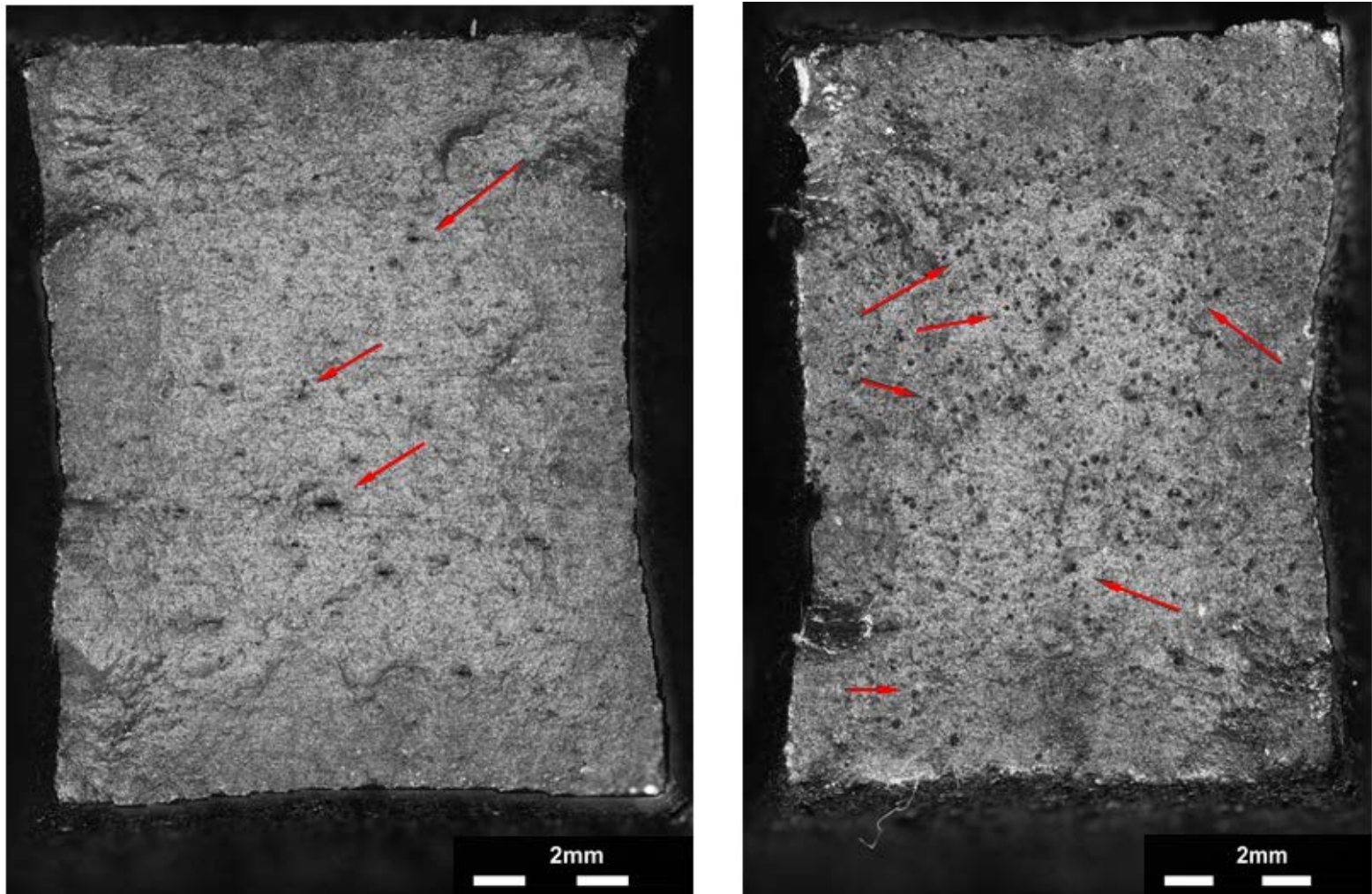


Figure 3-35: Higher magnification close up view of Sample A's up stream side (L/H side) and down stream side (R/H side), with more graphite nodules exposed on the down stream side which has higher graphitization levels.

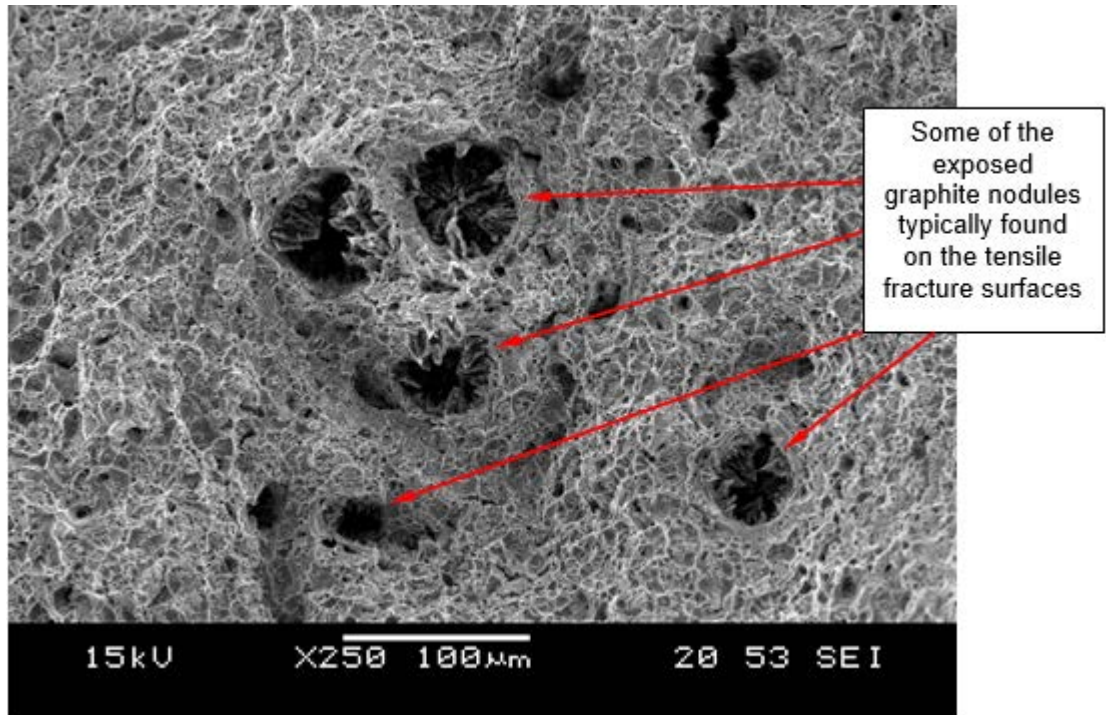


Figure 3-36: SEM image showing a typical example of the fractured graphite nodules surrounded by a fine dimpled fracture surface formed as a result of MVC.

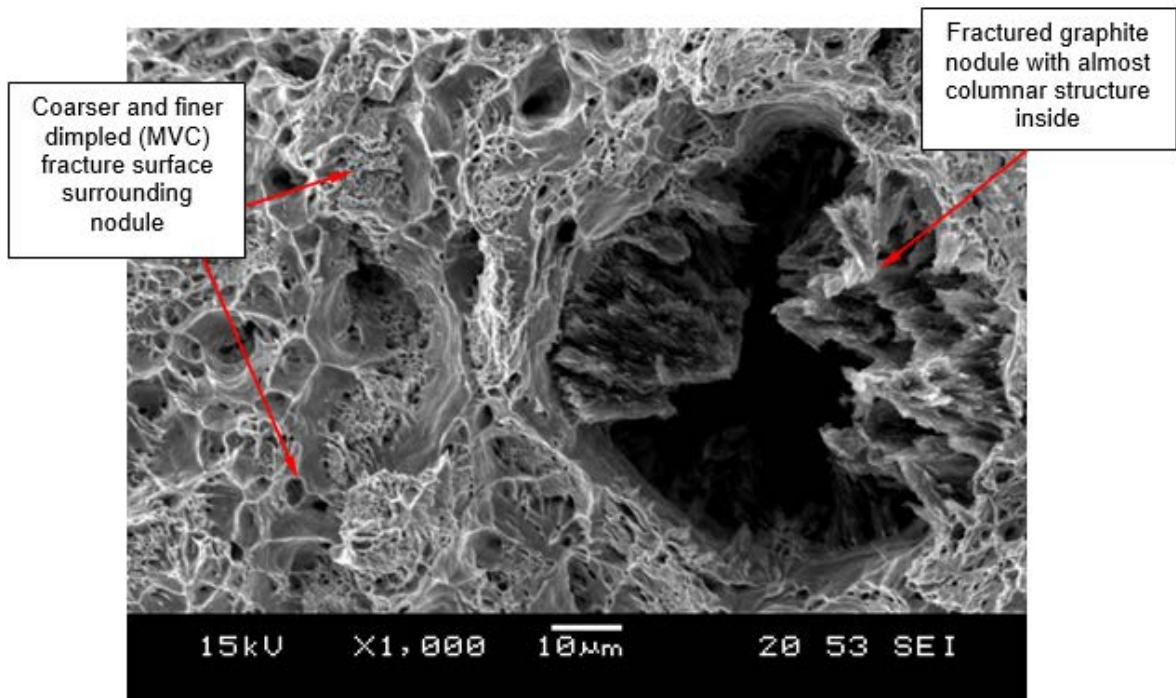


Figure 3-37: Higher magnification SEM image of one of the graphite nodules and surrounding MVC fracture surface, with the fracture going through and not around the nodule.

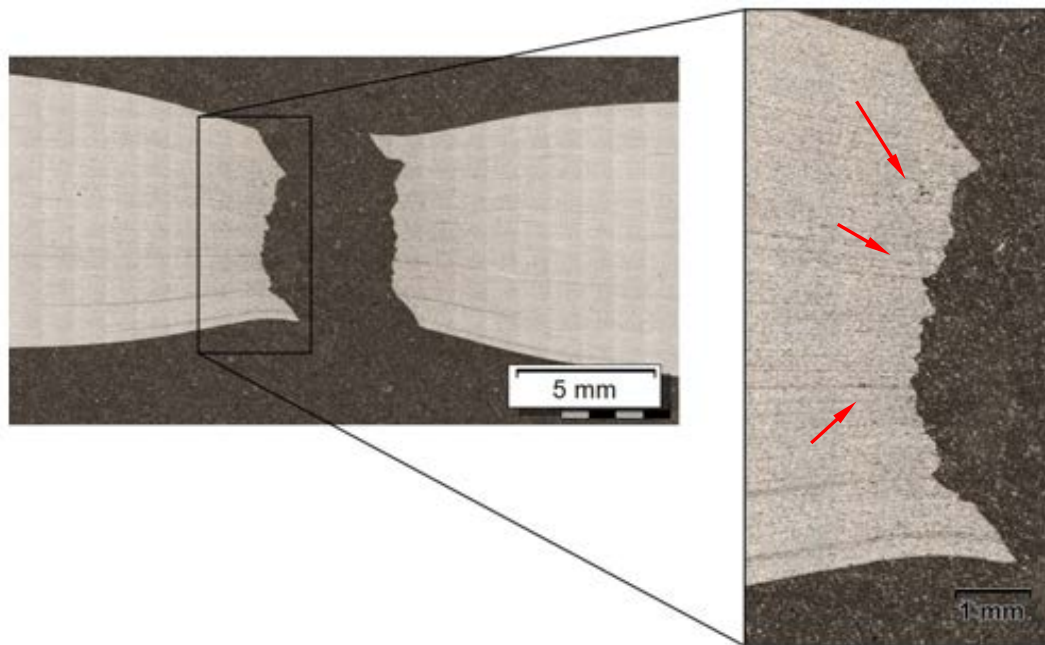


Figure 3-38: Polished and etched cross sectional view of pipe Sample A's up stream tensile, with less micro voids (indicated by arrows) being formed due to lower levels of graphitization.

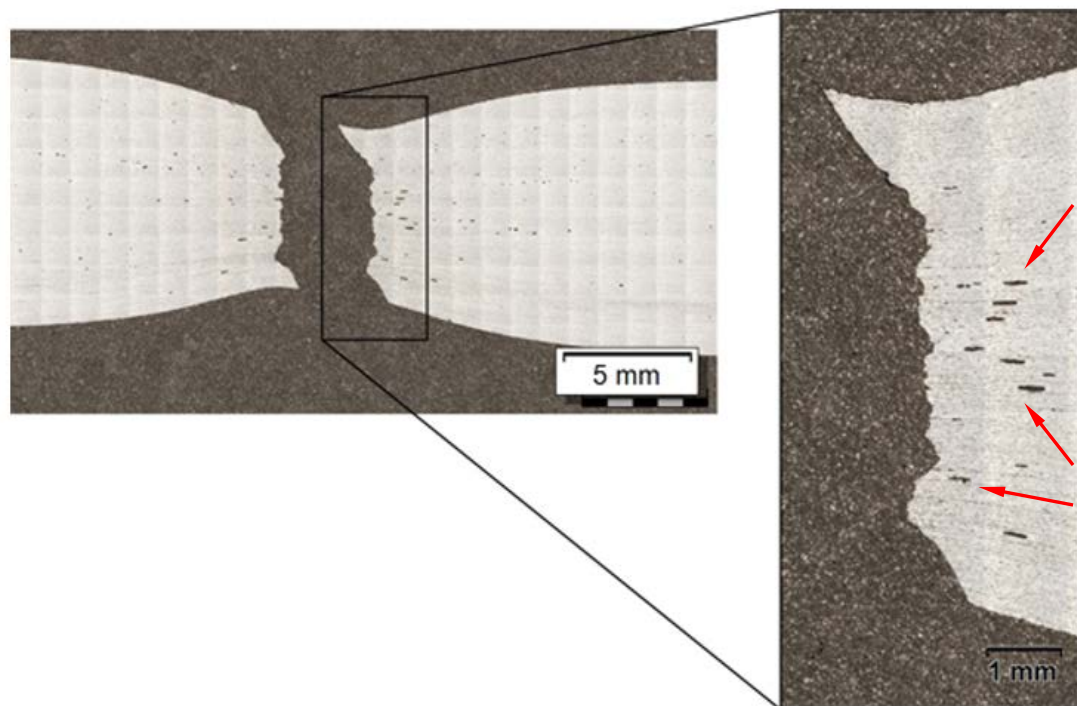


Figure 3-39: Polished and etched cross sectional view of pipe Sample A's down stream tensile, with more micro voids (indicated by arrows) being formed, due to higher levels of graphitization.

There was however one HAZ tensile sample from welded pipe Sample B, which fractured along the outer edge of the HAZ (see **Figure 3-40**). Evaluation of the fracture region showed little evidence of necking and the fracture surface had distinct dark colored regions as shown in **Figure 3-41**.



Figure 3-40: The side view of the only HAZ Tensile sample that fracture along the HAZ interface, where high levels of planar graphitization were evident.

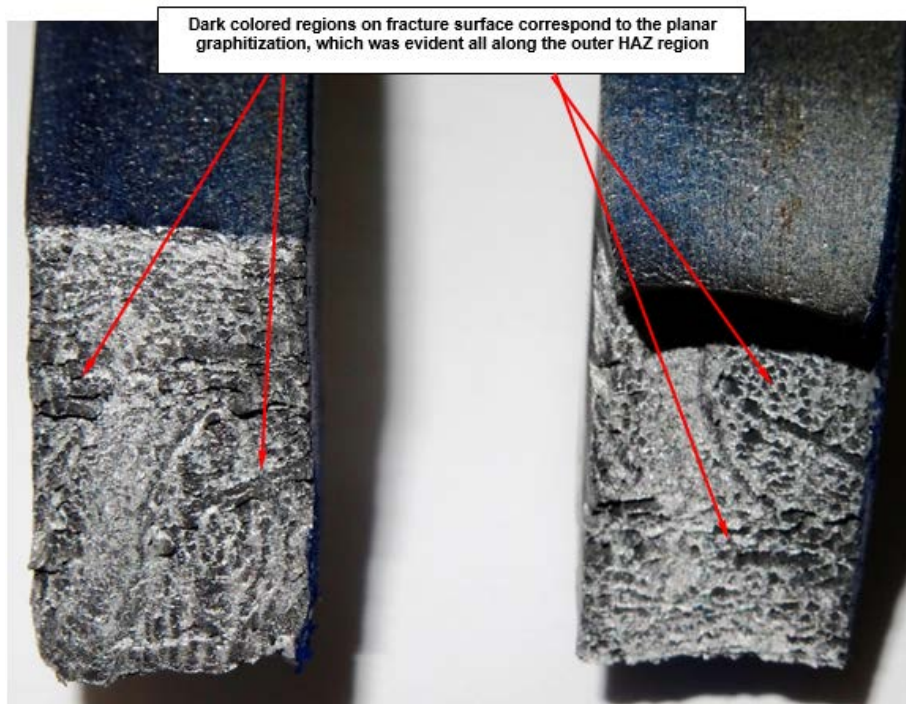


Figure 3-41: Close up view of the exposed fracture surfaces of the up stream HAZ tensile Sample of Welded pipe Sample B, which fractured along the HAZ outer interface region.

Two of pipe Sample A's down stream HAZ tensile samples tested at 420° C, showed evidence of similar intermittent dark colored fracture surface regions formed at an angle and a smoother shear lip region (see **Figure 3-42**).

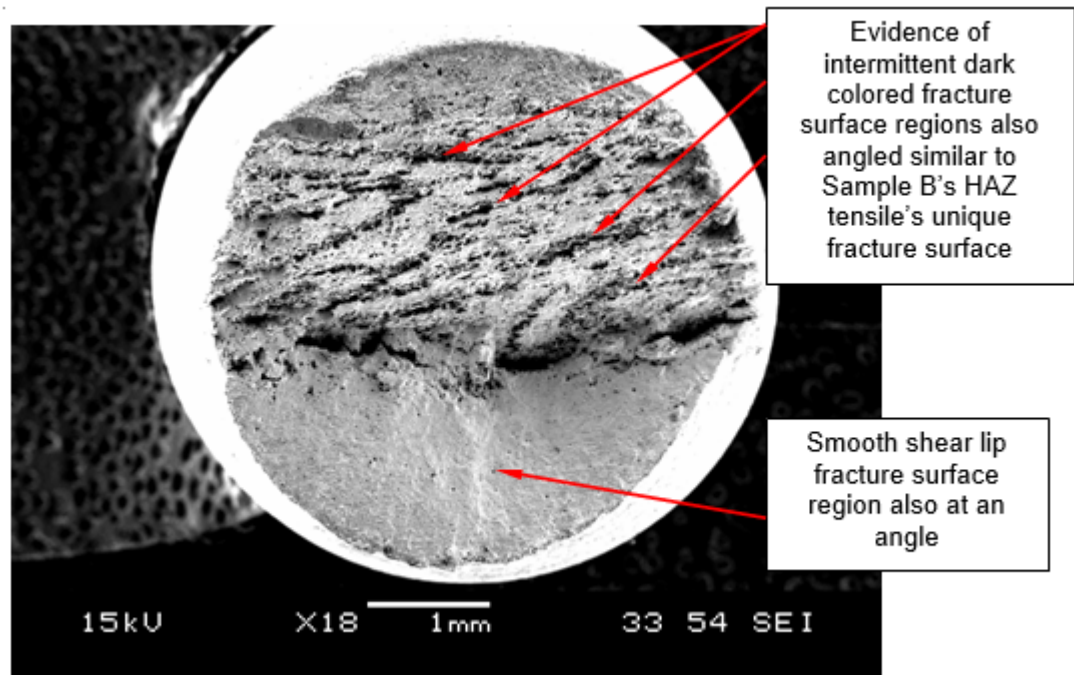


Figure 3-42: SEM low magnification image of the fracture surface of the one down stream HAZ tensile tested at 420°C, with similar dark colored intermittent regions.

Further high magnification evaluation work, done in the SEM on these unique fracture surfaces of the HAZ tensile samples, showed that the intermittent dark colored regions were made up of coarser and finer cluster regions of what appeared to be very fine fractured graphite nodules (see **Figure 3-43**). Furthermore, the lighter colored regions surrounding these banded clusters showed evidence of elongated MVC, indicating a ductile mode of fracture as shown in **Figure 3-44**.

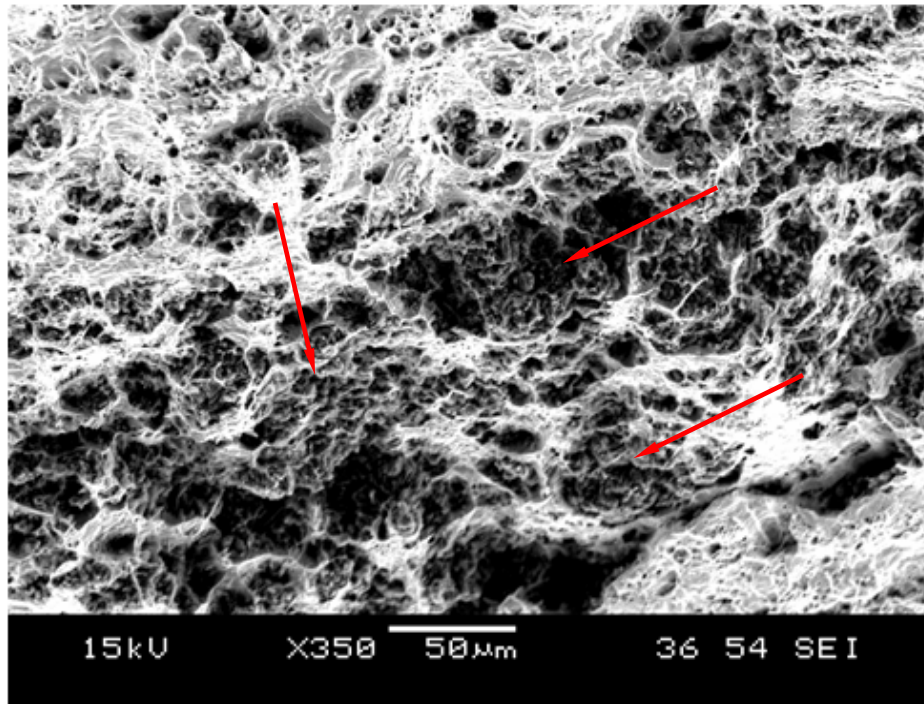


Figure 3-43: SEM close up image of one of the dark colored regions showing that it is made up of a cluster of what looks like very fine fractured graphite nodules.

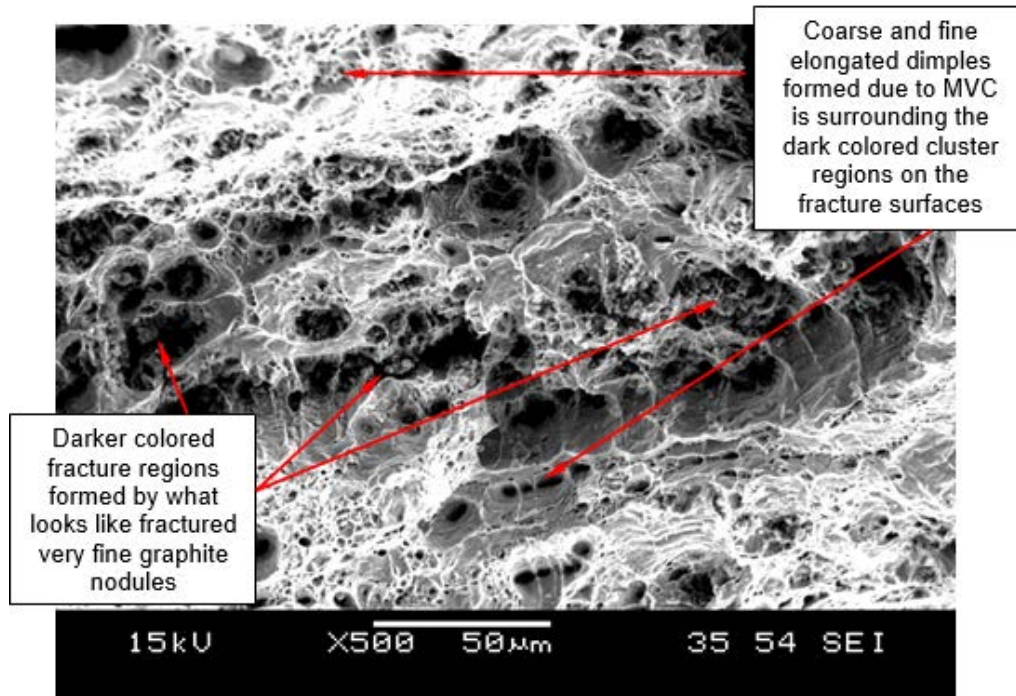


Figure 3-44: SEM close up image showing that the material surrounding the dark colored cluster regions fractured in a ductile manner evident from the MVC.

An element spectral image scan was done, using the SEM's Electron Dispersive Spectroscopy (EDS) system, on a level portion of pipe Sample B's HAZ tensile fracture surface as shown in **Figure 3-41**. This was performed to try and confirm the hypothesis that the dark colored cluster regions were very fine fractured planar graphite nodules, which weakened this region by reducing the ductility just outside the HAZ. The qualitative spectral scan results did indicate that the dark colored regions contained higher levels of carbon (colored blue) and the surrounding lighter colored regions showed higher levels of iron (Colored green) depicted in **Figure 3-45**.

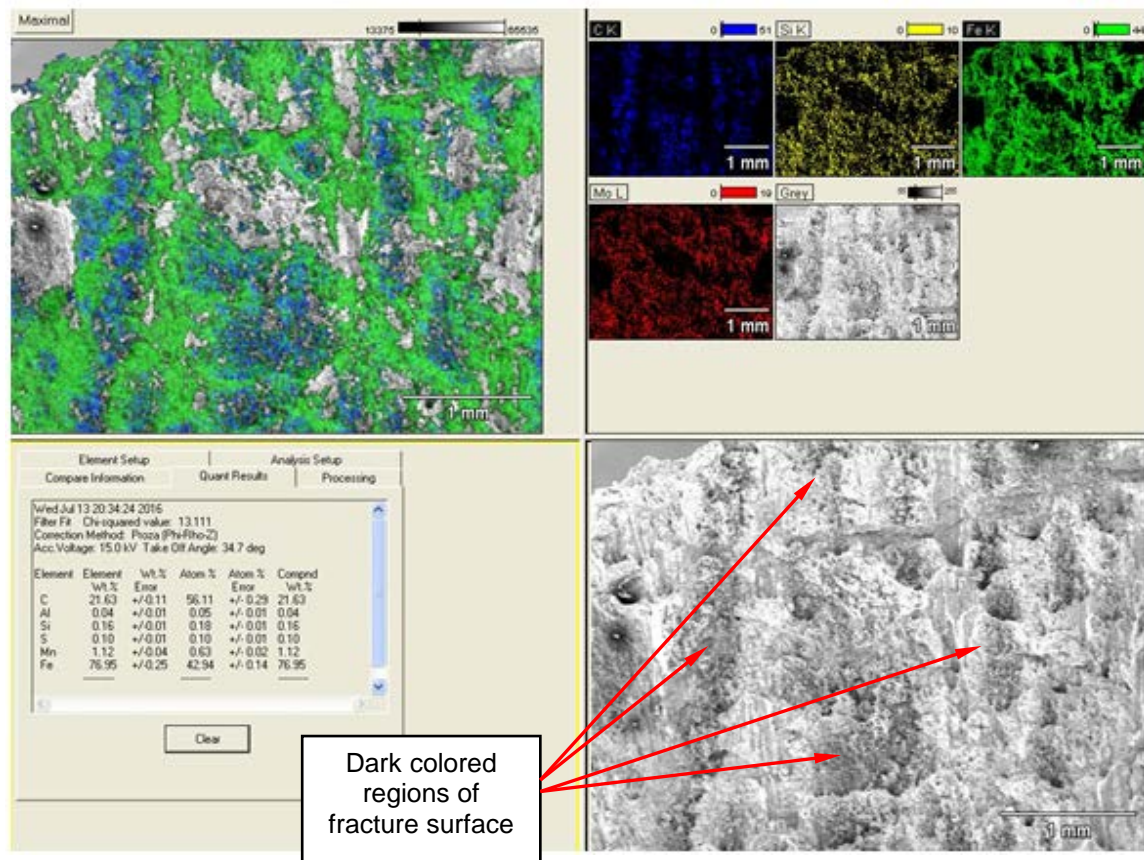


Figure 3-45: Element spectral image analysis results of the fracture surface of Sample B's HAZ tensile sample, with the carbon rich regions blue and the iron rich regions green.

To finally prove the hypothesis, a cross sectional sample was removed from the uniquely fractured HAZ tensile of pipe Sample B and this showed that the Carbon rich fracture surface cluster regions do correspond to the intermittent band of planar graphitization just outside the HAZ (see **Figure 3-46**).

Small portions of the intermittent planar graphitization just outside HAZ, still evident after fracturing and it corresponding to dark colored carbon rich regions on the fracture surface

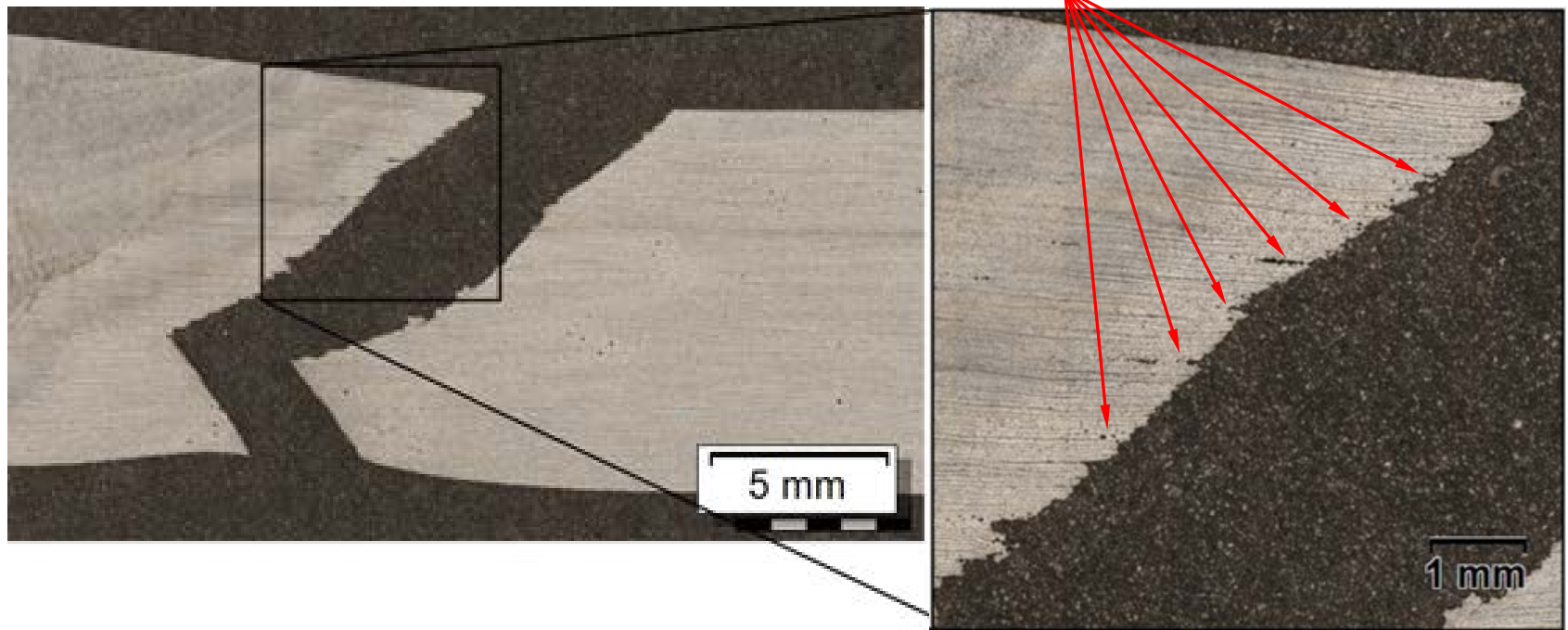


Figure 3-46: Polished and etched cross sectional view of the uniquely fractured HAZ tensile from pipe Sample B, showing that the fracture coincides with the intermittent planar graphitization.

3.6. The effect of Graphite on the Charpy Impact Toughness of Service Exposed Steam Pipe Material

3.6.1. Introduction

The main aim of this part of the research is to determine how the randomly dispersed graphitization in the parent pipe material and the planar graphitization just outside the weld HAZ affects the overall Impact toughness of the service exposed pipe material. Charpy Impact samples removed from the respective pipe samples were also orientated perpendicular to the connection seam welds similar to the tensile samples, to maintain consistency with regard to sample orientation throughout the research.

3.6.2. Charpy Impact Sample Orientation and Pipe Regions being Evaluated

Cross sectional slices were made perpendicular to the connection seam welds and three Charpy impact samples were removed from the parent steam pipe material on either side of the seam weld in the centre region as per **Figure 3-47**.

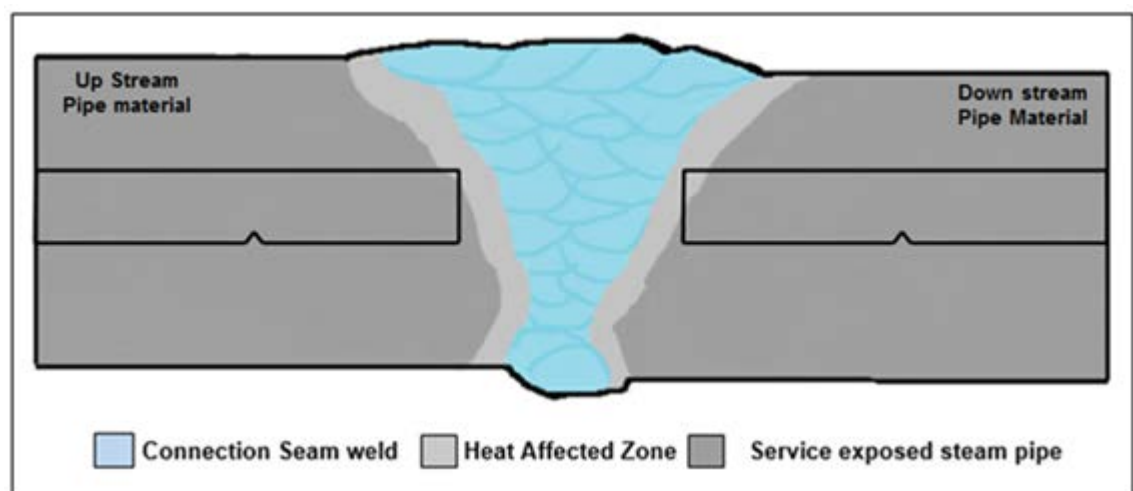


Figure 3-47: The positions where the Charpy Impact samples were removed from the service exposed steam pipe parent material.

Special care was taken during the preparation of the Weld HAZ Charpy impact samples. The cross sectional surface of these samples were initially polished and etched to determine the position of the planar graphitization just outside the HAZ. The respective weld HAZ Charpy impact samples were positioned in such a way that the notch tip coincided with the planar graphitization for the samples to fracture through the zone. HAZ Charpy Impact samples were removed on the side with the highest percentage planar graphitization as per **Figure 3-48**, to establish the effect the planar graphitization has on the Charpy impact energy.

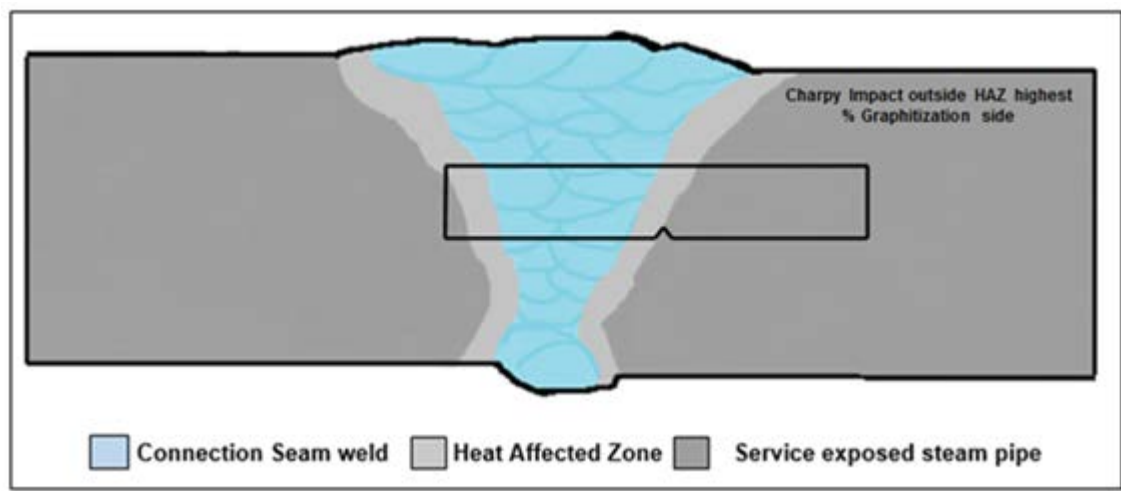


Figure 3-48: Shows where the Charpy Impact samples were taken from just outside the HAZ, with the notch coinciding with the planar graphitization.

3.6.3. Room Temperature Charpy Impact Testing

The Charpy impact samples were machined as per **ASTM E23 Type A** requirements, as shown in **Figure 3-49**, and these were tested at room temperature, according to the **ASTM E23** standard for notched bar impact testing of metallic materials. An instrumented Zwick Charpy impact test machine, as shown in **Figure 3-50**, was used to test the impact samples.

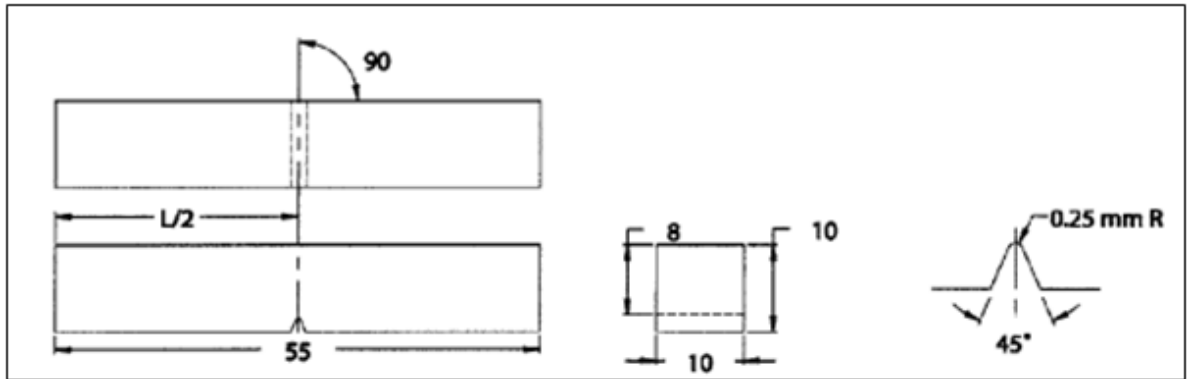


Figure 3-49: The dimensions of a Type "A" Charpy impact sample as per ASTM E23.

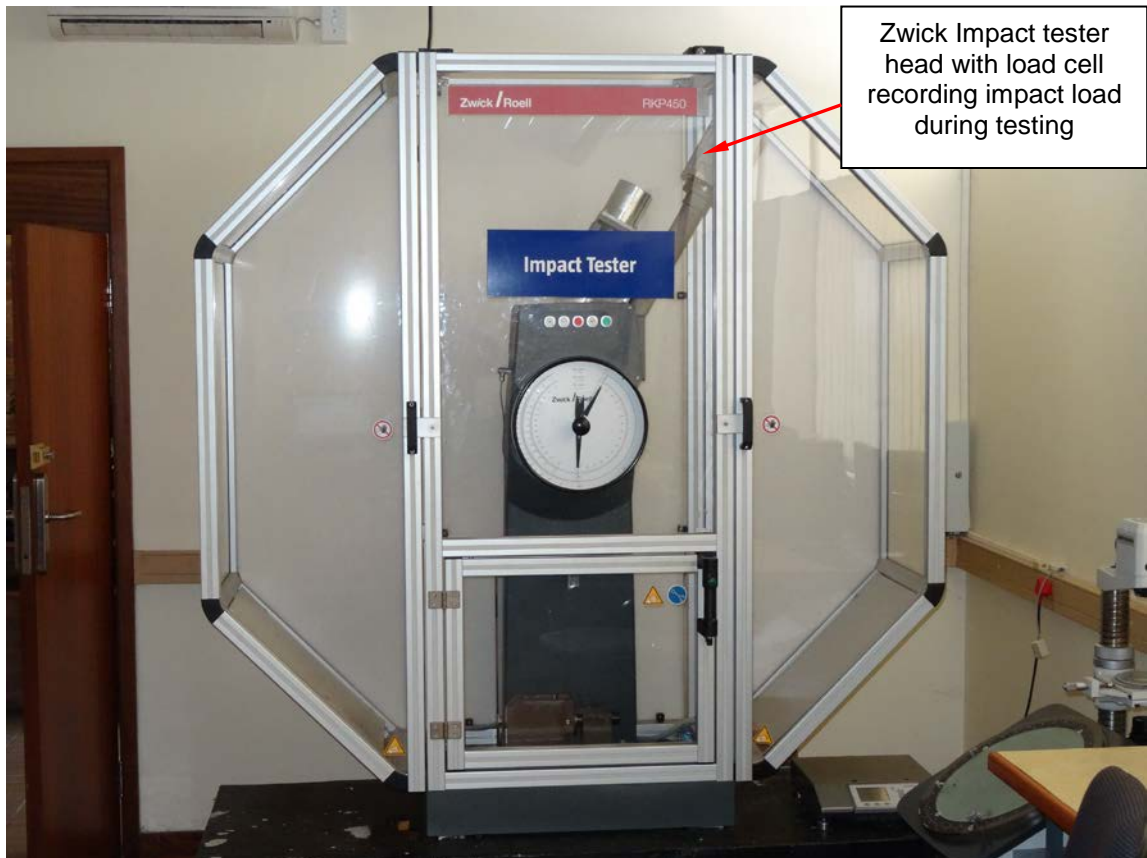


Figure 3-50: The Zwick Impact tester used to test the Charpy impact samples of the respective service expose steam pipe samples.

3.6.4. Impact Toughness of Service Exposed Steam Pipe with Graphitization

Charpy impact samples were removed from the up and down stream pipe material and from the region just outside the HAZ, on the side with the highest percentage planar graphitization. The room temperature Charpy Impact energy results of the samples were the plotted in relation to the % planar graphitization of the respective pipe samples (See **Figure 3-51** and Appendix D showing the impact strength evaluation results).

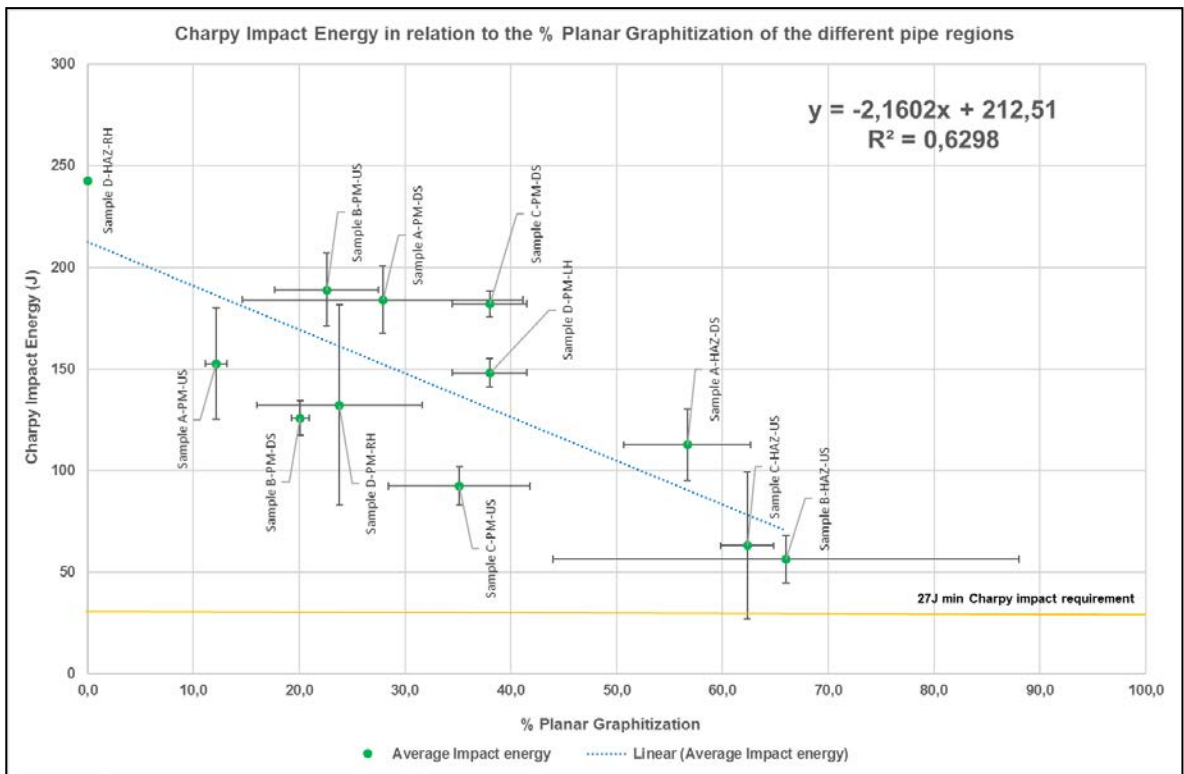


Figure 3-51: A graphical summary of Charpy Impact results at room temperature and the % Planar Graphitization of the respective pipe regions.

It was evident from **Figure 3-51** that all of the sample met and exceeded the minimum impact energy requirement. The plot show a negative correlation between the impact toughness and the %planar graphitization ($R^2 = 0.63$). This relationship was analyzed further using linear regression analysis and found to be statically significant within the 95% confidence ($p = 0.002$). It should be noted that the HAZ regions will have a different microstructure to the parent material which could have influenced the results.

Planar graphitization % also contributed to the trends seen in the data, specifically with regard to the HAZ regions samples, with Sample D's HAZ region exhibiting significantly higher impact strength due to the absence of planar graphitization in this region. Samples A to C obtained noticeably lower impact strengths due to the embrittling effect of the planar graphitization in the HAZ regions.

3.6.4.1. Evaluation of the Tested Charpy Impact Samples to Determine Graphitization Influence on the Mode of Fracture

The noticeable difference in impact strength between parent and HAZ Charpy samples can be related to the type of graphitization found in the respective regions. This was clearly evident when the instrumented Charpy impact data plotted for a typical parent material impact sample (with randomly dispersed graphite nodules) in comparison to the data of a corresponding HAZ Charpy impact sample (with planar graphitization) (see **Figure 3-52**).

According to **ASTM E23-12C Annex A4**, the shorter standard travel distance between the maximum force FM and point where the unstable crack extension is arrested Fa, indicates that the sample failed due to cleavage or brittle fracturing, while the larger travel distance between FM and Fa on the parent material sample indicates a typical ductile shear fracture mode.

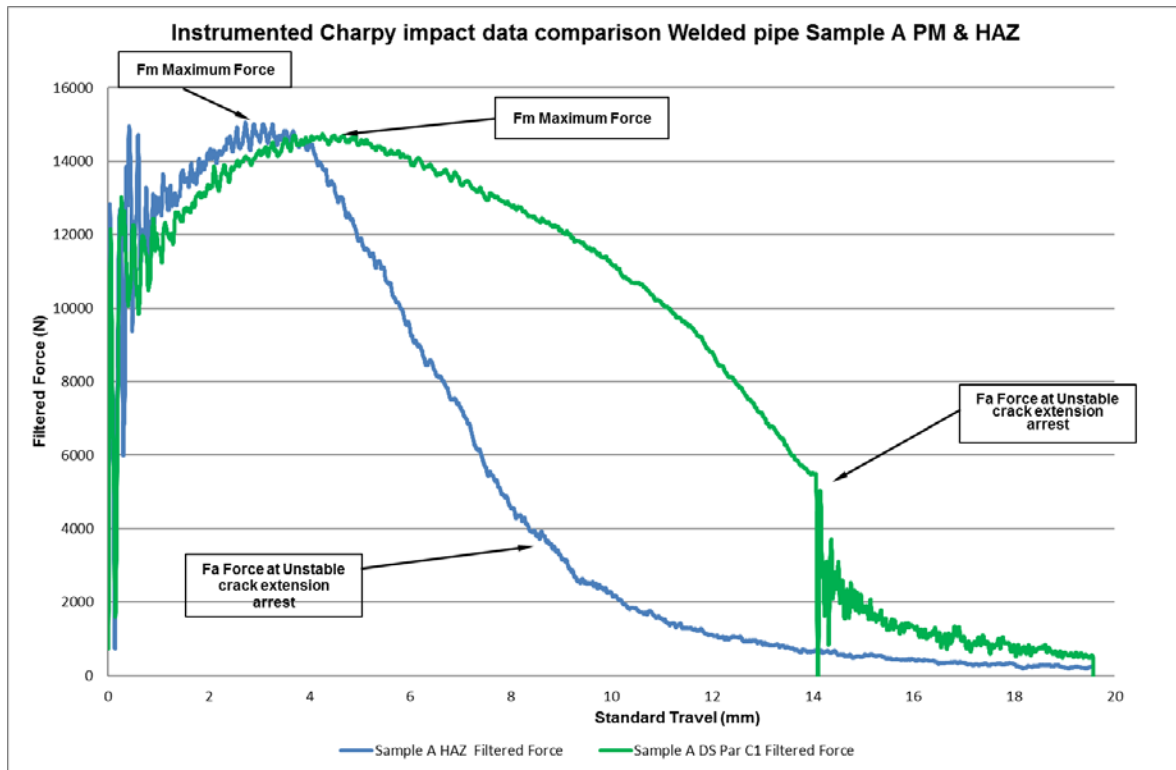
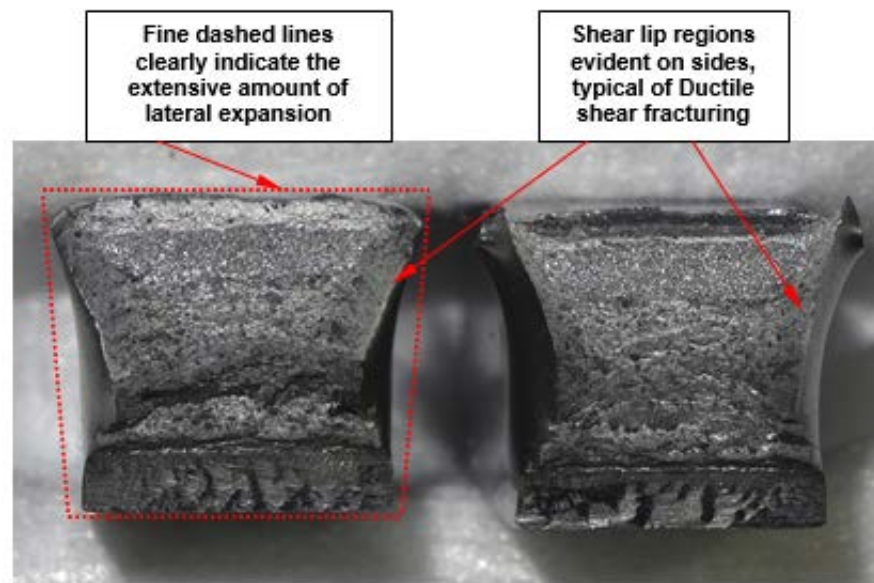


Figure 3-52: Graphical representation of recorded impact Load measurements of instrumented parent steam pipe and HAZ Charpy impact samples.

The different modes of failure between the parent steam pipe material and the HAZ Charpy impact samples, were also clearly visible on the actual samples. The parent material Charpy impact samples revealed a typical ductile shear fracturing with some lateral expansion (see **Figure 3-53**), while the Charpy impact samples removed from the HAZ region had less lateral expansion and showed evidence of what appeared to be brittle fracturing specifically at the intermittent darker colored regions. It was also found that the fracture surfaces of the HAZ Charpy samples were formed at an angle and it would appear that these surfaces coincided with the outer HAZ region where there was a high concentration of planar graphitization (see **Figure 3-54**).



Side view of one of the parent pipe material Charpy Impact samples tested

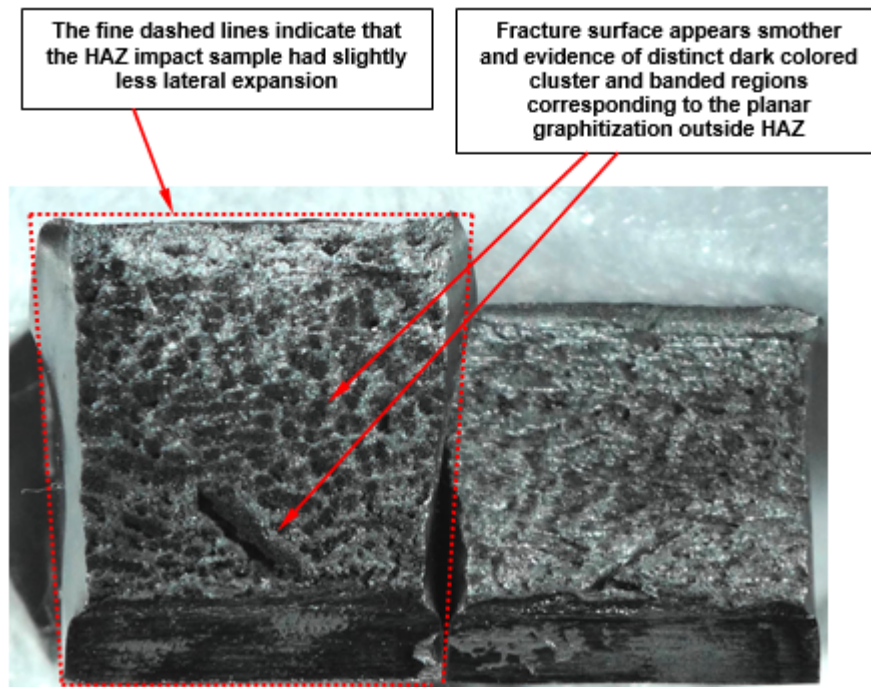


Close up view of the fracture surfaces of a parent pipe material Charpy Impact sample

Figure 3-53: A typical example of the mode of fracture of one of the parent pipe material Charpy Impact samples.



Side view of one of the HAZ material Charpy impact samples tested



Close up view of the fracture surfaces of a HAZ Charpy impact sample

Figure 3-54: A typical example of the mode of fracture of one of the HAZ Charpy Impact samples.

Further inspection of the fracture surfaces of the parent material Charpy impact samples showed that the up or down stream side with the highest percentage planar graphitization, had a larger number of graphite nodules exposed. The up and down stream fracture surface did however show similarities with regard to the outer shear lip and shinier final brittle fracture regions (see **Figure 3-55** showing Sample A's up and down stream fracture surfaces as a comparative example).

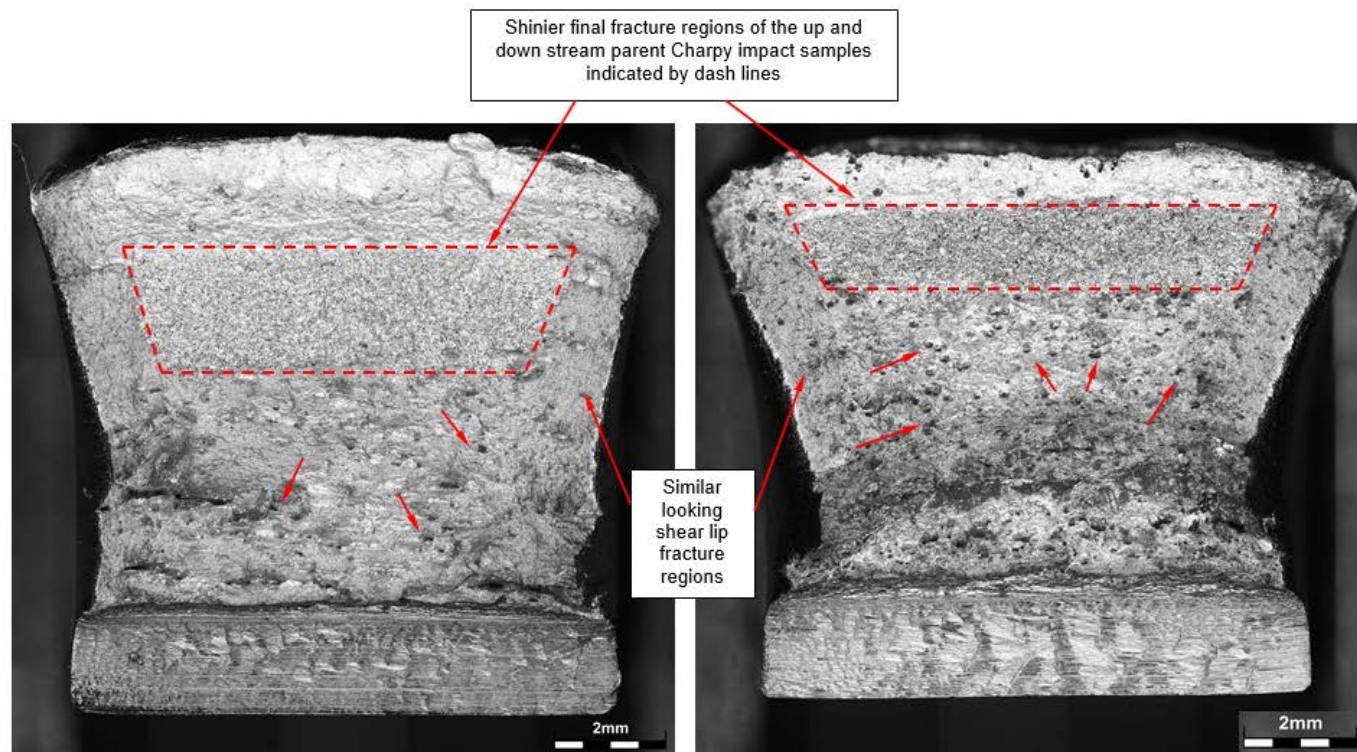


Figure 3-55: The fracture surfaces of Charpy impact samples from sample A's parent pipe up stream (L/H side) and down stream (R/H side), with more exposed graphitization on the down stream side.

Higher magnification inspection of the fracture surfaces of the parent material Charpy impact samples, using a Scanning Electron Microscope (SEM), confirmed their ductile shear fracture mode. This was evident from the elongated dimpled fracture surfaces which surrounded the fractured or opened-up graphite nodules. The elongated dimpled regions were formed as a result of micro void coalescence (MVC) in shear, as shown in **Figure 3-56**, while the shinier final fracture surface regions indicated in **Figure 3-55** show evidence of cleavage fracturing normally associated with a brittle fracture mode (see **Figure 3-57**). These regions were most likely to have formed during the unstable crack arrest stage of the Charpy impact testing.

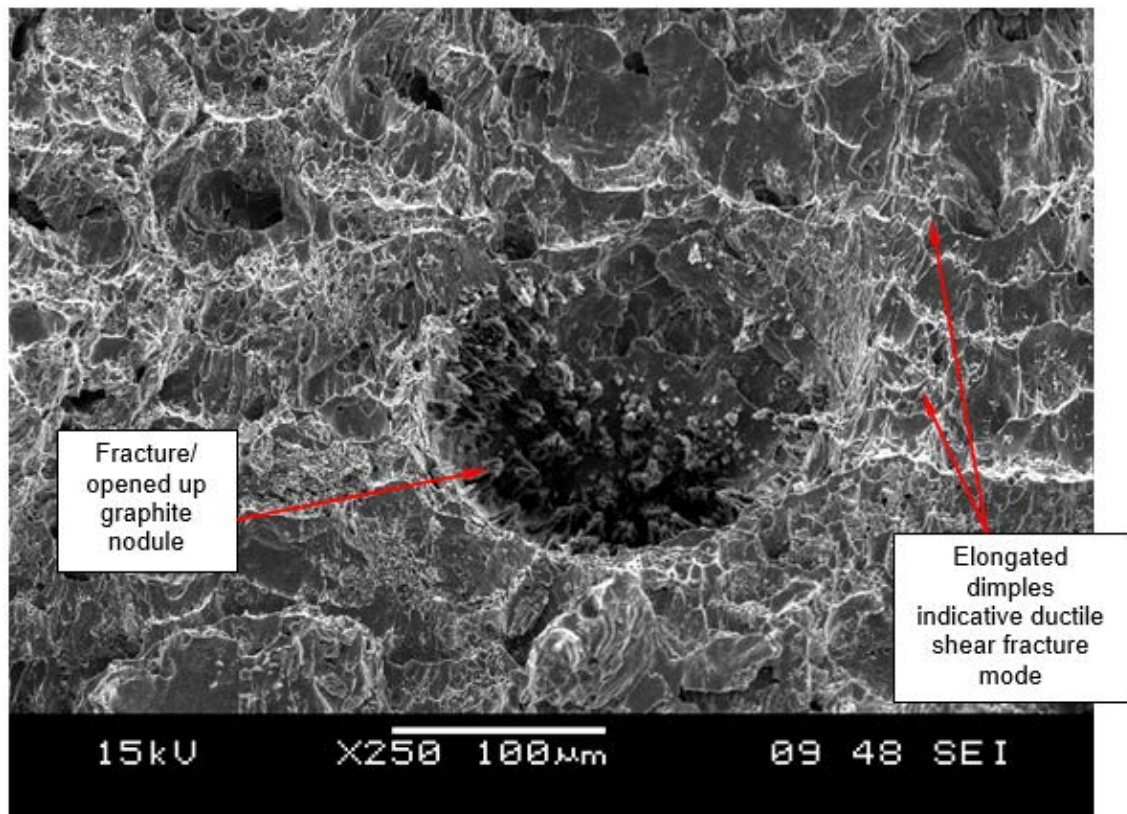


Figure 3-56: SEM image of a typical ductile shear overload fracture surface region of one of the parent Charpy impact samples.

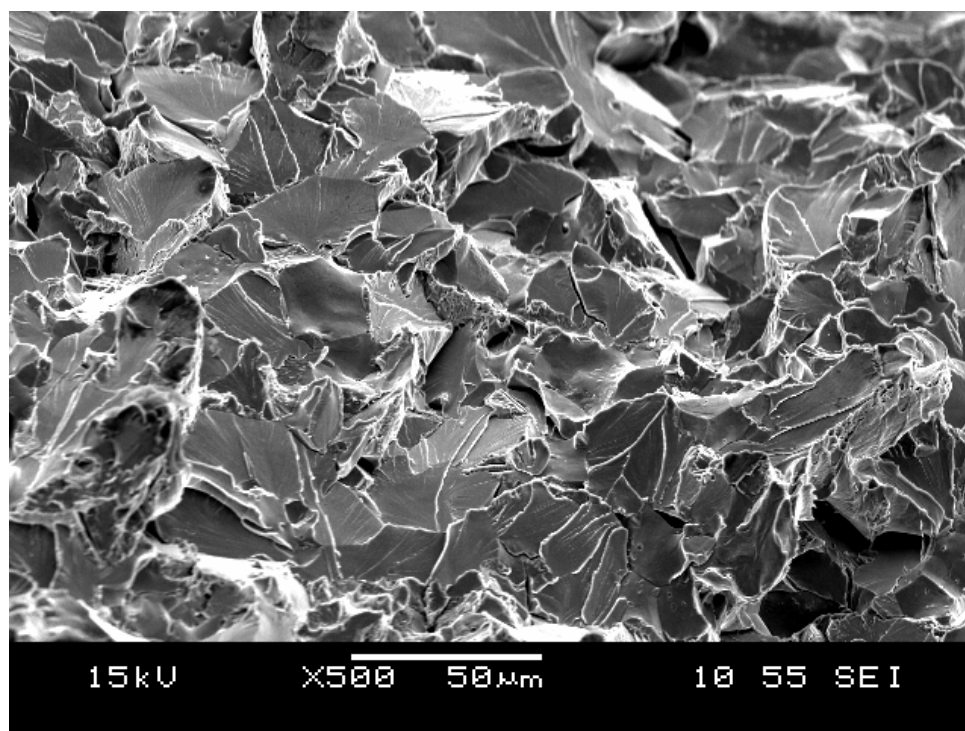


Figure 3-57: SEM image of the shinier final fracture region of one of the parent material Charpy impact samples, with a typical cleavage fracture appearance indicative of a brittle fracture mode.

Evaluation of a representative fracture surface from a HAZ Charpy impact sample in the SEM, showed that the dark colored regions were made up of clusters of fine brittle fractured material surrounded by fine dimpled MVC regions (see **Figure 3-58**), while the lighter colored regions show larger and smaller dimples (see **Figure 3-59**). Similar fracture surface features were observed on the fracture surfaces of the other HAZ Charpy impact samples from pipe Samples B and C. Pipe Sample D's HAZ Charpy impact samples showed similar fracture surface features to those found on the parent pipe material impact samples (see **Figure 3-55**).

A qualitative spectral elemental scan was then performed on a flat portion of the fracture surface, as shown in **Figure 3-54**, to try and identify the different colored cluster regions. From the scan results it was evident that the dark colored cluster contained higher levels of carbon (colored blue), while the fine dimpled light colored regions contained higher levels of iron (colored green) as seen in **Figure 3-60**.

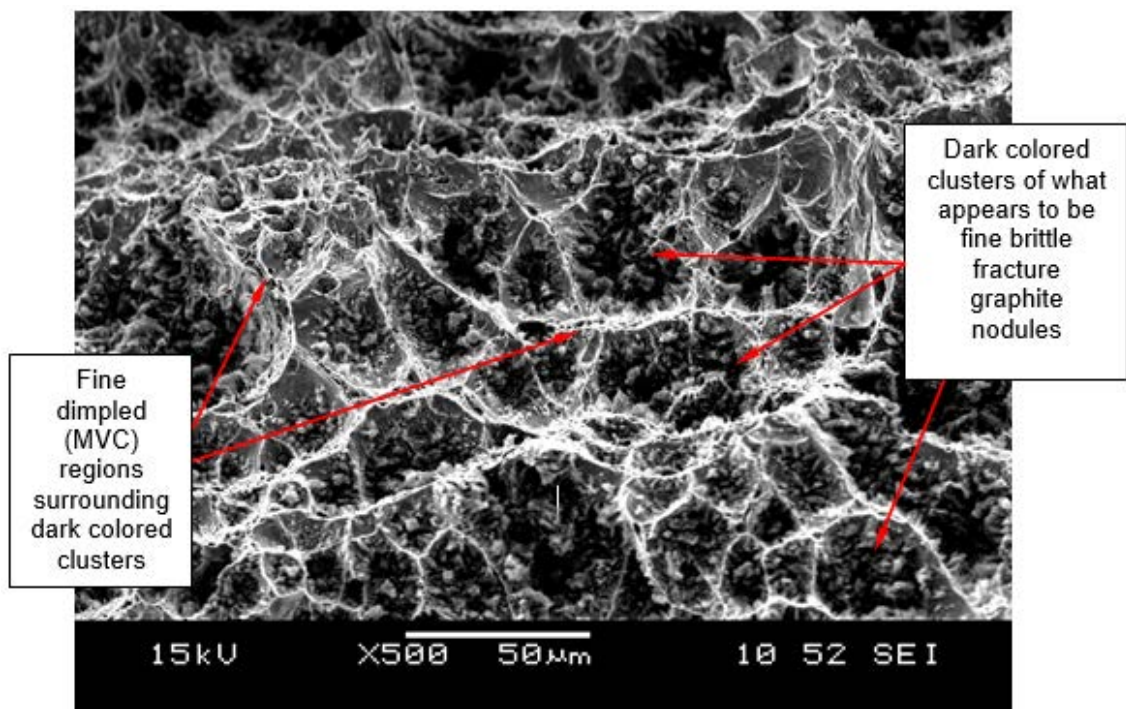


Figure 3-58: SEM close up image of one of the intermittent dark colored regions, with clusters of what appears to be fine brittle fractured graphite nodules.

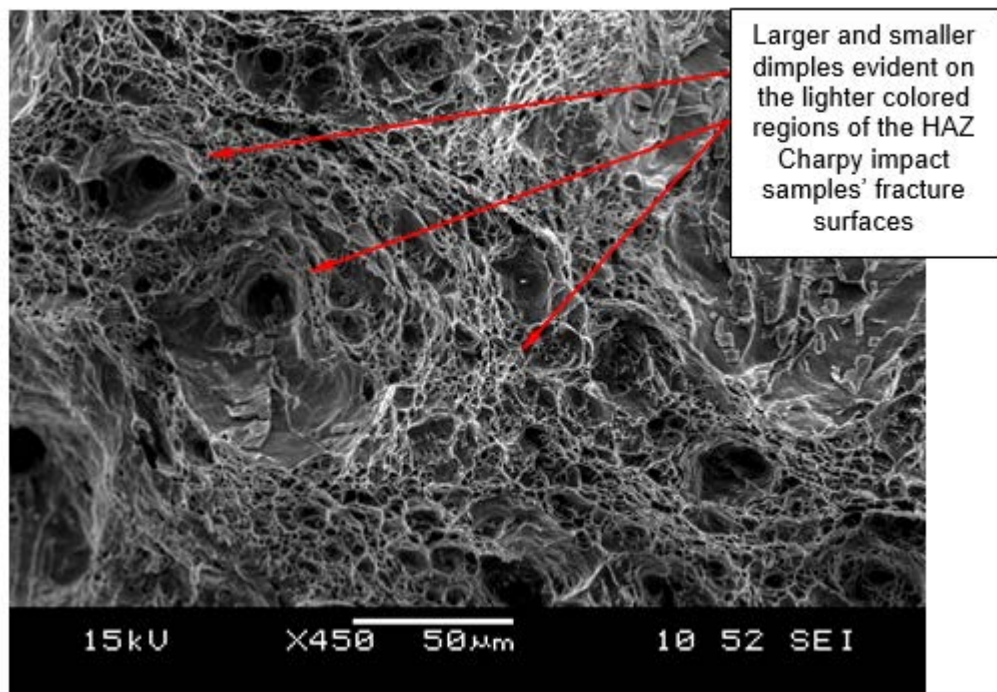


Figure 3-59: SEM close up image of lighter colored fracture surface regions of Charpy impact samples with larger and smaller dimples as a result of MVC.

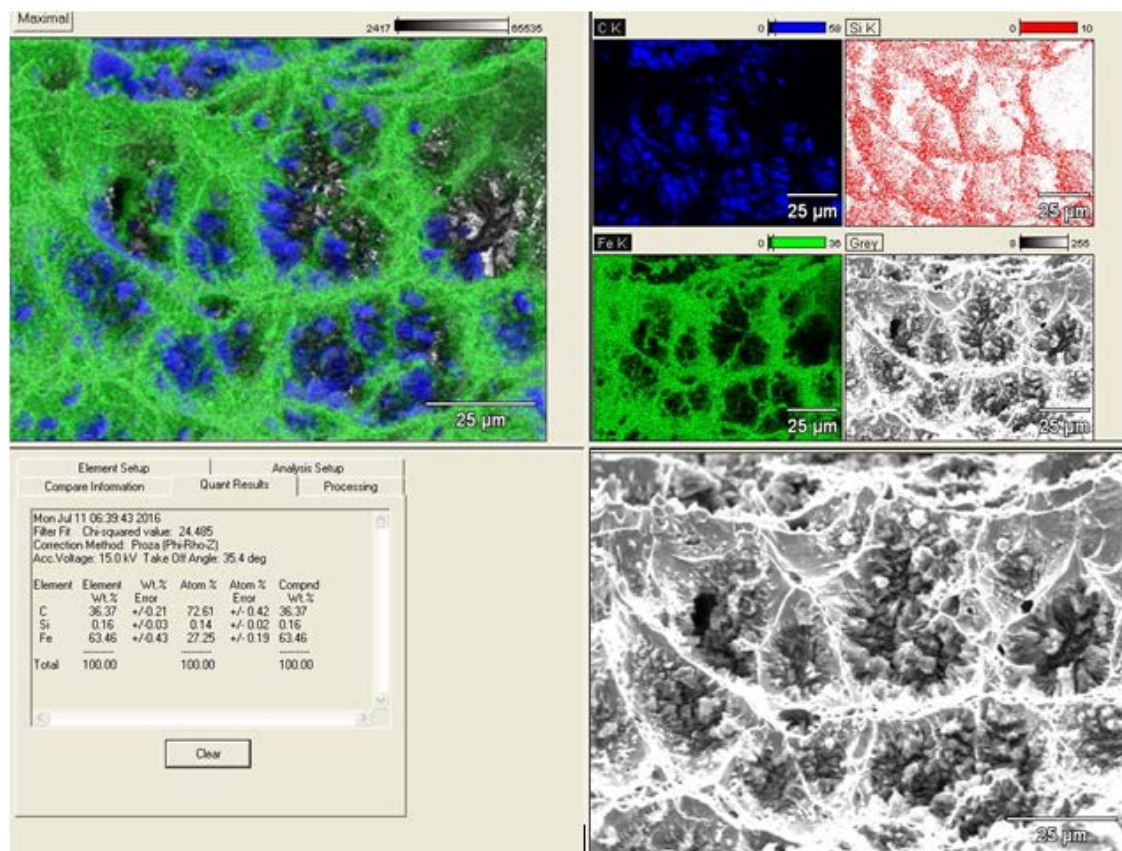


Figure 3-60: The spectral elemental scan results of a small portion of the dark colored fracture surface region, with the dark cluster showing higher levels of carbon (Blue) and the surrounding regions exhibited higher levels of iron (Green).

A cross sectional sample was then removed from the same Charpy impact sample evaluated in the SEM. This was done to determine whether these fine fractured graphite cluster regions corresponded to the intermittent planar graphitization identified outside the HAZ, which was confirmed as shown in **Figure 3-61**.

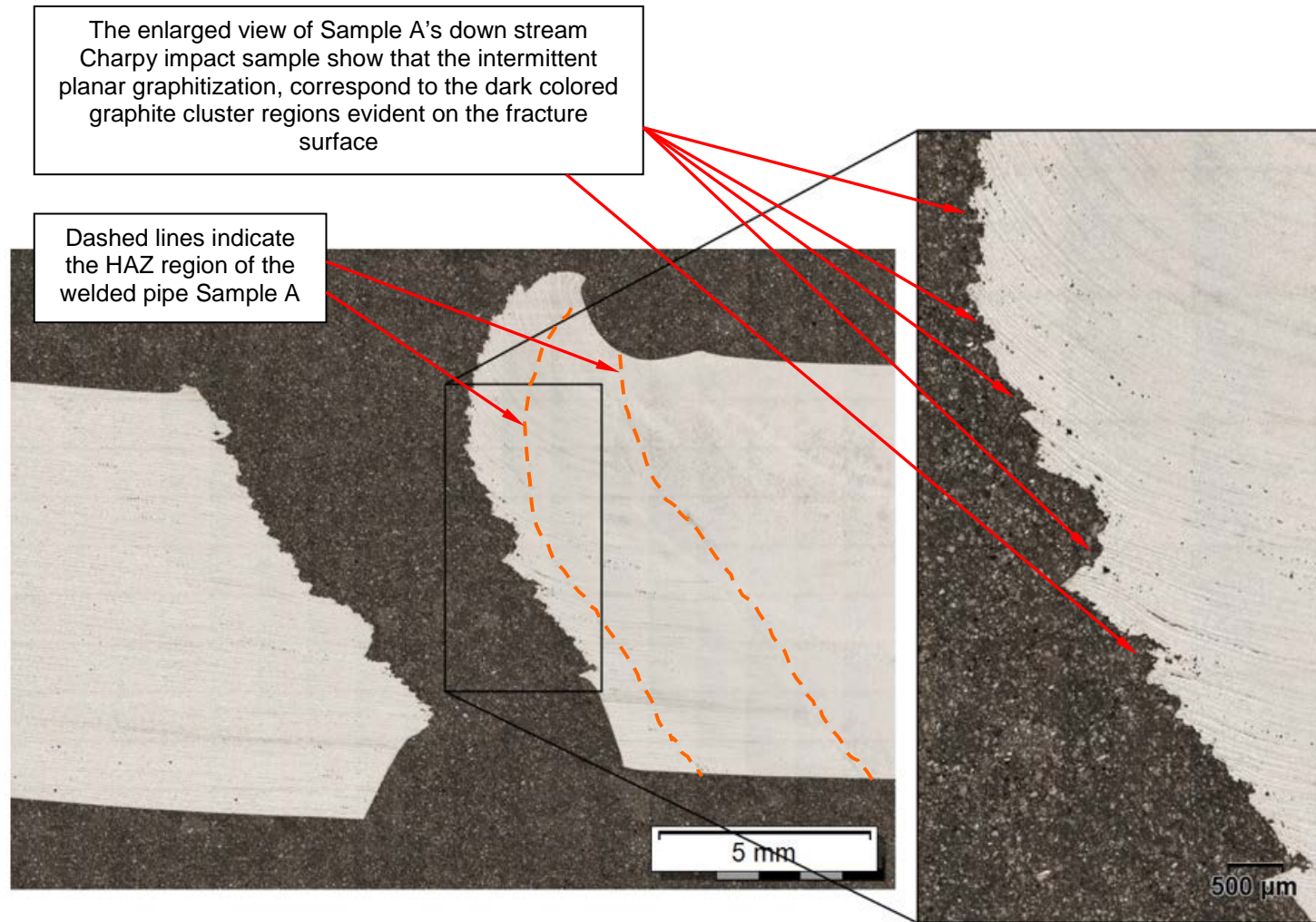


Figure 3-61: Cross sectional view of Sample A's down stream HAZ Charpy impact sample with clear evidence that the dark colored graphite cluster identified on the fracture surface corresponds to the intermittent planar graphitization outside the HAZ.

3.6.5. Evaluation of Newly Introduced Connection Seam Weld

Steam pipe Sample D, on which the newly seam weld with PWHT was introduced, had a similar chemical composition to the other service exposed steam pipe material evaluated (see **Table 3-2**). It also contained similar levels of aluminium and silicon as compared to the parent pipe material samples, which had the highest levels of graphitization, e.g. Sample A down stream, Sample B up stream and Sample C up stream.

Furthermore, Sample D's graphite size, spacing and percentage graphitization were similar to that documented for the other service exposed steam pipe parent material samples (see Appendix A). From the optical evaluation of macro samples taken from Sample D, no evidence of planar graphitization was found outside the HAZ, which would suggest that the newly introduced weld and subsequent post-weld heat treatment did not trigger the formation of planar graphitization as observed using optical microscopy.

The service exposed steam pipe material of Sample D obtained similar yield and upper tensile strengths as the other service exposed pipe material with similar levels of graphitization. It was also evident on these samples that the translated yield strengths were higher than the actual elevated yield strengths measured during the actual elevated temperature testing (see **Figure 3-30**). In addition the translated upper tensile strength values were also higher than the actual elevated temperature tensile test results (see **Figure 3-31**).

It is evident from the Charpy impact evaluation results that Sample D's parent material obtained impact strength values similar to those measured on the other service exposed steam pipe parent material. There was however a significant difference in the impact strength of the HAZ samples of Sample D in comparison to the other three weld's HAZ samples (see **Figure 3-51**) due to the absence of planar graphitization.

3.7. The effect of chemical composition on the formation of graphite

The effect of the chemical composition on the formation of graphite was investigated in the parent material by plotting the % planar graphitization in relation to the level of aluminium (**Figure 3-62**) and silicon (**Figure 3-63**).

In both cases there is no statistically significant correlation between the elemental composition and the % planar graphitization.

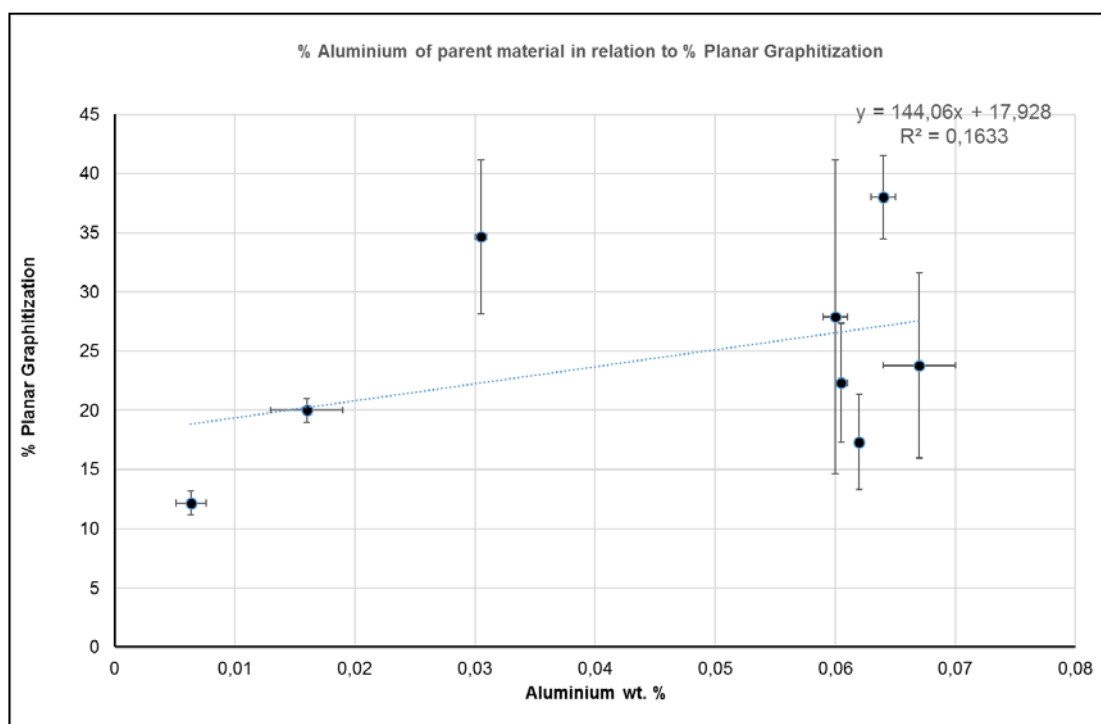


Figure 3-62: The relation between Aluminium wt.% of parent pipe material and the development of % Planar Graphitization

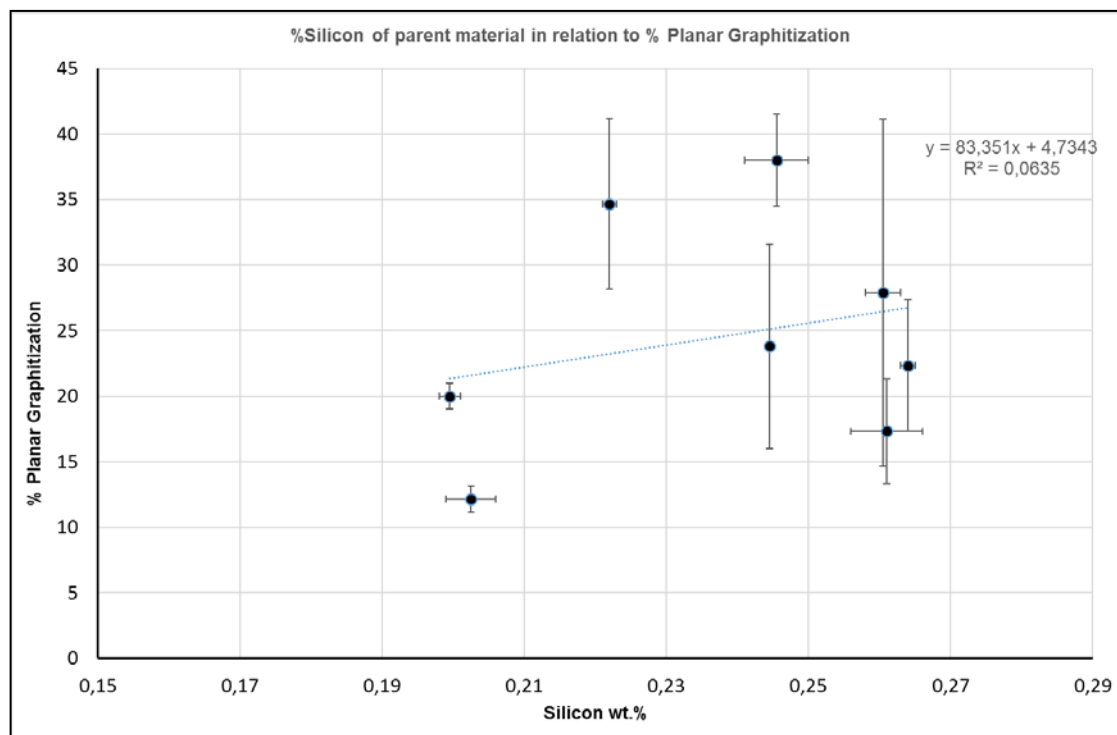


Figure 3-63: The relation between Silicon wt.% of parent pipe material and the development of % Planar Graphitization

3.8. Summary

From the results above the following can be concluded:

- 1) No correlation could be found between the level of deoxidization elements (Al & Si) and the levels of % planar graphitization in the parent pipe material.
- 2) The graphite nodules in the HAZ region had as smaller median nodule size, smaller median nearest neighbour spacing and increased % planar graphitization compared to the parent material.
- 3) The increased hardness of Sample A up stream parent material (145 HV) relative to the down stream parent material (131 HV) can be attributed to the increased carbon content and lower % planar graphitization.
- 4) The yield and ultimate tensile strength of the service exposed material did not show a statistically significant correlation with the % planar graphitization. The mechanical specification requirements were still met for elevated temperature operation.

- 5) The %planar graphitization had a statistically significant negative correlation with impact toughness measured using Charpy Impact testing. The HAZ regions of service exposed weldments (Sample A – C) had the largest % planar graphitization and the lowest impact toughness. Sample D had no planar graphitization in the region outside the HAZ and had the highest impact toughness. The mechanical specification requirements were still met for the impact toughness.
- 6) The current levels of graphitization did not reduce the ductility of the service exposed pipe material significantly because the majority of the tensile samples still failed in a ductile manner.

Chapter 4 : Experimental Methods used for Microstructural Characterization

4.1. Introduction

Typical metallographic investigations are limited to using the light microscope. Although this characterization method is very important and it should be the first method of choice, it is limited with regard to magnification, depth of focus and the ability to clearly resolve features below 1 μm . This study includes the use of scanning electron microscopy (SEM) and transmission electron microscopy (TEM) in order to investigate the factors that control the nucleation and growth of the graphite nodules in the line-pipe weldment.

Modern electron microscopes typically include a wide range of available techniques for imaging, measuring chemical composition and obtaining crystallographic information from the samples under investigation. SEM based techniques used in this study include imaging, using backscattered (BSE) and secondary electrons (SE), energy dispersive X-ray spectrometry (EDX) for measuring chemical composition, and electron backscattered diffraction (EBSD) for obtaining crystallographic information. TEM based techniques used in this study include imaging using the conventional parallel beam mode as well as convergent scanning mode (STEM). The STEM mode was used in conjunction with EDX to measure the chemical composition of the regions of interest. Site specific sections were removed from the microstructural regions of interest and prepared for TEM investigations using the focused ion beam (FIB) SEM. This chapter will aim to provide some background to the advanced electron microscopy techniques used in this study.

4.2. Scanning Electron Microscopy and Associated Techniques

4.2.1. Electron - specimen interactions

In the SEM a focused beam of electrons is scanned across the sample in a raster fashion. The electrons interact with the specimen in a number of different ways as illustrated in **Figure 4-1 A**. The signals of interest in this study include the secondary electrons, backscattered electrons, transmitted electrons, and the X-rays generated from the sample. Each of these signals are generated from different locations in the sample which are determined by the incident electron energy and the characteristics of the sample (e.g. atomic number) as shown in **Figure 4-1B**. This interaction volume is ultimately responsible for the resolution of a particular characterization technique in cases where the beam diameter is sufficiently small [22] [23].

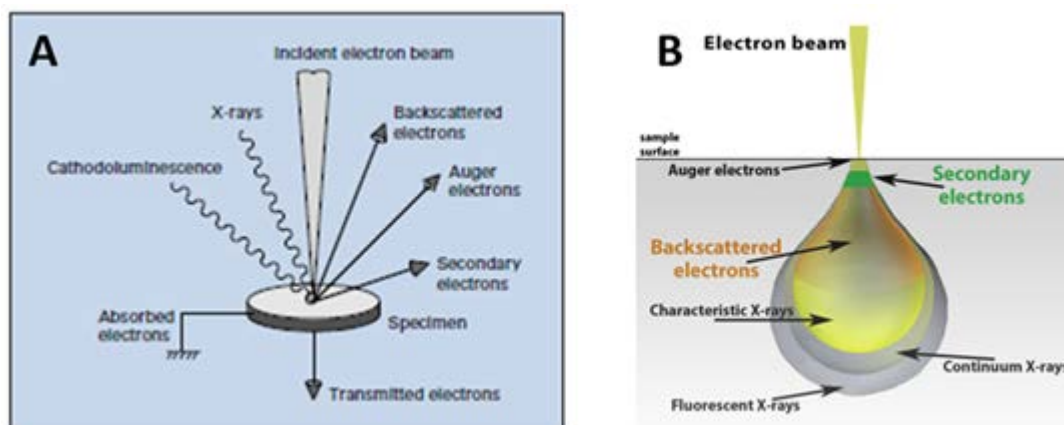


Figure 4-1: Illustration showing the A) possible signals generated from the electron-specimen interactions and B) interaction volume of for each signal in the specimen [22].

4.2.2. Imaging using Secondary and Backscattered Electrons

A scanning electron microscope produces images by focusing an electron beam on the sample surface and scanning it across the specimen with the help of scanning coils. Each point of the specimen that is struck by the accelerated electrons emits a signal as discussed in the previous section. The resulting signals are then collected and amplified by the appropriate detector.

This signal is then converted into an intensity value that is stored at a particular point, that would represent a pixel in the SEM image displayed on the computer screen or when saved as an image. **Figure 4-2** shows an overview of a typical SEM. The electrons are produced from either thermionic filaments made of tungsten or LaB₆ or consist of a field emitting source (FEG). The resulting electrons are then accelerated down the column where a series of apertures and electro-magnetic lenses control the beam current and beam diameter. Additional lenses are responsible for correcting any imperfections (e.g. astigmatism) in the resulting electron beam.

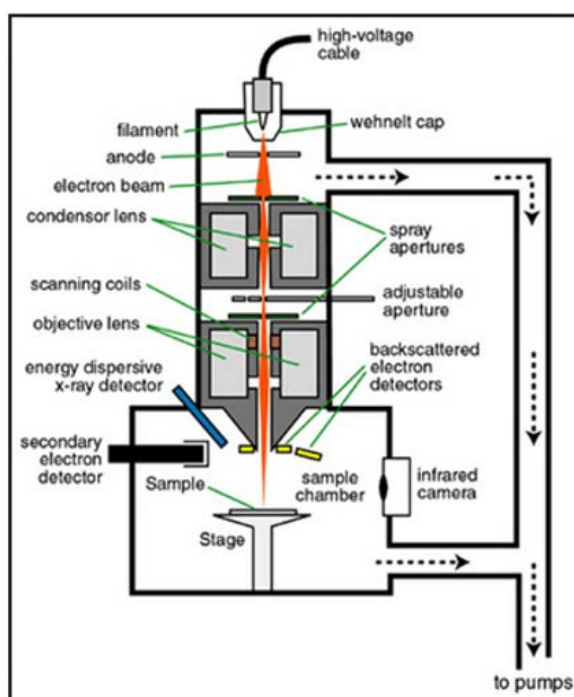


Figure 4-2: Schematic illustration of the basic SEM configuration (North Arizona University).

Secondary electrons get ejected from the specimen surface when the electron beam transfers energy to the specimen atoms and dislodge loosely bound outer shell valence electrons. These ejected electrons typically have energies of <50 eV and mainly originate from the top surface of the sample. The secondary electrons are attracted to the detector with the help of a Faraday cage biased to +250V, as shown in **Figure 4-3**.

The detector consists of a scintillator-photomultiplier that amplifies and converts the electrons into an electrical signal; this type of detector is known as an Everhart-Thornley detector (ETD) [24]. Secondary electrons are sensitive to topography of the sample surface, thus areas with different angles with respect to the incoming beam, will have different efficiencies in producing secondary electrons that are attracted into the detector. This is then noticed as intensity differences in the image to form a visualization of the sample surface. Areas consisting of small radii are also more effective in producing secondary electrons and will appear bright. Depending on the detector configuration and the sample composition, atomic number contrast can also be observed from secondary electrons.

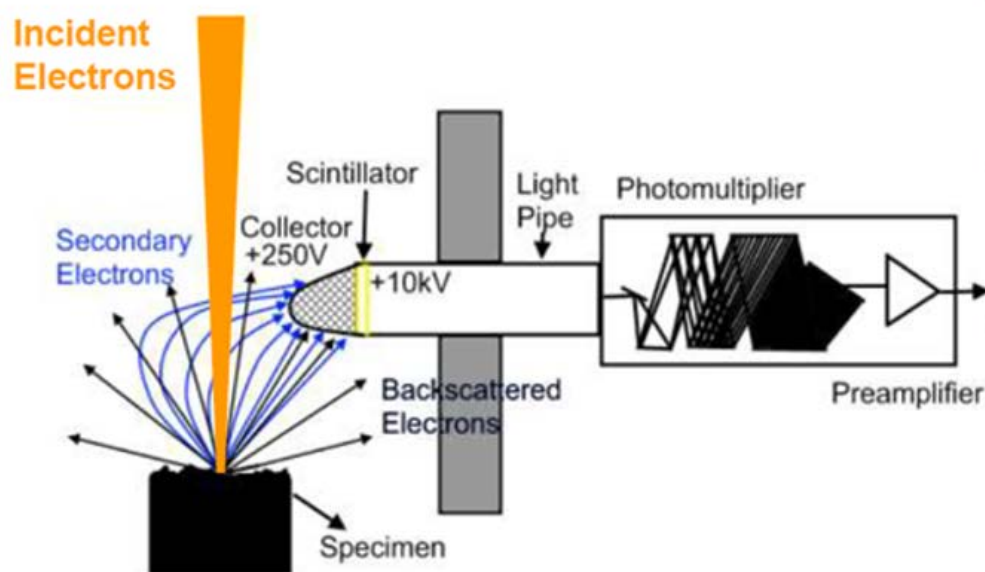


Figure 4-3: Everhart-Thornley secondary electron detector with a Faraday cage attracting the secondary electrons [24].

Backscattered electrons originate from the incoming electrons that are deflected back out of the specimen due to multiple elastic interactions with the specimen atom nuclei as shown in **Figure 4-4**. Owing to the elastic nature of the interaction, the backscattered electrons retain approximately 50% of the incoming energy (~5-10keV). Thus electrons are able to escape from a much larger volume within the sample depending on the incoming electron energy.

Electron backscatter detectors are typically located close to the beam in the form of a donut shape to collect a large solid angle of the backscattered electrons. The detectors are either a scintillator or semiconductor chip that converts the electrons into an electrical signal. The backscattered signal is a strong function of atomic number due to the multiple interactions with the nucleus of the specimen atoms, thus resulting in atomic number contrast. Topography on the sample surface can also be observed when detectors with multiple segments are used [23].

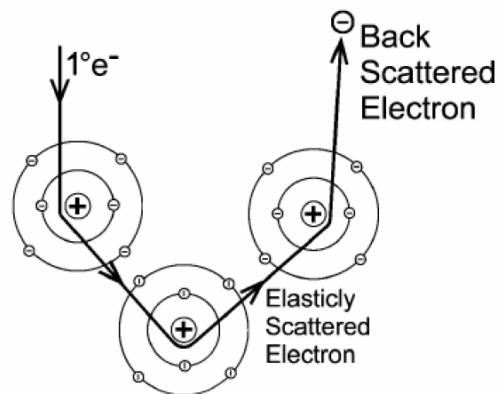


Figure 4-4: Backscattered electrons form as the result of multiple elastic interactions of the incoming electrons with the specimen atoms [23].

The relative orientation of the sample also gives rise to the so called channeling contrast from backscattered electrons. The variation in depth of electron penetration with angle of incidence relative to the target crystal structure results in either (a) near surface interactions and high BSE emission rates or (b) deep penetration and low BSE emission rates as illustrated in **Figure 4-5**.

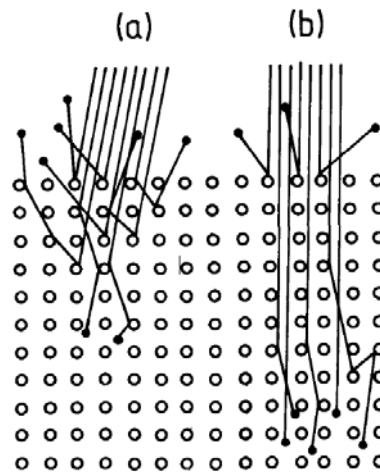


Figure 4-5: Two possibilities showing backscattered electrons emerging from either a) near surface interactions (strong BSE signal) or b) deeper penetration (weak BSE signal) resulting in channeling contrast [25].

4.2.3. Energy Dispersive X-ray Spectrometry

An incoming electron can cause the inner electron from the atoms in the sample to be ejected. This configuration is unstable and higher energy electrons from the outer shells will fill the hole that was created. The excess energy is emitted as an X-ray with a characteristic energy depending on the type of transition and the type of element. This process is illustrated in **Figure 4-6** which also shows the possible electron transitions and their naming convention. The characteristic X-ray lines are named according to the shell in which the initial vacancy occurs and the shell from which the electron drops to that vacancy [26].

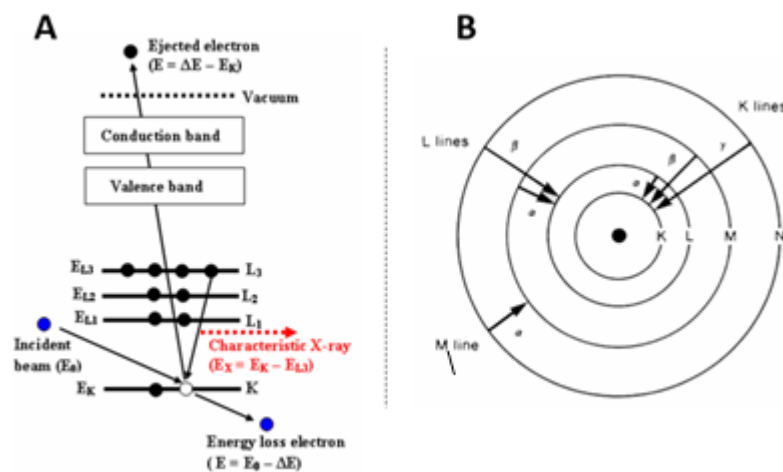


Figure 4-6: A) Generation of characteristic X-rays by the ejection of an inner shell electron which gets replaced by electrons from a higher energy state resulting in the photon emission. B) Naming convention of the possible electron transitions [26].

Additional X-rays are produced from the sample when the incoming electrons interact with the coulomb field surrounding the nucleus of the atoms in the sample. The electrons are slowed down and the excess energy is emitted as an X-ray. These X-rays are not characteristic and forms a continuum background superimposed on the characteristic X-ray peaks.

X-rays are detected using semiconductor (Si (Li) or Silicon Drift Detectors (SDD)) crystals in which electron-hole pairs are created when an X-ray enters the crystal. The number of electron-hole pairs created is proportional to the incoming energy of the X-ray. The detector is thus able to disperse the incoming X-rays according to energy. This signal is then amplified and processed to form the output that is read by the computer software that analysis and display the results.

The characteristic X-ray energy is used to identify the elements present in the sample. The intensity of a characteristic X-ray peak is proportional to the number of that particular atom in the sample. It can thus be used to quantitatively determine the *elemental composition* of the sample, after suitable corrections are made for X-ray-specimen interactions and the continuum background is subtracted. *Elemental mapping* can be performed by inserting a suitable energy window over the characteristic energy range and integrating the X-ray intensity. These intensity values are then displayed as a function of position on the sample resulting in the elemental map. *Qualitative mapping* as performed in this study does not automatically subtract the continuum background. The elemental maps produced are from X-ray signals that are superimposed on the continuum background. Changes in the continuum background due to height variations, sloped sample surface and X-ray shielding could create artifacts in the elemental maps, especially for low energy X-rays. Background subtracted and quantitative mapping overcome this limitation by correcting for these changing experimental conditions.

4.2.4. Electron Backscattered Diffraction

This technique is used to obtain crystallographic and grain orientation information from the sample. The sample surface is usually tilted to 70° with respect to the horizontal (see **Figure 4-7**). Electrons striking the surface are scattered in the direction of the incoming beam (forward scattered electrons). Some portion of electrons are diffracted by the crystallographic planes in the sample resulting in diffraction cones. These diffraction cones intersect to the EBSD detector consisting of a phosphor screen, optics and a CCD camera to form the Kikuchi lines in an electron backscattered pattern (EBSP) [27] [28].

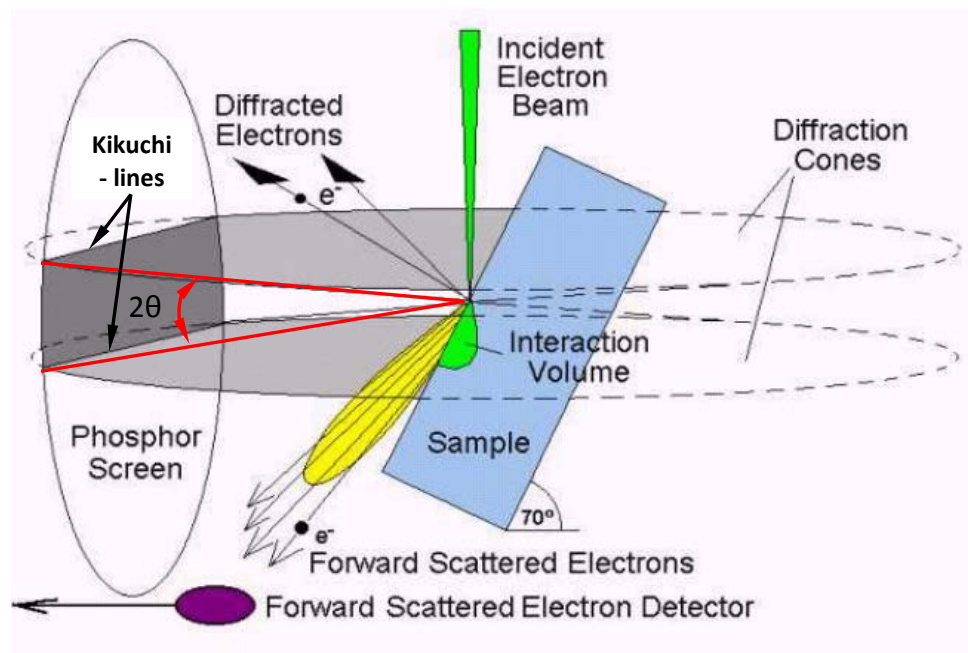


Figure 4-7: Generation of the signals (forward scattered and diffraction cones) when the electrons interact with the sample at an angle of 70° [28].

In EBSD analysis the electron beam is scanned across the sample surface and EBSD patterns are collected at the position of the sample. These patterns are then processed using Hough transformation to identify the zone-axis and match a particular phase and orientation using dedicated software (see **Figure 4-8**).

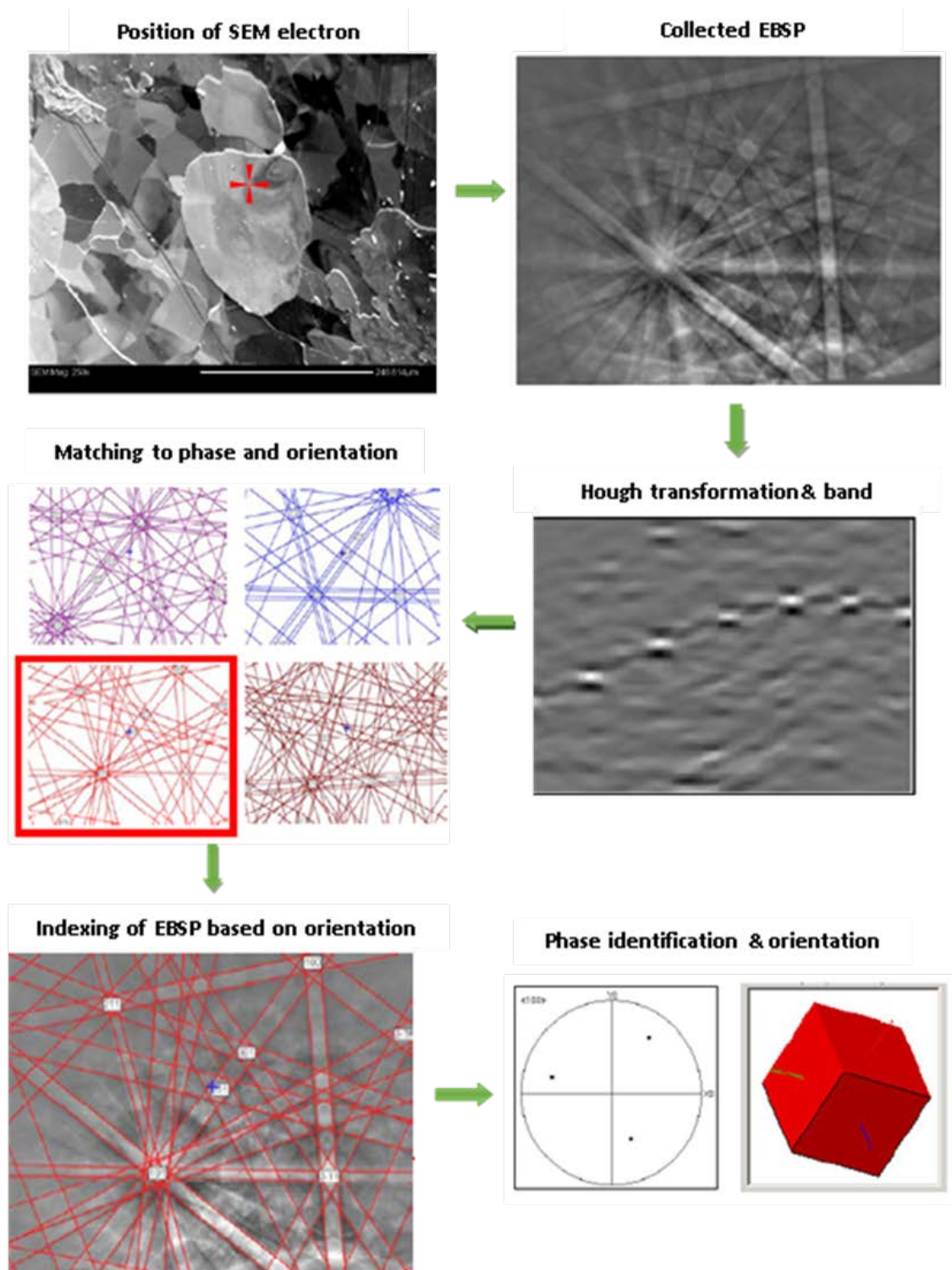


Figure 4-8: Collection, transformation and indexing of the EBSP using dedicated software [28].

For each position of the scanned area the EBSD analysis indexes the crystal phase and orientation. This information can be further processed to outline grains, grain boundaries, misorientations, and preferred orientations through texture analysis. The typical interaction volume of the electron specimen interaction is in the order of 100nm down the slope of the sample surface, which places a limit on the spatial resolution that can be achieved using this technique. One way to overcome this is to conduct the analysis on a thin sample and by tilting the sample to -20° with respect to the sample normal using a special pre-tilted holder as shown in **Figure 4-9**. This technique improves spatial resolution to roughly 10 nm for steel samples.

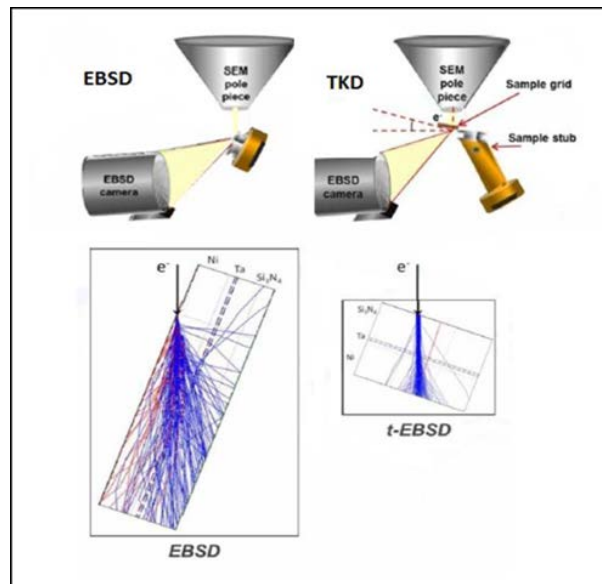


Figure 4-9: Comparison of the two diffraction geometries for SEM based diffraction orientation mapping with the corresponding Monte Carlo simulation showing the interaction volume [29].

4.3. Focused Ion Beam SEM

Focused Ion Beam (FIB) milling was used to remove and prepare thin sections from the microstructural regions of interest for further investigation in the TEM. Secondary electron SEM images show the various steps in the process (see **Figure 4-10**). The first step in the sample preparation process involves depositing a protective layer of carbon onto the surface to ensure that the top surface of the sample is not damaged during the milling process (see **Figure 4-10a**).

Two trenches are milled at either side of the carbon deposition (see **Figure 4-10b**). The sides of the sample are then milled parallel and two cuts are made to partially free the sample from the bulk. A micro-manipulator is then attached to the side of the sample using carbon deposition. The sample is then completely cut from the bulk and lifted out using the micro-manipulator (see **Figure 4-10c**). The sample is placed on one finger of a half-moon grid and attached using carbon deposition (see **Figure 4-10d**). The micro-manipulator is severed from the sample, which is approximately 2 μm thick at this stage. The sample is then polished to a final thickness (~ 100 nm) using successively lower beam currents and ion beam energies (see **Table 4-1**). A typical area of $5 \times 5 \mu\text{m}$ will be electron transparent and available for viewing in the TEM.

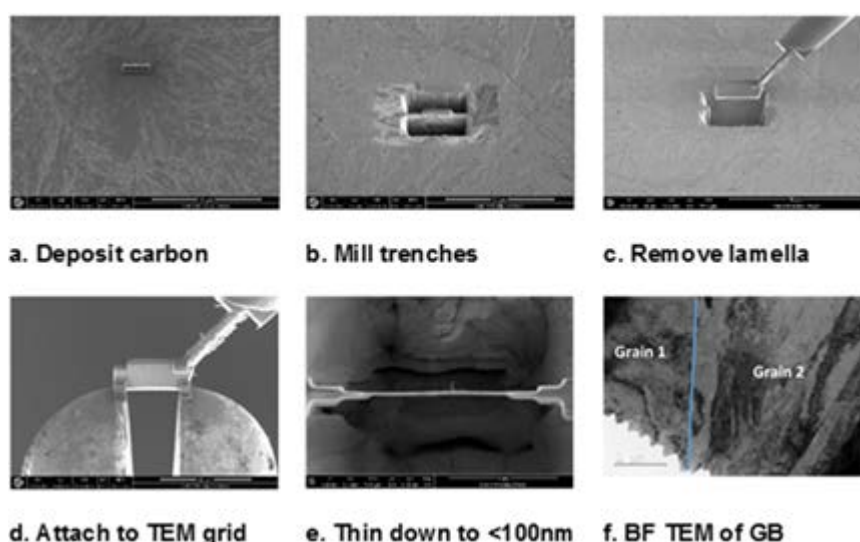


Figure 4-10: Secondary electron images of the various stages in the sample preparation using the FIB-SEM (a-e). Image f shows a bright-field TEM image of the sample.

Step	Thickness (nm)	Beam energy (keV)	Beam current (nA)	Sample tilt
Lift (a-d)	2000	30	47, 9, 2.5	
e	500	30	0.79	$\pm 1.5^\circ$
e	200	30	0.23	$\pm 1.2^\circ$
e	<100	5	0.041	$\pm 2.5^\circ$
e	<100	2	0.023	$\pm 7.0^\circ$
e	<100	0.5	0.011	$\pm 7.0^\circ$

Table 4-1: FIB parameters for TEM sample preparation.

4.4. Transmission Electron Microscopy and Associated Techniques

This technique uses a beam of high energy (200keV) electrons, which is transmitted through a thin (100 nm thick) sample to obtain information (structure and composition) of the different phases. Modern TEM can be operated in several different configurations. In conventional TEM the sample is illuminated using a near parallel beam of electrons. Contrast in the image is observed through variations in thickness and atomic number. Diffraction contrast can be observed when additional apertures are placed to select only electron traveling straight through the sample to form an image. This mode is very useful for general imaging and dislocation analysis.

In this study the TEM was mainly used in convergent scanning mode, which is very similar in operation to the SEM. This mode will be reviewed in more detail.

4.4.1. Scanning Transmission Electron Microscopy

In this mode the electron beam is focused to a small spot and scanned across the sample and is very similar in operation to the SEM. The main signal that is collected is from the original electrons that are scattered by traveling through the specimen (see **Figure 4-11**). The detectors are placed after the specimen to collect, amplify and convert the electrons into an intensity value that would represent a pixel on the resulting image. Angular dark-field detectors are donut shaped and collect electrons scattered at higher angles from the original beam path. The angular range that can be collected from these detectors are determined by the camera length (CL) (effective distance between sample and detector). Post specimen lenses project the scattered electrons onto the detector, in the case of short CL only electrons scattered at high angles will be detected, this mode is called high-angle annular dark-field (HAADF). Electrons scattered at high angles (>60 mRad) (Rutherford scattering) have a strong dependence on the atomic number and this results in atomic number contrast. HAADF-STEM images show very strong atomic number contrast [30].

Coherent Bragg diffraction information is typically only scattered at small angles (<10 mRad) with respect to the electron beam. These electrons can be detected using the bright-field detector centred on the electron beam. Another useful imaging mode involves the use of the annular dark-field detector at a longer camera length. In this imaging mode atomic number contrast is combined with diffraction information to show, not only atomic number variations but also dislocations and interfaces such as grain boundaries and precipitates (see **Figure 4-12**). Similar to the operation in the SEM, this technique can be used to control the beam position for site specific chemical analysis using EDX analysis in the sample.

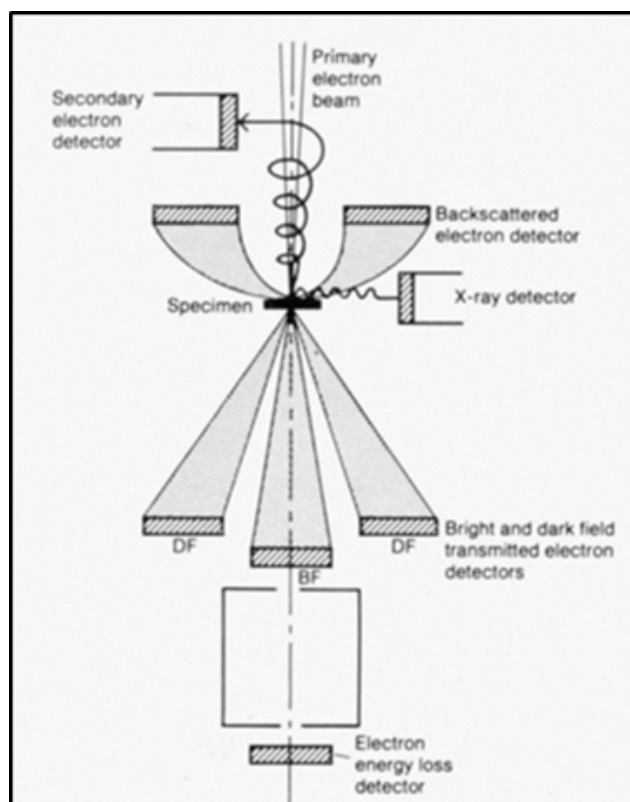


Figure 4-11: Schematic illustration of different detectors that can be attached to a STEM system to collect various signals from beam-specimen interactions [30].

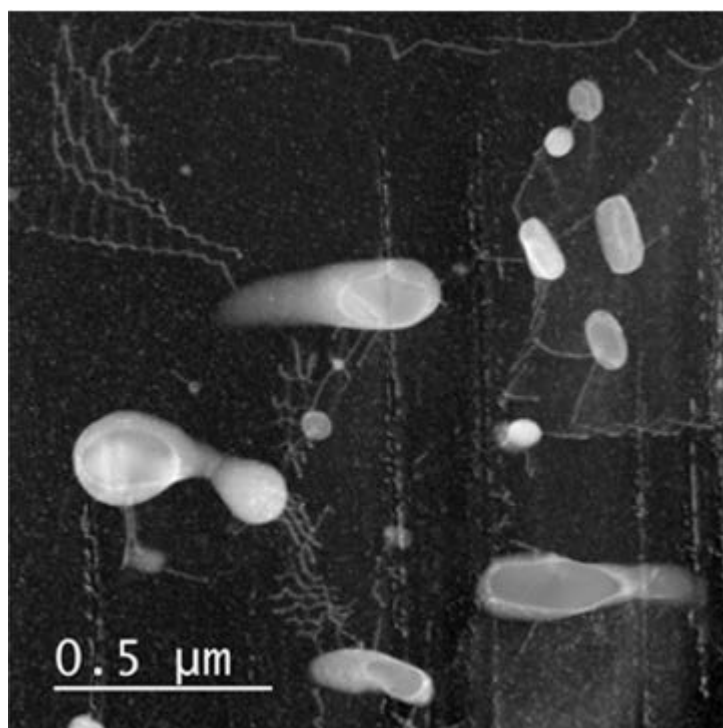


Figure 4-12: Low angle ADF image showing a combination of atomic number and diffraction contrast.

Chapter 5 : Microstructural Evaluation of the Welded Steam Pipe Samples

5.1. Introduction

The goal of this part of the study was to investigate the different regions of the welded service exposed pipe material to understand the factors that control the nucleation and growth of graphite in the material, especially in the planar graphitized zone just outside the HAZ region of the seam weld. Two welded samples were used for the microstructural investigation. Sample A consisted of a service exposed welded sample with noticeable levels of planar graphitization as determined in Chapter 3. Sample D consisted of service exposed material that was newly welded, in order to investigate the effect of welding and an extended post-weld heat treatment on the microstructure of the HAZ region.

Sample A was investigated using light microscopy to show the general microstructure in the different regions of the welded sample. Backscattered electron imaging was used to image the parent material as well as the planar graphitized zone of the sample showing the location of the graphite nodules. EBSD analysis was performed on the parent material and planar graphitized regions to obtain information regarding the grains-size, grain misorientation and the phases present. The FIB-SEM was used to remove and prepare samples from specific sites of the parent material and planar graphitized zones for further investigation in the TEM in order to determine; the crystal structure of the carbide particles, the location of the graphite nodules and possible nucleation sites for preferential graphite nucleation.

The HAZ region in Sample D was investigated using light microscopy for possible graphite formation in the newly welded pipe after being exposed to high temperature annealing. Site specific sampling with the FIB-SEM removed a small section from the region just outside the HAZ to determine the crystal structure of the carbide precipitates and locate possible nucleation of graphite that could not be resolved with the light microscope.

The results of this preliminary investigation could contribute towards the understanding of the nucleation and growth of graphite in this material. Knowledge of the growth of graphite can be combined with mechanical property data to predict the remaining life of the steam pipes.

5.2. Light Microscopic Evaluation of the Welded Samples

Cross sections of welded regions of Sample A and Sample D were removed, mounted, polished and imaged using optical microscopy. **Figure 5-1** shows the microstructures of the welded samples using DIC lighting. The location of the weld region, heat affect zone (HAZ) and parent material is indicated on the image. Both samples showed MnS inclusions along the rolling direction of the pipe. The planar graphitized zone on Sample A is located just outside the HAZ as indicated on the image. No clear evidence of graphitization in this zone could be found for Sample D.

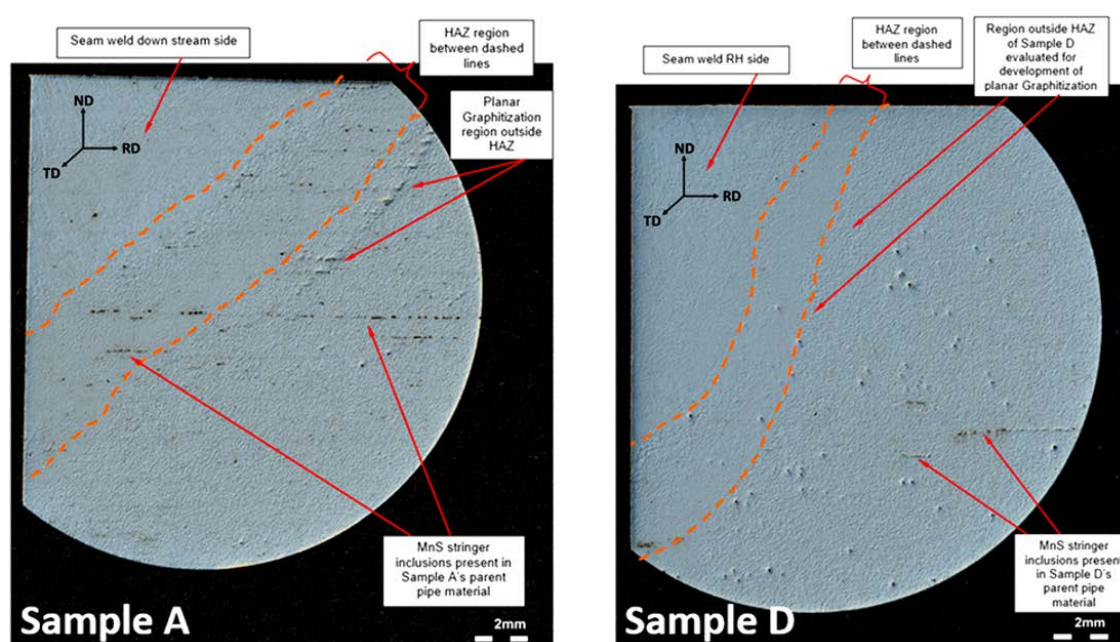


Figure 5-1: DIC Light microscope images of two welded samples showing an overview of the microstructural features

Light microscope images at a higher magnification of Sample A are shown in **Figure 5-2**, with the planar graphitization evident outside the HAZ and random of the graphite nodules visible in the parent material. Dark bands associated with the pearlite regions are visible along the rolling direction of the pipe. The planar Graphitized locations co-incident with the pearlite bands, suggesting that these carbon-rich regions dissolve during graphite formation.

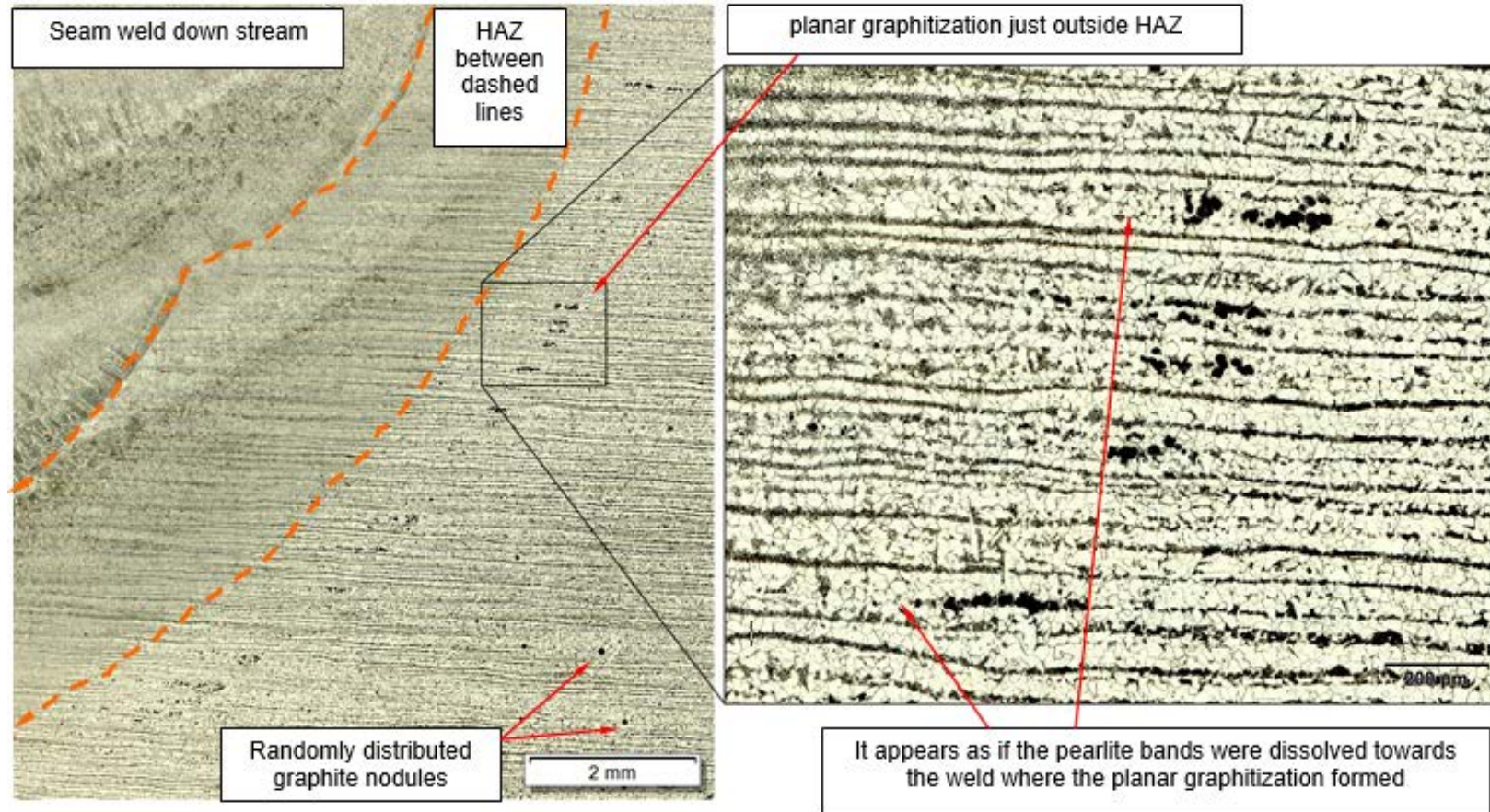


Figure 5-2: Light microscope images of the planar graphitized zone located outside the HAZ of the welded Sample A.

The development of the weld microstructure was discussed in the literature review. **Figure 5-3** shows light microscope images of the microstructural region surrounding the fusion line. The weld is formed from material cooling rapidly from the molten state. The resulting microstructure consist of a columnar structure of Allotriomorphic ferrite forming on the prior austenite grain boundaries, from which the Widmanstätten ferrite grows as the microstructure cools down further (**Region 1**). The coarse grained heat affected zone (**CGHAZ**) is formed due to the nucleation and growth of austenite grains when exposed to temperatures in the upper austenite stability region, followed by rapid cooling. The fine-grained heat affected zone (**FGHAZ**) is formed due to nucleation of austenite at temperatures just above the Ac3, without large grain growth. The planar graphitized zone is located just outside the visible HAZ region. The maximum temperatures in the region are close to Ac1, resulting in partial dissolution of the carbide precipitates causing supersaturation of the iron matrix (**Region 2**).

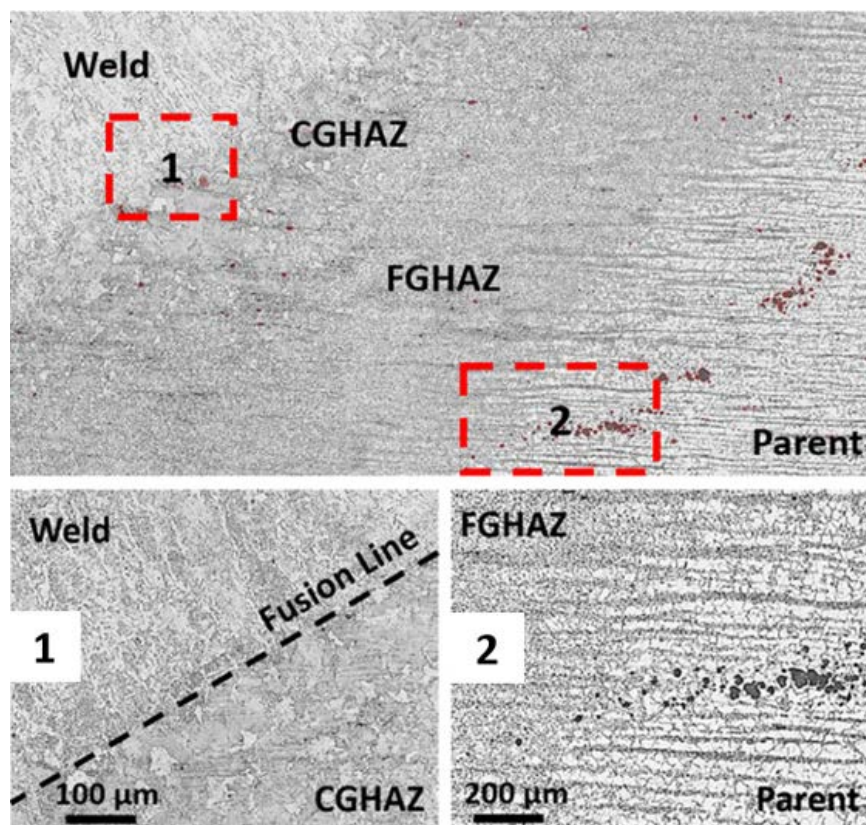


Figure 5-3: Light microscope image of the microstructural regions at the fusion line of Welded Sample A.

5.3. Scanning Electron Microscopy Evaluation of Welded Samples

Scanning electron microscopy was done to obtain higher resolution images of the different microstructural features within the material. The parent plate was investigated using the backscattered electron (BSE) SEM mode to show the ferrite/pearlite banded structure, MnS inclusions and the Graphitized regions. This method relies on channeling contrast (refer to 4.2.2 of Chapter 4) to show the different orientated grains in the sample.

Electron backscattered diffraction analysis of the parent plate and graphitized regions revealed the grain boundaries and local misorientations in the different regions.

5.3.1. Backscattered Electron

Figure 5-4 a and b show the banded pearlite/ferrite grain structure of the parent material for Sample A. As discussed in the literature review, this microstructure developed due to interdendritic segregation of manganese during solidification and subsequent hot-rolling of the material. This causes carbon enrichment into the untransformed austenite, which then leads to pearlite formation during final cooling. The pearlite region consists of a lamellar structure of interpenetrating structures made of ferrite and cementite. The parent material was exposed to long term service exposure temperatures at or above 420°C. This has not resulted in complete spheroidization of the cementite of the pearlite regions of the parent plate.

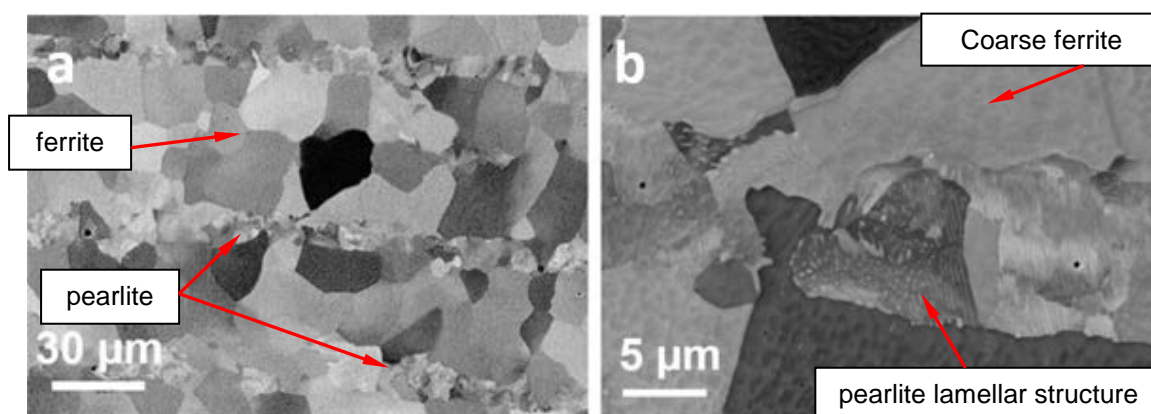


Figure 5-4: a) BSE SEM image of the ferrite/pearlite bands in the parent material, b) BSE image of the pearlite band showing the lamellar ferrite/ cementite structure.

The parent material of Sample A also contained a low percentage of random (non-planar) graphite nodules ranging from 10-100 μm in size. **Figure 5-5** shows such a graphite nodule using BSE at two different contrast levels. Several smaller grains surrounding the graphite nodule are noted from the image optimized for channeling contrast. The central part of the nodule contains trapped iron as shown in the image optimized for Z-contrast. The shape of these nodules is almost always spherical.

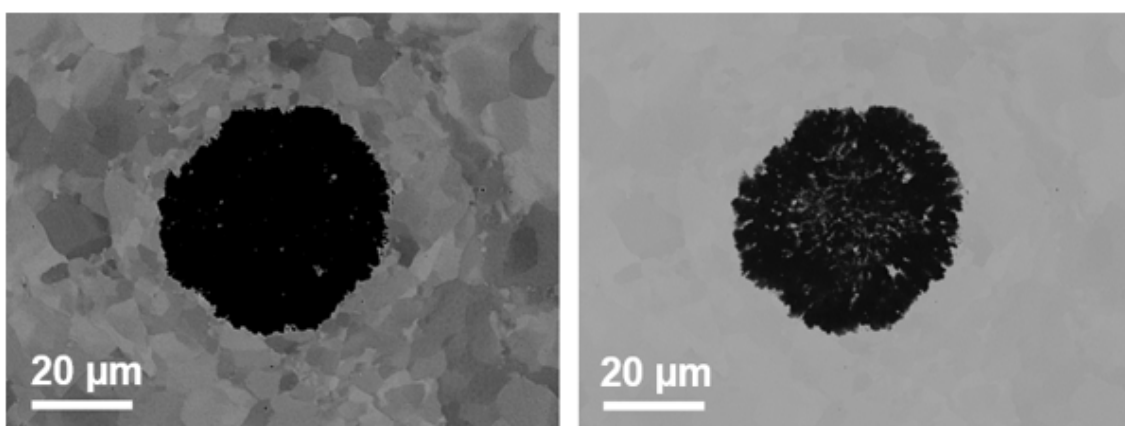


Figure 5-5: BSE SEM images of a random graphite nodule in the parent material of Sample A, shown at two different contrast settings. (Acceleration voltage = 15 kV)

As shown in the previous light microscope images, several MnS inclusions are located along the rolling direction of the pipe. In this case, they would absorb the manganese that could cause the carbon segregation responsible for the carbon-rich pearlite formation.

Figure 5-6 shows BSE SEM images of a typical MnS inclusion in the parent material of Sample A. The pearlite region just below the inclusion is absent in this case, this appears to be a general observation of the grain structure surrounding the MnS inclusions, although several MnS inclusions investigated were bounded with pearlite regions as well.

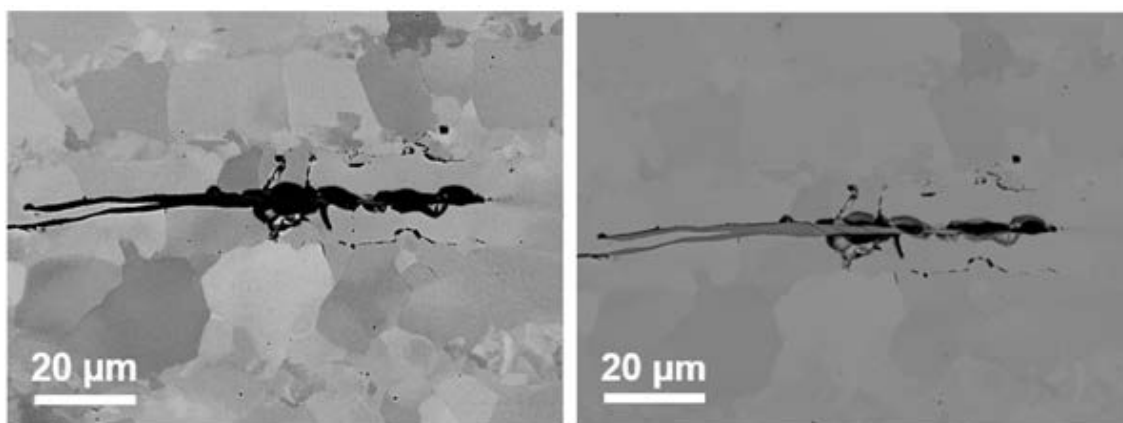


Figure 5-6: BSE SEM images of a MnS inclusion in the parent material of Sample A, shown at two different contrast settings

The planar graphitized region located just outside the HAZ region of Sample A was investigated using BSE SEM imaging. **Figure 5-7** shows images taken at different magnifications with the sample orientated in the same direction as the light microscope investigation. The “eye-brow” / planar graphitization is clearly visible in the images. The location of the planar graphite is clearly associated with the finer grained banded pearlite regions.

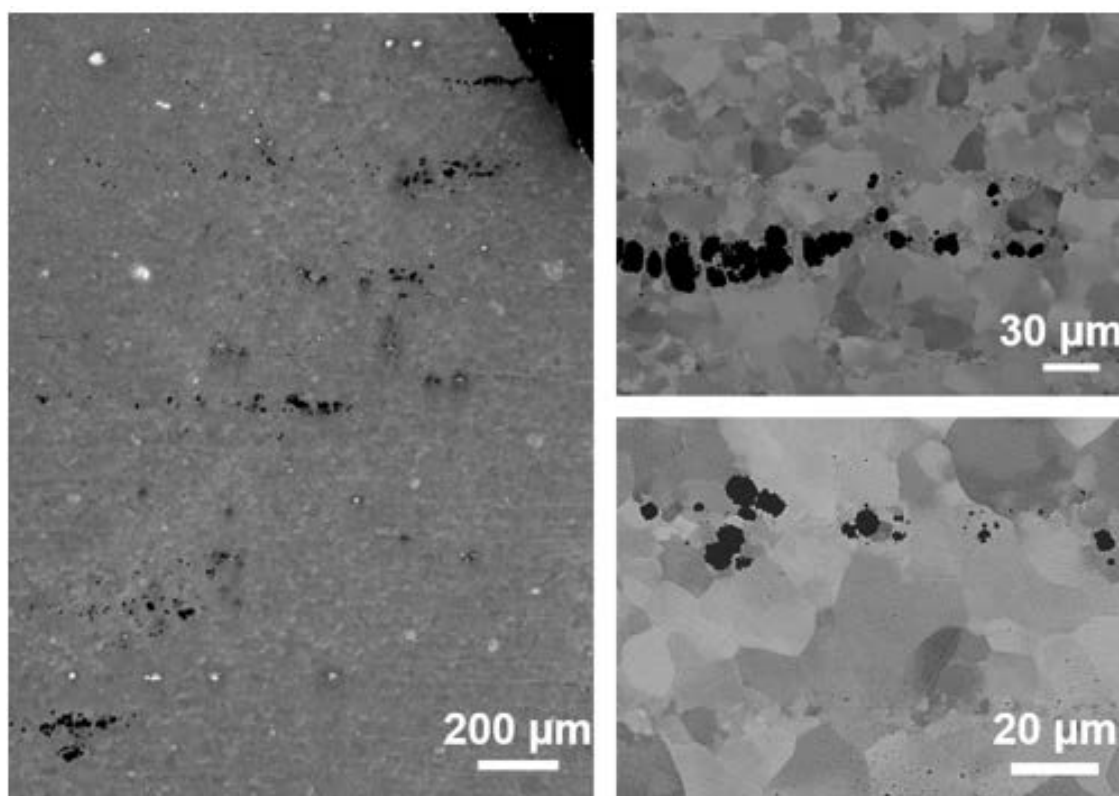


Figure 5-7: BSE-SEM images of the planar Graphitized zone of Sample A located just outside the HAZ zone.

5.3.2. Electron Backscattered Diffraction Analysis

The EBSD analysis was performed on parent material and the planar graphitized regions in order to investigate the grain boundaries and grain misorientations in the pearlite and graphitized zones of Sample A. EBSD maps (350 x 262 μm) were collected using a step size of 0.25 μm at 15 kV accelerating voltage from both regions. In addition, higher resolution EBSD maps (82 x 53 μm) were collected using a 0.1 μm step size at 15kV to focus on the pearlite region and on one particular graphite nodule.

Figure 5-8 (a-f) shows the EBSD maps for the parent plate. **Figure 5-8 (a-b)** shows inverse pole figure (IPF) maps of the banded microstructure. The higher magnification map shows the carbide precipitates as dark regions inside the grains and on the grain boundaries (GB). **Figure 5-8 (c-d)** shows the grain boundary angles as different colors. Low angle ($1-5^\circ$: green) boundaries are visible inside the pearlite regions of the microstructure, but are absent from the ferrite grains. Misorientation analysis using local misorientation (low angle GB) (**Figure 5-8e**) and grain orientation spread (GOS) (**Figure 5-8f**) indicate that the pearlite grain structure contain local misorientations of up to $4-5^\circ$, while the surrounding ferrite grains have very low ($<1^\circ$) misorientations.

Figure 5-9 (a-f) shows the EBSD maps for the planar graphitized zone. **Figure 5-9 (a-b)** shows inverse pole figure (IPF) maps indicating the banded microstructure with graphite. The higher magnification map shows the graphite nodule with the surrounding ferrite grains. **Figure 5-9 (c-d)** shows the grain boundary angles as different colors. Numerous low angle ($1-5^\circ$: green) boundaries are visible inside the ferrite grains surrounding the graphite nodules. This is confirmed by misorientation analysis using local misorientation (low angle GB) (see **Figure 5-9e**) and grain orientation spread (GOS) (see **Figure 5-9f**), which indicate that the ferrite grains surrounding the graphite nodule contain large local misorientations of up to $4-5^\circ$. These misorientations and ferrite sub-grains probably form due to mechanical stress from the formation of low density graphite material in the surrounding ferrite grains. No pearlite grains were found in the regions surrounding the graphite nodules.

This is expected, as the carbides/ cementite in the previous pearlite region acts as a source of carbon for the formation of the graphite nodules.

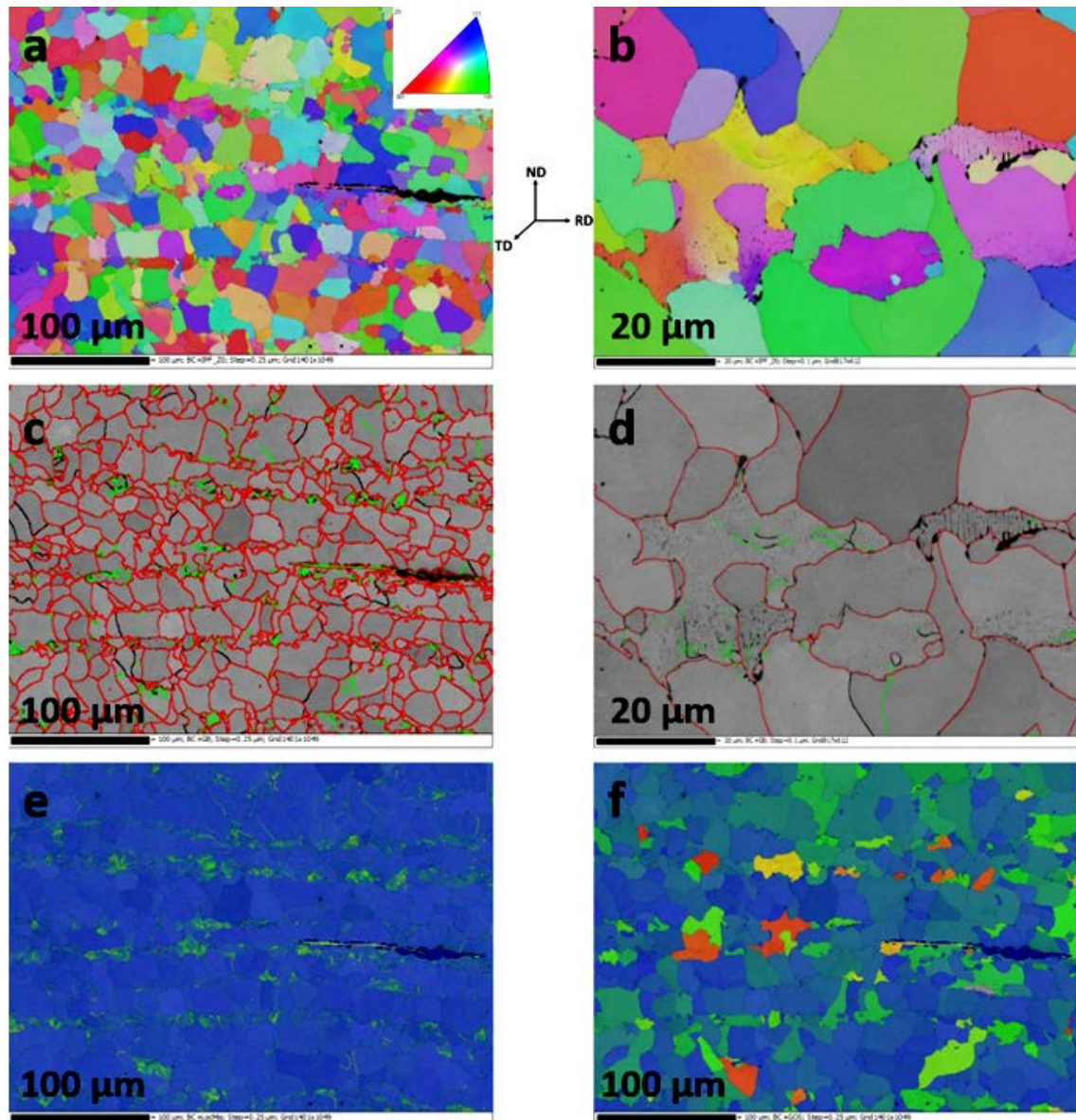


Figure 5-8: EBSD analysis of the parent material zone a-b) IPF showing the misorientations surrounding in the pearlite bands, c-d) grain boundaries (GB) (1-5°: green; 5-15°: black; >15°:red), e) local misorientation profile (3x3 pixels) showing low angle GB and f) Grain orientation spread (0°: blue – 5°: red).

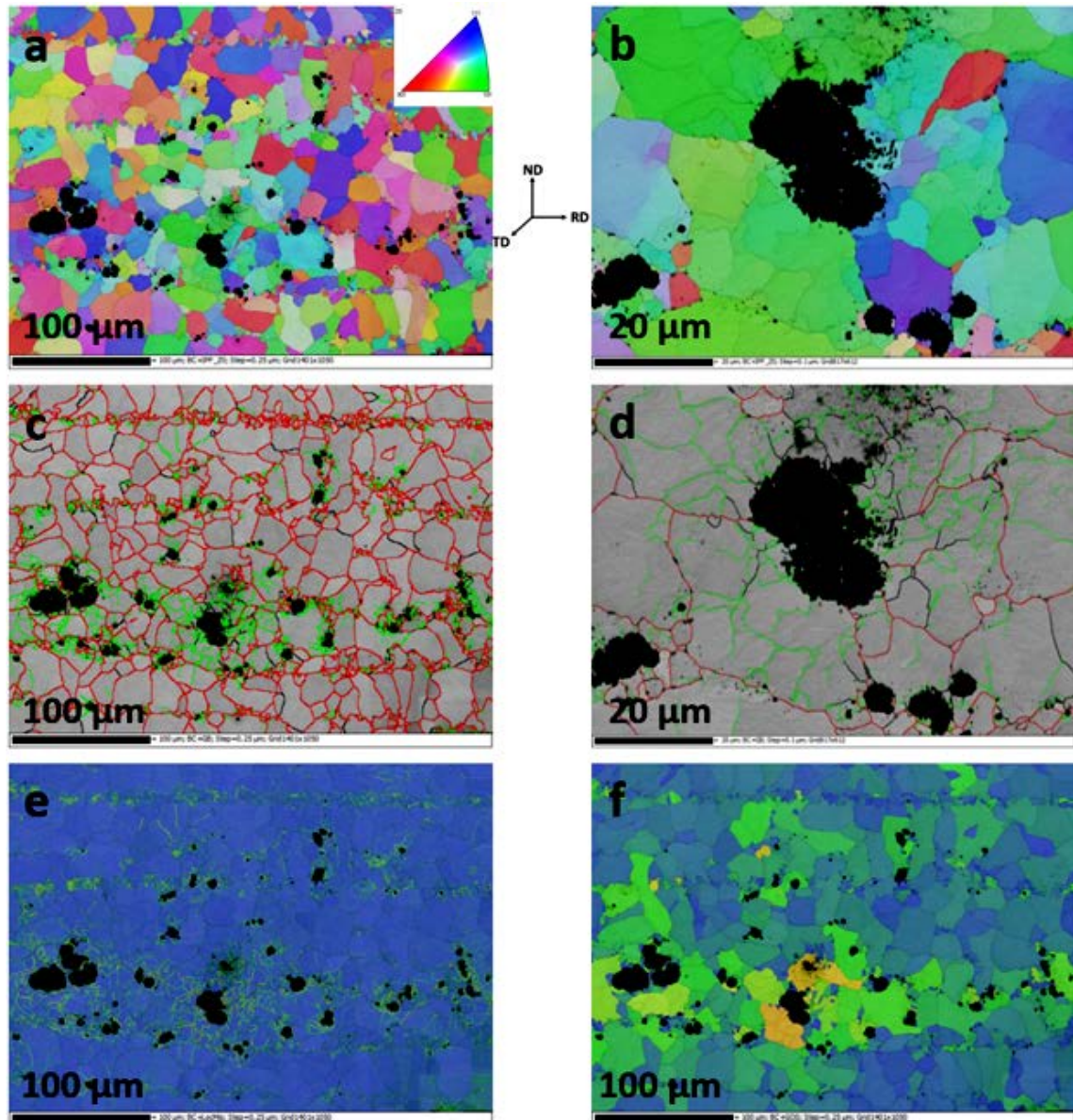


Figure 5-9: EBSD analysis of the planar Graphitized zone showing a-b) IPF showing the misorientations surrounding the graphite nodule, c-d) grain boundaries (GB) (1-5°: green; 5-15°: black; >15°: red), e) local misorientation profile (3x3 pixels) showing low angle GB and f) Grain orientation spread (0°: blue – 5°: red).

5.4. Transmission Electron Microscopy of Selected Areas

Site specific sampling with the FIB-SEM was done on selected areas of Sample A and Sample D weldments. The goal of the TEM investigation was to investigate the location of the carbide precipitates and graphite nodules, phase identification of the carbide precipitates and possible factors such as dislocations, grain boundaries and non-metallic inclusions that could promote the nucleation and growth of graphite in the material.

5.4.1. Sample A's Parent Material

Figure 5-10 shows the area from which the TEM sample was prepared in the parent material. A region across a pearlite and ferrite grain was selected which included a larger precipitate located at the grain interface.

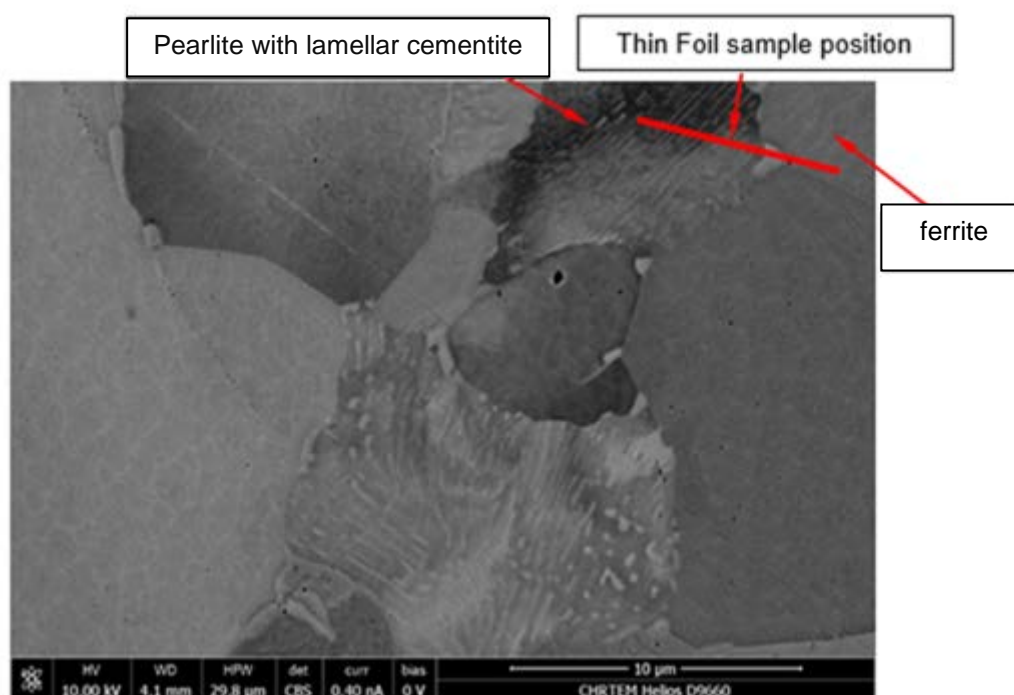


Figure 5-10: BSE SEM image of showing the location of the FIB-sample (pearlite/ferrite boundary) taken from the Sample A's parent material.

Figure 5-11 shows the ADF-STEM image of the sample. Large $(\text{Fe, Mn})_3\text{C}$ precipitates are located on the grain boundary between the pearlite region and the ferrite grain. The pearlite region consists of laminar precipitates of $(\text{Fe, Mn})_3\text{C}$ inside a highly dislocated ferrite grain.

The precipitates contained approximately 6 at. % manganese as determined using EDS spot analysis (see **Appendix E**). The adjacent ferrite grain was free from the smaller carbides and displayed relatively fewer dislocations. It should however be noted that the grain was not specifically orientated in a favorable orientation to view the dislocations.

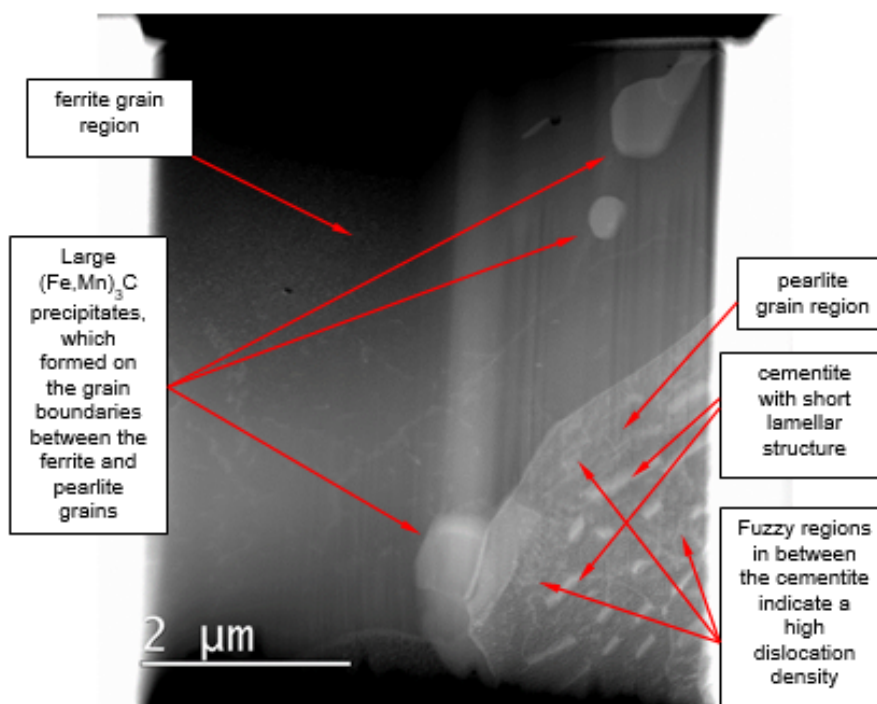


Figure 5-11: ADF-STEM image showing the microstructure of the ferrite and pearlite regions as well as the location of the precipitates.

5.4.2. Sample A's Planar Graphitized Zone

Site specific sampling using the FIB-SEM was done across two smaller graphite nodules in the planar graphitized zone of Sample A as shown in **Figure 5-12**. Evaluation of **Figure 5-13 (a)** ADF-STEM image showed that some of the graphite nodules are located inside a grain with spherical carbide precipitates. This region probably consisted of a pearlite region previously. SEM analysis of this zone also showed that the pearlite lamellar structure is absent from this region adjacent to the HAZ, indicating that spheroidization of the pearlite took place during the welding operation. The graphite nodule shown in **Figure 5-13 (b)** appears to grow preferentially along dislocations and grain boundaries. This qualitative observation needs to be confirmed with additional studies of the graphite nodules.

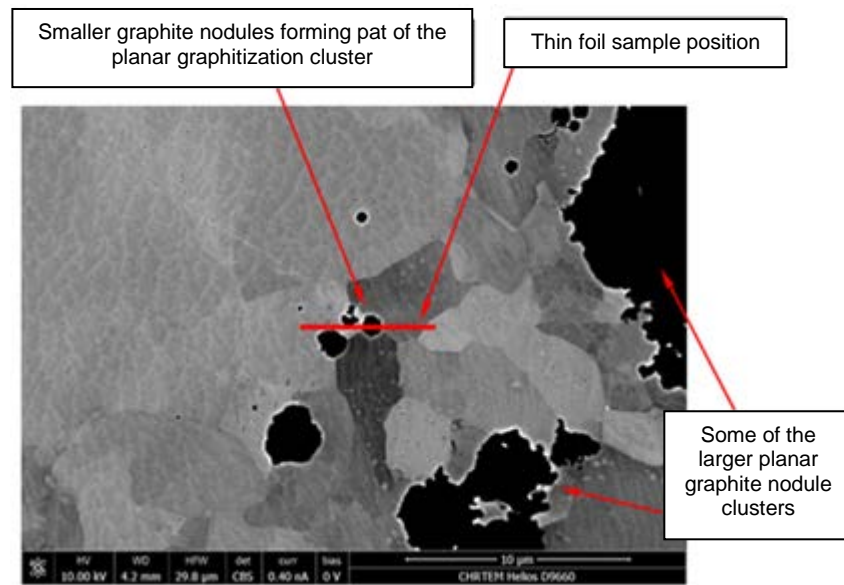


Figure 5-12: BSE SEM image showing the location of the FIB-sample taken across two graphite nodules in the planar graphitized zone outside the HAZ of welded Sample A.

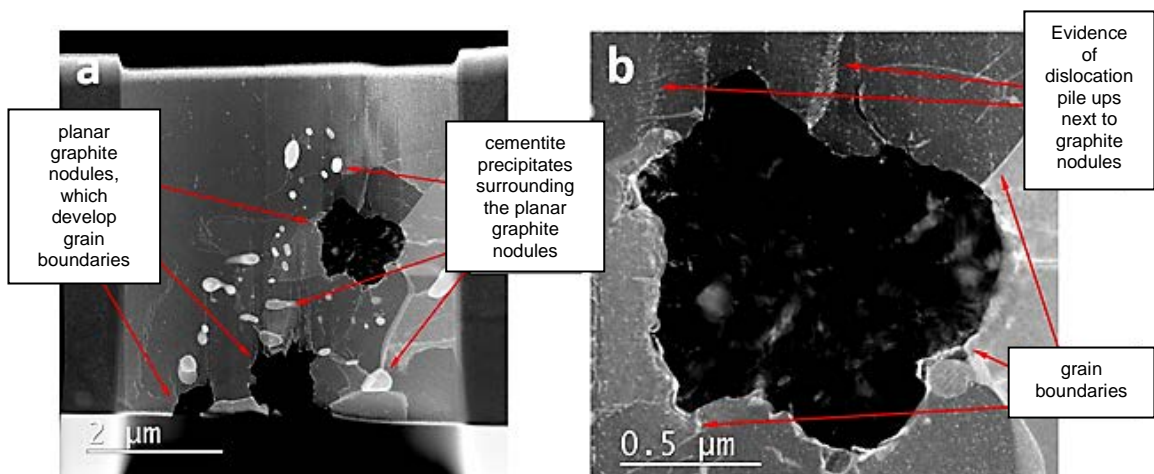


Figure 5-13: ADF-STEM images showing the a) location of the graphite nodules, carbide precipitates and dislocations, b) higher magnification image of the graphite nodule showing the grain boundaries and dislocations surrounding the graphite nodule.

TKD analysis was done on the sample using a step size of 20 nm and an accelerating voltage of 30 kV in the SEM. The results of the analysis are shown in **Figure 5-14**. The phase map shown in **Figure 5-14b** indexed the carbide precipitates as cementite. This result indicates that the carbides did not convert into meta-stable carbides during the welding process. The effect of long-term exposure on meta-stable carbides might convert them into cementite during the graphitization process.

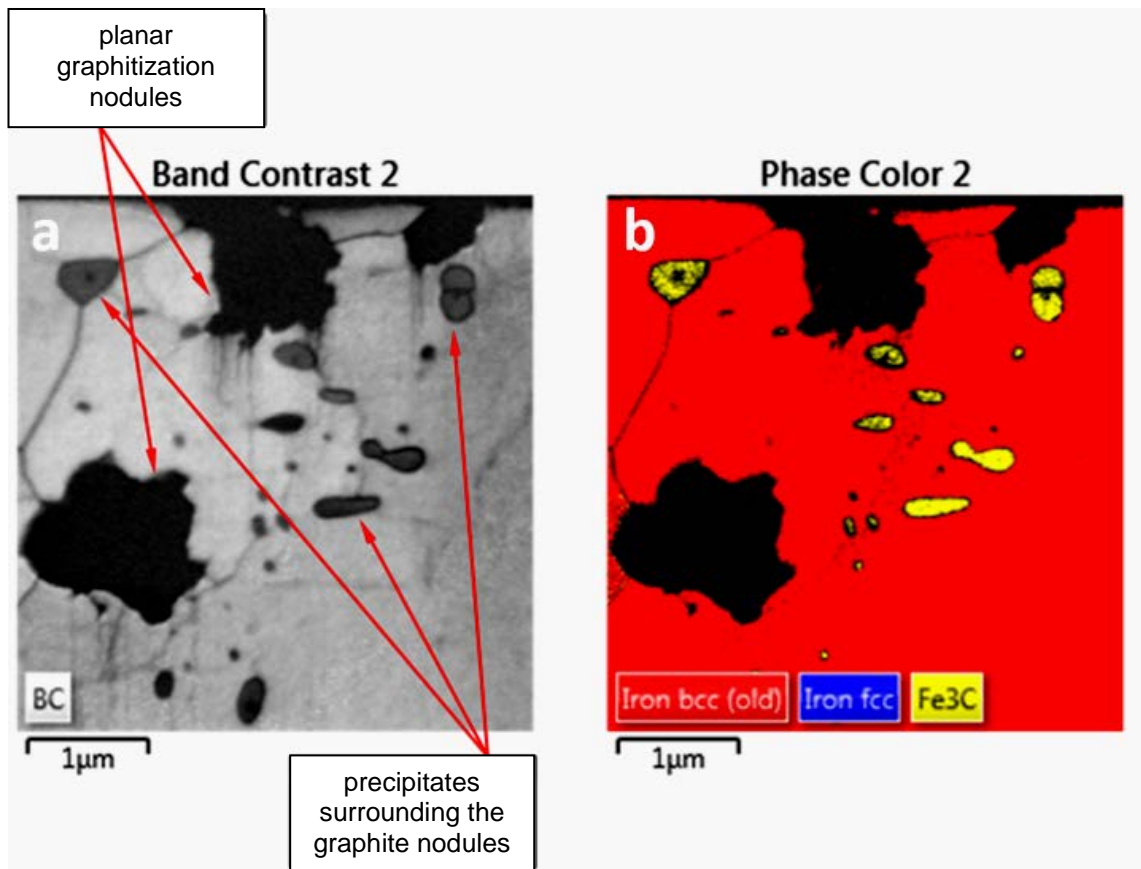


Figure 5-14: TKD analysis done on the TEM with a) the band contrast showing the location of the precipitates and grain boundaries, b) phase map identifying the carbide precipitates as cementite (yellow colored phase).

A second sample was prepared from a region showing no observable graphite on the surface, as shown in **Figure 5-15**, to further investigate the spherical carbide precipitates. ADF-STEM imaging (see **Figure 5-16**) shows the spheroidized carbide precipitates distributed throughout the bulk of the grain. This is most probably a previous pearlite region that converted due to the welding process.

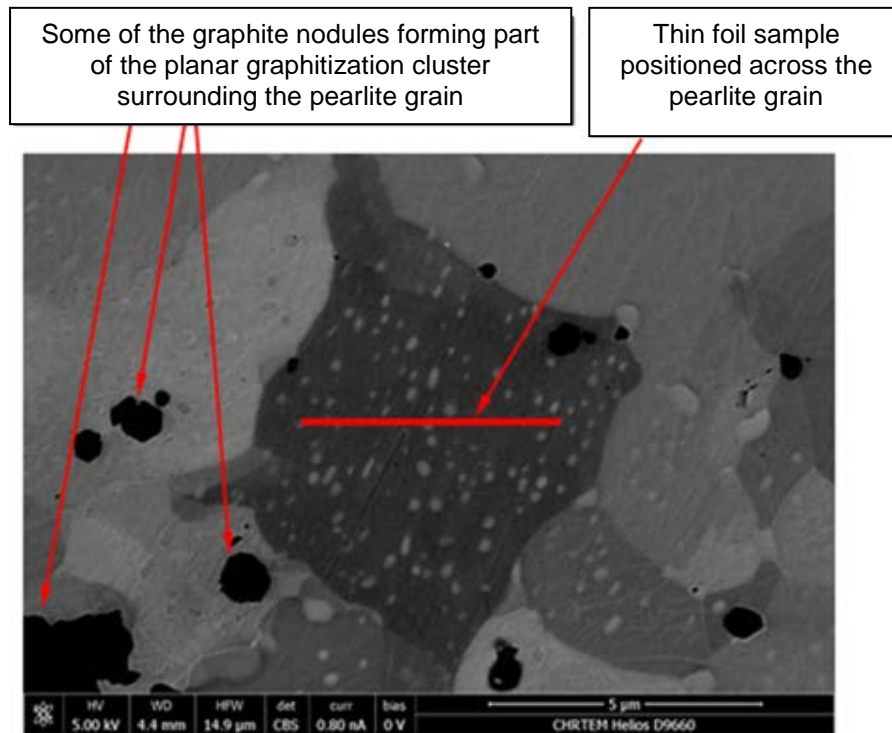


Figure 5-15: BSE SEM image of the second FIB-sample removed from the planar graphitized zone in order to study the spheroidization of the carbide precipitates.

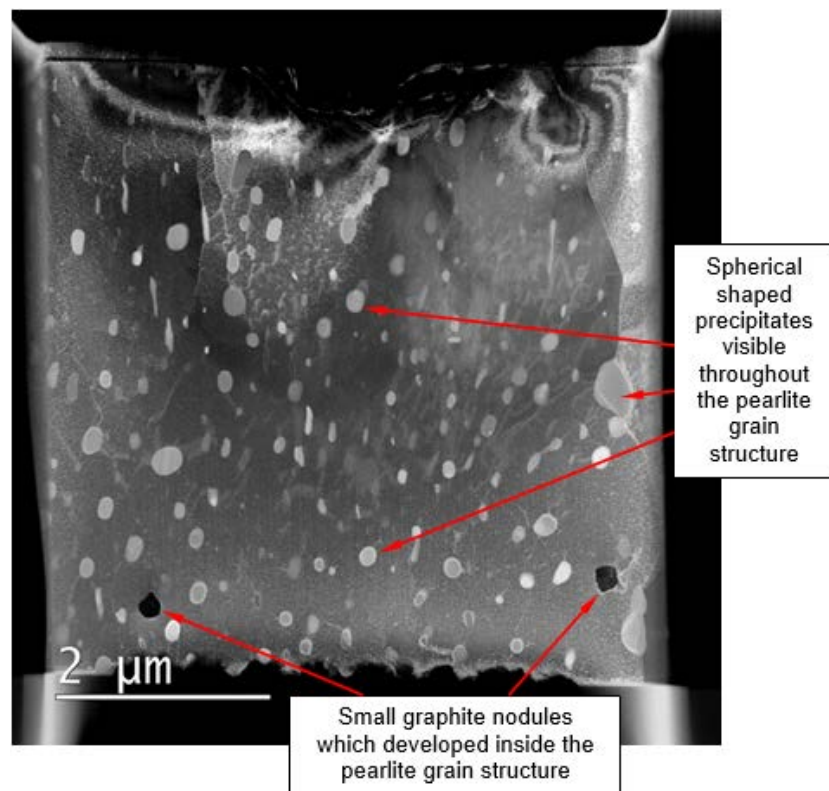


Figure 5-16: ADF-STEM image showing the Carbide precipitates as well as two smaller graphite nodules below the surface of the sample.

TKD analysis was performed on this sample to confirm the crystallographic structure of the carbide precipitates. The carbide precipitates indexed as M_3C (cementite) precipitates in the TKD analysis as shown in **Figure 5-17**. This provides further indication that the Cementite Carbides did not completely dissolve to meta-stable Carbides, if the possible effect of long-term exposure is ignored.

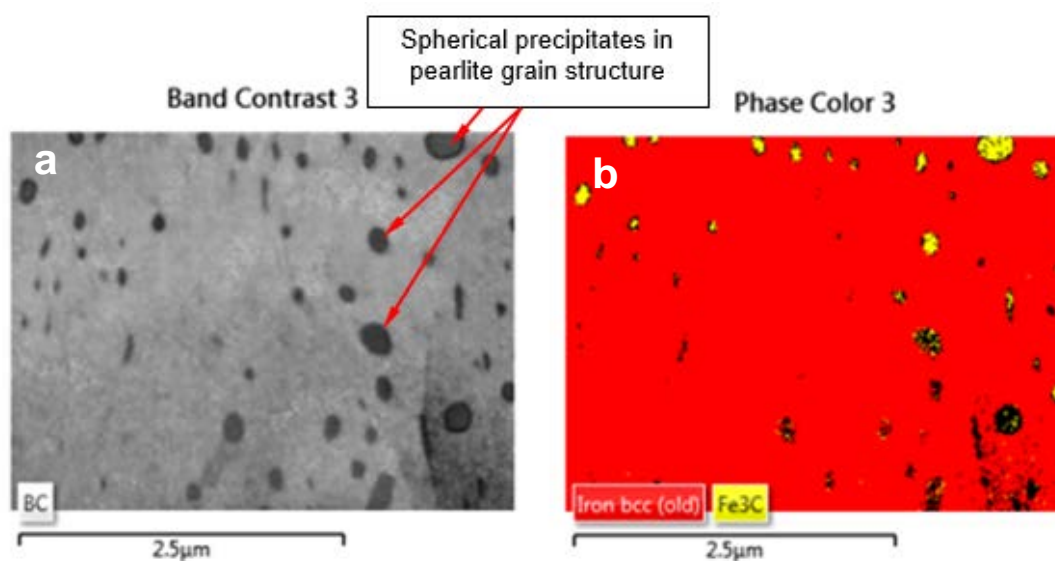


Figure 5-17: TKD analysis performed on the TEM sample showing a) band contrast and b) phase map identified the carbide precipitates as cementite phases

The second FIB-SEM sample shown in **Figure 5-16** also had two smaller graphite nodules (~200 nm in size) which were located below the original sample surface. This was quite fortunate, as this represents an opportunity to investigate the microstructural conditions during graphite nucleation. **Figure 5-18a** and **Figure 5-18b** show higher magnification TEM images of the two graphite nodules. The graphite nodule in **Figure 5-18a** has an Al-containing precipitate (indicated by the arrow) located at the centre as confirmed using spot EDS analysis (see **Appendix F**). The graphite nodule in **Figure 5-18b** shows preferential growth along a dislocation, indicating that dislocations in the material could act as potential growth regions for the graphite nodules.

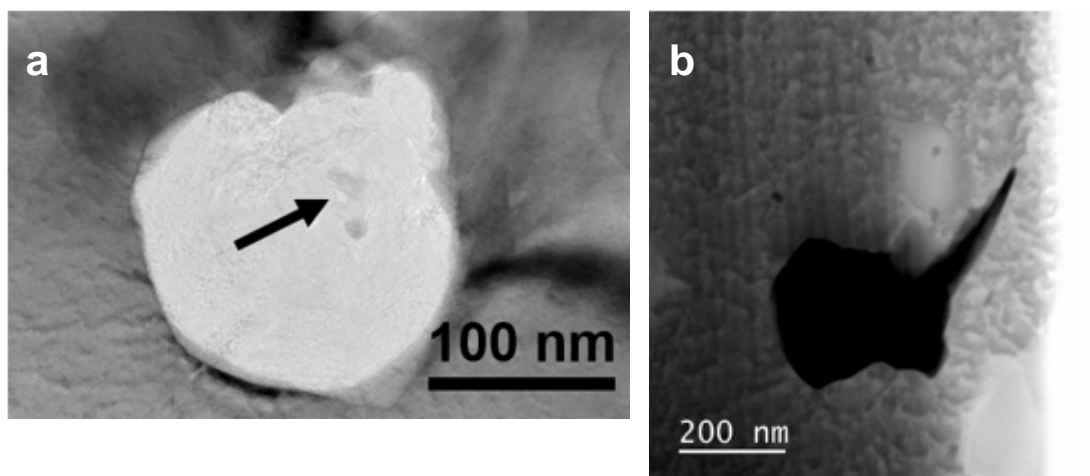


Figure 5-18: a) TEM image of a graphite nodule showing the presence of an Al-containing precipitate (indicated by the arrow) located inside and b) ADF-STEM image of the 2nd graphite nodule showing preferential growth along a particular direction.

Further investigation using ADF-STEM imaging revealed small (~10-20 nm) dark precipitates as shown in **Figure 5-19**. EDS analysis confirmed that these precipitates contained >10 at. % aluminium. Quantification was made difficult because the very small precipitate's signal overlapped with the surrounding iron matrix. No Oxygen was detected in the precipitate, which would rule out it being Al_2O_3 , leaving the possibility of it being an AlN precipitate. This needs to be confirmed through additional analysis.

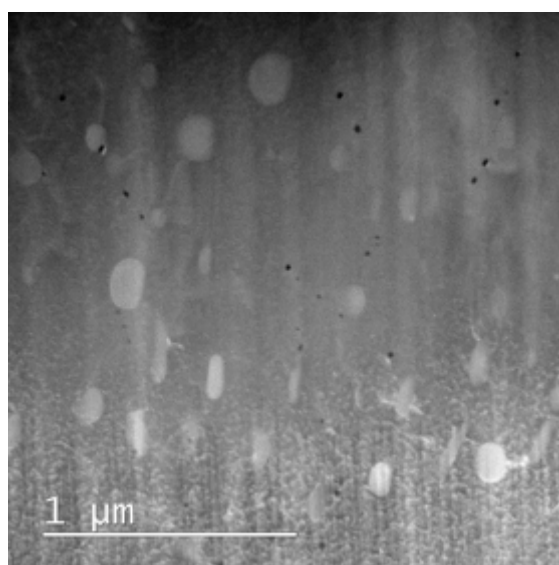


Figure 5-19: ADF-STEM image showing the location of cementite precipitates (bright) and the small Al-precipitates (dark).

5.4.3. Evaluation of Sample D's Microstructure Outside the HAZ

TEM evaluation results of the planar graphitized region of Sample A showed that the microstructure was influenced by the effect of the service exposure as well as the heat input from the multi-pass weld. Sample D on the other hand consisted of a newly introduced weld on the previously service exposed material. This sample was then heat treated using an extended post-weld heat cycle at 600 °C for 2 weeks, in an attempt to investigate the effect of the post-weld cycle on graphite nucleation. Sample D will also provide insight into the effect that welding and post weld heat treatment has on the carbide precipitates without the effect of service exposure.

Figure 5-20 shows the location from which a TEM sample was prepared using the FIB-SEM. This was a region just outside the HAZ of welded Sample D. It is expected that planar graphitization should occur in this region. No noticeable graphite could be seen from the light microscope and SEM investigations. Failure to see the graphite using the TEM would not prove the absence of graphite in this region.

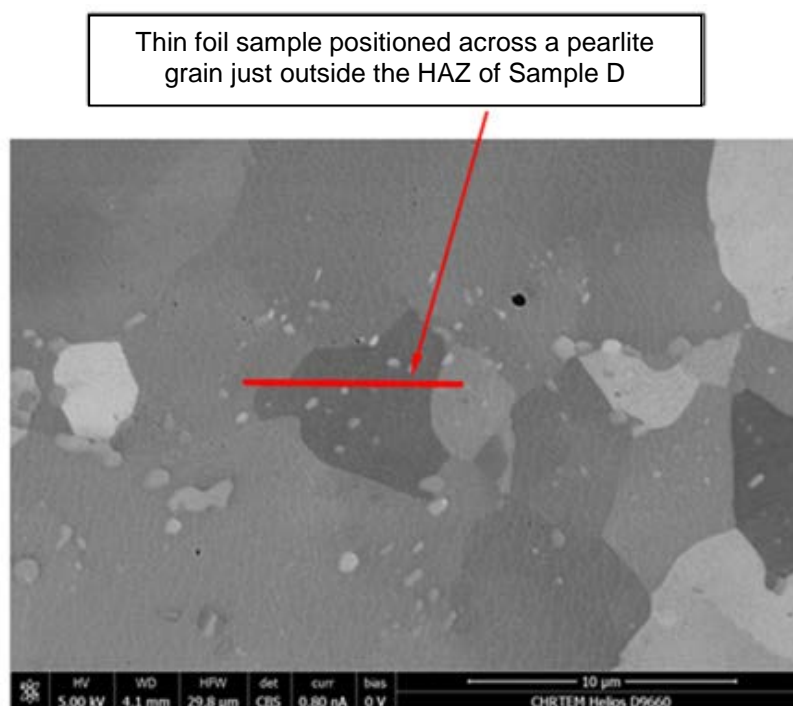


Figure 5-20: BSE SEM image of the FIB-sample taken from the region just outside the HAZ of Sample D.

Figure 5-21 shows the ADF-STEM image of Sample D's thin foil sample prepared with the FIB-SEM, with large carbide precipitates (>500 nm) which was identified as cementite during TKD evaluation (see **Figure 5-22**). This provides further evidence that the cementite particles did not completely dissolve and change into meta-stable carbides to act as favorable carbon sources for graphite nucleation.

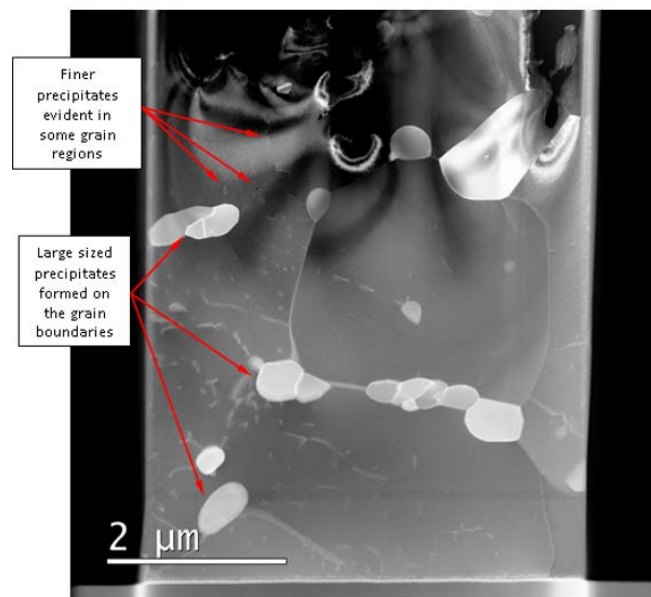


Figure 5-21: ADF-STEM image of Sample D's thin foil sample showing enlarged carbide precipitates located on the grain boundaries.

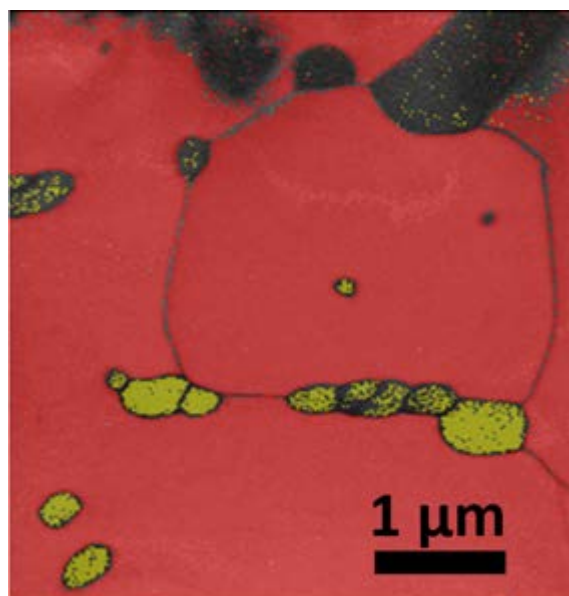


Figure 5-22: Phase map (ferrite: red and (Fe, Mn)₃C; yellow) showing that the precipitates are cementite.

5.5. Summary of Microstructural Evaluation

The *Parent plate* microstructure consisted of a banded microstructure of relatively coarser grained ferrite and finer grained pearlite, with its lamellar structure not being influenced by the service exposure. EBSD analyses of the microstructure revealed the presence of low angle grain boundaries and relatively large local grain misorientations up to 5° in the pearlite regions, while the surrounding ferrite regions was free of any misorientations. TEM investigations revealed that the pearlite regions consisted of lamellar Cementite precipitates in a ferrite matrix with a high dislocation density. Larger Cementite precipitates were also identified on the grain boundaries between the ferrite and pearlite interface. The chemical composition of these precipitates consisted of $(\text{Fe}_{0.69} \text{Mn}_{0.06})_3\text{C}$ as determined using EDS.

The microstructure of the *planar graphitized zone* consisted of the same banded microstructure as the parent material, with the lamellar pearlite structure completely spheroidized just outside the HAZ region. This region also contained numerous planar graphite nodule clusters, which originating from the pearlite bands. EBSD analysis showed that all the ferrite grains surrounding the graphite nodules had numerous low angle grain boundaries with large local grain misorientations up to 5° . This would indicate that the low density graphite caused plastic deformation in the surrounding matrix material.

TEM investigation of the regions which were previously pearlite, showed that the spheroidized carbides have a cementite (M_3C) crystal structure. Graphite nodules were also found in the bulk regions which were previously pearlite. One of the small nodules identified in the bulk region showed evidence of an Al-containing precipitate in its centre. Further evaluation of the bulk region revealed that small dark colored ($\sim 20\text{nm}$) AlN precipitates were distributed throughout the steel. From the graphite nodules investigated using TEM it appears that preferential growth of graphite occurs along high-angle grain boundaries and dislocations.

No graphitization was observed outside the HAZ region of Sample D. This does not prove the absence of graphite but at least it gives insight into the effect of the welding cycle on the carbide dissolution. No higher order carbides were observed in the sample that was investigated; only enlarged spherical carbides consisting of cementite decorated the grain boundaries. The heat input from the welding caused spheroidization of the pearlite structure in the regions located just outside the visible heat affected zone. BSE investigations (not shown) of the parent plate of Sample D showed a lamellar structure of the pearlite. This proves that the spheroidization of the cementite particles can be attributed to the heat input from the welding process and not due to the extended post-weld heat treatment (600°C for 2 weeks). The extended post-weld heat treatment could explain the increase in cementite precipitate size due to particle growth via Ostwald ripening.

The following factors could control the nucleation and growth of graphite in the sample:

- a) Possible AlN precipitates in the bulk region that are closely associated with the cementite precipitates inside the pearlite region could act as heterogeneous nucleation sites for graphite.
- b) Graphite growth will be constrained by the surrounding microstructure which is evident from the plastic deformation of the surrounding ferrite grains. If the chemical driving force for graphite formation is higher than the bulk volumetric misfit energy, graphite nodules will continue to grow, provided that there is sufficient carbon available.
- c) Dislocations and high-angle grain boundaries could provide preferential pathways for vacancy diffusion (space accommodation) and thus explain the preferential growth of the graphite nodules along these microstructural features for the initial stages of growth. It should be noted that the larger nodules are spherical in shape.

Chapter 6 : Discussion of Research Results and Conclusions

6.1. Introduction

In sections 6.2 to 6.7 the results of each of the different evaluation processes are discussed and the conclusions drawn from these results are summarized in section 6.8.

6.2. Discussion of Chemical Evaluation Results of Graphitized Service Exposed Steam Pipe Material and Findings based on these Results

It is evident from the chemical evaluation results that all of the steam pipe samples used in this research project conform to the chemical specification requirements of ASTM A516 Grade 65. Further evaluation of the chemical results revealed noticeable compositional differences between the up and down stream pipe material of the respective samples, specifically with regard to carbon, silicon and aluminium content.

A number of literature sources on graphitization of steam pipe material [10], [11], [12], [19], [21], indicated that deoxidization elements like Al and Si contribute to the formation of graphitization. The effect of these elements on the formation of graphite in the parent material was investigated during this study by plotting the % planar graphitization in relation to the level of aluminium (see **Figure 3-62**) and silicon (see **Figure 3-63**). No correlation could be found between the level of Al and Si and the levels of planar graphitization in the parent pipe material.

6.3. Discussion of the Graphite Nodule Size, Spacing and Percentage Graphitization found to be present in the Evaluated Service Pipe Samples

Evaluation of the macro samples removed from the respective service expose steam pipe samples, revealed the presence of two types of graphitization in the material. The one being randomly distributed graphite nodules which developed in the steam pipe parent material and the second being planar or chain graphite which developed just outside the HAZ on either side of the seam welds.

The two types of graphitization were evaluated across all the pipe samples with regard to size, nearest neighbour spacing and levels of planar graphitization as a percentage. The results indicated that the HAZ region had as smaller median nodule size (see **Figure 3-9**), smaller median nearest neighbour spacing (see **Figure 3-11**) and increased % planar graphitization in comparison to the parent material (see **Figure 3-14**). Variations were also noted in the level of planar graphitization on the different sides of the weldment, but these results need to be interpreted with care considering the limitations of the sampling and measurement methods.

6.4. Discussion of Hardness Evaluation Results of Service Exposed Pipe samples and how the Current Levels of Graphitization Influenced it

The hardness evaluation results of the respective service exposed pipe samples showed a similar trend on all of them, with lower hardnesses being measured on the parent regions where higher levels of planar graphitization were recorded (see **Figure 3-14** and **Figure 3-17** to **Figure 3-19**). Similar observations were made with regard to the hardness data from Pipe Sample A's in depth case study (see **Figure 3-22**) and the corresponding % planar graphitization values recorded for Sample A's parent pipe material as shown in **Figure 3-14**. It was also found that the difference in hardness was influenced by the carbon content of the respective pipe regions, with higher levels of carbon contributing to the formation of more pearlite phase which normally increases the material hardness.

However, during graphitization these pearlite regions are dissolved leading to an expected drop in hardness, which is clearly evident from Sample A's evaluation results that follows.

Sample A's up stream parent material has 12% planar graphitization and a carbon content of 0.161% giving it an average hardness of 145 HV, while the down stream parent material has 28% planar graphitization and a carbon content of 0.113% giving it an average hardness of 131 HV. The difference in hardness is expected, because higher carbon content and lower % planar graphitization would lead to higher measured hardness.

These results indicate that there is a correlation between the level of planar graphitization and the hardness of the material surrounding the planar graphitization, which corresponds to findings reported by Samuels *et al.* [21].

6.5. Discussion of the Yield and Tensile Strength Evaluation Results of Service Exposed Pipe Samples and how the Current Levels of Graphitization Influenced it

The yield and tensile strength evaluation work done in this research project was carried out at room temperature due to lack of elevated temperature tensile testing equipment. The room temperature results were converted to expected yield and tensile strengths at 420°C using the conversion methods of the **API 579-1 Fitness-For-Service** specification. These results were then benchmarked against elevated temperature tensile tests done at 420°C on service exposed material taken from the HAZ of pipe Sample A. This was performed to determine how close the expected mechanical properties were to the actual elevated temperature mechanical properties measured.

This showed that the converted yield strength values were slightly more conservative in comparison to the actual yield strength measurements at 420°C, while the converted tensile strength/ UTS values were found to be higher than the actual tensile strength/ UTS values measured at 420°C.

The majority of the converted yield and tensile strength results still met the mechanical specification requirements for elevated temperature operation with the current levels of planar graphitization. Only pipe Sample C's up stream parent and HAZ yield strength results did not meet the minimum requirement of 168 MPa (see **Figure 3-30** and **Figure 3-31**). **Figure 3-30** also showed that the yield strength of the service exposed pipe material appears to be negatively correlated to the % planar graphitization, it was however found that this correlation was not of statistical significance. Evaluation of the upper tensile strength of the service expose pipe material showed no correlation to the % planar graphitization with a $R^2 = 0.0079$ as shown on **Figure 3-31**.

It was also evident from the converted results that the yield and tensile strengths of the service exposed pipe were close to the minimum specification requirements for steam pipe material operating at 420°C. Further use of the evaluated service exposed steam pipe material would require monitoring of the planar graphitization growth on a regular basis.

The yield and tensile strength results of the tensile samples removed from the parent pipe material and the region just outside the HAZ, on the same side of welded pipe samples, showed no significant difference between the results of the respective pipe regions. This can be attributed to the fact that almost all of the parent and HAZ tensile samples fractured in the parent pipe material, while one of the HAZ tensile samples fractured just outside the HAZ along the intermittent planar graphitization.

Cross sectional samples removed from the evaluated tensile samples indicated that the graphite nodules aid in the formation of elongated micro voids during the tensile testing of the material, more predominately on the side with the highest levels of graphite nodules (see **Figure 3-38** and **Figure 3-39**).

6.6. Discussion of the Charpy Impact Strength Evaluation Results of the Service Exposed Pipe Material and how the Current Levels of Graphitization Influenced it

The Charpy impact evaluation results shown in **Figure 3-51** indicate that all of the samples met and exceeded the minimum impact energy requirement of 27 Joules. The plot show a negative correlation between the impact toughness and the % planar graphitization ($R^2 = 0.63$). This relationship was analyzed further using linear regression analysis and it was found to be of statically significance within the 95% confidence ($p = 0.002$). It should however be noted that the HAZ regions have a different microstructure to the parent material which could have influenced the results.

Planar graphitization % also contributed to the trends seen in the data, specifically with regard to the HAZ regions samples, with Sample D's HAZ region exhibiting significantly higher impact strength due to the absence of planar graphitization in this region. Samples A to C obtained noticeably lower impact strengths due to the embrittling effect of the planar graphitization in the HAZ regions.

Evaluation of the respective regions Charpy impact samples fracture surfaces yielded supporting evidence in the form of ductile shear overload features on the parent impact samples with random graphitization (see **Figure 3-53**). While the impact samples removed from the region just outside the HAZ with planar graphitization exhibited brittle overload features (See **Figure 3-54**). These results correspond to findings reported by Samuels *et al.* [21].

6.7. Discussion of the Microstructural Evaluation Results of Samples A and D obtained using Advanced Electron Microscopy

It was evident from the microstructural evaluation that Sample A's parent material had a banded microstructure with coarse grained ferrite and finer grained pearlite. The pearlite's lamellar structure appeared not to be influenced by the service exposure (see **Figure 5-4**). EBSD analyses done on the banded parent microstructure indicated that the pearlite regions have relatively large local grain misorientations up to 5° , while the surrounding ferrite regions were free of any misorientations (see **Figure 5-8**). Further examination of the parent material in the TEM revealed that large cementite precipitates formed on the grain boundaries between the ferrite and pearlite. The TEM evaluation study also showed that the pearlite has a high dislocation density in between its lamellar cementite precipitates (see **Figure 5-11**).

Sample A's planar graphitization region, just outside the HAZ, exhibited a similar banded microstructure to that of the parent material. It was also found that the planar graphitization clusters in this region coincided with some of the pearlite bands from which they originated as shown in **Figure 5-2** and **Figure 5-7**. EBSD analyses of the ferrite grains surrounding the planar graphite nodules, show that they have numerous low angle grain boundaries with large local grain misorientations up to 5° . This would indicate that the low density graphite caused plastic deformation on the surrounding matrix material (see **Figure 5-9**).

Further evaluation of Sample A's planar graphitization region in the TEM revealed that the carbides completely spheroidized in the previously pearlite grain structure surrounding the planar graphitization (See **Figure 5-16**). TKD analyses done on the planar graphitization region specifically with regards to the previously pearlite regions, indicated that the spheroidized carbides have a cementite (M₃C) crystal structure as shown in **Figure 5-17**.

It was also evident from the TEM evaluation of the planar graphitization, that the graphite nodules develop on the grain boundaries between the ferrite and the previously pearlite regions (see **Figure 5-13**) and in some instances inside the previously pearlite regions as shown in **Figure 5-16**.

One of the small nodules identified in the previously pearlite region showed evidence of an Al-containing precipitate in its centre as shown in **Figure 5-18**. Small dark colored AlN precipitates were also found throughout the previous pearlite region during the TEM evaluation (see **Figure 5-19**).

Sample D's TEM evaluation yielded no evidence of planar graphitization development. This does not prove the absence of planar graphitization. Sample D's TEM evaluation revealed that large spherical Carbides consisting of cementite (see **Figure 5-22**) developed on the grain boundaries as indicate in **Figure 5-21**. The spheroidization of the carbide in the pearlite structure of the evaluated region just outside the visible HAZ, was most probably caused by the heat input from the welding.

6.8. Conclusions Drawn from the Results of the Different Evaluation Processes

The following conclusions can be drawn from the results of the various evaluation processes:

- 1) No correlation could be found between the level of deoxidization elements (Al & Si) and the levels of % planar graphitization in the parent pipe material.
- 2) The graphite nodules in the HAZ region had as smaller median nodule size, smaller median nearest neighbour spacing and increased % planar graphitization compared to the parent material.
- 3) The increased hardness of Sample A up stream parent material (145 HV) relative to the down stream parent material (131 HV) can be attributed to the increased carbon content and lower % planar graphitization.

- 4) The yield and ultimate tensile strength of the service exposed material did not show a statistically significant correlation with the % planar graphitization. The mechanical specification requirements were still met for elevated temperature operation.
- 5) The %planar graphitization had a statistically significant negative correlation with impact toughness measured using Charpy Impact testing. The HAZ regions of service exposed weldments (Sample A – C) had the largest % planar graphitization and the lowest impact toughness. Sample D had no planar graphitization in the region outside the HAZ and had the highest impact toughness. The mechanical specification requirements were still met for the impact toughness.
- 6) The current levels of graphitization did not reduce the ductility of the service exposed pipe material significantly because the majority of the tensile samples failed in a ductile manner.
- 7) No substantiating proof of planar graphitization development in the newly welded service exposed pipe material could be obtained using optical and high end microscopic evaluation methods. This does not rule out the possibility that planar graphitization did in actual fact form.
- 8) The newly introduced seam weld on the service exposed steam pipe material improved the toughness of the pipe material outside the HAZ.
- 9) The free carbon needed for the formation of the planar graphitization outside the HAZ most probably originated from the carbon rich region which formed during the welding of the pipe material, when the cementite inside the pearlite banded structure dissolved.
- 10) The planar graphitization appears to develop preferentially along high angled grain boundaries and in regions where there are high dislocation pile ups.

6.9. Future Work and Recommendations

It is recommended that any future mechanical testing of this steam pipe material be conducted at elevated operating temperature which will give the actual yield and tensile strength of the material eliminating the need for conversion formulas. Another recommendation would be to use image analysis software for future graphite nodule microstructural evaluation work. This will eliminate measuring and evaluation errors with regards to size, spacing and % graphitization and it will also make it possible to evaluate larger areas of the graphitized material accurately.

Future work to supplement this current study would be a computational thermodynamics study on the driving forces for nucleation and growth of graphite, as a function of temperature, time and chemical composition for this steam pipe steel.

References

1. Carbon and Low-Alloy Steel Plate: ASTM Specifications for Pressure Vessel Quality Steel Plate, *Properties and Selection: Irons, Steels, and High Performance Alloys, ASM Handbook, Volume 1*; 2005. pp. 385-398.
2. L.E. Samuels. Low-Carbon Structural Steels, *Optical Microscopy of Carbon Steels*. : ASM International; 1999. pp. 81-85.
3. L.E. Samuels. Ferrite Pearlite Banding. *Optical Microscopy of Carbon Steels*. : ASM International; 1999. pp. 110-118.
4. *Carbon Steel Handbook, EPRI, 10146702007*. Palo Alto, CA; March 2007.
5. H.K.D.H. Bhadeshia. Phase transformations contributing to the properties of modern steels. *Bulletin of The Polish Academy of Sciences*. 2010; 58(2): pp. 255-262.
6. G. Krauss. Solidification, Segregation, and banding in Carbon and Alloy steels. *Metallurgical and Materials transactions B* 2003; 34B: pp. 781-792.
7. R.W.K. Honeycombe; H.K.D.H. Bhadeshia. Weld Microstructures. *Steels Microstructure and Properties*, 2nd ed. : Edward Arnold, a Division of Hodder Headline; 1995. pp. 280-301.
8. Carbon and Low-Alloy Steels: Microstructures, Processing, and properties of steels. *Properties and Selection: Irons, Steels, and High Performance Alloys, ASM Handbook, Volume 1*; 2005. pp. 211-213.
9. Fusion and Heat affected zones in multipass Weldments. *Welding, Brazing and Soldering, ASM Handbook, Volume 6*; 2005. pp. 205-210.
10. H.C. Furtado. Graphitization in Low alloy steel Pressure Vessel and Piping. *Failure Analysis and Prevention* 2011; 11: pp. 3-9.
11. J.R. Foulds; R. Viswanathan. Graphitization of Steels in Elevated-Temperature Service. *Materials Engineering and Performance* 2001; 10(4): pp. 484-492.
12. C.J. Moss; J.L. Davidson. Graphitization in Type 201 Carbon Steel in Petro-Chemical plant after long Term Service. *Materials Forum* 1993; 17: pp. 351-359.

13. J.G. Wilson. Graphitization of Steel in Petroleum Refining Equipment. *Welding Research Council Bulletin Series* 1957; 32: pp. 1-22.
14. J.R. Foulds; J.P. Shingledecker. An Updated Assessment of Graphitization of Steels in Elevated Temperature Service. *Materials Engineering and Performance* 2015; 24(2): pp. 586-597.
15. Graphitization. *Failure Analysis and Prevention, ASM Handbook, Volume 11*; 2002.
16. M. Bharadwaj. *Study of Graphitization in Carbon Steel Weldments for Remaining Life Assessment*. Tennessee: University of Tennessee; 2016
17. O.P. Ostash. Structural Microdamageability of steels of the Steam Pipelines of thermal Power Plants. *Material Science* 2009; 45(3): pp. 340-349.
18. A.A. Baranov. Effect of Plastic Strain on Graphitization of Steel. *Metallurgical Institute*: pp. 17-19.
19. J. Yang. *Influence of Graphitization on phase transformation kinetics and mechanical properties of low alloy steels*. Oregon: Oregon Heath & Science University; 1999.
20. A. Inam; R. Brydson; D.V. Edmonds. Effect of starting microstructure upon the nucleation sites and distribution of graphite particles during Graphitizing anneal of an experimental medium-carbon machining steel. *Materials Characterization* 2015; 106: pp. 86-92.
21. L.E. Samuels. Graphitization at Subcritical Temperatures. *Light Microscopy of Carbon Steels*. : ASM International; 1999. pp. pp. 176-183.
22. *Scanning Electron Microscope A to Z*. : Jeol; 2005.
23. B. Hafner. *Scanning Electron Microscopy Primer*. : Characterization Facility, University of Minnesota-Twin Cities; 2015; pp. 1-28.
24. J. Mabon. Scanning Electron Microscopy (SEM) and Focused Ion Beams (FIB) in Materials research. 2012; pp. 1-61.
25. G.E. Lloyd. *Mineralogical Magazine* 1987; 51: pp. 3-19.
26. B. Hafner. *Energy Dispersive Spectroscopy on the SEM: A Primer* : Characterization Facility, University of Minnesota-Twin Cities; 2015.
27. W. Zhou. Electron Backscatter Diffraction (EBSD) Technique and Materials Characterization Examples. *Scanning Microscopy for Nanotechnology Techniques and Applications*. 2007; pp. 41-75.

28. K. Dicks. *Introduction to EBSD*. : Oxford Instruments Analytical; 2003; pp. 1-63.
29. R. Keller; R. Geiss. Transmission Kikuchi Diffraction in Scanning Electron Microscope. *National Institute of Standards and Technology*; 2013.
30. M. Cantoni. Scanning Transmission Electron Microscopy. *MSE-603*; 2013.

Appendix A

graphitization evaluation results of the different service expose pipe samples with regards to graphite spacing, size and % graphitization

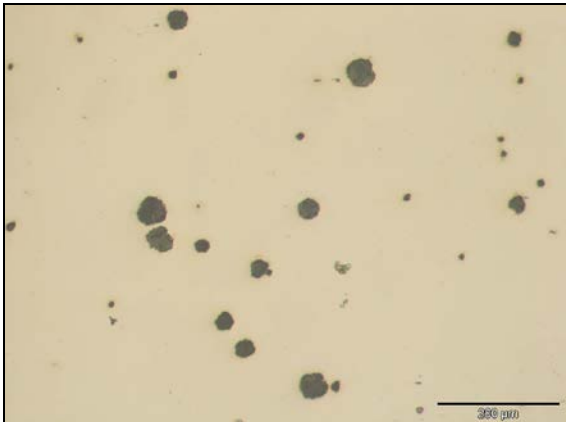
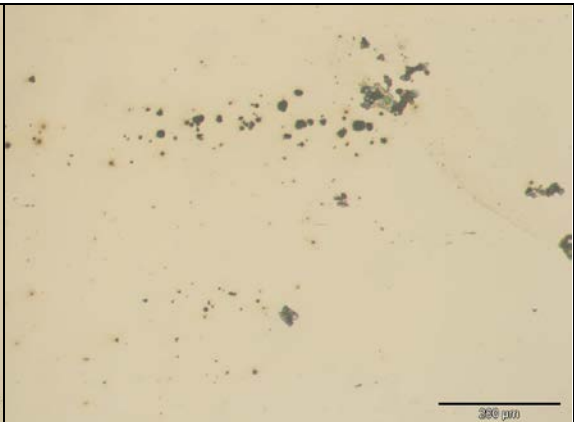
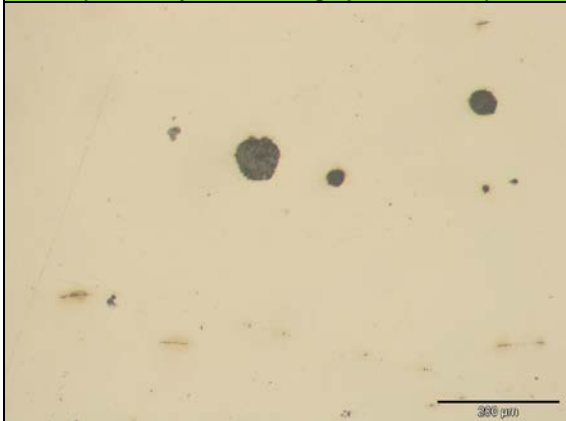
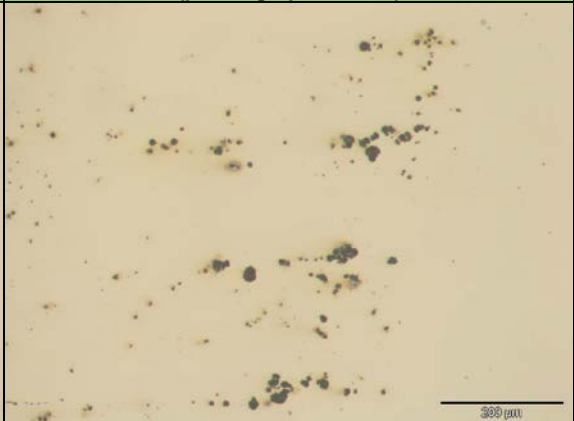
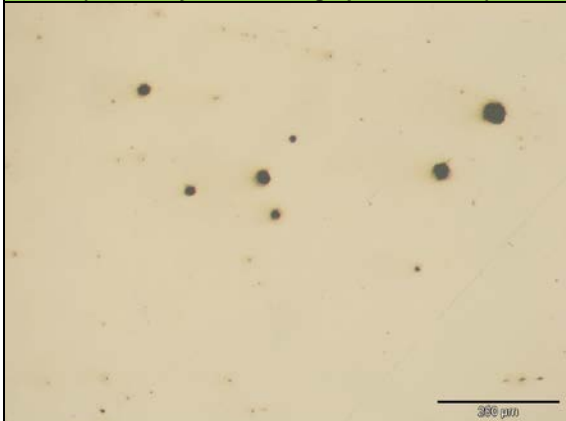
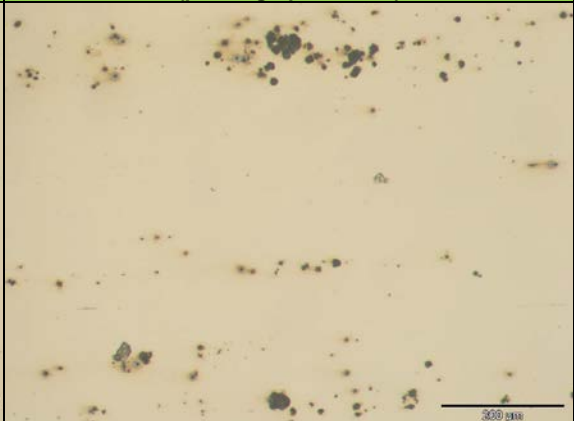
Sample A graphitization evaluation results for the various pipe regions						
Pipe regions evaluated	Up stream parent			Up stream Outside HAZ		
	Outer	Center	Inner	Outer	Center	Inner
Shape	Random Nodules	Random Nodules	Random Nodules	planar graphite	planar graphite	planar graphite
Spacing (µm)	382 - 513	230 - 313	426	0 - 139.0	0 - 52.12	0 - 295.3
Size (µm)	12.98 - 21.03	8.95 - 42	12.98 - 22.37	9.40 - 22.37	9.40 - 23.17	8.05 - 30.87
% graphitization	12.5	13	11	45	57	31
Average % graphitization	12.2			44		
Pipe regions evaluated	Down stream parent			Down stream outside HAZ		
	Outer	Center	Inner	Outer	Center	Inner
Shape	Random Nodules	Random Nodules	Random Nodules	planar graphite	planar graphite	planar graphite
Spacing (µm)	17.55 - 272.65	82.8 - 292.1	48.53 - 256.39	0 - 187.3	0 - 84.19	0 - 230.2
Size (µm)	8.05 - 48.32	11.63 - 72.93	12.98 - 38.93	10.29 - 28.19	7.16 - 34	9.40 - 38.93
% graphitization	44	22.2	17.5	52	54	64
Average % graphitization	28.2			57		

Sample B graphitization evaluation results for the various pipe regions						
Pipe regions evaluated	Up stream parent			Up stream Outside HAZ		
	Outer	Center	Inner	Outer	Center	Inner
Shape	Random Nodules	Random Nodules	Random Nodules	planar graphite	planar graphite	planar graphite
Spacing (µm)	50.72 - 458	80.12 - 374.39	164.16 - 351.13	0 - 201.46	0 - 181.2	0 - 83.93
Size (µm)	8.05 - 39.82	8.05 - 71.59	4.92 - 39.82	7.16 - 35.35	9.40 - 31.77	8.05 - 59.06
% graphitization	21.2	28.2	18.4	49	56	93
Average % graphitization	22.6			66		
Pipe regions evaluated	Down stream parent			Down stream outside HAZ		
	Outer	Center	Inner	Outer	Center	Inner
Shape	Random Nodules	Random Nodules	Random Nodules	planar graphite	planar graphite	planar graphite
Spacing (µm)	22.84 - 377.9	40.50 - 447.92	7.07 - 331.79	0 - 448.12	0 - 255.91	0 - 210.11
Size (µm)	8.50 - 48.32	11.63 - 44.74	6.71 - 43.85	8.05 - 23.71	7.16 - 21.48	8.05 - 52.80
% graphitization	19.3	20	21	37	55	34
Average % graphitization	20.1			42		

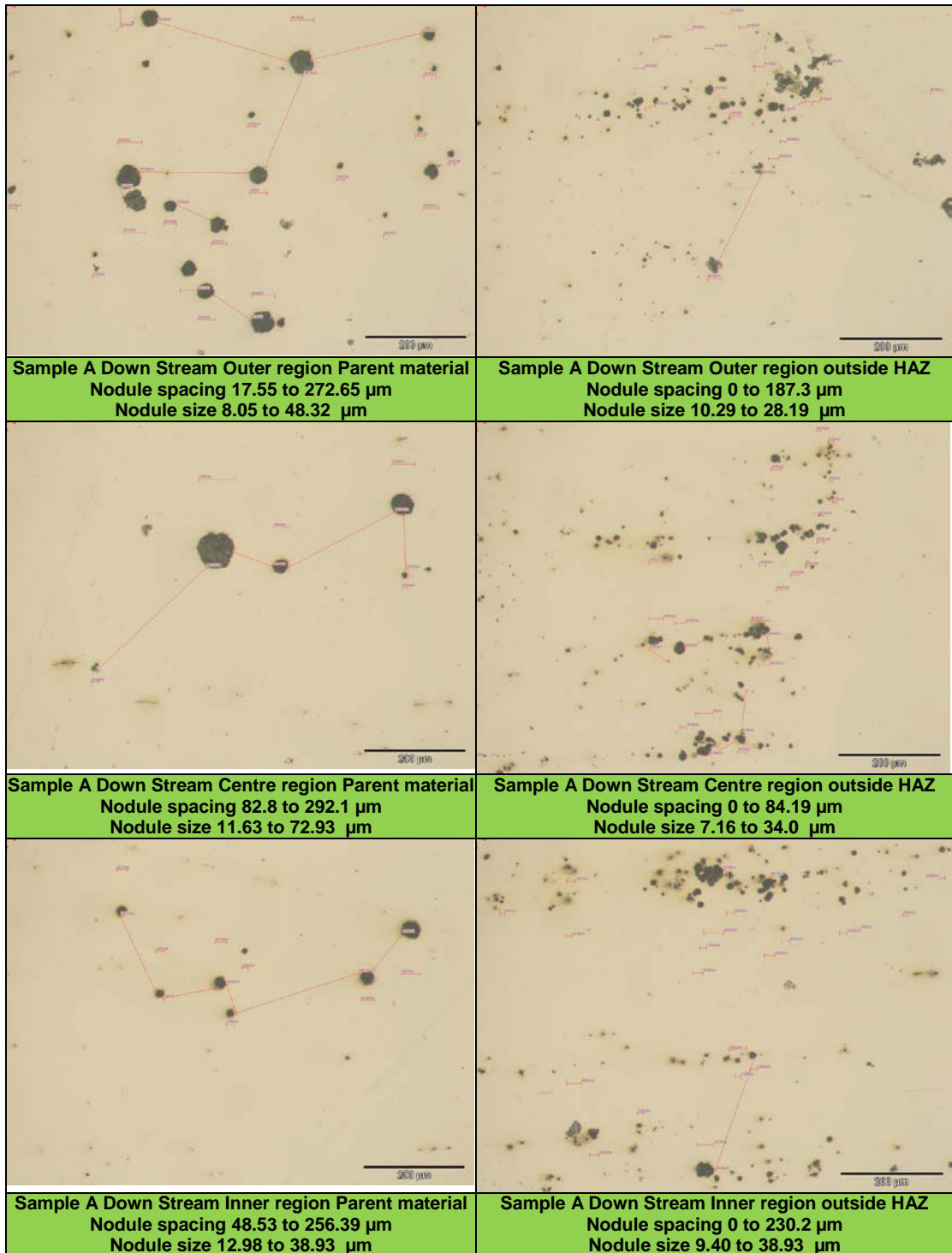
Sample C graphitization evaluation results for the various pipe regions						
Pipe regions evaluated	Up stream parent			Up stream Outside HAZ		
	Outer	Center	Inner	Outer	Center	Inner
Shape	Random Nodules	Random Nodules	Random Nodules	planar graphite	planar graphite	planar graphite
Spacing (μm)	13.94 - 323.8	109.5 - 263.6	14.32 - 393.91	0 - 347.6	0 - 192.77	0 - 296.66
Size (μm)	7.16 - 37.58	15.66 - 36.24	5.82 - 54.14	6.71 - 44.74	6.26 - 34.45	8.50 - 36.24
% graphitization	33.4	29.3	42.7	64	59	64
Average % graphitization	35.1			62		
Pipe regions evaluated	Down stream parent			Down stream outside HAZ		
	Outer	Center	Inner	Outer	Center	Inner
Shape	Random Nodules	Random Nodules	Random Nodules	planar graphite	planar graphite	planar graphite
Spacing (μm)	124.34 - 299.16	79.55 - 386.38	456.2	0 - 291.9	0 - 282.9	30.10 - 438
Size (μm)	15.21 - 37.58	9.40 - 41.61	29.08 - 31.77	9.40 - 30.43	5.82 - 29.53	7.16 - 11.63
% graphitization	21.4	18.3	13	30	37	30
Average % graphitization	17.6			32		

Sample D graphitization evaluation results for the various pipe regions						
Pipe regions evaluated	L/H side parent			L/H side Outside HAZ		
	Outer	Center	Inner	Outer	Center	Inner
Shape	Random Nodules	Random Nodules	Random Nodules	None	None	None
Spacing (μm)	35.58 - 347.36	55.47 - 433.18	42.07 - 404.23	None	None	None
Size (μm)	6.26 - 57.72	7.16 - 59.06	7.16 - 24.61	None	None	None
% graphitization	41	39	34	None	None	None
Average % graphitization	38			None		
Pipe regions evaluated	R/H side parent			R/H side outside HAZ		
	Outer	Center	Inner	Outer	Center	Inner
Shape	Random Nodules	Random Nodules	Random Nodules	None	None	None
Spacing (μm)	32.57 - 248.86	18.26 - 388.99	65.33 - 546.53	None	None	None
Size (μm)	7.16 - 21.03	8.05 - 44.74	5.82 - 29.53	None	None	None
% graphitization	30	27	14.4	None	None	None
Average % graphitization	23.8			None		

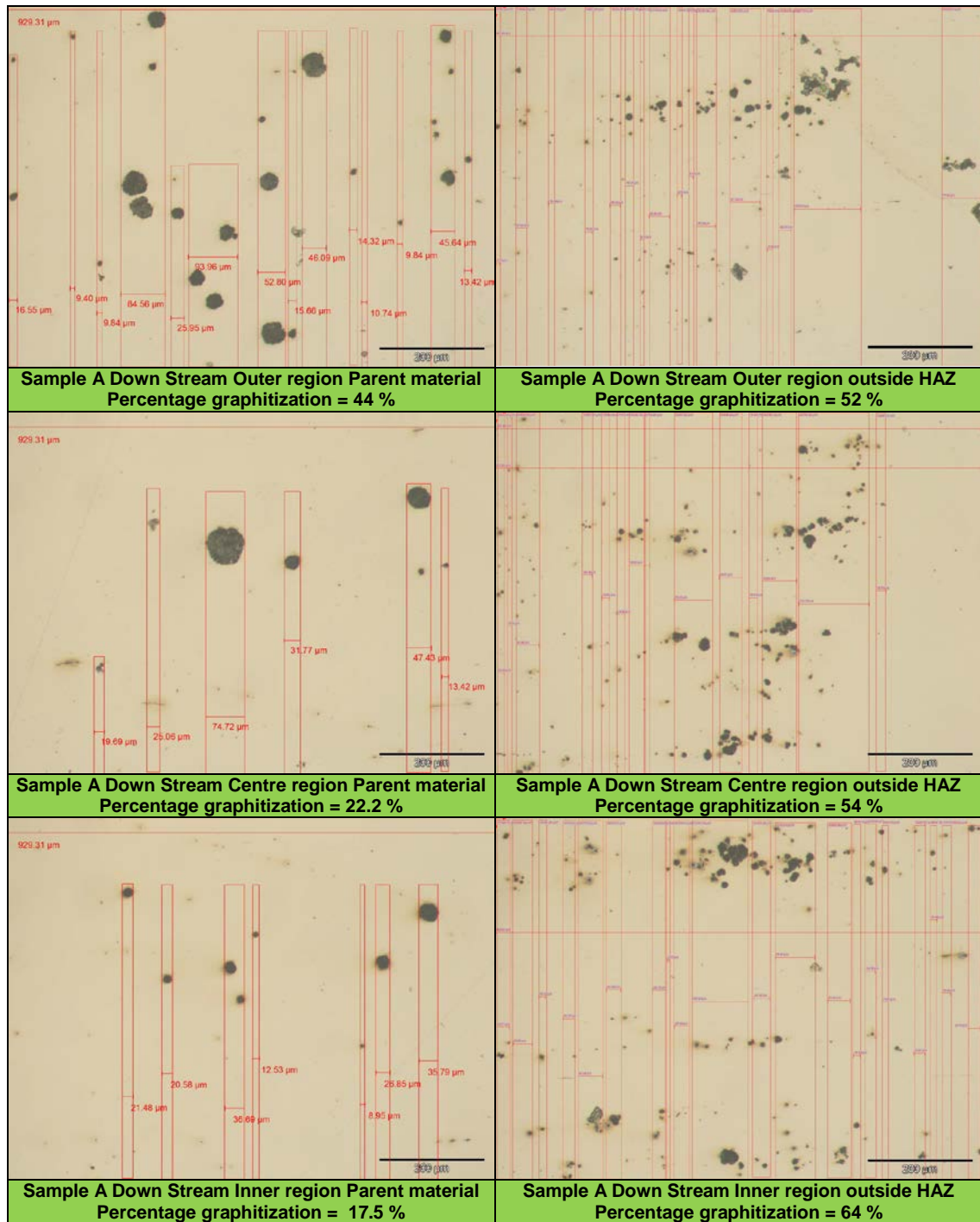
Sample A's Down stream parent and HAZ micrographs of different regions used for the graphite evaluation (Shown as example)

	
<p>Sample A Down Stream Outer region Parent material (Randomly distributed graphite nodules)</p>	<p>Sample A Down Stream Outer region outside HAZ (planar graphitization)</p>
	
<p>Sample A Down Stream Centre region Parent material (Randomly distributed graphite nodules)</p>	<p>Sample A Down Stream Centre region outside HAZ (planar graphitization)</p>
	
<p>Sample A Down Stream Inner region Parent material (Randomly distributed graphite nodules)</p>	<p>Sample A Down Stream Inner region outside HAZ (planar graphitization)</p>

Sample A's Down stream parent and HAZ micrographs of different regions evaluated with regards to graphite nodule size and spacing (Shown as example)



Example of parent and HAZ micrographs of different regions evaluated with regards to Percentage planar graphitization:



Appendix B

Vickers Micro Hardness evaluation results for the respective service exposed pipe samples

Sample A Vickers Micro hardness evaluation results								
Hardness measurement	Up Stream				Down Stream			
	Outer region's hardness (HV0,3)	Centre region's hardness (HV0,3)	Inner region's hardness (HV0,3)	Average hardness (HV0,3)	Outer region's hardness (HV0,3)	Centre region's hardness (HV0,3)	Inner region's hardness (HV0,3)	Average hardness (HV0,3)
1	138	131	133	133	137	131	133	134
2	125	132	125	127	127	138	136	134
3	132	125	129	129	129	122	143	131
4	142	130	130	134	129	124	141	131
5	140	131	133	135	132	128	132	130
6	143	132	128	134	131	145	119	132
7	141	138	122	134	128	120	128	124
8	151	148	125	141	138	122	130	130
9	155	139	134	143	131	126	137	131
10	160	156	140	152	140	136	125	134
11	161	141	130	144	128	139	125	131
12	169	137	130	145	128	134	133	131
13	158	147	134	146	138	127	131	132
14	145	133	123	134	129	122	127	126
15	140	143	135	139	138	120	128	128
16	136	139	145	140	130	131	129	130
17	178	134	147	153	139	132	139	136
18	186	117	156	153	143	138	136	139
19	190	139	176	168	134	141	148	141
20	174	143	181	166	142	138	167	149
21	174	179	183	178	168	142	168	159
22	170	186	181	179	151	138	178	156
23	177	185	164	175	150	177	159	162
24	172	166	156	165	153	187	160	167
25	193	167	170	177	168	184	168	173
26	188	161	174	174	163	178	167	169
27	181	166	187	178	179	180	180	180
28	177	164	168	170	178	173	181	177
29	184	152	178	171	193	178	173	181
30	199	158	183	180	180	177	160	172

Color coded pipe regions
Parent material
HAZ (Heat Affected Zone) material
Seam Weld material

Sample B Vickers Micro hardness evaluation results								
Hardness measurement	Up Stream				Down Stream			
	Outer region's hardness (HV0,3)	Centre region's hardness (HV0,3)	Inner region's hardness (HV0,3)	Average hardness (HV0,3)	Outer region's hardness (HV0,3)	Centre region's hardness (HV0,3)	Inner region's hardness (HV0,3)	Average hardness (HV0,3)
1	132	129	127	129	133	128	150	137
2	131	129	129	130	140	128	141	136
3	131	122	130	128	129	105	143	126
4	132	119	130	127	144	133	137	138
5	130	121	131	127	138	134	143	138
6	131	119	132	127	128	133	143	135
7	124	123	132	127	122	141	149	137
8	131	123	129	128	140	138	142	140
9	129	123	143	132	141	136	137	138
10	125	128	140	131	142	138	138	140
11	128	125	142	131	143	136	139	139
12	132	121	145	133	150	145	146	147
13	136	126	147	136	159	142	142	148
14	127	127	132	129	189	147	147	161
15	131	128	140	133	148	148	144	147
16	131	134	146	137	151	148	143	147
17	135	129	143	136	147	138	146	144
18	136	130	147	138	159	145	145	150
19	137	133	149	140	151	150	152	151
20	145	135	145	141	147	154	156	152
21	146	126	145	139	153	157	152	154
22	144	133	142	140	152	163	167	160
23	146	132	140	139	142	148	165	152
24	143	141	162	148	148	149	172	156
25	141	140	183	155	151	150	177	159
26	145	143	179	155	150	161	186	166
27	140	149	175	155	150	179	192	174
28	141	169	186	165	148	166	178	164
29	171	199	182	184	151	165	182	166
30	162	186	182	177	146	163	191	167

Color coded pipe regions
Parent material
HAZ (Heat Affected Zone) material
Seam Weld material

Sample C Vickers Micro hardness evaluation results								
Hardness measurement	Up Stream				Down Stream			
	Outer region's hardness (HV0,3)	Centre region's hardness (HV0,3)	Inner region's hardness (HV0,3)	Average hardness (HV0,3)	Outer region's hardness (HV0,3)	Centre region's hardness (HV0,3)	Inner region's hardness (HV0,3)	Average hardness (HV0,3)
1	132	150	120	134	130	131	141	134
2	140	145	130	138	133	130	146	137
3	140	142	127	136	134	129	139	134
4	138	133	121	131	140	129	135	135
5	135	134	124	131	133	128	145	135
6	140	132	117	130	143	132	137	137
7	134	135	125	131	147	129	138	138
8	133	131	122	129	142	130	143	139
9	141	136	126	134	149	132	145	142
10	132	131	118	127	141	139	152	144
11	140	132	124	132	144	130	147	140
12	141	138	121	133	138	129	135	134
13	141	134	135	137	136	132	146	138
14	136	138	129	135	133	143	146	141
15	136	132	132	133	143	131	145	139
16	141	130	138	136	136	143	145	141
17	143	143	147	144	140	138	159	146
18	135	145	146	142	138	143	170	150
19	145	161	150	152	140	156	162	153
20	140	168	166	158	132	138	177	149
21	145	184	204	178	133	142	191	155
22	151	192	202	182	135	141	209	162
23	156	198	198	184	142	142	208	164
24	175	192	196	188	141	146	212	166
25	163	195	206	188	150	165	215	176
26	153	191	207	184	163	180	201	181
27	163	185	204	184	169	181	204	185
28	140	181	196	172	180	174	218	191
29	141	181	197	173	200	169	209	193
30	142	178	197	172	185	175	208	189

Color coded pipe regions
Parent material
HAZ (Heat Affected Zone) material
Seam Weld material

Sample D Vickers Micro hardness evaluation results								
Hardness measurement	LH Side				RH Side			
	Outer region's hardness (HV0,3)	Centre region's hardness (HV0,3)	Inner region's hardness (HV0,3)	Average hardness (HV0,3)	Outer region's hardness (HV0,3)	Centre region's hardness (HV0,3)	Inner region's hardness (HV0,3)	Average hardness (HV0,3)
1	140	129	140	136	133	130	141	134
2	139	128	133	133	143	135	143	141
3	141	135	144	140	138	148	138	141
4	133	128	149	137	140	134	145	140
5	134	129	152	138	136	126	134	132
6	132	122	151	135	140	128	140	136
7	138	131	142	137	135	136	141	137
8	141	133	150	141	146	141	144	143
9	136	150	150	145	142	139	139	140
10	144	137	147	143	139	137	141	139
11	154	130	142	142	132	129	141	134
12	152	131	149	144	140	130	142	137
13	147	145	150	147	149	117	139	135
14	145	147	149	147	145	133	146	141
15	146	141	152	146	147	153	143	148
16	151	145	146	147	164	152	154	157
17	167	163	153	161	187	150	160	165
18	166	167	153	162	176	143	158	159
19	168	191	152	170	210	162	163	178
20	166	172	192	177	196	161	181	179
21	196	182	196	191	209	167	177	184
22	184	175	174	178	192	177	167	179
23	188	167	189	182	205	180	206	197
24	195	177	207	193	213	191	204	203
25	185	169	186	180	218	181	204	201
26	194	175	187	185	213	192	198	201
27	180	175	178	178	204	189	211	201
28	169	159	186	171	215	196	209	207
29	173	177	185	178	209	187	211	203
30	171	168	186	175	193	209	206	203

Color coded pipe regions
Parent material
HAZ (Heat Affected Zone) material
Seam Weld material

In depth Vickers micro hardness evaluation data of Sample A's centre region

In Depth hardness study's Vickers Micro Hardness evaluation data of Sample A's Up Stream Centre region						
Hardness measurement	Hardness Profile line 1 (HV0,3)	Hardness Profile line 2 (HV0,3)	Hardness Profile line 3 (HV0,3)	Hardness Profile line 4 (HV0,3)	Hardness Profile line 5 (HV0,3)	Average Hardness (HV0,3)
1	141	141	152	151	145	146
2	139	140	160	160	167	153
3	133	141	146	154	166	148
4	143	137	166	144	160	150
5	143	137	154	154	170	152
6	133	154	145	153	159	149
7	138	155	151	151	157	150
8	142	161	140	144	153	148
9	153	156	130	135	156	146
10	147	145	134	132	150	142
11	160	143	137	135	167	148
12	147	142	135	136	155	143
13	149	129	146	136	173	147
14	141	140	144	143	153	144
15	145	137	152	152	150	147
16	140	145	157	147	149	148
17	134	142	158	150	145	146
18	130	142	144	140	145	140
19	135	144	146	145	159	146
20	130	164	134	136	162	145
21	148	150	137	133	152	144
22	145	142	144	140	146	144
23	153	147	133	135	161	146
24	154	155	143	153	157	152
25	152	156	141	134	137	144
26	148	154	137	143	170	151
27	177	158	120	158	161	155
28	175	163	164	171	163	167
29	172	159	172	163	163	166
30	171	159	167	171	221	178
31	160	171	171	169	163	167
32	170	178	169	171	165	171
33	168	177	164	163	169	168
34	178	169	162	156	176	168
35	193	164	159	170	180	173
36	176	171	156	160	172	167
37	170	166	166	156	182	168
38	173	154	165	163	189	169
39	165	170	163	166	173	167
40	164	168	163	159	157	162
41	173	157	157	160	178	165
42	168	160	165	154	173	164
43	164	167	165	162	181	168
44	159	160	165	164	179	165
45	161	168	158	151	196	167
46	166	169	159	171	178	169
47	168	163	165	174	195	173
48	181	155	167	181	198	176
49	167	165	155	183	192	172
50	168	166	167	185	191	175
51	171	171	164	177	197	176
52	178	174	157	202	201	182
53	175	160	193	214	171	183
54	182	179	196	213	165	187
55	162	163	195	175	150	169

In Depth hardness study's Vickers Micro Hardness evaluation data of sample A's Down Stream Centre region						
Hardness measurement	Hardness Profile line 1 (HV0,3)	Hardness Profile line 2 (HV0,3)	Hardness Profile line 3 (HV0,3)	Hardness Profile line 4 (HV0,3)	Hardness Profile line 5 (HV0,3)	Average Hardness (HV0,3)
1	129	120	124	137	119	126
2	128	131	122	153	127	132
3	143	112	134	133	137	132
4	151	117	134	129	130	132
5	136	127	126	128	130	129
6	126	121	126	131	135	128
7	131	137	133	134	129	133
8	121	125	121	129	129	125
9	125	126	123	123	139	127
10	125	125	125	125	138	128
11	128	129	130	127	138	131
12	130	127	132	131	136	131
13	123	133	122	137	128	129
14	132	126	122	129	131	128
15	141	136	128	117	136	131
16	143	132	130	124	135	133
17	133	149	120	137	128	134
18	144	143	142	126	137	138
19	142	136	137	118	132	133
20	135	135	142	125	134	134
21	128	129	126	129	134	129
22	133	127	117	132	124	127
23	141	124	121	129	122	127
24	148	126	120	134	129	131
25	129	122	127	120	134	126
26	139	133	126	123	119	128
27	143	146	143	122	123	135
28	144	142	136	137	156	143
29	128	142	151	144	143	142
30	130	154	156	151	145	147
31	142	152	170	150	196	162
32	145	168	180	170	184	170
33	185	168	174	236	184	189
34	165	165	179	176	190	175
35	162	173	175	189	182	176
36	168	163	170	185	189	175
37	172	163	175	191	195	179
38	170	168	170	185	186	176
39	162	170	170	194	195	178
40	159	168	163	177	181	170
41	167	164	165	187	177	172
42	174	168	178	189	175	177
43	163	116	168	180	171	160
44	166	166	167	182	164	169
45	160	167	196	187	162	174
46	165	161	180	186	171	173
47	164	157	182	194	170	173
48	167	163	180	181	177	173
49	160	159	190	167	174	170
50	155	167	181	171	167	168
51	163	159	164	172	172	166
52	156	182	178	161	161	168
53	175	167	170	174	154	168
54	155	158	161	165	161	160
55	175	168	156	166	158	164

Appendix C

Converted yield strength evaluation results of respective service exposed pipe samples

Sample & Pipe region evaluated	Minimum Yield strength req. of ASTM A516 Gr 65 (MPa) at room temp. of 25 °C	Yield strength at room temp (MPa)	Yield strength at 420 °C (MPa) (API 579-1 Table F.2)	Yield strength at 420 °C (MPa) (API 579-1 Table F.6)	Minimum Yield strength req. of ASTM A516 Gr 65 (MPa) at 420 °C
SAMPLE A PM T1 Up Stream	240,0	270,6	189,5	167,4	168,0
SAMPLE A PM T2 Up Stream	240,0	283,0	198,1	175,1	168,0
SAMPLE A PM T3 Up Stream	240,0	271,2	189,9	167,8	168,0
SAMPLE A PM T1 Down Stream	240,0	279,1	195,4	172,7	168,0
SAMPLE A PM T2 Down stream	240,0	275,6	192,9	170,5	168,0
SAMPLE A PM T3 Down Stream	240,0	281,8	197,3	174,3	168,0
SAMPLE A OHAZ T1 Down Stream	240,0	283,2	198,3	175,2	168,0
SAMPLE A OHAZ T2 Down stream	240,0	283,2	198,3	175,2	168,0
SAMPLE A OHAZ T3 Down Stream	240,0	277,2	194,1	171,5	168,0
SAMPLE B PM T1 Up Stream	240,0	284,9	199,5	176,3	168,0
SAMPLE B PM T2 Up Stream	240,0	294	205,8	181,9	168,0
SAMPLE B PM T3 Up Stream	240,0	284,2	199,0	175,8	168,0
SAMPLE B PM T1 Down Stream	240,0	293,4	205,4	181,5	168,0
SAMPLE B PM T2 Down Stream	240,0	297,9	208,6	184,3	168,0
SAMPLE B PM T3 Down Stream	240,0	297,9	208,6	184,3	168,0
SAMPLE B OHAZ T1 Up Stream	240,0	281,83	197,3	174,4	168,0
SAMPLE B OHAZ T2 Up Stream	240,0	286,83	200,8	177,5	168,0
SAMPLE B OHAZ T3 Up Stream	240,0	280,62	196,5	173,6	168,0
SAMPLE C PM T1 Up Stream	240,0	264,4	185,1	163,6	168,0
SAMPLE C PM T2 Up Stream	240,0	258,8	181,2	160,1	168,0
SAMPLE C PM T3 Up Stream	240,0	257,0	179,9	159,0	168,0
SAMPLE C PM T1 Down Stream	240,0	291,6	204,2	180,4	168,0
SAMPLE C PM T2 Down Stream	240,0	303,3	212,4	187,6	168,0
SAMPLE C PM T3 Down Stream	240,0	274,6	192,2	169,9	168,0
SAMPLE C OHAZ T1 Up Stream	240,0	266,2	186,4	164,7	168,0
SAMPLE C OHAZ T2 Up Stream	240,0	261,6	183,2	161,8	168,0
SAMPLE C OHAZ T3 Up Stream	240,0	261,7	183,2	161,9	168,0
SAMPLE D PM T1 LH	240,0	283,7	198,6	175,5	168,0
SAMPLE D PM T2 LH	240,0	282,8	198,0	175,0	168,0
SAMPLE D PM T3 LH	240,0	279,9	195,9	173,1	168,0
SAMPLE D PM T1 RH	240,0	275,8	193,1	170,6	168,0
SAMPLE D PM T2 RH	240,0	278,3	194,9	172,2	168,0
SAMPLE D PM T3 RH	240,0	288,4	201,9	178,4	168,0
SAMPLE D OHAZ T1 RH	240,0	290,5	203,4	179,7	168,0
SAMPLE D OHAZ T2 RH	240,0	300,3	210,3	185,8	168,0
SAMPLE D OHAZ T3 RH	240,0	287,8	201,5	178,1	168,0

API 579-1 fit for service tables used to convert the room temperature yield strength values to their respective value at an operating temperature of 420°C

Table F.2M – Minimum Specified Yield Strength as a Function of Temperature

Material Pointer (PYS)	Temperature (°C)		$\sigma_{yz} = \sigma_{yz}^r \cdot \exp [C_0 + C_1T + C_2T^2 + C_3T^3 + C_4T^4 + C_5T^5]$ (°C, MPa)					
	Min	Max	C_0	C_1	C_2	C_3	C_4	C_5
1	21	593	3.79335351E-02	-1.86385965E-03	6.69470079E-06	-1.82518378E-08	2.31521177E-11	-1.22947065E-14
2	21	593	3.38037095E-02	-1.73554380E-03	8.32638097E-06	-2.11471664E-08	3.29874954E-11	-2.69329508E-14
3	21	593	4.38110535E-02	-2.17153985E-03	1.21747825E-05	-3.89315704E-08	6.43532344E-11	-4.71714972E-14
4	21	816	6.40556561E-02	-2.79373298E-03	4.35401064E-06	-3.71656211E-09	3.92086989E-12	-4.31837715E-15
5	21	816	3.62948800E-02	-1.62644958E-03	6.77655338E-07	8.40865268E-10	3.51869766E-12	-5.66933503E-15
6	21	816	7.27926926E-02	-3.08574021E-03	5.93930041E-06	-4.67184681E-09	-2.21760045E-12	2.81716608E-15
7	21	816	3.71292469E-02	-1.82515595E-03	8.12857283E-06	-2.44881384E-08	3.61939674E-11	-2.06727194E-14
8	21	816	2.74884019E-02	-1.25543600E-03	1.19583839E-06	-4.80520518E-09	1.19491660E-11	-9.51321531E-15
9	21	816	8.85957654E-02	-4.35640722E-03	1.58095415E-05	-3.30171850E-08	3.65796603E-11	-1.65924112E-14

Table F.6 – Minimum Yield and Tensile Strength Values from API STD 530 (1) (2)

Material	Temperature Limits and Room Temperature Strength Parameters (3) (4)	Yield Strength: σ_{yz} (3)		Tensile Strength: σ_{utz} (4)	
		A_0		B_0	
Low Carbon Steel (Figure 4A) A161 A192	$T_{min} = 149^\circ C$ (300° F) $T_{max} = 621^\circ C$ (1150° F) $\sigma_{yz}^{T_{min}} = 157$ MPa (22.8 ksi) $\sigma_{utz}^{T_{min}} = 298$ MPa (43.2 ksi)	A_0	1.6251089E+00	B_0	1.1720989E+00
		A_1	-3.3124966E-03	B_1	-2.0580032E-03
		A_2	5.0904910E-06	B_2	7.6239020E-06
		A_3	-3.3374441E-09	B_3	-9.9459690E-09
		A_4	4.9690402E-13	B_4	3.7189699E-12
		A_5	0.0	B_5	0.0

- Data for tensile and yield strength in this table are from Figures 4A through 4S of API STD 530 *Calculation of Heater Tube Thickness in Petroleum Refineries*.
- Units for the equations in this table are as follows: σ_{yz} and σ_{utz} are in ksi and the temperature, T , is in degrees Fahrenheit (see notes 3 and 4).
- σ_{yz} is the value of the yield stress at temperature where $\sigma_{yz}^{T_{min}}$ is the value of the yield stress (minimum, average, or maximum as applicable) at the minimum temperature limit defined in this table.

$$\sigma_{yz} = \sigma_{yz}^{T_{min}} \cdot (A_0 + A_1T + A_2T^2 + A_3T^3 + A_4T^4 + A_5T^5)$$
- σ_{utz} is the value of the ultimate tensile stress at temperature where $\sigma_{utz}^{T_{min}}$ is the value of the ultimate tensile stress (minimum, average, or maximum as applicable) at the minimum temperature limit defined in this table.

$$\sigma_{utz} = \sigma_{utz}^{T_{min}} \cdot (B_0 + B_1T + B_2T^2 + B_3T^3 + B_4T^4 + B_5T^5)$$
- Data for Figures 4R and 4S are not provided in API STD 530.

Converted upper tensile strength evaluation results of respective service exposed pipe samples

Sample	Minimum Upper Tensile Strength req. of ASTM A516 Gr 65 (MPa) at room temp. of 25 °C	Upper Tensile Strength measured at room temp (MPa)	Upper tensile strength at 420 °C (MPa) (API 579-1 Table F.4)	Upper tensile strength at 420 °C (MPa) (API 579-1 Table F.6)	Minimum Upper Tensile Strength req. of ASTM A516 Gr 65 (MPa) at 420 °C
SAMPLE A PM T1 Up Stream	380,0	454	375,5	386,7	324,0
SAMPLE A PM T2 Up Stream	380,0	458,4	379,2	390,4	324,0
SAMPLE A PM T3 Up Stream	380,0	456,53	377,6	388,8	324,0
SAMPLE A PM T1 Down Stream	380,0	437,7	362,0	372,8	324,0
SAMPLE A PM T2 Down stream	380,0	437,1	361,6	372,3	324,0
SAMPLE A PM T3 Down Stream	380,0	441,6	365,3	376,1	324,0
SAMPLE A OHAZ T1 Down Stream	380,0	440,0	364,0	374,8	324,0
SAMPLE A OHAZ T2 Down stream	380,0	441,3	365,0	375,9	324,0
SAMPLE A OHAZ T3 Down Stream	380,0	441,0	364,8	375,6	324,0
SAMPLE B PM T1 Up Stream	380,0	447,1	369,8	380,8	324,0
SAMPLE B PM T2 Up Stream	380,0	448,0	370,5	381,6	324,0
SAMPLE B PM T3 Up Stream	380,0	442,6	366,1	376,9	324,0
SAMPLE B PM T1 Down Stream	380,0	460,7	381,1	392,4	324,0
SAMPLE B PM T2 Down Stream	380,0	476,9	394,4	406,2	324,0
SAMPLE B PM T3 Down Stream	380,0	474,9	392,8	404,5	324,0
SAMPLE B OHAZ T1 Up Stream	380,0	447,16	369,9	380,9	324,0
SAMPLE B OHAZ T2 Up Stream	380,0	445,54	368,5	379,5	324,0
SAMPLE B OHAZ T3 Up Stream	380,0	446,64	369,4	380,4	324,0
SAMPLE C PM T1 Up Stream	380,0	438,3	362,6	373,3	324,0
SAMPLE C PM T2 Up Stream	380,0	433,6	358,6	369,3	324,0
SAMPLE C PM T3 Up Stream	380,0	429,4	355,2	365,7	324,0
SAMPLE C PM T1 Down Stream	380,0	436,8	361,3	372,0	324,0
SAMPLE C PM T2 Down Stream	380,0	443,9	367,2	378,1	324,0
SAMPLE C PM T3 Down Stream	380,0	444,2	367,4	378,4	324,0
SAMPLE C OHAZ T1 Up Stream	380,0	438,3	362,6	373,3	324,0
SAMPLE C OHAZ T2 Up Stream	380,0	434,9	359,7	370,4	324,0
SAMPLE C OHAZ T3 Up Stream	380,0	432,2	357,5	368,1	324,0
SAMPLE D PM T1 LH	380,0	441,0	364,8	375,6	324,0
SAMPLE D PM T2 LH	380,0	441,6	365,2	376,1	324,0
SAMPLE D PM T3 LH	380,0	445,5	368,5	379,5	324,0
SAMPLE D PM T1 RH	380,0	444,4	367,6	378,5	324,0
SAMPLE D PM T2 RH	380,0	442,0	365,6	376,5	324,0
SAMPLE D PM T3 RH	380,0	446,6	369,4	380,4	324,0
SAMPLE D OHAZ T1 RH	380,0	450,2	372,4	383,5	324,0
SAMPLE D OHAZ T2 RH	380,0	448,2	370,7	381,7	324,0
SAMPLE D OHAZ T3 RH	380,0	452	373,9	385,0	324,0

API 579-1 fit for service tables used to convert the room temperature Upper Tensile strength values to their respective value at an operating temperature of 420°C

Table F.4M – Minimum Specified Ultimate Tensile Strength as a Function of Temperature

Material Pointer (PUS)	Temperature (°C)		$\sigma_{utz} = \sigma_{utz}^{rt} \cdot \exp [C_0 + C_1 T + C_2 T^2 + C_3 T^3 + C_4 T^4 + C_5 T^5]$ (°C, MPa)					
	Min	Max	C_0	C_1	C_2	C_3	C_4	C_5
1	21	593	3.55835868E-02	-8.87531986E-04	-4.52108819E-06	4.67964163E-08	-1.07882077E-10	6.38793289E-14
2	21	593	5.63401650E-02	-2.54673855E-03	4.83029306E-06	1.40154694E-08	-3.85657189E-11	1.47716803E-14
3	21	593	3.35950169E-02	-1.59542267E-03	4.19028077E-06	3.21310030E-09	-2.14741795E-11	9.85350689E-15
4	21	816	6.97780335E-02	-3.33253782E-03	1.20867754E-05	-2.28840524E-08	2.50349101E-11	-1.48927063E-14
5	21	816	7.07824139E-02	-3.31892068E-03	1.44954873E-05	-2.77818452E-08	2.42415074E-11	-1.06232848E-14
6	21	816	5.60554916E-02	-2.64356837E-03	8.21908457E-06	-7.53881321E-09	-3.76242022E-12	3.17742712E-15
7	21	816	6.31803836E-02	-3.38199124E-03	2.55006790E-05	-8.88172175E-08	1.46057908E-10	-9.31091055E-14
8	21	816	6.70451917E-02	-3.62422838E-03	2.89321732E-05	-1.08234025E-07	1.89076439E-10	-1.24630192E-13
9	21	816	8.25387660E-02	-4.23802883E-03	1.71532015E-05	-2.85726267E-08	1.87824828E-11	-5.11800326E-15

Table F.6 – Minimum Yield and Tensile Strength Values from API STD 530 (1) (2)

Material	Temperature Limits and Room Temperature Strength Parameters (3) (4)	Yield Strength: σ_{yz} (3)		Tensile Strength: σ_{utz} (4)	
		A_0		B_0	
Low Carbon Steel (Figure 4A) A161 A192	$T_{min} = 149^\circ C (300^\circ F)$ $T_{max} = 621^\circ C (1150^\circ F)$ $\sigma_{yz}^{T_{min}} = 157 MPa (22.8 ksi)$ $\sigma_{utz}^{T_{min}} = 298 MPa (43.2 ksi)$	A_0	1.6251089E+00	B_0	1.1720989E+00
		A_1	-3.3124966E-03	B_1	-2.0580032E-03
		A_2	5.0904910E-06	B_2	7.6239020E-06
		A_3	-3.3374441E-09	B_3	-9.9459690E-09
		A_4	4.9690402E-13	B_4	3.7189699E-12
		A_5	0.0	B_5	0.0

- Data for tensile and yield strength in this table are from Figures 4A through 4S of API STD 530 *Calculation of Heater Tube Thickness in Petroleum Refineries*.
- Units for the equations in this table are as follows: σ_{yz} and σ_{utz} are in ksi and the temperature, T , is in degrees Fahrenheit (see notes 3 and 4).
- σ_{yz} is the value of the yield stress at temperature where $\sigma_{yz}^{T_{min}}$ is the value of the yield stress (minimum, average, or maximum as applicable) at the minimum temperature limit defined in this table.

$$\sigma_{yz} = \sigma_{yz}^{T_{min}} \cdot (A_0 + A_1 T + A_2 T^2 + A_3 T^3 + A_4 T^4 + A_5 T^5)$$
- σ_{utz} is the value of the ultimate tensile stress at temperature where $\sigma_{utz}^{T_{min}}$ is the value of the ultimate tensile stress (minimum, average, or maximum as applicable) at the minimum temperature limit defined in this table.

$$\sigma_{utz} = \sigma_{utz}^{T_{min}} \cdot (B_0 + B_1 T + B_2 T^2 + B_3 T^3 + B_4 T^4 + B_5 T^5)$$
- Data for Figures 4R and 4S are not provided in API STD 530.

Evaluation results of Elevated Tensile tests performed at 420°C

Sample tested	Yield strength (MPa)	Tensile Strength (MPa)	%Elongation
Sample A OHAZ DS T1	172	323,57	12
Sample A OHAZ DS T2	192,1	320,9	22
Sample A OHAZ DS T3	171,2	324,9	14
Average	178,4	323,1	16,0
Sample D OHAZ R T1	197,6	326,8	18
Sample D OHAZ R T2	195,2	313,2	15,7
Average	196,4	320,0	16,9

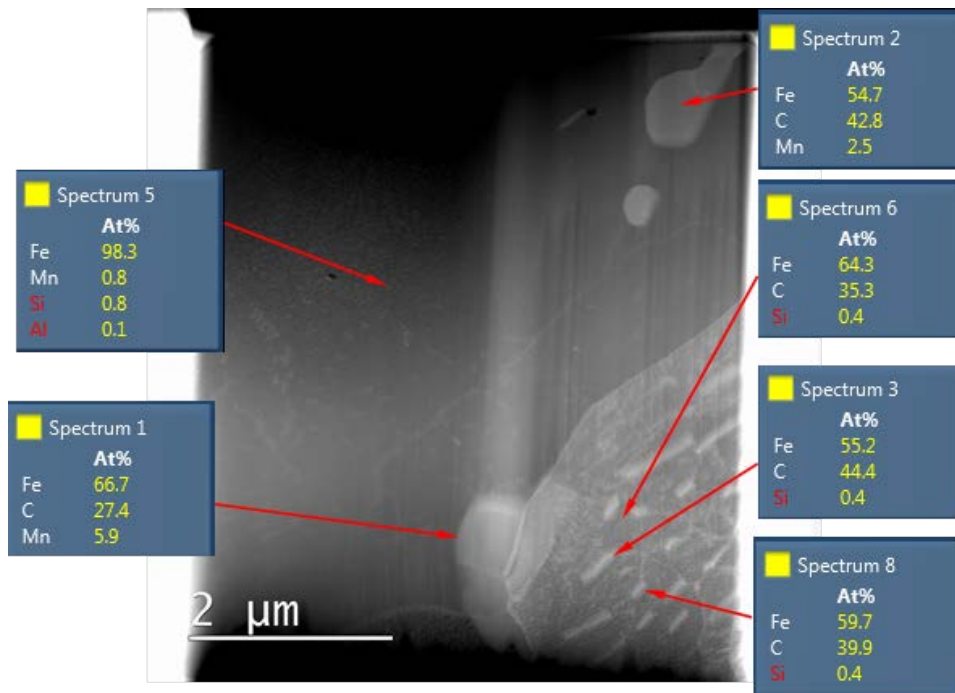
Appendix D

Charpy impact strength evaluation results of the respective service exposed pipe samples

Charpy Impact Sample Name:	Notch Radius (mm)	Angle of Notch	Depth of Notch (mm)	Measured Impact Energy (J)
Sample A Down Stream OHAZ C1	0,2535	44,8 °	1,9589	103
Sample A Down Stream OHAZ C2	0,2535	44,97°	2,028	99,8
Sample A Down Stream OHAZ C3	0,2537	44,88°	1,9935	135
Sample A Up Stream PM C1	0,2532	44,24°	2,03	169
Sample A Up Stream PM C2	0,2554	44,82°	2,009	117
Sample A Up Stream PM C3	0,2529	44,27°	2,02	172
Sample A Down Stream PM C1	0,2554	44,71°	1,95	168
Sample A Down Stream PM C2	0,2501	44,58°	2,02	183
Sample A Down Stream PM C3	0,2554	45,16°	1,97	201
Sample B Up Stream OHAZ C1	0,2511	45,68°	1,986	46
Sample B Up Stream OHAZ C2	0,2511	44,43°	1,95	54
Sample B Up Stream OHAZ C3	0,251	44,33°	1,94	69
Sample B Up Stream PM C1	0,2527	44,49°	1,97	187
Sample B Up Stream PM C2	0,2527	45,17°	1,95	208
Sample B Up Stream PM C3	0,276	44,5°	1,96	172
Sample B Down Stream PM C1	0,2527	45,19°	1,95	135
Sample B Down Stream PM C2	0,2554	44,77°	2,034	118
Sample B Down Stream PM C3	0,2554	45,19°	2,03	124
Sample C Up Stream OHAZ C1	0,2521	45,66°	2,009	54
Sample C Up Stream OHAZ C2	0,242	44,49°	1,97	103
Sample C Up stream OHAZ C3	0,2501	44,76°	1,97	31
Sample C Up Stream PM C1	0,253	44,54°	2,038	102
Sample C Up Stream PM C2	0,263	44°	2,04	83
Sample C Up Stream PM C3	0,2557	45,87°	1,95	92
Sample C Down Stream PM C1	0,271	44,12°	1,967	183
Sample C Down Stream PM C2	0,253	44,7°	2,004	188
Sample C Down Stream PM C3	0,25	45,89°	2,012	175
Sample D RH Outside OHAZ C1	0,25	45,2°	1,97	242
Sample D RH Outside OHAZ C2	0,253	44,9°	1,96	243
Sample D R/H PM C1	0,26	44,07°	1,99	154
Sample D R/H PM C2	0,266	44,3°	1,96	149
Sample D R/H PM C3	0,256	44,3°	2	140
Sample D L/H PM C1	0,272	44,1°	1,96	154
Sample D L/H PM C2	0,269	45,2°	1,975	171
Sample D L/H PM C3	0,253	44°	1,97	72

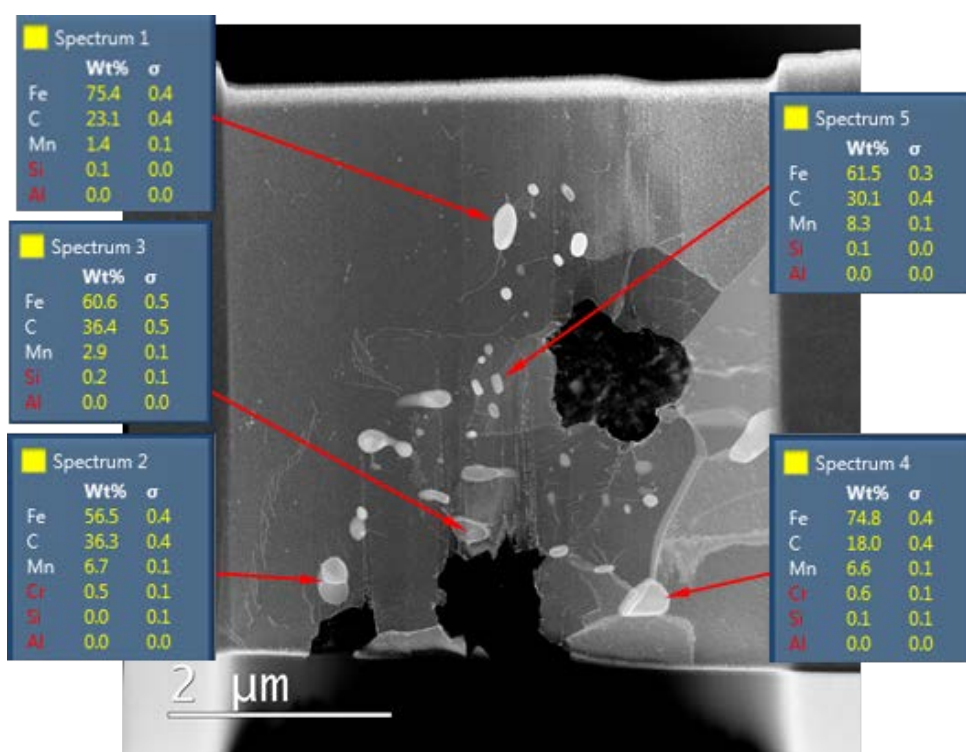
Appendix E

Summary of EDS analyses done on the different microstructural regions of the thin foil sample removed from Sample A's parent pipe material

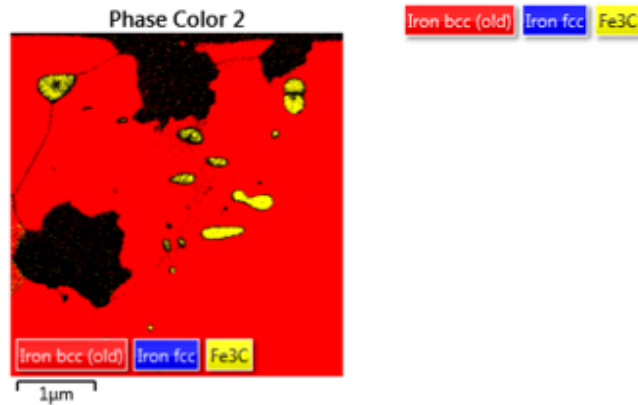


Appendix F

Summary of EDS analyses done on the different precipitates identified in the thin foil sample removed from Sample A's planar graphitized region



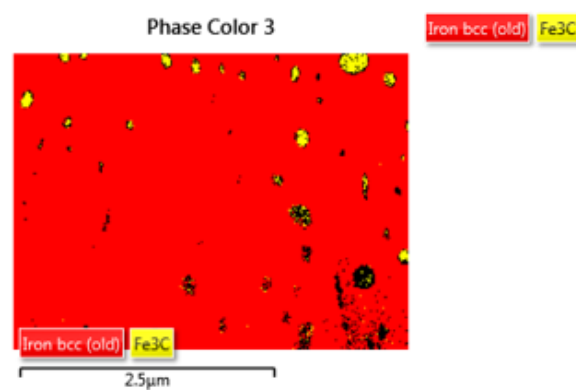
TKD phase analysis results of the thin foil sample taken across a small planar graphitization nodule just outside the HAZ of Sample A



Phase Fraction

Phase Name	Phase Fraction (%)	Phase Count	Mean Band Contrast	Standard Deviation Band Contrast	Min Band Contrast	Max Band Contrast	Mean MAD	Standard Deviation MAD	Min MAD	Max MAD
Iron bcc (old)	80.83	153264	136.43	61.55	36.00	186.00	0.29	0.45	0.06	2.00
Iron fcc	0.01	22	83.59	7.41	69.00	94.00	1.21	0.21	0.71	1.68
Fe ₃ C	2.21	4188	70.85	16.92	30.00	163.00	0.46	0.31	0.07	1.99
Zero Solutions	16.95	32144	56.58	15.30	0.00	167.00				

TKD phase analysis results of the thin foil sample removed from a pearlite grain in the planar graphitization region outside the HAZ of Sample A



Phase Fraction

Phase Name	Phase Fraction (%)	Phase Count	Mean Band Contrast	Standard Deviation Band Contrast	Min Band Contrast	Max Band Contrast	Mean MAD	Standard Deviation MAD	Min MAD	Max MAD
Iron bcc (old)	95.96	48214	142.18	NaN	32.00	202.00	0.33	NaN	0.08	2.00
Iron fcc	0.00	0	0.00	0.00	0.00	0.00	0.00	0.00	0.00	0.00
Fe ₃ C	1.26	633	68.03	12.45	36.00	143.00	0.61	0.41	0.10	1.98
Zero Solutions	2.78	1399	65.03	19.66	0.00	213.00				

EDS analysis of the fine precipitate inside one of the small graphite nodules found inside the previous pearlite region

